

Copyright is owned by the Author of the thesis. Permission is given for a copy to be downloaded by an individual for the purpose of research and private study only. The thesis may not be reproduced elsewhere without the permission of the Author.

*Structural Glaciology, Dynamics and
Evolution of Te Moeka o Tuawe Fox
Glacier, New Zealand*

John Richard Appleby

*Thesis submitted in partial fulfilment of the degree of Doctor of
Philosophy in Geography, at Massey University, Palmerston
North, New Zealand.*

July 2012

“Raki, the Sky Father, wedded Papa-tui-nuku, the Earth Mother. After the marriage, the four sons of Raki who were named Ao-raki, Raki-ora, Raki-rua, and Raraki-roa came down to greet their father's new wife in the canoe of the eldest brother Ao-raki, known as Te Waka o Aoraki. They cruised around Papa-tui-nuku, then, keen to explore, the voyagers set out to sea, but no matter how far they travelled, they could not find land. They decided to return to their celestial home, but the karakia which should have lifted the waka back to the heavens failed and the canoe fell back into the sea and turned over onto its side, and settled with the west side much higher out of the water than the east, thus the whole waka formed Te Waka o Aoraki, the South Island. Ao-raki and his brothers clambered on to the high side and were turned to stone, where they remain today, Aoraki being the highest peak, surrounded by his younger brothers. The permanent snows of these peaks were known as whenuahuka and the great snow fields hukapapa. The glaciers that flowed out of them were called huhapo. Nearby in the darkened valleys was kopakanui or ice and in places cut off from the sun was thick ice of waiuka meaning solid water”

-Māori Mythology

“As a glacier of the first class, the Fox will always take a high position, not only for its scenery, which will attract the non-climbing tourist, but for the scientific lessons to be learned by those who take an interest in such matters”.

-Charlie “Explorer” Douglas, 1896

Abstract

The aim of this thesis is to investigate and identify relationships between glacier structure, dynamics and debris transport at *Te Moeka o Tuawe* Fox Glacier; a temperate, maritime glacier in South Westland, New Zealand. Structural analyses of steep, exceptionally dynamic alpine glaciers that respond rapidly to changes in mass balance are rare. In particular, an appreciable dearth of New Zealand-focussed investigations into structural glaciology and glacial dynamics is found in the literature.

Structural glaciology of Fox Glacier is determined by field observations, analysis of remotely sensed images, and ground-penetrating radar (GPR). Dynamics are investigated and quantified by the measurement of ice flow velocity and surface deformation. Debris transport processes occurring at Fox Glacier are investigated using field and laboratory analysis of grain size and clast morphology.

The structures identified on Fox Glacier during this study display similar patterns to structural features of temperate valley glaciers reported in other studies. Strain-rates measured on the surface of Fox Glacier are higher than those reported for both cold-based glaciers and warm-based alpine-style glaciers in the European Alps. However, strain rates are lower than values typically reported for surging glaciers during surge phases. Unequivocal relationships between measured strain-rates and structures are not evident from this research. This may be because many structures are undergoing passive transport down-glacier, and do not reflect the prevailing local stress regime. Or, some structures, such as crevasse traces, may be close to crevassing, without crevasses actually forming.

Results and findings from this study are a useful addition to the accumulating body of work that has emerged over the last decade on the South Westland glaciers. The vast majority of that research has typically focused on glacier fluctuations in response to climate, or has attempted to link late-glacial moraine-forming events to glacier dynamics. In contrast, the present study has attempted for the first time in New Zealand, to characterise and explain the spatial pattern of structures within a valley glacier in its entirety from the névé to the snout.

Acknowledgements

A large number of people have, either directly or indirectly, provided a great deal of help and advice during my research and the production of this thesis. Thanks go to all of them.

- My supervisors Dr Martin Brook, Dr Ian Fuller and Dr Kat Holt.
- Jackson Wong, Hayden Short, Simon Vale, Andy Fogal, and Robert Dykes for invaluable field assistance.
- Marius Bron, Passang Sherpa and all of the guides of Alpine Guides Westland for local knowledge and field support.
- The pilots and staff of Glacier Helicopters for logistical support.
- Jo Macpherson and the staff of the Department of Conservation South Westland *Weheka* Area Office for allowing research in the Fox Glacier valley.
- Professor Mike Hambrey and Professor Neil Glasser for advice and suggestions during a visit to Switzerland and Aberystwyth University.
- Dr Trevor Chinn for his incredible knowledge of New Zealand glaciology.
- Members of the New Zealand Snow & Ice Research Group (SIRG) for discussion of ideas at annual meetings.
- Dr Anja Möebis (Massey University) for advice and instruction on the use of the particle size analyser.
- Dr Travis Horton (Canterbury University) for laboratory analysis of isotope samples.
- Associate Professor Bob Stewart (Massey University) for very useful discussion on the basal geology of the Fox Glacier region.
- Finally, thanks to Clare for keeping me fed with cake and biscuits, and always being there when I needed her.

Table of Contents

List of Figures	vii
List of Tables.....	xxiii
Chapter 1 : Introduction, Aims and Objectives.....	1
1.1 Introduction	1
1.2 Aims and Objectives	2
1.3 Thesis Structure.....	3
Chapter 2 : Field Site	5
2.1 Introduction	5
2.2 Fox Glacier.....	5
2.3 The Southern Alps of New Zealand.....	8
2.3.1 Glacier Fluctuations in the Southern Alps.....	14
2.3.1.1 Otiran Glaciation and Last Glacial Maximum (LGM)	14
2.3.1.2 Late glacial climate transitions.....	15
2.3.1.3 Neoglaciation in the Southern Alps	16
2.3.1.4 Little Ice Age (LIA) advances.....	16
2.3.1.5 Post-LIA fluctuations.....	20
2.4 Previous Research on the South Westland Glaciers.....	22
2.4.1 Early surveys.....	22
2.4.2 Glaciers and climate.....	23
2.4.3 Dynamics & Structural Glaciology.....	26
Chapter 3 : Current Theories and Methods in Structural Glaciology	27
3.1 Introduction	27
3.2 A Review of Structural Glaciology	27
3.2.1 Introduction.....	27
3.2.2 Primary Stratification (S ₀)	28
3.2.3 Crevasses (S ₂)	29
3.2.4 Crevasse Traces (S ₂)	31
3.2.5 Foliation (S ₁).....	32
3.2.6 Folding (F ₁).....	33
3.2.7 Thrust Faults (S ₃)	34
3.2.8 Arcuate Bands (Ogives).....	37
3.2.8.1 Band Ogives	40
3.2.8.2 Wave Ogives	40
3.2.8.3 Faulting Theory.....	41

3.2.8.4 Other Considerations.....	42
3.2.9 Moulins	43
3.2.10 Boudinage	45
3.2.11 The Ice and Rock Deformation Analogy	46
3.2.12 Review of Previous Structural Evolution Studies	46
3.3 Methods of Structural Investigation	47
3.3.1 Mapping of Surface Structures	48
3.3.1.1 Remote Sensing.....	48
3.3.1.2 Aerial Photography	48
3.3.1.3 Satellite Imagery	48
3.3.1.4 Field Mapping.....	49
3.3.1.5 Presentation of Surface Mapping Results	51
3.3.2 Isotopic Fractionation	53
3.3.2.1 Isotope Analysis of Glacier Ice	54
3.3.2.2 Collection of Isotope Samples	55
3.3.2.3 Isotope Sample Analysis	56
3.3.2.4 Isotope Data Presentation.....	57
Chapter 4 : The Historical and Contemporary Structural Glaciology of Fox Glacier	59
4.1 Introduction	59
4.2 The Historical Evolution of Structures at Fox Glacier.....	59
4.2.1 Structural Changes to Fox Glacier 1896-2006	60
4.2.1.1 1896.....	61
4.2.1.2 1911	63
4.2.1.3 1935.....	63
4.2.1.4 1950.....	65
4.2.1.5 1965.....	68
4.2.1.6 1974.....	70
4.2.1.7 1986.....	71
4.2.1.8 1990.....	73
4.2.1.9 2000.....	73
4.2.1.10 2006.....	75
4.2.1.11 Relative Changes in Ice Surface Elevation	75
4.3 The Contemporary Structure of Fox Glacier.....	77
4.3.1 Structural Domains	77
4.3.2 Contemporary Structural Features of Fox Glacier.....	81
4.3.2.1 Icefalls.....	85
4.3.2.2 Primary Stratification (S_0).....	88
4.3.2.3 Foliation (S_1).....	91
4.3.2.4 Crevasses and Crevasses Traces (S_2).....	93
4.3.2.5 Thrust and Reverse Faults (S_3).....	100
4.3.2.6 Folding (F_1) and Faulting.....	102

4.3.2.7 Arcuate Bands (Ogives)	104
4.3.2.8 Flow-Unit Boundaries	106
4.3.2.9 Supraglacial Drainage Networks	108
4.3.2.9.1 Moulins	108
4.3.2.9.2 Englacial Conduits	110
4.3.2.10 Other Features of Interest	110
4.3.3 Isotopic Fractionation as an Indicator of Internal Structural Deformation ...	113
4.3.3.1 δD and $\delta^{18}O$ Relationships	116
4.4 Discussion on the Structural Glaciology of Fox Glacier	120
4.4.1 Historical Structural Glaciology	120
4.4.1.1 Structural Features	120
4.4.1.2 Terminus Position	122
4.4.2 Contemporary Structural Glaciology	126
4.4.2.1 Icefalls and Valley Over-Deepening	126
4.4.2.2 Foliation (S_1)	128
4.4.2.3 Crevasses and Crevasse Traces (S_2)	128
4.4.2.4 Arcuate Features (Thrust Faults) (S_3)	131
4.4.2.5 Arcuate Bands (Ogives)	133
Chapter 5 : Sedimentology of Fox Glacier	135
5.1 Introduction	135
5.2 Glacial Debris Transport	135
5.2.1 Subglacial Transport	136
5.2.2 Supraglacial and Englacial Transport	137
5.3 Analysis of Glacial Sediments	138
5.3.1 Collection of Samples	139
5.3.2 Clast Analysis	139
5.3.2.1 Clast Data Presentation	140
5.3.3 Grain Size Analysis	141
5.3.3.1 Refractive Index	142
5.3.3.2 Calculation of Fractal Dimensions	142
5.3.3.3 Grain Size Data Presentation	142
5.4 Contemporary Sedimentology of Fox Glacier	144
5.4.1 Supraglacial Debris	144
5.4.2 Subglacial Debris	150
5.4.3 Proglacial Sediments	152
5.4.4 Morphological Analysis of Glacial Sediments	153
5.4.4.1 Proglacial Clast Analysis	154
5.4.4.2 Lower Glacier Clast Analysis	154
5.4.4.3 Victoria Flat Clast Analysis	156
5.4.4.4 Clast Shape and Morphology of Thrust Plane Sediments	158
5.4.4.5 Grain-Size Analysis of Thrust Plane Sediments	159

5.4.5 Trends in glacial sediment morphology along Fox Glacier.....	162
5.4.6 Covariance of Clast Analysis.....	164
5.5 Discussion on the Sedimentology of Fox Glacier.....	165
5.5.1 Sediment Provenance.....	165
5.5.2 Medial Moraine Formation.....	166
5.5.3 Thrusting and Elevation of Subglacial Sediment.....	167
5.5.4 Fluted Moraines.....	168
Chapter 6 : Ground-Penetrating Radar.....	171
6.1 Introduction.....	171
6.2 A Review of Ground-Penetrating Radar.....	171
6.2.1 Introduction.....	171
6.2.2 Principle of Ground-Penetrating Radar.....	172
6.2.3 Ground-Penetrating Radar in Glaciology.....	173
6.2.3.1 Depth Profiling.....	174
6.2.3.2 Structural Glaciology.....	174
6.2.3.3 Hydrology.....	175
6.2.3.4 Periglacial, Paleoglacial and Permafrost.....	176
6.2.3.5 Geophysics in New Zealand Glaciology.....	177
6.2.4 Common Survey Methods.....	177
6.2.4.1 Reflection/Common Offset.....	178
6.2.4.2 Common mid-point.....	178
6.2.4.3 Transillumination/Borehole.....	179
6.2.4.4 Wide Angle Reflection and Refraction.....	180
6.2.4.5 Choice of frequency.....	180
6.2.5 Directional Dependence of GPR.....	181
6.3 Methods of Ground-Penetrating Radar Investigation.....	181
6.3.1 Timing of Surveys.....	181
6.3.2 Survey Type.....	182
6.3.3 GPR Parameters.....	183
6.3.4 Post-processing of Data.....	183
6.3.4.1 Filtering.....	183
6.3.4.2 Gain.....	184
6.3.4.3 Migration.....	184
6.3.4.4 Applying Topography.....	185
6.3.5 Presentation of Results.....	186
6.4 A Ground-Penetrating Radar Survey of Fox Glacier.....	187
6.4.1 Calculation of Radar Velocity.....	187
6.4.2 Antenna Orientation Effects.....	187
6.4.3 Post-Processing of Data.....	190
6.4.4 Locations of GPR Profiles.....	191
6.4.5 Common Offset Surveys.....	192

6.4.5.1 Fox Glacier Névé	193
6.4.5.2 Victoria Flat	207
6.4.5.3 Lower Fox Glacier	213
6.5 Discussion on Ground-Penetrating Radar Surveys	220
6.5.1 GPR in Temperate Glacier Structural Investigations	221
Chapter 7 : Dynamics of Fox Glacier	223
7.1 Introduction	223
7.2 Review of Glacial Dynamics.....	223
7.2.1 Introduction.....	223
7.2.2 Processes of Glacier Motion	223
7.2.2.1 Deformation of Ice	225
7.2.2.2 Deformation of the Bed.....	226
7.2.2.3 Basal Sliding	226
7.2.2.4 Stress and Strain of Glacier Ice.....	227
7.3 Methods for Determining the Dynamic Behaviour of Fox Glacier.....	229
7.3.1 Measuring Ice Deformation.....	230
7.3.2 Calculating Strain	231
7.3.3 Presentation of Results.....	231
7.4 Dynamics of Fox Glacier	232
7.4.1 Lower Fox Glacier and Victoria Flat.....	232
7.4.2 Fox Glacier Névé.....	235
7.4.3 Flow and Deformation of Fox Glacier.....	240
7.4.3.1 Deformation of Polygons	240
7.4.3.2 Ice Flow Velocity.....	243
7.4.3.3 Strain Rate.....	244
7.4.3.4 Strain Orientation.....	245
7.4.3.5 Areal Change.....	245
7.5 Interpretation and Discussion on the Dynamics of Fox Glacier	247
7.5.1 Ice Velocity.....	247
7.5.2 Areal Change	249
7.5.3 Strain Rates.....	250
7.5.3.1 Fox Glacier Strain Rates in a Global Context.....	250
Chapter 8 : General Discussion.....	253
8.1 Introduction	253
8.2 Relationship between Dynamics and Structure.....	253
8.3 The Evolution of Structures on Fox Glacier	255
Chapter 9 : Conclusions	261
9.1 Introduction	261

9.2 Glacier Dynamics and Structure: Summary	263
9.3 Broader Implications of this study	263
9.4 Future Work at South Westland Glaciers	265
References	267
Appendices	303
Appendix 1: Structural Evolution Images	303
Appendix 2: Isotope Analysis Data	313
Appendix 3: Clast Analysis Data	315
Appendix 4: Mathematical Calculation of Strain	321
Appendix 5: Strain Data	325

List of Figures

- Figure 2.1: Location of Fox Glacier (denoted by star) within *Tai Poutini* South Westland World Heritage Area, on the West Coast of New Zealand's South Island, with the approximate location of the Southern Alps Main Divide denoted by the dashed line. 6
- Figure 2.2: Fox Glacier flowing from below Douglas Peak (3077m) on the main divide of the Southern Alps, to its terminus at an altitude of only ~280 m asl. (Photo: J. Appleby, January 2009) 7
- Figure 2.3: Map of Fox Glacier and its associated tributaries and icefalls. 8
- Figure 2.4: Location of Fox Glacier (denoted by star) on the western side of New Zealand's Southern Alps. Snow highlights the Southern Alps, extending almost the entire length of New Zealand's South Island (NASA, 2007). 9
- Figure 2.5: Geological map of the Fox Glacier region showing a down glacier change from interbedded Greywacke and Argillite to various grades of Schist. The Alpine Fault lies at the range front, North West of Fox Glacier (Developed from Cox and Barrell, 2007) 11
- Figure 2.6: Geological cross-profile of Fox Glacier showing; Tt, Triassic greywacke interbedded with argillite; Tt (III), strong schistosity with weak or no foliation; Ya, Pelitic schist and minor psammitic schist; and Q1a, Grey or brown angular gravel, sand and silt associated with sloping alluvial fans (Developed from Cox and Barrell, 2007) 12
- Figure 2.7: West-East gradient of end-of-summer snowlines across the Southern Alps showing a general trend of lower equilibrium line altitudes (ELAs) on the Western side of the Main Divide than on the Eastern Side. Trend lines represent (a) a high ELA year, (b) the steepest slope year, (c) long-term mean ELAs, (d) the year with the least-steep slope, and (e) a year with low ELAs (from Lamont *et al.*, 1999). 14
- Figure 2.8: The timing of Holocene glacier fluctuations in New Zealand's Southern Alps, together with published ^{14}C ages on soils buried by Mount Cook glacier expansion events (11) over the past 4 kyr, and a tree ring reconstruction of austral summer temperature in New Zealand over the past 11 kyr (21), compared with glacier fluctuations in the Northern Hemisphere. Probability plots (bottom) are summary curves of all individual ^{10}Be boulder ages from each moraine dated in New Zealand, while the blue bars show the arithmetic means of the moraine age. The ^{10}Be ages are from Mueller Glacier moraines, except for the 1650-year moraine (Tasman Glacier) and 1370- and 1020-year moraines (Hooker Glacier). For a Northern Hemisphere-Southern hemisphere comparison, the top half shows fluctuations of two index glaciers in the Swiss Alps (Aletsch, and Gorner Glaciers), along with glacier advances in coastal

Alaska and the Canadian Rockies over the same time span (from Schaefer <i>et al.</i> , 2009).	17
Figure 2.9: ‘Fox Glacier, Weheka or Cooks River, Westland, New Zealand’, painted by William Fox (1872), showing the glacier close to its little ice age (LIA) position down-valley of Cone Rock. Fox recorded an earlier trim line in his painting defined by the boundary between vegetation and bare rock on the side of Cone Rock (Alexander Turnbull Library).	18
Figure 2.10: Approximate limits of mid- to late Quaternary ice advances in the greater Aoraki Mount Cook area (A) and the areas immediately adjacent to Fox Glacier (B), derived from geological mapping and geomorphological interpretation, relative to the present topography and coastline (A), and (Developed from Cox and Barrell, 2007). .	19
Figure 2.11: Mean annual departures from the steady-state equilibrium line altitude (ELA) as monitored by the National Institute of Water and Atmospheric Research (NIWA) in annual snowline surveys to 2005, overlain by variations in the Southern Oscillation Index (SOI). The pattern of El Niño years (negative SOI) shows a similarity to those with negative snowline departures, corresponding to positive mass gains (from Purdie <i>et al.</i> , 2008).	21
Figure 2.12: Topographical map of Fox Glacier produced by Douglas and Wilson (1896) showing the extent of glacierized area in the névé and the position of the glacier terminus (Alexander Turnbull Library).	22
Figure 2.13: A 1911 topographical map of Fox and Franz Josef Glacier region showing glacierized extent of névés and the terminus positions of the two glaciers, compiled from surveys by the Geological Department, and Westland Lands & Survey Department (Bell and Grenville, 1911).	23
Figure 2.14: Map of fluctuating terminus positions of Fox Glacier from 1894 to 1967 (from Sara, 1970).	24
Figure 2.15: Map of fluctuating terminus positions of Fox Glacier from 1987 to 2007. The most substantial increase was from 1987 to 1998/1999. This was followed by a retreat, and then a regular advance from 2005 until 2007 (from Purdie <i>et al.</i> , 2008).	25
Figure 2.16: Map of fluctuating terminus positions of Fox Glacier from 17 th Century to 2009 (from Brook and Paine, 2012).	25
Figure 3.1: Primary stratification seen in the collection area of Weissmies, Switzerland. Annual layers including wind-blown dust can be identified. (Photo: M. Hambrey)	28
Figure 3.2: Crevasses in the snowpack of Fox Glacier névé. (Photo: J. Appleby, February, 2011)	29
Figure 3.3: Typical crevasse patterns in a valley glacier. (a) Chevron Crevasses resulting from shear stress exerted by the walls; (b) Transverse Crevasses resulting from a	

combination of shear stress and longitudinal tensile stress (extending flow); and (c) Splaying Crevasses due to a combination of shear stress and longitudinal compressive stress (compressive flow) (after Nye, 1952; Benn and Evans, 1998). 30

Figure 3.4: Snow-filled crevasse trace on Vadret da Morteratsch, Bernina, Switzerland. (Photo: J. Appleby, September, 2009) 31

Figure 3.5: Foliation seen on the surface of Vadret Pers, Bernina, Switzerland. Bands of darker, coarse-bubbly ice can be identified between bands of white ice. (Photo: J. Appleby, September, 2009)..... 32

Figure 3.6: Development of foliation by folding and transposition showing a) horizontally stratified ice; b) folding of stratified ice; c) folds becoming tighter and vertical foliation beginning to develop; and, d) new foliation becomes dominant and only traces of original stratification survive (after Hambrey, 1994)..... 33

Figure 3.7: Folded dirt bands at the advancing front of Crusoe Glacier, Axel Heiberg Island. Originally parallel layers of inter-bedded ice and dirt have become folded as the flow regime of the ice has changed. (Photo: M. Hambrey) 34

Figure 3.8: Debris-rich thrust faults in the lower Fox Glacier. Glacier flow is from right to left. (Photo: J. Appleby, February, 2011) 35

Figure 3.9: Illustration of thrust faults at the terminus showing transport pathways and accumulation of bed-derived debris on the ice surface (after Moore *et al.*, 2010). 37

Figure 3.10: Ogives on Svinafellsjökull, southern Iceland. The distance between successive bands can be seen to increase down-glacier. (Photo: J. Alean)..... 38

Figure 3.11: The flow of a glacier through an icefall causes primary stratification to become rotated and allows basally derived material to be exposed at the surface due to fracture and thrust planes within the body of the ice (from Leighton, 1951). 42

Figure 3.12: Moulin and supraglacial streams on the surface of Fox Glacier. (Photo: M. Brook) 44

Figure 3.13: Supraglacial pond formed from a closed Moulin on the surface of Fox Glacier. (Photo: S. Winkler)..... 44

Figure 3.14: Boudins produced from stratified layers within stretched glacier ice in areas of extending flow. Competence of boudinage increases from D (discrete layer) to A (discrete boudin) (from Hambrey and Milnes, 1975). 45

Figure 3.15: Structural map of Griesgletscher, Switzerland, constructed using standard structural mapping techniques including structural notation (S_0 , S_1 , S_2 ,...etc), and equal-area stereonet projections of feature orientation (from Hambrey and Lawson, 2000). 52

Figure 3.16: Co-isotopic plots of ice, snow and precipitation samples from Flutes and Balgesvarri Glaciers, Lyngen, Norway (from Gordon <i>et al.</i> , 1988).	54
Figure 3.17: Modelled isotopic variation in regelation ice, resulting from the preferential incorporation of heavy isotopes in the first ice to form in each cycle (after Hubbard and Sharp, 1993; Benn and Evans, 1998).	55
Figure 3.18: An example of a bivariate co-isotopic plot ($\delta D/\delta^{18}O$) of a glacier ice sampled on Fox Glacier.	57
Figure 4.1: Source and date of imagery used for reconstruction of structural temporal evolution of Fox Glacier (A selection of these images is reproduced in <i>Appendix One</i>).	61
Figure 4.2: Structural interpretations from a) 1896 showing (1) debris-covered terminus down-valley of Cone Rock, and (2) chaotic crevassing in Lower Icefall; and b) 1911 showing (1) terminus close to Cone Rock, (2) Lower Icefall, and (3) Upper Icefall.	62
Figure 4.3: Photograph of lower Fox Glacier acquired in 1935 from Cone Rock. Chancellor Shelf can be seen at the centre left of the photograph with Douglas peak on the right of the skyline (Photo courtesy of T. Chinn).	65
Figure 4.4: Structural interpretations from a) 1935 showing (1) crevassed and debris-covered terminus level with Cone Rock, and (2) crevassing and debris in Lower Icefall; and b) 1950 showing (1) terminus up-valley of Cone Rock, (2) Lower Icefall, and (3) flow boundaries in névé.	66
Figure 4.5: Oblique aerial photograph of Fox Glacier acquired ~1950 with Cone Rock in the lower right corner and Douglas Peak on the skyline at the head of the glacier (Photo courtesy of T. Chinn).	67
Figure 4.6: Structural interpretations from a) 1965 showing (1) crevassing and debris on the lower glacier, (2) chaotic crevassing in Upper Icefall, and (3) crevassing in the névé; and b) 1974 showing (1) terminus 1 km up-valley of Cone Rock, (2) debris on Victoria Flat, and (3) flow boundaries in névé.	69
Figure 4.7: Fox Glacier from Cone Rock, November 1966 (from Sara, 1970).	70
Figure 4.8: Structural interpretations from a) 1986 showing (1) terminus at its position of greatest retreat, (2) arcuate bands on Victoria Flat, and (3) flow boundaries in the névé; and b) 1990 showing (1) longitudinal structure emanating from Upper Icefall, and (2) crevassing of Explorer Glacier.	72
Figure 4.9: Structural interpretations from a) 2000 showing (1) moraine continuing from Victoria Flat to lower glacier, (2) flow boundaries, and (3) longitudinal structures of unknown origin; and b) 2006 showing (1) terminus crevassed lower glacier, (2) arcuate bands on Victoria Flat, and (3) flow boundaries in névé.	74

Figure 4.10: Change in approximate ice surface elevation between 1896 and 2006 measured approximately at the 1986 terminus position; the time at which Fox Glacier was at its position of greatest retreat (Developed from Sara (1968; 1970) and Purdie (2005)).	76
Figure 4.11: Composite satellite image of Fox Glacier used for determining surface structural glaciology. The imagery was acquired in 2006 and 2007 using the QuickBird Satellite owned by DigitalGlobe.	78
Figure 4.12: Structural domains identified on Fox Glacier. The three domains comprise the Névé, Victoria Flat and the Lower glacier. (Photo: J. Appleby, January, 2009)	79
Figure 4.13: View looking northeast from Pioneer Ridge towards Mt's Mallory and Barnicoat, which separate the Fox Glacier and Franz Josef Glacier névés. The photograph displays many of the characteristic features of Fox Glacier névé including prominent rock buttresses, deep crevasses and undulating snow slopes. (Photo: J. Appleby, January, 2011)	79
Figure 4.14: Composite panoramic image of part of the lower Fox Glacier showing many of the features typical of this structural domain. Viewed from the true left of the glacier, ice flow is from right to left. (Photo: J. Appleby, January, 2010)	80
Figure 4.15: Structural glaciological interpretation of Fox Glacier surface features identified through field observations and satellite image analysis.	83
Figure 4.16: Icefalls of Fox Glacier: a) Aerial view of the Lower Icefall looking towards the terminus (ice flow from left to right); b) Aerial view of the Upper Icefall and upper part of Victoria Flat (Chancellor shelf is the grassy area above the true-right of the glacier); c) Upper Icefall viewed from Chancellor shelf; and d) Aerial view of part of the Pioneer Icefall viewed from above the Albert Glacier (ice flow from right to left). The prominent rock buttress at the right of the photograph marks the lower end of Pioneer Ridge. (Photos: J. Appleby)	86
Figure 4.17: Composite image of the Pioneer Icefall viewed towards the southeast from beneath Chancellor Dome. The distal end of Pioneer Ridge is visible as the rock buttress at the centre of the photograph. Mount Tasman (3497 m) is the prominent, snow-capped peak to the right of the photograph. (Photo: J. Appleby, January, 2011)	87
Figure 4.18: View of the Lower Icefall looking up glacier. A step in the valley profile has been caused by over-deepening down-valley of the Fox Glacier-Victoria Glacier confluence. (Photo: J. Appleby, February, 2010)	88
Figure 4.19: Primary stratification exposed in a crevasse wall in the névé. Layers of wind-blown dust are interspersed between layers of clean snow and firn. (Photo: J. Appleby, January, 2011)	89

Figure 4.20: Primary stratification visible as dirt layers in séracs at the true right of the Lower Icefall, rotated to almost 90°. The icefall is viewed up-valley from the lower glacier. (Photo: J. Appleby, January, 2011)..... 89

Figure 4.21: Field measurements of primary stratification (S_0). Strike and dip of primary stratification measurements are represented by three-dimensional equal area stereographic projections, where the centre of the circle and the circle itself represent a dip of 90° and 0° respectively. Strike is recorded according to degrees from north. 90

Figure 4.22: Modified primary stratification (S_0) forming longitudinal foliation (S_1), observed in the true right margin of the lower glacier. The proglacial sandur can be seen in the distance. (Photo: J. Appleby, January, 2011)..... 92

Figure 4.23: Transverse foliation observed on Victoria Flat. Clear blue ice is interbedded with coarse white ice. Direction of ice flow is from right to left. (Photo: J. Appleby, June, 2010)..... 93

Figure 4.24: A selection of crevasse types observable on Fox Glacier: a) Chevron Crevasses on the true left of Victoria Flat caused by friction between flowing ice and the valley side (flow is from right to left); b) Transverse crevasses in the zone of longitudinal extension as ice flows from Victoria flat into the Lower Icefall; c) Transverse crevasses in the snow-pack of Fox Glacier névé; and d) Splaying crevasses seen in the true-right of the snout, viewed from the proglacial sandur. (Photos: J. Appleby)..... 95

Figure 4.25: An incipient transverse crevasse forming in the névé. The crevasse has formed an en echelon pattern as the surface has ruptured. Direction of ice flow is from left to right. (Photo: J. Appleby, January, 2011)..... 96

Figure 4.26: Incipient crevasse forming transverse to flow on the lower part of Victoria Flat. At this stage the crevasse is <0.15 m wide. Flow is from right to left. (Photo: J. Appleby, June, 2010)..... 97

Figure 4.27: Intersecting, cross-cutting crevasse traces observed on the lower glacier. Crevasse traces in this area persist for almost the entire width of the glacier. Ice flow is from right to left. (Photo: J. Appleby, January, 2009)..... 98

Figure 4.28: Field measurements of transverse arcuate structures (crevasse traces) (S_2). Strike and dip of crevasse trace measurements are represented by three-dimensional equal area stereographic projections, where the centre of the circle and the circle itself represent a dip of 90° and 0° respectively. Strike is recorded according to degrees from north. 99

Figure 4.29: View of the true-right side of the lower glacier close to the terminus showing up-glacier dipping planar structures, which are interpreted as thrust planes. 100

Figure 4.30: A) Surface expression of thrust fault close to the glacier snout; and B) Close up of the thrust fault showing clear, bubble-free regelation ice and fine subglacial material that has been thrust to the surface. (Photos: J. Appleby, January, 2011)..... 101

Figure 4.31: Folding on the surface of Victoria Flat. The axial plane is normal to the surface when viewed from above. (Photo: J. Appleby, June, 2010)..... 103

Figure 4.32: Offset primary stratification observed on the surface of Victoria Flat close to the base of the Upper Icefall. The parallel faults have created a distinct fault-block. The primary stratification is oriented approximately transverse to ice flow with flow being from bottom right to top left of photograph. (Photo: J. Appleby, June, 2010) ... 103

Figure 4.33: Wave and trough arcuate bands at the base of the Upper Icefall. The person is standing in a trough with the lower slope of a ridge immediately to their right. Ice flow is from left to right. (Photo: J. Appleby, June, 2010) 104

Figure 4.34: Map showing a 550 m longitudinal section of ridge and trough ogives on the upper part of Victoria Flat at the base of the Upper Icefall, identified from satellite imagery. Ice flow is from bottom right to top left. Supraglacial debris on the true left and true right in this area is also mapped (stippled area)..... 105

Figure 4.35: Weak dark and light arcuate band ogives at the lower end of Victoria Flat looking south from above the true right valley side of the Fox Glacier valley. Ice flow is from left to right. Curvature of the bands can be seen to increase down valley. (Photo: J. Appleby, January, 2009) 106

Figure 4.36: Flow-unit boundary (dashed line) delineating the confluence of the Albert and Explorer Glaciers immediately below the distal end of Pioneer Ridge. Flow is towards the camera..... 107

Figure 4.37: Map of flow-unit boundaries in the Fox Glacier névé identified from satellite images and field observations. Flow-unit boundaries down-glacier of Pioneer Ridge converge immediately above the Upper Icefall as flow is constrained in the narrow valley..... 107

Figure 4.38: Pooling of water on the surface of Fox Glacier due to the closure of part of the glacier drainage system. (Photo: S. Winkler)..... 108

Figure 4.40: Englacial conduit exposed on the surface of Victoria Flat beneath the Upper Icefall. (Photo: J. Appleby, January, 2009)..... 110

Figure 4.41: ‘The Trough’ viewed from the up-valley end of Chancellor Shelf looking west towards the Main Divide. The upper part of the Upper Icefall is visible at the right of the photograph with the lower slopes of Chancellor Dome visible on the left. Flow separation has caused stagnation of the extreme true right of the Upper Icefall. (Photo: J. Appleby, January, 2011) 111

Figure 4.42: Longitudinal foliation observable on the surface of ‘The Trough’ looking down-valley towards the narrowest part of the Upper Icefall. The upper end of Chancellor Shelf can be seen on the right of the photograph. (Photo: J. Appleby, January, 2011)..... 112

Figure 4.43: Longitudinal (L1 to L10) and thrust regelation ice (T1 & T2) isotope sample locations on Fox Glacier..... 114

Figure 4.44: Mean and standard deviation of A) $\delta^{18}\text{O}$, and B) δD in snow and ice facies identified on Fox Glacier. 117

Figure 4.45: Bivariate co-isotopic plots ($\delta\text{D}/\delta^{18}\text{O}$) of sample facies identified on Fox Glacier: A) basal ice; B) thrust ice; C) névé; D) Victoria Flat; E) lower glacier, and; F) All longitudinal surface samples constituted of névé, Victoria Flat and lower glacier, showing y-intercept and r^2 value..... 118

Figure 4.46: Bivariate co-isotopic plot of $\delta\text{D}/\delta^{18}\text{O}$ measured at Invercargill, New Zealand, between 2005 and 2008, as part of the Global Network of Isotopes in Precipitation (GNIP) database. Invercargill is the closest location to Fox Glacier with recorded GNIP data (IAEA, 2006). 119

Figure 4.47: Altitudinal variation in mean δD and $\delta^{18}\text{O}$ for sample locations along a longitudinal section of Fox Glacier..... 119

Figure 4.48: Deviation of terminus position between 1896 and 2006 (bottom) relative to 2006 position showing steady retreat from 1896 to 1950, followed by rapid retreat to 1965, and then a pattern of cyclic advance and retreat 1965 to 2006. Terminus position is compared to Southern Oscillation Index (SOI) (middle) showing annual fluctuations in sea surface air pressure between Darwin and Tahiti from 1890 to 2000 (negative values represent El Niño conditions whilst positive values represent a La Niña year), and Interdecadal Pacific Oscillation (IPO) (top) showing annual mean fluctuations in sea surface temperature (SST) between 1890 and 2009 (Developed from Biondi *et al.*, 2001; JISAO, 2010). 124

Figure 4.49: Location of faults bisecting the Fox Glacier Valley and névé (ticks on downthrown side of fault). Fault A is located at the top of the Lower Icefall; Faults B and C are located at the bottom and top of the Upper Icefall respectively; Fault D is extrapolated (dashed line) across the névé from confirmed locations north and south, and runs approximately parallel to the location of the Pioneer Icefall (Developed from Cox and Barrell, 2007)). 127

Figure 4.50: Simplified schematic diagram describing the thrusting of subglacial sediments along arcuate shear planes from the bed to the glacier surface..... 132

Figure 5.1: Covariant plot of RA index (percentage of angular and very angular clasts) against C_{40} (percentage of clasts with c/a ratio ≤ 0.4) for lithofacies in the Laguna San Rafael, Chile, compared with facies envelopes based on data from Benn and Ballantyne

(1994) and Bennett <i>et al.</i> (1997) giving an indication of clast provenance (from Bennett <i>et al.</i> , 1999).	136
Figure 5.2: Examples of clast shape and morphology of surficial debris data presentation for clasts collected on the lower Fox Glacier. Frequency histograms show the frequency of clast shape (well rounded, rounded, sub-rounded, sub-angular, angular, and very angular), with the proportion of angular and very angular clasts represented by RA (%) values. Clast morphology is represented by ternary diagrams and C_{40} values.	141
Figure 5.3: Particle size distribution (A) and double logarithmic ($\log d$ versus $\log N$) plot (B) of basal till from a Patagonian glacier (from Benn and Gemmell, 2002).	143
Figure 5.4: Map of the distribution of supraglacial debris on the lower glacier and Victoria Flat.	144
Figure 5.5: Composite image of the medial moraine located towards the true left of the lower area of Fox Glacier. The view is towards the true left valley side. (Photo: J. Appleby, January, 2010)	145
Figure 5.6: Contour map of supraglacial debris measured on the surface of the lower glacier. Debris thickness increases down-glacier. Steep topography and crevassing prevented debris thickness measurements of the true-left of the moraine.	146
Figure 5.7: Lower glacier medial moraine viewed from below the Lower Icefall looking down-glacier. A distinct boundary can be seen (denoted by dashed line) between darker, supraglacial argillite and greywacke (right) and lighter schist (left) produced by rock fall from Paschendale Ridge. (Photo: J. Appleby, January, 2011)	146
Figure 5.8: A large supraglacial debris deposit on the surface of the Explorer Glacier in the Fox Glacier névé, produced during a rock fall from Mt Barnicoat (2800 m), photographed in 2011. Numerous other debris sources have also been identified in this area (circled), all contributing material to the glacier sedimentary system. (Photo: E. Hawke)	147
Figure 5.9: Large-scale (~6 m high) mega-clast of schist, observed immediately beneath the Lower Icefall. No other individual clasts of this scale were identified on the glacier surface. (Photo: J. Appleby, January, 2011)	147
Figure 5.10: Point of exhumation of englacial debris below the Lower Icefall. This is the point at which supraglacial debris first appears in the lower glacier structural domain. (Photo: J. Appleby, January, 2011)	149
Figure 5.11: In-situ orientation measurement of a clast being exhumed below the Lower Icefall. The clast a -axis azimuth is approximately parallel to the ice flow direction. (Photo: J. Appleby, January, 2011)	149

Figure 5.12: Collecting ice and sediment samples from the entrance of a subglacial tunnel and cave formed by subglacial water action and ice over-riding a bed obstacle at the true-right margin of the lower glacier. (Photo: J. Appleby, January, 2011) 150

Figure 5.13: Poorly-sorted glaciofluvial debris constituting the floor of subglacial tunnels and caves exposed beneath the true right margin of the lower glacier and Victoria Flat. (Photo: J. Appleby, January, 2011) 151

Figure 5.14: Entrained clast exposed in a subglacial cave roof at the true-right margin of the lower glacier. The clast *a*-axis is approximately 0.3 m long and aligned with glacier flow. (Photo: J. Appleby, January, 2011) 151

Figure 5.15: Ridge of proglacial debris (ridge crest denoted by dashed line) approximately 1.5 m high observed immediately in front of the true-right of the glacier snout. The ridge axis is approximately 10 m in length and parallel to glacier flow, forming a feature similar to seasonal flutes as described by van der Meer (1997). The debris in the background is part of the true right lateral moraine bounding the proglacial zone. (Photo: J. Appleby, January, 2011) 152

Figure 5.16: Map of the location of clast analysis samples. Sample location numbers relate to frequency histograms and ternary diagrams in Figures 5.17, 5.18, 5.19 and 5.20..... 153

Figure 5.17: Clast shape (RA) and morphology (C_{40}) of debris measured on the proglacial sandur immediately in front of the true right of the glacier snout. Frequency histograms show the frequency of clast shape (Very Angular, Angular, Sub-Angular, Sub-Rounded, Rounded and Well Rounded), with the proportion of angular and very angular clasts represented by RA (%) values. Clast morphology is represented by ternary diagram and C_{40} value. 154

Figure 5.18: Clast shape (RA) and morphology (C_{40}) of debris measured on the true lower glacier medial moraine. Frequency histograms show the frequency of clast shape (Very Angular, Angular, Sub-Angular, Sub-Rounded, Rounded and Well Rounded), with the proportion of angular and very angular clasts represented by RA (%) values. Clast morphology is represented by ternary diagram and C_{40} value..... 155

Figure 5.19: Clast shape (RA) and morphology (C_{40}) of debris measured on the true right of Victoria Flat. Frequency histograms show the frequency of clast shape (Very Angular, Angular, Sub-Angular, Sub-Rounded, Rounded and Well Rounded as defined by Benn and Ballantyne (1994)), with the proportion of angular and very angular clasts represented by RA (%) values. Clast morphology is represented by ternary diagram and C_{40} value..... 156

Figure 5.20: Clast shape (RA) and morphology (C_{40}) of debris measured on the true left of Victoria Flat. Frequency histograms show the frequency of clast shape (Very Angular, Angular, Sub-Angular, Sub-Rounded, Rounded and Well Rounded as defined by Benn and Ballantyne (1994)), with the proportion of angular and very angular clasts

represented by RA (%) values. Clast morphology is represented by ternary diagram and C_{40} value.....	157
Figure 5.21: Section of a thrust plane exposed in a crevasse wall in the lower glacier. The thrust plain contains a layer of hard, bubble-free regelation ice and a layer of coarse, bubbly clast-rich ice.....	158
Figure 5.22: Clast shape (RA) and morphology (C_{40}) of material found in a thrust plane exposed in a crevasse wall in the lower glacier structural domain. Frequency histogram shows the frequency of clast shape (Very Angular, Angular, Sub-Angular, Sub-Rounded, Rounded and Well Rounded), with the proportion of angular and very angular clasts represented by RA (%) values. Clast morphology is represented by ternary diagram and C_{40} value. Sample size $n = 30$	159
Figure 5.23: Grain-size distribution of sediments sampled from the surface expressions of thrust planes on the lower Fox Glacier. Frequency histograms represent sample locations Thrust 1, Sample A and B (A, B); Thrust 2, Sample A and B (C, D); and Thrust 3, Sample A and B (E, F).....	160
Figure 5.24: Double logarithmic plots of grain size versus grain frequency. Plots represent sample locations Thrust 1, Sample A and B (A, B); Thrust 2, Sample A and B (C, D); and Thrust 3, Sample A and B (E, F).	161
Figure 5.25: Cross profile of the Lower Fox Glacier and Victoria Flat showing results of clast roundness measurements. Frequency histograms A, B, and C represent Victoria Flat, Lower glacier and Proglacial Area sample locations, respectively.	163
Figure 5.26: Covariance plot of C_{40} against RA for debris measured at sample locations 1 to 11 (<i>refer Figure 5.16</i>). The covariance of each location has been plotted with facies envelopes described by Glasser <i>et al.</i> (2006)	164
Figure 6.1 A) Transmission of high frequency radio waves from a transmitter T_x , reflected by a feature, and detected by a receiver R_x . B) A simplified, typical profile produced from the feature seen in A).....	172
Figure 6.2: Common offset survey in which the transmitter and receiver are kept at a constant separation and moved along the survey line at a constant step size.	178
Figure 6.3: Common mid-point survey in which the transmitter and receiver are moved apart at a constant rate to determine the wave velocity through a specified material or substance.	179
Figure 6.4: Pulse EKKO Pro ground-penetrating radar unit being used to identify englacial structures on a part of Fox Glacier N�ev�e using common-offset reflection surveys. (Photo: J. Appleby, January, 2009).....	182
Figure 6.5: (a) Unformatted GPR profile from the lower Fox Glacier and (b) the same profile with GPS derived topographical data applied.	186

Figure 6.6: Varying profiles produced from the same 20m transect using a 100 MHz antenna, according to antenna orientation. Profile letter (A, B, C or D) relates to the corresponding antenna orientation shown according to relative position along the transect line. Orientation A is the conventional method as described by Sensors & Software Inc. (Anonymous, 2003). Transmitter and receiver are represented by Tx and Rx respectively. 189

Figure 6.7: Map showing the locations of ground-penetrating radar surveys undertaken on Fox Glacier: A) the Lower Glacier & Victoria Flat, and B) Fox Glacier névé. 192

Figure 6.8: Location of GPR Transects undertaken on Fox Glacier Névé. Transect names correspond to profiles N1 to N9 as shown in Figures 8.5 to 8.8. 193

Figure 6.9: Approximate location of transects N8 and N9 as an example of the surface of the Fox Glacier névé (person for scale). The skyline ridge forms part of the Main Divide of the Southern Alps, with the glacier flowing left to right (east-west) across the photograph. (Photo: J. Appleby, January, 2009)..... 194

Figure 6.10: Interpreted ground-penetrating radar profiles N1, showing parallel (a) and dipping (b and c) reflectors. 195

Figure 6.11: Interpreted ground-penetrating radar profiles N2, showing cross-cutting dipping reflectors (b)..... 196

Figure 6.12: Interpreted ground-penetrating radar profiles N3, showing various parallel reflectors..... 197

Figure 6.13: Interpreted ground-penetrating radar profiles N4, showing broken parallel reflectors (a). 198

Figure 6.14: Interpreted ground-penetrating radar profiles N5 collected on the Albert Glacier, showing displaced parallel reflectors (a)..... 200

Figure 6.15: Interpreted ground-penetrating radar profiles N6 collected on the Albert Glacier, showing parallel reflectors interspersed with point reflectors (a). 201

Figure 6.16: Interpretation of ground-penetrating radar profile N7, showing parallel reflectors..... 202

Figure 6.17: Interpretation of ground-penetrating radar profiles N8, showing a large-scale layering event (a), above closely-spaced parallel reflectors (b)..... 203

Figure 6.18: Interpretation of ground-penetrating radar profile N9, showing widely-spaced parallel reflectors and an incipient crevasse (a). 204

Figure 6.19: Primary stratification created by annual layering, observed in exposed crevasse walls in the Fox Glacier névé. (Photo: J. Appleby, January, 2009) 205

Figure 6.20: Low density, incipient transverse crevasses observed on the glacier surface at the head of the Albert Glacier. These crevasses are identified in GPR radargrams N2 as dipping reflectors. (Photo: J. Appleby, January, 2009)	206
Figure 6.21: Location of GPR Transects undertaken on Victoria Flat. Transect names refer to transects V1 to V3 as shown in figures 6.24 to 6.26.	207
Figure 6.22: Approximate location of transect V1 (red line) as an example of Victoria Flat GPR study area. The view is towards the true left valley side with the glacier flowing left to right across the photograph. GPR transects were located so as to avoid interference from supraglacial pools and slush ponds such as those pictured. (Photo: J. Appleby, July, 2009).....	208
Figure 6.23: Crevasses and crevasse traces (arrowed) observed on the surface of Victoria Flat. (Photo: J. Appleby, July, 2009)	208
Figure 6.24: Interpretation of ground-penetrating radar profile V1, showing stacked parabolic reflectors (a) and parabolic reflectors (b). Vertical exaggeration = 2.75, depth of penetration = ~60 m.....	210
Figure 6.25: Interpretation of ground-penetrating radar profile V2, showing various point reflectors and stacked parabolic reflectors. Vertical exaggeration = 5.5, depth of penetration = ~30 m.	211
Figure 6.26: Interpretation of ground-penetrating profile V3, showing a large number of point-source reflectors. Vertical exaggeration = 2.7, depth of penetration = ~43 m.	212
Figure 6.27: Location of GPR Transects undertaken on the lower Fox Glacier. Transect names refer to transects L1 to L3 as shown in figures 6.29 to 6.31.....	214
Figure 6.28: Approximate location of transect L2 (red line) as an example of the lower study area. The view is towards the true right valley side of the Lower Icefall with the glacier flowing diagonally right to left. The break in the ridgeline at centre-right of the photograph is the hanging valley created by the former confluence of the Fox and Victoria Glaciers. (Photo: J. Appleby, July, 2009)	214
Figure 6.29: Interpretation of ground-penetrating profile L1 showing a prominent stacked hyperbolic reflector (a). Vertical exaggeration = 2.2, depth of penetration = ~30 m.....	216
Figure 6.30: Interpretation of ground-penetrating radar profiles L2, showing a steep surface topography. Vertical exaggeration = 1.5, depth of penetration = ~35 m.	217
Figure 6.31: Interpretation of ground-penetrating radar profiles L3, showing a large number of parabolic reflectors (a). Vertical exaggeration = 2.25, depth of penetration = ~40 m.	218

Figure 6.32: Longitudinal englacial channel (arrowed) bisected by radar profile L3. (Photo: J. Appleby, July, 2009)..... 219

Figure 7.1: Modes of glacier motion showing (a) a glacier frozen to the bed flowing due to deformation of ice (U_F); (b) a glacier resting on an unfrozen bed flowing due to deformation of ice (U_F) and basal sliding (U_S), and; (b) a glacier resting on a sediment layer at the ice-bed interface flowing due to a combination of deformation of ice (U_F), basal sliding (U_S), and deformation of subglacial sediments (U_D) (from Boulton, 1996). 224

Figure 7.2: Longitudinal cross section of a valley glacier showing schematic representations of mass balance and gradient (from Hooke, 2005). 225

Figure 7.3: Normal force due to mass of ice z , and shear-stress force x , of a body of ice. Horizontal velocity is defined u , whilst perceived shear stress is demonstrated by the arrowed-box (Hooke, 2005). 228

Figure 7.4: 25 mm plastic ablation stakes drilled into the glacier surface using a Kovac ice auger used for measurement of surface strain (Photo: M. Brook). 229

Figure 7.5: Idealised polygon for measurement of strain rate on the surface of a glacier. Each strain diamond is divided into two triangles (1 and 2) with corners A, B, and C. The changing distance between the corners allows for the calculation of strain rate and cumulative strain. 230

Figure 7.6: An example of the graphical representation of extensional and compressive strain rates mapped on the surface of Mendenhall Glacier, Alaska (from Boyce *et al.*, 2007). 232

Figure 7.7: Strain stake transect locations on the lower Glacier and Victoria Flat..... 233

Figure 7.8: Location of ‘lower glacier’ strain stake transects on the lower Fox Glacier. (Photo: J. Appleby, February, 2009)..... 234

Figure 7.9: Location of ‘Victoria Flat’ strain stake transects on Victoria Flat, viewed from Chancellor Shelf near Chancellor Hut. The lower part of the Upper Icefall can be seen at the bottom left of the photograph, below Paschendale Ridge. (Photo: J. Appleby, January, 2010)..... 234

Figure 7.10: Strain stake transect locations in Fox névé. The dashed line indicates the location of the ‘Explorer’ stake transect that was not re-surveyed at the end of the study period due to increased crevassing. Crevasses are represented by grey lines, while flow unit boundaries are represented by dashed lines. 235

Figure 7.11: Location of ‘Pioneer’ strain stake transect on the Albert Glacier, viewed from Pioneer Ridge looking southwest. Ice flow is from left to right. Scale of transverse crevasses is shown in Figure 7.12. (Photo: J. Appleby, February, 2010)..... 236

Figure 7.12: Location of ‘Pioneer’ strain stake transect on the Albert Glacier, looking northeast towards Pioneer Ridge from the Albert Glacier. Crevasse scale can be seen relative to the people. (Photo: J. Appleby, February, 2010)	236
Figure 7.13: Location of ‘Ridge’ strain stake transect on Pioneer Ridge. Ice flow is from right to left, towards the south face of the ridge. Width of crevasses is shown in figure 5.14. (Photo: J. Appleby, February, 2010).....	237
Figure 7.14: Location of ‘Ridge’ strain stake transect on Pioneer Ridge, looking west towards the distal end of the ridge. (Photo: J. Appleby, February, 2010)	238
Figure 7.15: Location of ‘Albert’ strain stake transect on the Albert Glacier. Ice flow is from left to right. View is southwest towards the Main Divide, with Pioneer Pass and the prominent north buttress of Mt Haast (3114 m) at the top right of the photograph. (Photo: J. Appleby, February, 2010).....	238
Figure 7.16: Location of ‘Albert’ strain stake transect situated on a low gradient terrace viewed from Pioneer Ridge. The skyline is the Main Divide of the Southern Alps, with Douglas Peak (3077 m) being prominent at the left side of the photograph. (Photo: J. Appleby, February, 2010)	239
Figure 7.17: Location of ‘Explorer’ strain stake transect on the Explorer Glacier, looking northwest from Pioneer Hut. Ice flow is from right to left. The strain network was inaccessible for re-surveying due to increased crevassing. (Photo: J. Appleby, February, 2010).....	239
Figure 7.18: Albert Glacier deformation transect showing initial and final (deformed) polygons A to C.	240
Figure 7.19: Ridge deformation transect showing initial and final (deformed) polygons A to C.	241
Figure 7.20: Pioneer deformation transect showing initial and final (deformed) polygons A to C.	241
Figure 7.21: Victoria Flat deformation polygons showing initial and final (deformed) polygons A to D.	242
Figure 7.22: Lower Glacier deformation polygons showing initial and final (deformed) polygons A to D.	242
Figure 7.23: Horizontal ice surface displacement of Fox Glacier determined from ASTER images with a 15 m ground resolution over a 15 day period during the Austral summer. Highest velocities (displacement/time) can be seen through the upper and Lower Icefalls with the lowest in the névé (Developed from Herman <i>et al.</i> , 2011).	244

Figure 8.1: Schematic diagram of the evolution of surface structures of Fox Glacier, beginning in the névé (A) then moving down through the Upper Icefall (B), Victoria Flat (C) and finally the lower glacier (D). 257

List of Tables

Table 3.1: Summary of ogive formation hypotheses, along with hypothesis proponents (developed from Goodsell <i>et al.</i> , 2002).	39
Table 3.2: Descriptive criteria for identification of glacial structures identified from aerial photographs and field observations (Adapted from Goodsell <i>et al.</i> , 2005).	50
Table 4.1: Ice facies sampled for isotope analysis on Fox Glacier, with descriptive characteristics and associated mean δD and $\delta^{18}O$ values relative to Vienna Standard Mean Ocean Water (VSMOW).	114
Table 4.2: Statistics for best-fit linear regression relationships between δD and $\delta^{18}O$. The 95% range for b_1 ($\delta^{18}O$) coefficient is calculated as the mean ± 2 standard errors of the estimate. p is the significance level at which r^2 and F are significant.	115
Table 6.1 Approximate depth of penetration and resolution of data detection, according to choice of antenna frequency. This assumes a resolution of $\frac{1}{4}$ the wavelength.	180
Table 7.1: Average daily (m/d) and annual (m/a) horizontal ice surface velocities of each strain polygon calculated from the changing position of individual stakes.	243
Table 7.2: Surface-parallel logarithmic strain-rates ($\dot{\epsilon}_1$ and $\dot{\epsilon}_2$), orientation of maximum strain of triangles, shear strain-rates and % surface area change of triangle.	245
Table 7.3: Previous strain rate research undertaken on a variety of glacier types and locations.	251

Chapter 1 : Introduction, Aims and Objectives

1.1 Introduction

This research focusses on the dynamics and structural glaciology of Fox Glacier, a temperate, maritime, valley glacier located on the west coast of the South Island of New Zealand. In essence, it is an investigation into what structures are present in and upon Fox Glacier, how Fox Glacier moves and deforms over time, and how these two components are interlinked. In addition, the research provides a test of structural glaciology methods and considers their use on glaciers such as Fox Glacier. Intricate linkages exist between the general dynamic behaviour (how the motion of glaciers varies in time and space) and the structural configuration (the visual representation of strain and deformation) of glaciers, whereby structures can influence flow dynamics, and vice versa. Forces external to the glacier system also exert a strong influence on structure and dynamics, in particular climate and valley topography. The myriad of structures occurring within and expressed upon the surface of valley glaciers are often the most striking feature of valley glacier environments, and can provide a substantial quantity of information with regard to the behaviour and dynamics of these alpine ice bodies.

A considerable amount of research into glacier dynamics and glacier structure has been conducted on polythermal (e.g. Hambrey and others, 2005), surging (e.g. Lawson, 1996, Lawson and others, 1994, Sharp and others, 1988a, Woodward and others, 2002), Arctic (e.g. Hudleston & Hooke, 1980) and alpine glaciers (e.g. Allen and others, 1960, Glasser and others, 2003, Goodsell and others, 2003, Goodsell and others, 2005c, Hambrey & Milnes, 1977, Herbst and others, 2006), however, structural analyses of steep, exceptionally dynamic alpine glaciers that respond rapidly to changes in mass balance are rare. In particular, an appreciable dearth of New Zealand-focussed investigations into structural glaciology and dynamics of valley glaciers is found in the literature.

Studies of New Zealand glaciers have largely focussed on the larger, debris covered glaciers east of the Main Divide of the Southern Alps, and have been concerned with

mass balance and snowline measurements (e.g. Chinn, 1995, Chinn and others, 2005b, Willsman and others, 2008). The only published work on the structural glaciology of a New Zealand glacier prior to Appleby *et al.* (2010) was by Gunn (1964).

There are a number of reasons why glacier structures have been a research focus, because they:

1. can control the distribution of sediment facies within a glacier (e.g. Bennett and others, 1996);
2. can control the delivery of sediments to glacier margins and therefore sediment-landform associations (e.g. Roberson, 2008);
3. provide a way of determining glacier flow dynamics (reviewed in Hambrey and Lawson 2000);
4. may provide information on the conditions leading to ice-shelf collapse (e.g. Glasser & Scambos, 2008);
5. may provide an analogy to deformation within rocks (Hambrey & Milnes, 1977, Herbst and others, 2006); and
6. may provide information for the prediction of future sea level and climate change (e.g. Lemke and others, 2007, IPCC, 2007, Oerlamans, 2001, Vincent and others, 2004, Azam and others, 2012).

1.2 Aims and Objectives

The overarching aim of this thesis is to determine the structure and dynamics of Fox Glacier. To address this aim, a number of specific research objectives have been developed. These are:

1. To document the key aspects of the structure of the glacier, through identifying and classifying different suites of surficial and englacial structures using aerial photography, satellite images, field-based observations, ground-penetrating radar, isotopic fractionation analysis and sedimentary analysis;
2. To assess the appropriateness of ground-penetrating radar as a technique for structural glaciology research in temperate, maritime glaciers;

3. To sample and classify the characteristics and provenance of different glacial sedimentary facies including thrust planes, medial moraines and proglacial deposits, determine the structural processes involved in their transport and deposition and compare these facies and their origin with other glacial environments;
4. To analyse surface strain-rates on Fox Glacier using velocity measurements and deformation polygons and to investigate the relationship between these measured strain-rates and the distribution of visible structures;
5. To analyse the structure and dynamics of Fox Glacier in the context of current theories on structural glaciology including ideas behind the location and cause of specific structures within the valley glacier environment; with the aim of further enhancing knowledge in the field of structural glaciology.

Further to objective five, specific research questions have been posed, including: Which (if any) theory of ogive formation sufficiently explains their presence and location on temperate ice bodies such as Fox Glacier? Are current theories on the formation of shear planes sufficient to explain their occurrence on temperate glaciers? And, can the formation of smaller scale structures such as crevasse traces and foliation be explained by current deformation models?

1.3 Thesis Structure

This thesis is divided into nine chapters. *Chapter Two* introduces Fox Glacier as the study site, describes the glacial history of New Zealand and considers previous glaciological research undertaken in the region. *Chapter Three* reviews existing literature and research relevant to structural glaciology. The chapter then describes the research methods used as part of the structural investigations of this research. *Chapter Four* describes the structural evolution of Fox Glacier over a ~110 year period, along with the contemporary structures observable at Fox Glacier. This chapter is intended to provide a ‘complete’ investigation into the contemporary and historical structural glaciology of Fox Glacier, by discussing the presented results in terms of existing

literature and theories. *Chapter Five* details a study of the sedimentology of Fox Glacier, with the aim of identifying how sedimentary patterns relate to structure and dynamism. *Chapter Six* introduces the technique of ground-penetrating radar and reviews its use as a tool for investigating glacial structures, then describes the results of a ground-penetrating radar survey of the structural glaciology of Fox Glacier. *Chapter Seven* outlines the theories behind strain-rate investigations on glaciers, describes the methods used for measuring strain-rate and presents results of a strain-rate study at Fox Glacier. *Chapter Eight* provides interpretation and a discussion of the results presented in *Chapters Four, Five, Six and Seven*. Following this, *Chapter Nine* provides general conclusions and a summary of the key findings of the research and suggests areas of interest for future research, both on Fox Glacier and overseas. Each chapter is intended to provide a distinct investigation into a certain aspect of the structural glaciology or dynamic behavior of Fox Glacier; Investigations which, when combined into a general discussion will provide a great deal of additional knowledge and understanding of the Fox Glacier system.

Chapter 2 : Field Site

2.1 Introduction

Chapter Two describes the geographical, glaciological and geological setting of Fox Glacier and discusses how the glacier has adjusted over time to changing climatic and synoptic patterns. The change of other New Zealand glaciers and the Southern Alps as a whole, due to changing climatic conditions is also discussed. Finally, *Chapter 2* outlines research previously conducted on Fox Glacier along with other glaciers of New Zealand's Southern Alps.

2.2 Fox Glacier

Fox Glacier is located in *Tai Poutini* South Westland National Park (a UNESCO World Heritage Area), on the West Coast of New Zealand's South Island (Figure 2.1). The glaciers of South Westland can be classified as temperate and maritime (e.g. Oerlemans, 2001) due to their location at approximately 43° south, and little more than 17 km from the west coast of the South Island, adjacent to the Tasman Sea.

The longest of the West Coast Glaciers, Fox Glacier (Figure 2.2) flows for approximately 13 km from its 68 km² névé (Carrivick & Rushmer, 2007) in a north-westerly direction down a steep, narrow valley terminating at approximately 280 m asl, 17 km from the present coastline. Along its course, the glacier makes a left (westerly) turn, finishing with a westerly aspect. In long-profile, the glacier surface slope is broken by two large icefalls firstly as the névé is channelled into the main valley, and secondly, immediately above the left turn close to the terminus (Figure 2.3). Newton (1939) described Fox Glacier as being “rather more than half the length of Tasman Glacier, but with over twice the fall; A sudden descent meaning broken ice, seracs, and magnificent icefalls”. Between the two icefalls, a subdued, broad area (Victoria Flat) is located between ~1000 m and ~700 m asl, beneath Victoria Falls, where Victoria Glacier was once confluent with Fox Glacier on the true right. At Victoria Flat, the glacier is ~1000 m wide, compared with a width of ~700 m above and ~500 m below. At the terminus

the glacier is approximately 200 m wide, with a steep 50 to 70 m high terminal cliff (at the time of writing).

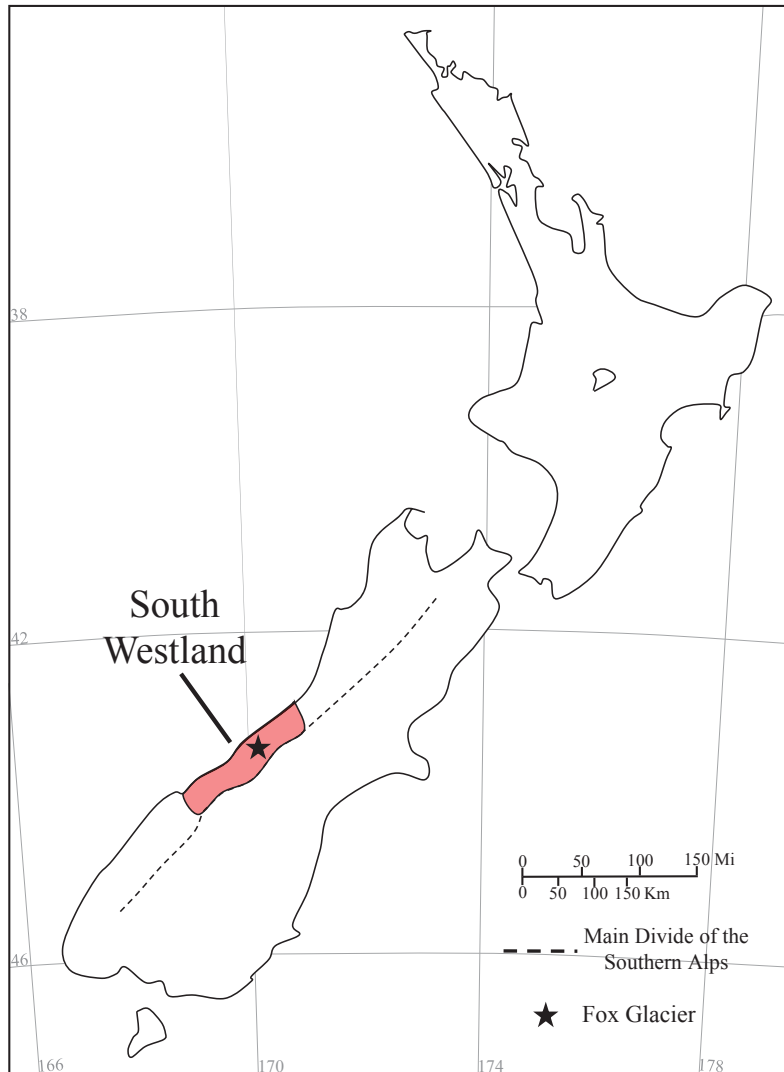


Figure 2.1: Location of Fox Glacier (denoted by star) within *Tai Poutini* South Westland World Heritage Area, on the West Coast of New Zealand's South Island, with the approximate location of the Southern Alps Main Divide denoted by the dashed line.



Figure 2.2: Fox Glacier flowing from below Douglas Peak (3077m) on the main divide of the Southern Alps, to its terminus at an altitude of only ~280 m asl. (Photo: J. Appleby, January 2009)

Originally named the Albert Glacier (also referred to as Prince Alfred Glacier on an early map by Haast (McClymont, 1935)), the name was changed in 1870 in honour of Prime Minister William Fox. The name Albert Glacier is retained in the upper part of the névé, constituting part of the accumulation area along with the Explorer, Abel Janszoon, and Heemskerck Glaciers, all of which merge in an area of heavy crevassing at the névé entrance. At the snout (~280 m asl), water flows from a portal to form the Fox River, which then flows approximately 13 km before joining the Cook *Weheka* River. Fox Glacier flows at a rate of approximately 0.8 m/d during the summer ablation season (Purdie, 2005) and 0.6 m/d during the winter (Purdie and others, 2008b), however, velocities of over 9 m/d have been recorded in the two icefalls (Ruddell, 1995). Purdie, *et al.* (2008a) recorded average surface ablation on the lower glacier of 129 mm/d during the summer and 22 mm/d during the winter.

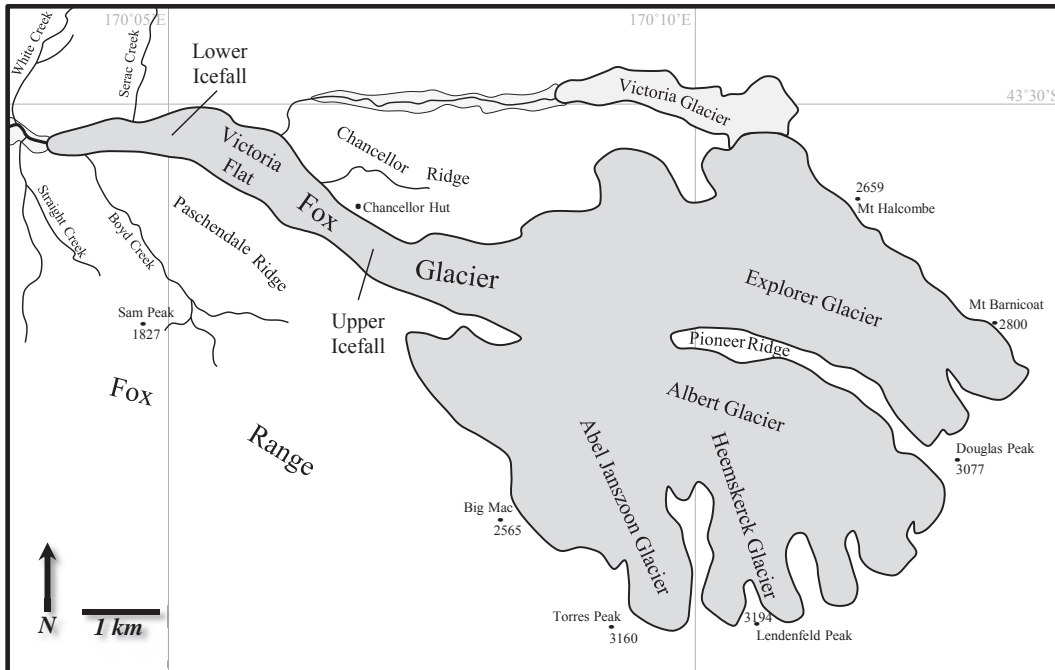


Figure 2.3: Map of Fox Glacier and its associated tributaries and icefalls.

2.3 The Southern Alps of New Zealand

A topographic expression of tectonic convergence during the late Cenozoic (<8 Ma ago) between the Pacific and Indo-Australian crustal plates (Tippett & Kamp, 1995), the Southern Alps extend for approximately 500 km, almost the entire length of the South Island (Figure 2.4). This surface manifestation of a transform fault with a strong compressional component (Cox & Barrell, 2007) is bordered to the west by the line of the Alpine Fault at the mountain front, and to the east by the Canterbury plains.

Constructed principally of greywacke bedrock, the Main Divide of the Southern Alps is being uplifted at a rate of between 0.8 mm a^{-1} and 15 mm a^{-1} , varying with distance from the main fault line (Shi and others, 1996, Tippett & Kamp, 1995, Wellman, 1979). Despite the high uplift rate, the elevation of the Southern Alps is thought to be in 'steady-state', with erosion almost equalling uplift (Furkert, 1947, Adams, 1978, Hales & Roering, 2002, Wellman, 1955). The high rate of erosion is largely a product of the $\sim 15 \text{ m}$ of annual precipitation (Coates & Chinn, 1999, Willsman and others, 2008) experienced in the narrow zone between the Main Divide and the Alpine Fault, which in

turn is a product of the prevailing westerly airflow bisected by the Southern Alps in conjunction with the highly brittle and fractured nature of the uplifted greywacke.



Figure 2.4: Location of Fox Glacier (denoted by star) on the western side of New Zealand's Southern Alps. Snow highlights the Southern Alps, extending almost the entire length of New Zealand's South Island (NASA, 2007).

Significant variation in basement geology of the Fox Glacier valley may be useful in determining the provenance/point of entrainment of glacial debris. The basement geology of the valley comprises quartzofeldspathic greywacke, argillite and schist of the Torlesse terrane (Cox & Barrell, 2007). Metamorphic grade increases from the head of the valley near the main divide, westwards down valley towards the Alpine Fault.

At the head of the valley (around Pioneer Ridge) the rocks comprise inter-bedded Argillite and Greywacke to low-grade schist (Figure 2.5). With increasing distance down-valley, rock becomes dominated by higher grades of schist and semi-schist (Figure 2.6). Importantly, biotite appears approximately around the former Victoria Glacier/Fox Glacier confluence, so any biotite-grade schist on or within the glacier has been sourced from this point or down-valley. At the range front the basement geology transitions to highly quartzose sandstone and mudstone of the Buller Terrane, which are overlain with till deposited during the Last Glacial Maximum, in-filled with floodplain-associated river gravels, incorporating sand and silt units (Cox & Barrell, 2007). The proglacial sandur contains angular gravel, sand and silt associated with sloping alluvial fans.



Figure 2.5: Geological map of the Fox Glacier region showing a down glacier change from interbedded Greywacke and Argillite to various grades of Schist. The Alpine Fault lies at the range front, North West of Fox Glacier (Developed from Cox & Barrell, 2007)

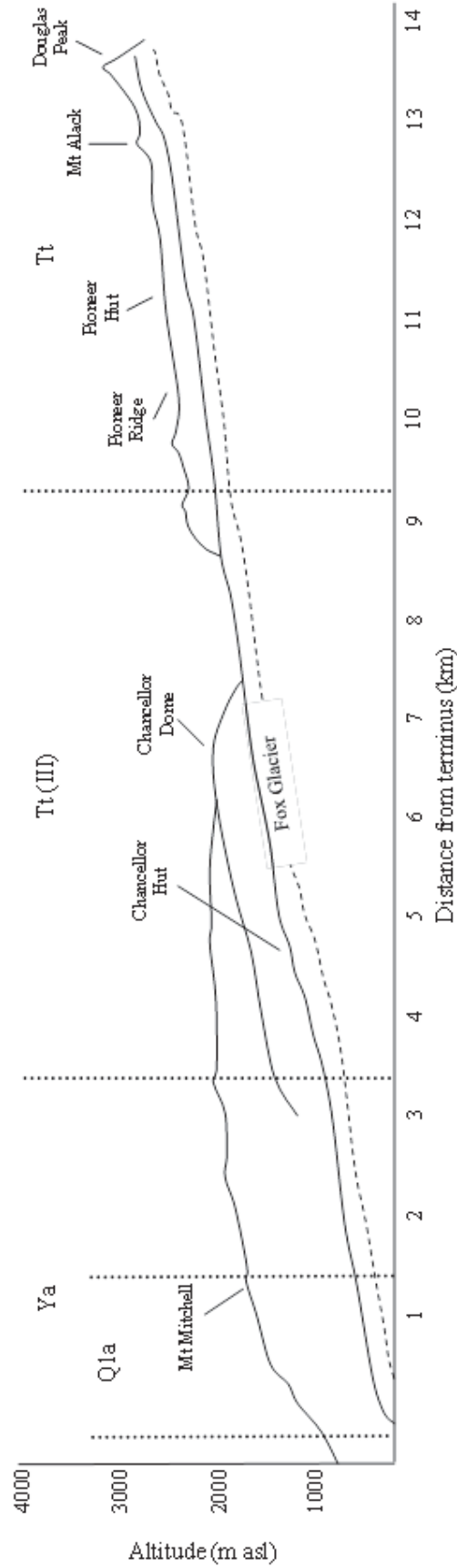


Figure 2.6: Geological cross-profile of Fox Glacier showing; Tt, Triassic greywacke interbedded with argillite; Tt (III), strong schistosity with weak or no foliation; Ya, Pelitic schist and minor psammitic schist; and Q1a, Grey or brown angular gravel, sand and silt associated with sloping alluvial fans (Developed from Cox & Barrell, 2007)

The Main Divide, in excess of 3700 m asl at its highest point (*Aoraki* Mount Cook, 3754 m), provides a topographic barrier to the prevailing westerly and south-westerly air flow, leading to rapid orographic uplift, cooling and precipitation on the westerly (windward) side of the Alps. The high rate of precipitation coupled with the altitude of the Alps means a substantial component of the annual precipitation falls as snow, accumulating in the névé fields. The total number of glaciers (exceeding 0.01 km² in area) in the Southern Alps is thought to be approximately 3,155 (Chinn, 2000); having an estimated area of 1158 km² (Chinn and others, 2005a) and a total volume of 48.74 km³ as of 2005 (Chinn and others, 2008). The volume and area of ice coverage in the region is in constant flux, undergoing cycles of advance and retreat in response to regional climate forcing, though a general pattern of post-1850 retreat has been observed across the region (Chinn, 1996, Chinn and others, 2008, Fitzharris and others, 1992, Gellatly, 1985).

Annual surveys of 50 index glaciers have been undertaken since 1977 (e.g. Willsman and others, 2008) to monitor the flux of ice bodies in the Southern Alps, using altitudes of end-of-summer glacier snowlines (EOSS) as a proxy for annual glacier mass balance measurements. EOSSs represent the equilibrium line altitude (ELA) of the glacier and so the altitude at which accumulation equals ablation (Benn & Evans, 1998). Variations in the level of ELAs in the Southern Alps give an indication as to temporal trends in the change in mass balance and volume. Spatial trends and patterns can also be observed in ELAs such as a West-East gradient (Figure 2.7).

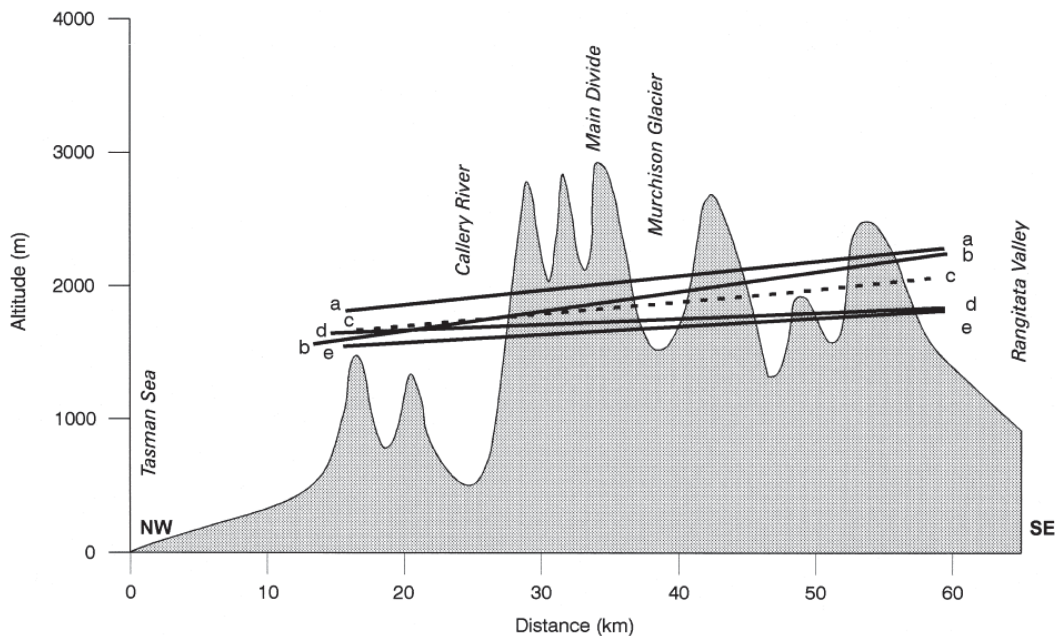


Figure 2.7: West-East gradient of end-of-summer snowlines across the Southern Alps showing a general trend of lower equilibrium line altitudes (ELAs) on the Western side of the Main Divide than on the Eastern Side. Trend lines represent (a) a high ELA year, (b) the steepest slope year, (c) long-term mean ELAs, (d) the year with the least-steep slope, and (e) a year with low ELAs (from Lamont and others, 1999).

2.3.1 Glacier Fluctuations in the Southern Alps

2.3.1.1 Otiran Glaciation and Last Glacial Maximum (LGM)

During the Pleistocene a complex system consisting of extended valley and piedmont glaciers covered much of the South Island, extending approximately 700 km along the length of the Southern Alps and averaged 100 km wide (NZGS, 1973), extending into the Tasman Sea, beyond the present coast. The full extent of the Late Quaternary Southern Alps ice sheet is not fully known, although a detailed chronology has been developed over the last decade (Thomson, 1909, Rother & Shulmeister, 2006, Almond and others, 2001, Newnham and others, 2003, Barrell and others, 2011). The general pattern of late glacial and early Holocene advance and retreat in Westland can be characterised by glacial advance from the Kaihinu Interglacial to the Otiran Glacial. The Kaihinu Interglacial occurred during marine isotope stage (MIS) 5E and 5D, whilst the Otiran Glacial occurred during MIS 3 and 2 (Moar and others, 2008) culminating in the last glacial maximum (LGM) as early as 27 kyr BP. During the Otiran Glacial at least

three ice advances have been suggested; these being at 34 to 28 kyr BP; 24.5 to 21.5 kyr BP; and 20.5 to 19 kyr BP (Fitzsimons, 1997, Suggate & Almond, 2005).

2.3.1.2 Late glacial climate transitions

Between 16 and 14 kyr BP the Kumara 3 advance occurred (possibly involving two separate advances) during which glaciers reached positions close to those attained at the LGM. After 14 kyr BP, however, there was a significant retreat marking the beginning of a post-glacial interval known locally as the Aranui Interglacial (Fitzsimons, 1997). The term 'Aranuian' is only used in New Zealand and a distinction should be made between this and the Holocene as, despite the similarity in dates, the term 'Aranuian' does not refer to the Holocene period. During the Aranui Interglacial there is limited evidence for a small advance around 11 kyr BP that may have been coeval with the Younger Dryas (~12.8-11.5 kyr BP) stage; a cooling period seen extensively in the Northern Hemisphere (e.g. Ivy-Ochs *et al.*, 2008), but opinions on this are still mixed (Applegate and others, 2008, Lowell & Kelly, 2008, Newnham and others, 1999). The Waiho Loop moraine has been interpreted as a consequence of Younger Dryas cooling (Denton & Hendy, 1994) and, as such, provides evidence for synchronicity in climate change between the Northern and Southern Hemispheres (Denton & Hendy, 1994, Broecker, 2000, Newnham and others, 1999), although this remains controversial (Turney and others, 2003, Singer and others, 1998). It is now more widely accepted that the Waiho Loop is linked to the Antarctic Cold Reversal (ACR) advance (Putnam and others, 2010, Kaplan and others, 2010a) Recent work has implicated a major landslide event rather than Younger Dryas cooling as the cause of ice advance and subsequent formation of the Waiho Loop (Barrows and others, 2007, Evans, 2008, Tovar and others, 2008, Vacco and others, 2010). It has been proposed that a major landslide or rock avalanche event may deposit large volumes of material onto the glacier surface (Larsen and others, 2005), which is then carried supraglacially and deposited at the end of the glacier (Shulmeister and others, 2009) to form a terminal moraine such as the Waiho Loop. In addition, a surge mechanism has also been proposed (Gardner & Hewitt, 1990, Hewitt, 2009) whereby this sudden increase in surface debris severely limits ablation, altering the mass balance and causing surge-type behaviour of the ice body, potentially extending the glacier terminus beyond the point it would have otherwise reached within the same climatic parameters.

Further confusing the issues of synchronicity between cooling of the Northern and Southern Hemispheres; the Antarctic Cold Reversal (ACR) is believed to have been active at a similar time to the Younger Dryas (Blunier and others, 1997, Blunier and others, 1999). An important episode of cooling in the Earth's climatic history, the ACR caused a disruption to the Lateglacial (17.5-10 kyr BP) warming trend of the Southern Alps and much of the Southern Hemisphere (Moreno and others, 2009), producing a summer temperature depression of ~2-3 °C (Vandergoes and others, 2008). Blunier *et al.* (1999) suggest Younger Dryas cooling in the Northern Hemisphere began while the ACR was still ongoing, with the ACR ended in the midst of the Younger Dryas.

2.3.1.3 Neoglaciation in the Southern Alps

There is common acceptance that during the latter part of the Holocene Epoch (the last 11.5 kyr), a cooling of the global climate resulted in a growth of Polar and mountain glaciers (Renssen and others, 2007, Clapperton, 1993, Kelly and others, 2008, Porter, 2000). This 'Neoglacial' period of advance followed the hypsithermal or Holocene Climatic Optimum (occurring approximately 6-7 kyr BP (Iriondo, 1999)), and culminated between ~5.4 and 4.9 kyr BP (Porter, 2000), however, Thompson, *et al.* (2006) and Schaefer, *et al.* (2009) suggest Neoglaciation may have occurred as early as 6.4 kyr BP, dependent on location. Schaefer, *et al.* (2009) summarised Holocene glacial fluctuations in the Southern Alps (Figure 2.8) relative to fluctuations of glaciers in North America and Europe during the time period.

2.3.1.4 Little Ice Age (LIA) advances

More recently, a detailed chronology of Little Ice Age (LIA) glacial advances has been detailed for Europe (Grove, 1988, Grove, 2001, Mann, 2002). Very little work exists on glacier fluctuations in New Zealand during this period, and those ages that do exist do not correspond directly with the European LIA models. Dates of LIA maximum cooling events in New Zealand, range from as early as AD1600 (Wardle, 1973, Gellatly, 1985, McKinzey and others, 2004) to the mid-1700s depending on the response time of certain glaciers (Chinn and others, 2005a). The first surveys around the mid- to late-19th and early 20th Century (Figure 2.9) showed most glaciers in the region were still close to their LIA maximum positions (Gellatly, 1985, Chinn, 1996).

Cox & Barrell (2007), summarised the approximate limits of mid- to late Quaternary ice advances in the *Aoraki* Mount Cook area (Figure 2.10), using morphological interpretation. Little Ice Age advances are relatively limited compared to the much greater expanses of ice seen during the last glacial maximum.

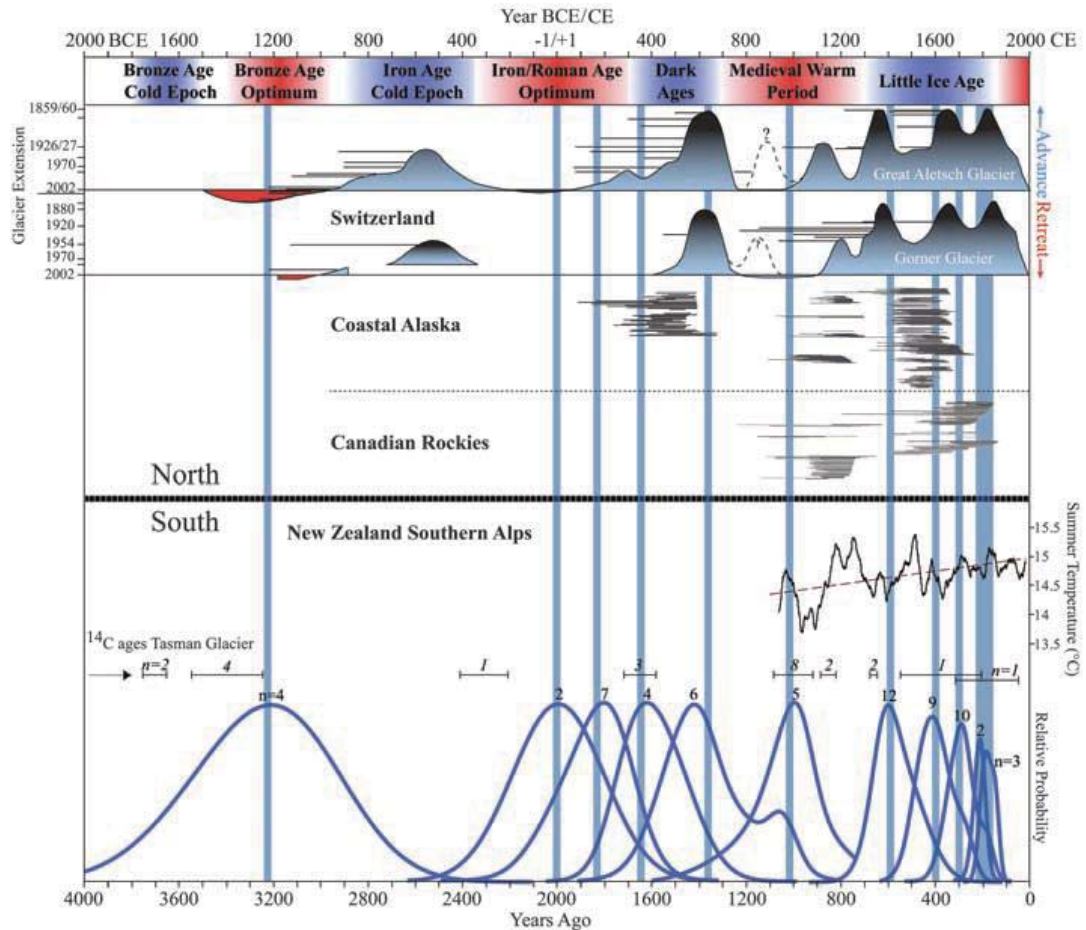


Figure 2.8: The timing of Holocene glacier fluctuations in New Zealand's Southern Alps, together with published ¹⁴C ages on soils buried by Mount Cook glacier expansion events (11) over the past 4 kyr, and a tree ring reconstruction of austral summer temperature in New Zealand over the past 11 kyr (21), compared with glacier fluctuations in the Northern Hemisphere. Probability plots (bottom) are summary curves of all individual ¹⁰Be boulder ages from each moraine dated in New Zealand, while the blue bars show the arithmetic means of the moraine age. The ¹⁰Be ages are from Mueller Glacier moraines, except for the 1650-year moraine (Tasman Glacier) and 1370- and 1020-year moraines (Hooker Glacier). For a Northern Hemisphere-Southern hemisphere comparison, the top half shows fluctuations of two index glaciers in the Swiss Alps (Aletsch, and Gorner Glaciers), along with glacier advances in coastal

Alaska and the Canadian Rockies over the same time span (from Schaefer and others, 2009).

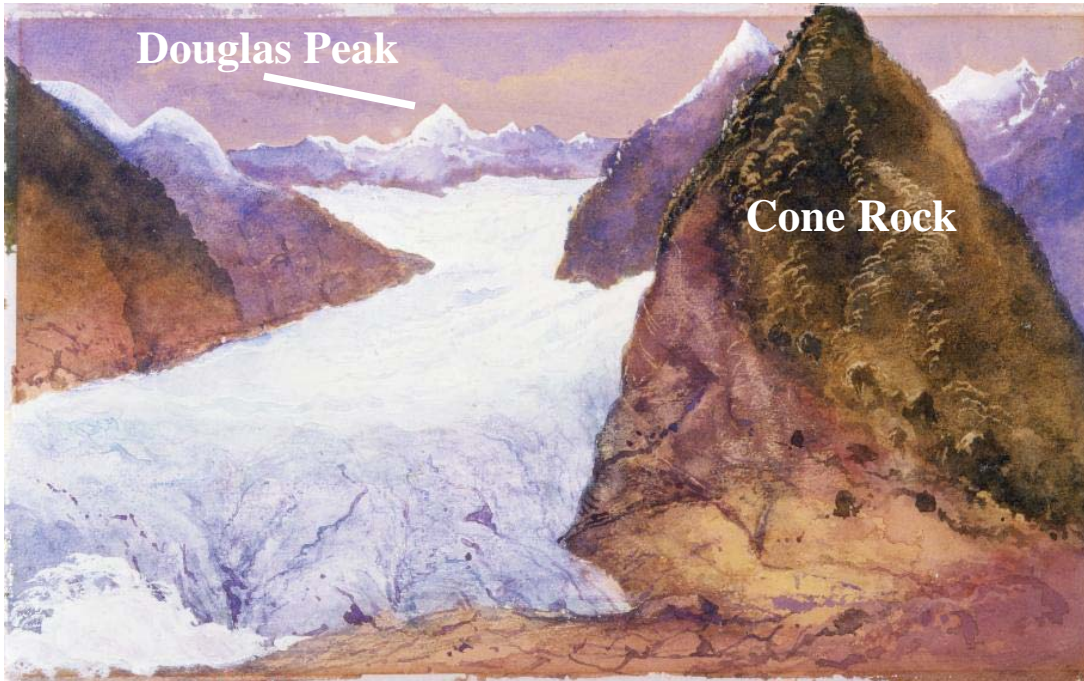


Figure 2.9: 'Fox Glacier, Weheka or Cooks River, Westland, New Zealand', painted by William Fox (1872), showing the glacier close to its little ice age (LIA) position down-valley of Cone Rock. Fox recorded an earlier trim line in his painting defined by the boundary between vegetation and bare rock on the side of Cone Rock (Alexander Turnbull Library).

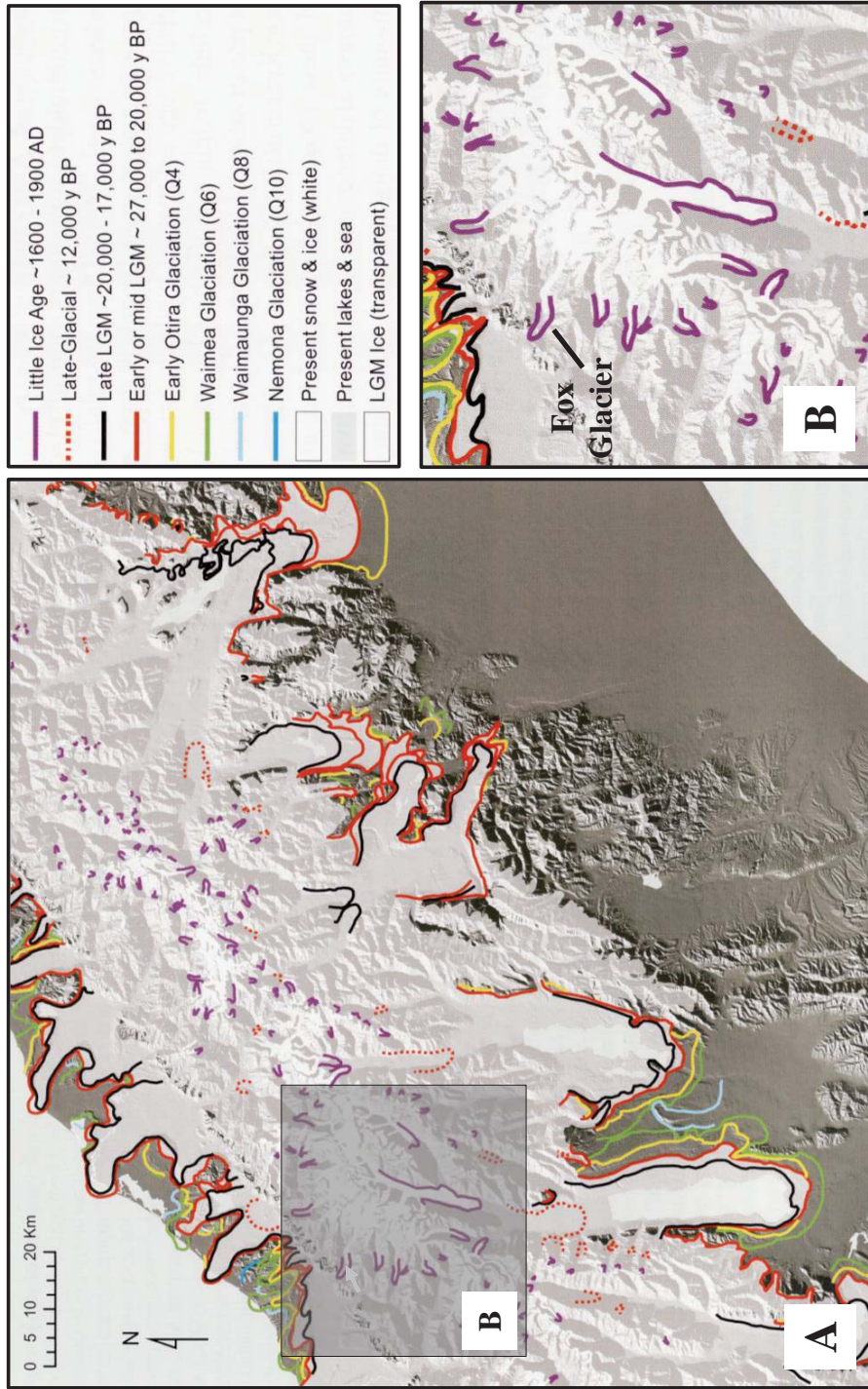


Figure 2.10: Approximate limits of mid- to late Quaternary ice advances in the greater Aoraki Mount Cook area (A) and the areas immediately adjacent to Fox Glacier (B), derived from geological mapping and geomorphological interpretation, relative to the present topography and coastline (A), and (Developed from Cox & Barrell, 2007).

2.3.1.5 Post-LIA fluctuations

These terminus positions remained largely unchanged during the first part of the 20th Century, and not until the 1930s were major frontal retreats seen at most of the larger glaciers of the Southern Alps (Kirkbride, 1993). As with most glaciers globally, the glaciers of the Southern Alps have experienced considerable retreat since the middle of the 20th Century. For the more responsive glaciers, such as Fox and Franz Josef Glaciers, this general 20th Century retreat was interrupted by intermittent re-advances. Franz Josef and Fox Glaciers experienced a substantial advance from 1983 (Chinn, 1995), continuing until the late 1990s / early 2000s when a small retreat occurred, since which they have re-advanced, with Fox Glacier experiencing more than 100 m of advance between 2004 and 2008 (Purdie and others, 2008b, WGMS, 2008). Associated with general 20th Century retreat there has been a loss of between 23% and 32% of glacierised area in the Southern Alps (Chinn, 1996).

A proposed driver for post Little Ice Age fluctuations in terminus position/length is the El Niño Southern Oscillation (ENSO) and the Interdecadal Pacific Oscillation (IPO). During an El Niño year, the Southern Alps experience a more frequent westerly wind during summer bringing more precipitation to the west of the main divide and less to the east. A more consistent southerly wind is seen during the winter, bringing colder conditions to the region (Mullan, 1996). Combined, this increase in summer precipitation and decrease in winter temperatures can impact the mass balance of Southern Alps glaciers (Figure 2.7), lowering ELAs and (following a response period) causing advance of glacier termini (Chinn and others, 2005a, Chinn and others, 2005b). Chinn, *et al.* (2005c) provide the 1983 advance of Franz Josef Glacier as an example of the interaction between meteorological trends and mass balance. A re-advance of some 1200 m between 1983 and 2000 saw Franz Josef Glacier regain ~41% of the length lost since 1900. The five to seven year response time of Franz Josef Glacier (Hooker & Fitzharris, 1999) indicates a mass balance change between 1976 and 1979, coinciding with a phase change of the IPO which occurred in 1976/1977 (Chinn and others, 2005c). Taking this relationship into consideration, the negative phase of the Southern Oscillation Index (SOI) seen during the mid 2000's (Figure 2.11) suggests a period of negative mass balance and glacier recession in the near future.

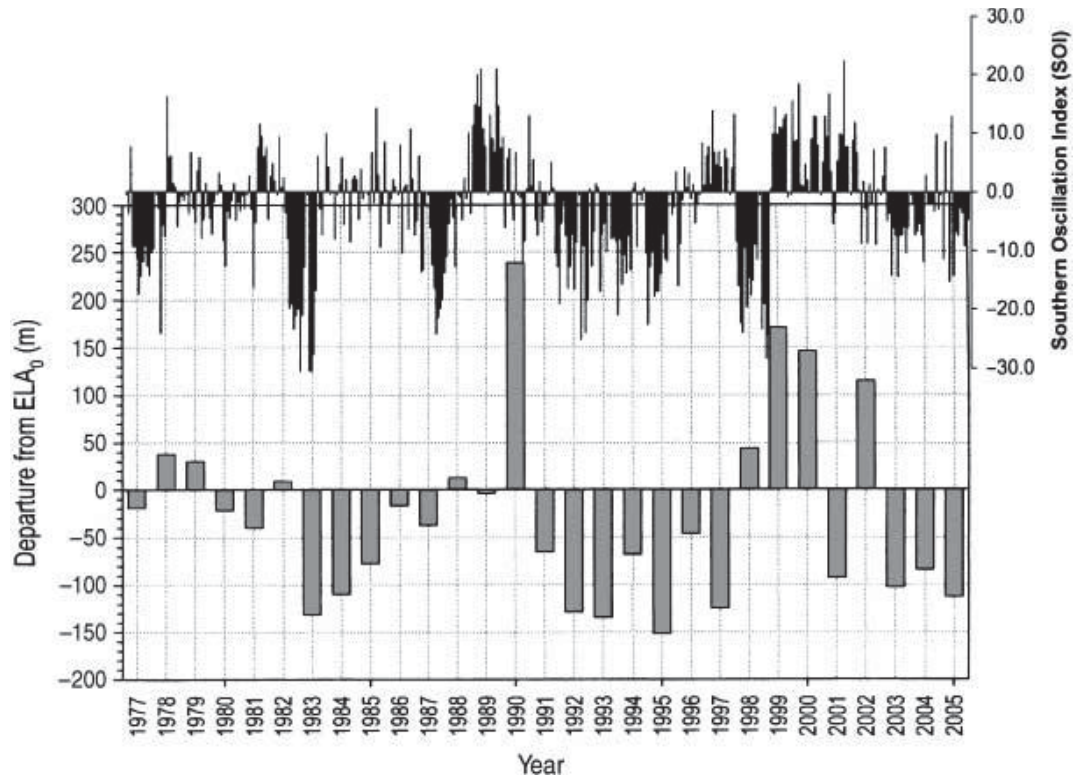


Figure 2.11: Mean annual departures from the steady-state equilibrium line altitude (ELA) as monitored by the National Institute of Water and Atmospheric Research (NIWA) in annual snowline surveys to 2005, overlain by variations in the Southern Oscillation Index (SOI). The pattern of El Niño years (negative SOI) shows a similarity to those with negative snowline departures, corresponding to positive mass gains (from Purdie and others, 2008b).

2.4 Previous Research on the South Westland Glaciers

2.4.1 Early surveys

As with most areas in New Zealand, research in the South Westland Region began in the 19th Century with government-commissioned geographic and geological surveys (e.g. Cox, 1876, Cox, 1877, Fox, 1872, von Haast, 1871, Wilson, 1896). These surveys were carried out by explorers such as Douglas and Wilson (1896) (Figure 2.12) and also government survey departments such as the Lands and Surveys Department (Figure 2.13). These surveys continued into the 20th century with more of a scientific focus (e.g. Lillie and others, 1957, Lillie & Mason, 1955, Wellman & Willett, 1942, Bell & Grenville, 1911).

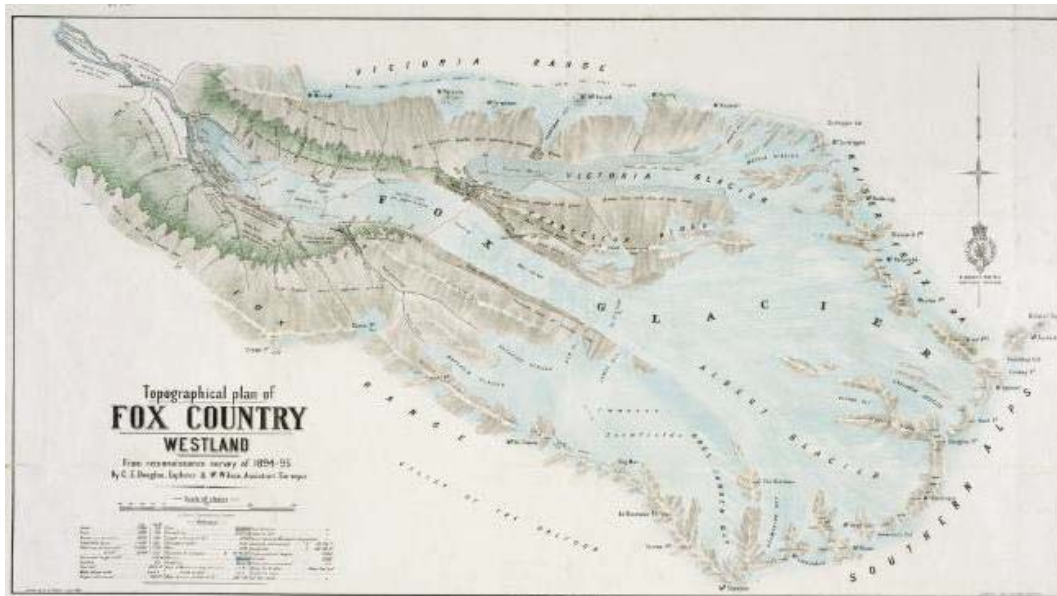


Figure 2.12: Topographical map of Fox Glacier produced by Douglas and Wilson (1896) showing the extent of glacierized area in the névé and the position of the glacier terminus (Alexander Turnbull Library).

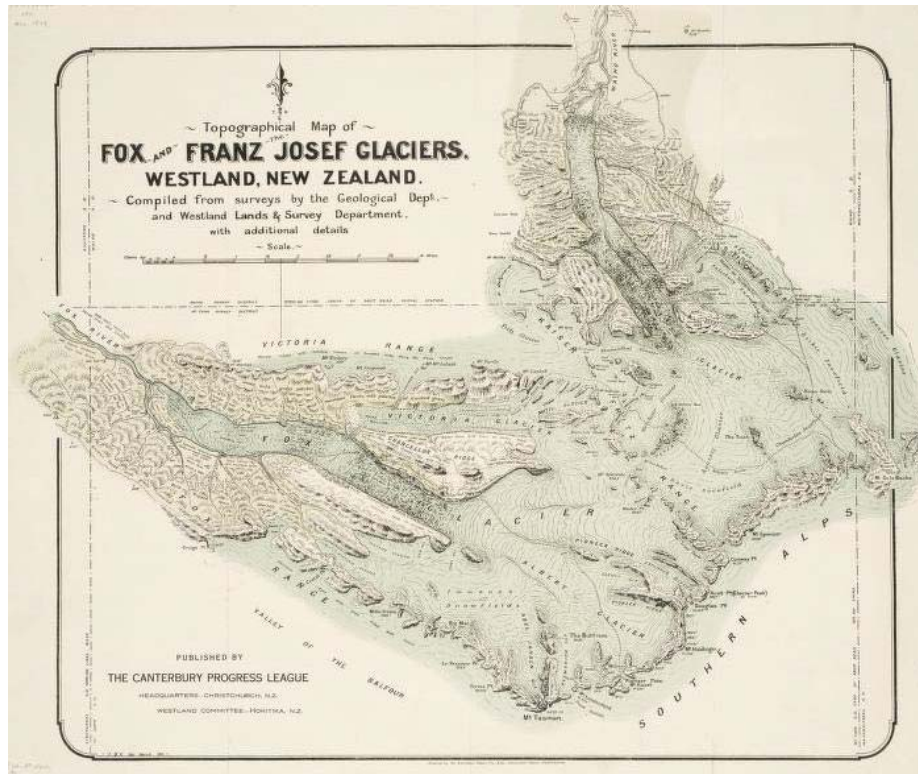


Figure 2.13: A 1911 topographical map of Fox and Franz Josef Glacier region showing glacierized extent of névés and the terminus positions of the two glaciers, compiled from surveys by the Geological Department, and Westland Lands & Survey Department (Bell & Grenville, 1911).

2.4.2 Glaciers and climate

Building on these early investigations, more general discussions of the region have occurred, some with a more glacier-focussed research aim (Coates & Chinn, 1999, Fitzharris and others, 1999, Odell, 1960, Sara, 1968, Sara, 1970, Speight, 1921, Speight, 1934, Speight, 1941, Suggate, 1950) along with more specific investigations into the geomorphology of particular South Westland landforms (e.g. Carrivick & Rushmer, 2007).

Over the last few decades a great deal of interest has developed into the interactions between climate and the glaciers of Westland (e.g. Anderson & Mackintosh, 2006, Batt and others, 2000, Chinn, 1996, Chinn, 1997, Chinn, 1999, Chinn and others, 2008, Chinn and others, 2005b, Fitzsimons, 1997, Ruddell, 1995, Vandergoes & Fitzsimons, 2003), as temperate glaciers with short response times act as indicators for climate fluctuations. The vast majority of these studies have concentrated on Franz Josef

Glacier (e.g. Anderson and others, 2008, Anderson and others, 2006a, Hessel, 1983, Oerlamans, 1997), leaving Fox Glacier largely unstudied.

The effects of variations in the climatic interactions on conditions of the Westland glaciers has been quantified in studies of glacier mass balance (e.g. Cutler & Fitzharris, 2005, Hay & Fitzharris, 1988, Woo & Fitzharris, 1992) and fluctuations or cycles of advance and retreat of the terminal positions of both Fox Glacier (Figures 2.14-2.16) and Franz Josef Glaciers (Chinn, 1995, Gellatly, 1985, Hooker & Fitzharris, 1999, McKinzey and others, 2004, Owens, 2005, Soons, 1971, Wardle, 1973, Bowen, 1960, Ruddell, 1995).

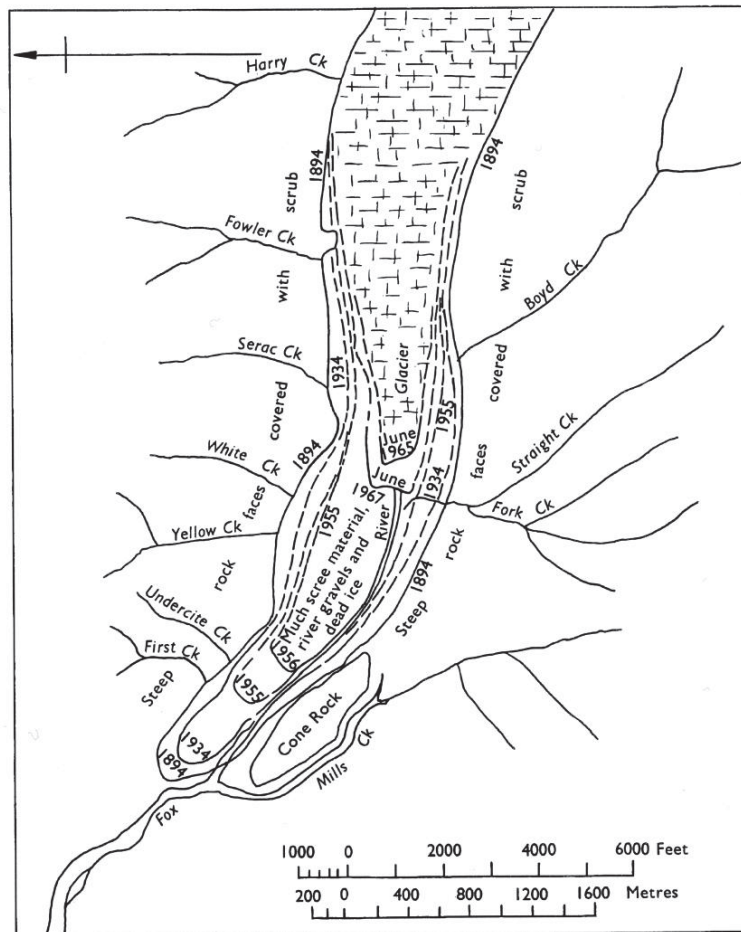


Figure 2.14: Map of fluctuating terminus positions of Fox Glacier from 1894 to 1967 (from Sara, 1970).

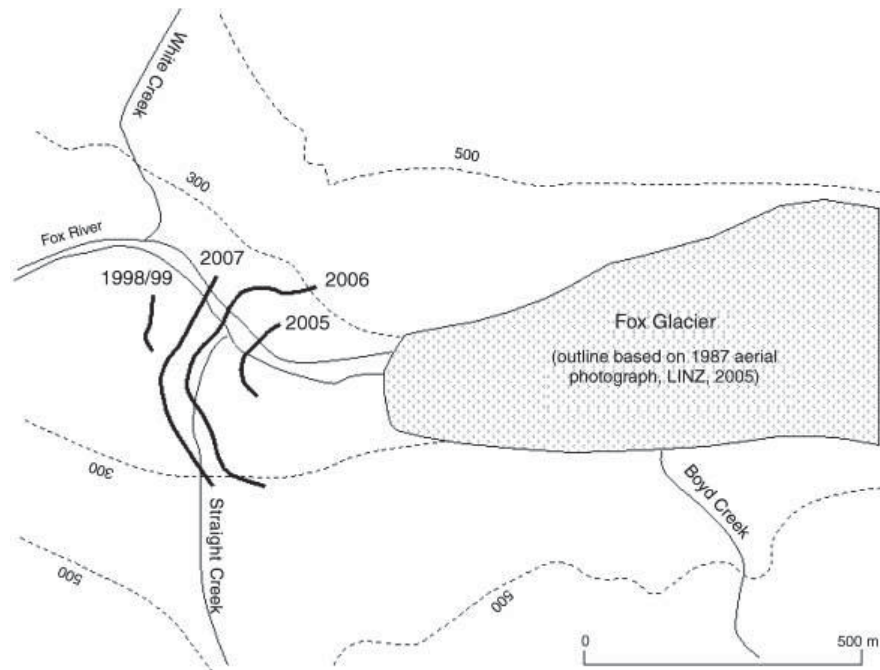


Figure 2.15: Map of fluctuating terminus positions of Fox Glacier from 1987 to 2007. The most substantial increase was from 1987 to 1998/1999. This was followed by a retreat, and then a regular advance from 2005 until 2007 (from Purdie and others, 2008b).

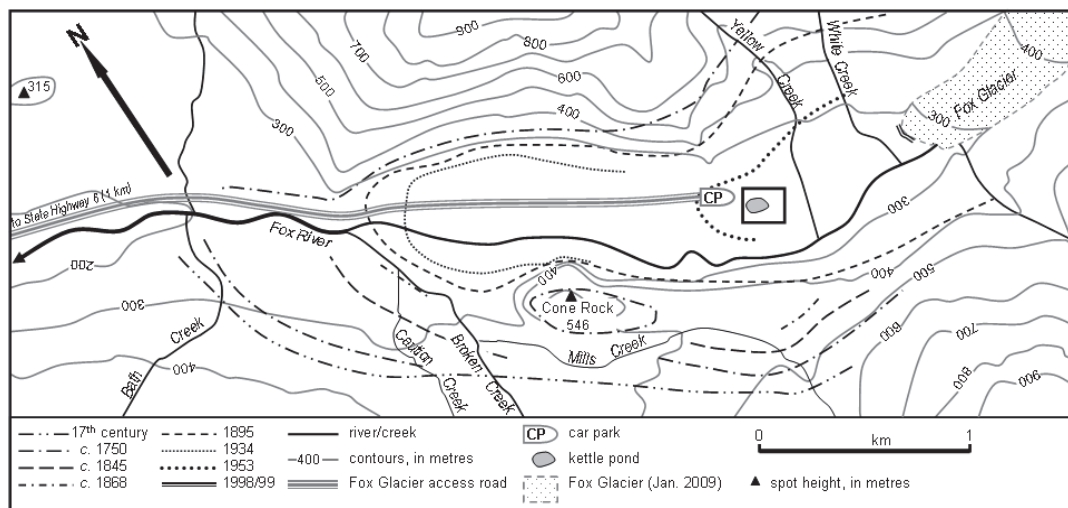


Figure 2.16: Map of fluctuating terminus positions of Fox Glacier from 17th Century to 2009 (from Brook & Paine, 2012).

On a much broader scale, research has considered teleconnections between West Coast glaciers and other glaciers globally (Chinn and others, 2005c, Fitzharris and others, 2007, Hoelzle and others, 2007, Koch and others, 2009), including the influence of global atmospheric circulations and orbital forcing (Clare and others, 2002, Fitzharris and others, 1992, Lamont and others, 1997, Sutherland and others, 2007, Vandergoes & Fitzsimons, 2003) and abrupt Northern Hemisphere climatic events such as the Younger Dryas stage (Applegate and others, 2008, Barrows and others, 2007, Denton & Hendy, 1994, Ivy-Ochs and others, 1999, Kaplan and others, 2010b, Kirkbride, 2010) on the behaviour of these glaciers.

2.4.3 Dynamics & Structural Glaciology

A limited number of structural investigations (mainly concentrating on the routing of subglacial and englacial water) (e.g. Davies and others, 2003, Goodsell and others, 2003, Goodsell and others, 2005a) have been undertaken in the region, with researchers preferring to focus on the dynamic nature including flow rates and ablation of Fox Glacier (e.g. Purdie, 2005, Purdie and others, 2008b, Purdie and others, 2008a) and Franz Josef Glacier (e.g. Evans, 2003, Goodsell and others, 2005a, Ishikawa and others, 1992, Kelliher and others, 1996, Marcus and others, 1985, McSaveney & Gage, 1968, Owens and others, 1992). Interactions and relationships between the structural and dynamic nature of Fox Glacier have also been identified (Appleby, 2007, Gunn, 1964, Appleby and others, 2010). An extension to structural investigation is the ground-penetrating radar work that has been undertaken (e.g. Jol and others, 2004, Nobes, 1999, Nobes and others, 1994) on Franz Josef Glacier, and the glaciers of *Aoraki* Mount Cook National Park.

Linking the structural, dynamic and climatic nature of West Coast glaciers, dating of ice (Morgenstern and others, 2000, Morgenstern and others, 2006) has been undertaken using isotopic analysis to determine residence periods of snow and ice in the glacier system. Initial ice age measurements from Fox Glacier indicated an age of ~800 years (Morgenstern and others, 2000), but this has since been reduced to ~50 years (Morgenstern and others, 2006); a much more acceptable residence time for ice when the glacier's length and velocity are considered.

Chapter 3 : Current Theories and Methods in Structural Glaciology

3.1 Introduction

Chapter Three is concerned with the current theories and literature regarding glacial structures, along with the methods used in their investigation. It provides a review of existing literature describing the structures commonly found within glaciers and a description of the methods used in this structural glaciology study, including the use of field observations and remotely sensed images.

3.2 A Review of Structural Glaciology

3.2.1 Introduction

Glacier ice exhibits a wide variety of internal and superficial structures such as crevasses, icefalls, ogive banding, and layering (e.g. Hooke, 2005), each of which reflect glacier formation and dynamics (Hambrey & Lawson, 2000) including flow and deformation. Although these structural attributes are described extensively in both the glacial and geological literature, the origin and significance of these structures in ice remains unclear (Glasser and others, 1998). A greater understanding of the evolution of these structures will lead to a better knowledge of the behaviour of alpine valley glaciers such as Fox Glacier.

Hambrey and Lawson (2000) categorised structures in glacier snow and ice into two general groups; primary and secondary structures. Primary structures are those structures which experience no deformation and develop from the accumulation of material such as annual layering occurring in the névé of a glacier. Secondary structures are those resulting in the plastic deformation or brittle fracture of snow and ice as a result of glacial motion and movement (*refer Chapter Six*). A system of classification has been used by a number of researchers (e.g. Hambrey & Lawson, 2000, Lawson and others, 1994, Hambrey & Milnes, 1977, Hambrey and others, 2005, Ragan, 1969), to simplify and standardise structural nomenclature. The most common method currently

in use consists of a 'structural level' of S_0 , S_1 , S_2 ...etc. following structural geology notation (e.g. Hatcher, 2007), with primary stratification starting at the S_0 level.

3.2.2 Primary Stratification (S_0)

A snowpack forming from a series of individual precipitation events is usually heavily stratified (Figure 3.1) where single layers accumulating from individual events can be easily identified (Male & Gray, 1981). This is also true at an intra-annual level, whereby winter snowfall can be seen as often thick layers of coarse bubbly snow and ice, whilst summer precipitation or melting demonstrates a coarse, clear appearance as a result of the ablation and recrystallisation of surface snow (Grey & Male, 2004).



Figure 3.1: Primary stratification seen in the collection area of Weissmies, Switzerland. Annual layers including wind-blown dust can be identified. (Photo: M. Hambrey)

3.2.3 Crevasses (S_2)

Crevasses (Figure 3.2) have been defined as V-shaped clefts with a measurable opening (Holdsworth, 1965) formed in the upper, brittle part of a glacier as a result of the fracture of ice (Hambrey & Alean, 2004). This occurs once critical conditions of stress and strain are reached in the surface of the ice mass (Kehle, 1964, Vaughan, 1993), whereby tensile stresses exceed the cohesive strength of the ice (Paterson, 1994), causing the upper layers of ice to permanently deform beyond its elastic limit. Crevasses usually form perpendicular to principal tensile stress directions, and are a good indicator of stress directions (Nye, 1952).



Figure 3.2: Crevasses in the snowpack of Fox Glacier névé. (Photo: J. Appleby, February, 2011)

Three main types of crevasse (Figure 3.3) have been identified at the surface of valley glaciers: chevron (also known as marginal), transverse, and splaying crevasses. In addition, longitudinal and radial crevasses are often found close to the terminus of some valley glaciers. These common crevasse orientations in relation to glacier flow allow for an approximate indication of stress and strain directions within the ice (Benn & Evans, 1998), and give an indication of how ice flow and valley topography interact, affecting the surface morphology of the glacier. Chevron crevasses are the result of retarded flow at the margins due to friction from valley sides: Transverse crevasses result from

longitudinal extensional flow when there is a change in flow velocity, as is often seen above an icefall: Splaying crevasses are characteristic of lateral expansion of the ice, down-flow of a topographic constriction such as a narrow section of valley or a riegel. They are curved, being roughly parallel to flow direction in the glacier centre-line, but oriented at $\sim 45^\circ$ at the glacier margin.

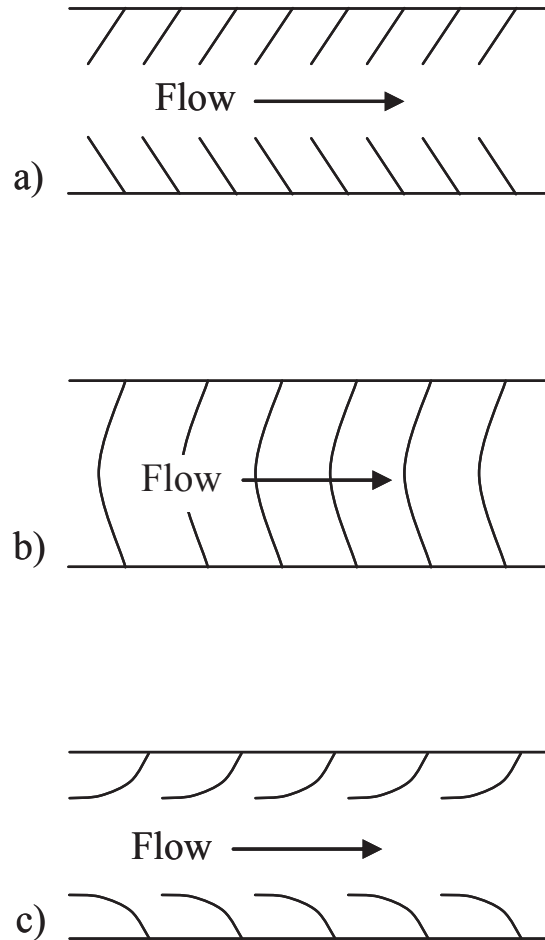


Figure 3.3: Typical crevasse patterns in a valley glacier. (a) Chevron Crevasses resulting from shear stress exerted by the walls; (b) Transverse Crevasses resulting from a combination of shear stress and longitudinal tensile stress (extending flow); and (c) Splaying Crevasses due to a combination of shear stress and longitudinal compressive stress (compressive flow) (after Nye, 1952, Benn & Evans, 1998).

3.2.4 Crevasse Traces (S_2)

Upon closing, crevasses may leave linear ‘scars’ (Figure 3.4) a few centimetres in width, known as crevasse traces (Hambrey, 1994). Traces usually appear as either blue ice layers formed by the freezing of water in the crevasse prior to closure, or as bubbly, white layers indicating a previously snow-filled crevasse (Benn & Evans, 1998). In both cases it is common to find individual particles or clusters of debris that entered the crevasse whilst it was open. Another theory, described by Hambrey and Alean (2004) is that crevasse traces are formed by veins of clear ice formed as a result of fracture and recrystallization of ice without separation of the two walls. This theory is analogous to tensional veins formed in rocks (Hambrey & Müller, 1978). Usually less than 20 cm in width, crevasse traces can often be followed for tens of metres, cross-cutting other structures (Goodsell and others, 2005c) such as primary stratification or other, open crevasses.



Figure 3.4: Snow-filled crevasse trace on Vadret da Morteratsch, Bernina, Switzerland. (Photo: J. Appleby, September, 2009)

3.2.5 Foliation (S_1)

Foliation is identified as alternating, discontinuous layers of bubble-rich and bubble-free white and blue ice (Figure 3.5). In addition, alternate layers of coarse and fine-grained ice may also be seen (Paterson, 1994). Foliation is a structure seen in almost all glaciers (Hambrey & Lawson, 2000), being found parallel or sub-parallel to surface ice flow (Goodsell and others, 2005c). Hambrey and Alean (2004) suggest foliation is likely to be produced in regions of the glacier experiencing exceptionally high stress as a result of shear or compression, such as at the base of an icefall (Paterson, 1994). In addition, Hooke and Huddleston (1978) suggest that foliation develops in areas of pre-existing inhomogeneities, such as sedimentary stratification or crevasse traces which have undergone high strains and may have been rotated by glacier flow. The process by which an existing inhomogeneity is transformed into foliation is called transposition (Figure 3.6). This involves flattening, stretching, and then folding, with the new structure (foliation) developing in the limbs of the folds (Hambrey, 1975).



Figure 3.5: Foliation seen on the surface of Vadret Pers, Bernina, Switzerland. Bands of darker, coarse-bubbly ice can be identified between bands of white ice. (Photo: J. Appleby, September, 2009)

A contrasting theory is that foliation may be an entirely new structure not related to any existing inhomogeneity (Goodsell, 2005, Ximenis and others, 2000), whereby folia

consisting of layers of bubble-rich and bubble-free ice. Most prominent in englacial and supraglacial ice in ablation areas (Benn & Evans, 1998), foliation of this type may also be seen deep in crevasse walls in the accumulation area (Hooke, 2005).

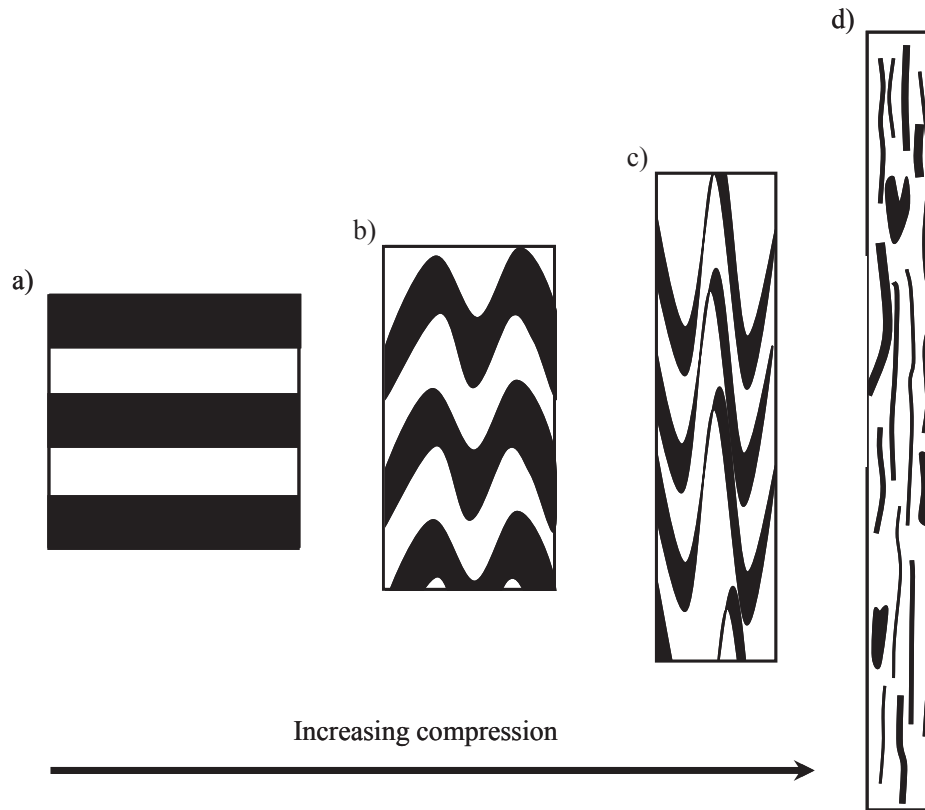


Figure 3.6: Development of foliation by folding and transposition showing a) horizontally stratified ice; b) folding of stratified ice; c) folds becoming tighter and vertical foliation beginning to develop; and, d) new foliation becomes dominant and only traces of original stratification survive (after Hambrey, 1994).

3.2.6 Folding (F_1)

As a glacier flows, layers within the ice such as foliation or stratification may be deformed into curved shapes known as folds (Figure 3.7) (Hambrey & Alean, 2004), at a range of spatial scales. Folds can develop to such an extent that in many valley glaciers (particularly if they are heavily crevassed, have turbulent flow, or are very active), stratification is almost completely destroyed and may not be recognisable (Hambrey & Müller, 1978). Folding may occur when stratification develops under a certain regime over time. Folding can be identified simply as isolated linear features

which can be followed in one direction before turning through a fold hinge and then followed in a different direction (Goodsell and others, 2005c). When this regime changes, such as from normal to compressive flow, a perturbation in flow is created, sufficient to fold the ice (Hudleston, 1976). This change to a compressive flow regime maybe due to changes in channel geometry (Hambrey & Lawson, 2000) or long-profile slope. Folding has been identified as being prevalent at flow unit boundaries (Hambrey & Lawson, 2000). It is especially common in surging glaciers, for example Eyjabakkajökull, Iceland (Sharp, 1985b), and Kongsvegen, Svalbard (Woodward and others, 2002) where, during a surge phase, flow regimes have changed too rapidly for ice to adjust and creep.



Figure 3.7: Folded dirt bands at the advancing front of Crusoe Glacier, Axel Heiberg Island. Originally parallel layers of inter-bedded ice and dirt have become folded as the flow regime of the ice has changed. (Photo: M. Hambrey)

3.2.7 Thrust Faults (S_3)

Dipping, arcuate bands of outcropping debris-rich ice on a glacier surface are often interpreted as thrust faults, originating in zones of longitudinal compression (Moore and others, 2010). Thrusting is a form of brittle deformation of ice, occurring when a stress applied to the body of ice becomes too great for plastic deformation and ductile flow to occur, which would otherwise allow for a change in shape of the ice unit. Brittle deformation can cause fracture lines, usually referred to as thrust faults or shear planes

(Figure 3.8), with a dip of less than 45° according to Twiss and Moores (1992), although features described as thrust faults in glaciological literature often have a dip of up to 80° (Lawson and others, 1994). Collectively, a region on a glacier in which many thrust faults occur can be called a shear zone. Within shear zones, systematically stepped (en echelon) faults can develop with an inclination relative to the shear direction (Herbst and others, 2006). Pure open fractures within shear zones are termed tension gashes, whilst fractures developing from shearing are termed Riedel shears. Herbst *et al.* (2006) suggest complex fracture patterns may occur, with younger fractures offsetting and cross-cutting earlier structures, as progressive shearing and rotation of existing fracture and fault segments causes the formation of new tension gashes and Riedel shears.



Figure 3.8: Debris-rich thrust faults in the lower Fox Glacier. Glacier flow is from right to left. (Photo: J. Appleby, February, 2011)

Work considering thrust faults has focused on polythermal glaciers (Hambrey and others, 1996, Hambrey and others, 1997, Glasser and others, 1998), although temperate glaciers have also been studied (Bennett and others, 2000, Herbst & Neubauer, 2000).

According to Benn and Evans (1998), thrusting occurs when ice decelerates and compressive flow occurs. Three common situations when this may occur are: (a) when ice flows into a topographic barrier; (b) at the snout/margins of surging glaciers; and (c) when wet-based ice decelerates against cold-based ice down-glacier (i.e. during winter when a 'cold-wave' penetrates to the bed at the margins of a temperate glacier, or year-round on the margins of sub-polar or polythermal glaciers).

The process of thrusting has, however, been controversial. It has long been suggested that thrusting can occur in glaciers (Chamberlain, 1895) and be responsible for elevating basal ice and debris (Figure 3.9) to a supraglacial or englacial position (Goldthwait, 1951, Ward, 1952, Bishop, 1957), and be an important mechanism of sediment transfer (Alley and others, 1997). However, Weertman (1961) and Hooke (1973) have argued that the hypothesis of debris thrusting is theoretically unsound. Weertman (1961) for example, explained debris deposits by the freezing of ice and basal sediment onto the glacier base and then being uplifted by the normal processes of ice flow in ablation zones, giving the appearance of debris being uplifted by tectonic-type processes. This process of 'Weertman regelation' involves the pressure melting of basal ice against the up-stream side of an obstacle, which is then refrozen on the lee of the obstacle forming a lamination of clear and debris-laden ice superimposed on the glacier sole (Souchez & Lorrain, 1987, Hubbard & Sharp, 1989, Hubbard & Sharp, 1993). In addition, the debris layers associated with thrusts have been explained by the filling of basal crevasses with material (Sharp, 1985a, Ensminger and others, 2001). Boulton (1967) identified a degree of sorting within the sediment of thrust layers, which would be unlikely if the material had been scraped from the bed, although, sorting could occur during transport within the thrust fault.

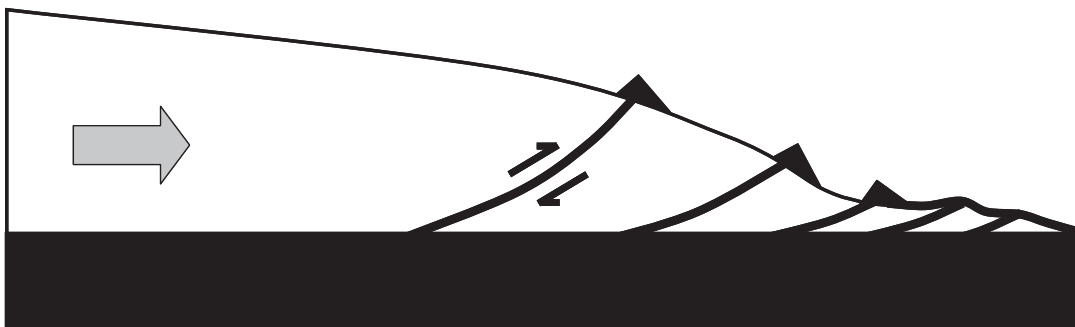


Figure 3.9: Illustration of thrust faults at the terminus showing transport pathways and accumulation of bed-derived debris on the ice surface (after Moore and others, 2010).

Sharp *et al.* (1988b) observed thrusting taking place during the 1982-83 surge episode of Variegated Glacier, Alaska in which thrust faults were seen to move at approximately 0.1 m/hr^{-1} . Swinson (1962) interpreted silt, boulders, gravel and clay-rich layers of ice found in an excavated tunnel in the margin of the Greenland ice sheet at Thule, as material being dragged from the glacier bed along curving planes, referring to them as 'shear moraines'. Hambrey and Müller (1978) also used thrusting to explain features observed on White Glacier, Northwest Territories, Canada. Subglacial and englacial fluvial sediments were observed by Krüger (1994) being transported to the surface along a series of debris-laden thrust planes at the snout of the Myrdalsjökull glacier, Iceland.

It has been suggested (Sharp and others, 1988b) that thrust faults occur in association with englacial folding. As compressive flow occurs, sedimentary layers become folded until their fold apex fractures producing a shear zone which may then outcrop at the glacier surface. As compression continues, the sediment within the fold is squeezed and forced out to become deposited on the glacier surface. Andrews and Smithson (1966) also considered material being forced to the glacier surface through shear planes, but suggested melt water as the transport medium. An influx of summer melt water can fluidise the basal till layer and force this highly pressurised fluid to the surface via shear zones (Gravenor & Kupsch, 1959, Price, 1970).

3.2.8 Arcuate Bands (Ogives)

Ogives are one of the most enigmatic indicators of glacier flow and are of two main types: wave ogives and band ogives (Goodsell and others, 2002). Ogives can be seen as arcuate bands or waves (Figure 3.10), with their apices pointing down-glacier (Hambrey & Alean, 2004). They appear convex down-flow, with an initially lunate form but becoming more parabolic with the amount of curvature increasing in each successive band, due to the greater velocity of the central part of the glacier compared with the margins (Benn & Evans, 1998).



Figure 3.10: Ogives on Svinafellsjökull, southern Iceland. The distance between successive bands can be seen to increase down-glacier. (Photo: J. Alean)

Agassiz (1847) first applied the name “Ogives” to arcuate glacial banding, however they were first described as “dirt bands” by James Forbes, during his early work in the European Alps (Forbes, 1845, Forbes, 1859), although they are now more commonly known as Forbes bands.

Washburn (1935) introduced a fundamental principal to the study of glacier banding when he called attention to fact that Forbes bands or ogives only appear on glaciers on which a substantial icefall exists further up-glacier. However, Waddington (1986) notes that not all icefalls produce ogives, as wave amplitude is modulated by a factor related to icefall length.

Several general hypotheses have been proposed for the genesis of both band and wave ogives (Table 3.1) by numerous authors including the *stratification hypothesis* (Agassiz, 1847, Hess, 1904), the *depression hypothesis* (Tutton, 1927, Washburn, 1935, Streiff-Becker, 1943), the *block-ridge hypothesis* (Fisher, 1947), *summer versus winter passage hypothesis* (Washburn, 1935, Miller, 1949, Nye, 1958, King & Lewis, 1961, Fisher, 1962, Liboutry & Reynaud, 1981), *ice-type hypothesis* (Leighton, 1951, Ives & King, 1954, Liboutry, 1958, King & Lewis, 1961), the *rhythmic compression hypothesis*

(Haeferli, 1951, Atherton, 1963), the *ablation/plastic stretching theory* (Nye, 1958, Waddington, 1986), and the *shearing hypothesis* (Chamberlain, 1895, Chamberlain, 1928, Leighton, 1951, Miller, 1952, Posamentier, 1978, King & Ives, 1954).

Table 3.1: Summary of ogive formation hypotheses, along with hypothesis proponents (developed from Goodsell and others, 2002).

Hypothesis	Key Features	Workers
Band Ogives		
Stratification hypothesis	Ogives represent primary stratification carried through the icefall	Agassiz (1840) Hess (1904)
Shearing hypothesis	Ogives are suggested as the surface expression of shear planes produced during compressive flow. Dark bands are representative of debris-laden thrust planes	Chamberlain (1895) Chamberlain (1928) Leighton (1951) Miller (1952) King and Ives (1954) Posamentier (1978)
Block-ridge hypothesis	Glacier-wide blocks of dirty ice are separated by relatively clean, snow-filled crevasses, producing a contrast between light and dark bands.	Fisher (1947)
Depression hypothesis	Ogives are formed by the accumulation of surface debris in glacier-wide crevasses or troughs at the base of an icefall	Tutton (1927) Washburn (1935) Streiff-Becker (1943)
Ice-type hypothesis	Higher debris concentrations result in dark ice bands, which then preferentially adsorb wind-blown debris	Leighton (1951) Ives and King (1954) Liboutry (1958) King and Lewis (1961)
Summer versus winter passage hypothesis	Ice travelling through an icefall during summer collects more wind-blown debris than ice travelling through during winter, which collects more snow. This produces a contrast between light and dark	Washburn (1935) Miller (1949) Nye (1958) King and Lewis (1961) Fisher (1962)
Wave Ogives		
Rhythmic compression hypothesis	Changes in velocity due to a change in gradient or season produce pressure waves and troughs at the base of an icefall	Haeferli (1951) Atherton (1963)
Ablation/plastic stretching hypothesis	An interaction between annual mass balance and plastic deformation produce annual waves at the base of an icefall	Nye (1958) Waddington (1986)

3.2.8.1 Band Ogives

Alternating light and dark bands are called band ogives or Forbes bands named after James Forbes who first suggested a method for their formation whilst working on the Mer de Glace in the Mont Blanc Massif (Forbes, 1859, Forbes, 1845). Each pair of bands is believed to represent a year's movement through the icefall (Nye, 1958, Hambrey & Alean, 2004). Notwithstanding this, the precise reasons for the observed colour differences in band ogives remains a highly contentious issue (e.g. Goodsell and others, 2005c).

Fisher (1947) suggested Forbes bands originate from the mechanism of a crevasse opening and closing annually in an icefall, and derive discolouration from localised surface dirt. Washburn (1935), Miller (1949), Nye (1958) and King and Lewis (1961) point to discolouration due to preferential summer debris entrainment in these crevasses. Gut *et al.* (2002) support this, citing the fusion of mineral debris into ice causing the observed dark bands, whilst Atherton (1963) identifies wind-blown dust as the source of the debris, which is then preferentially adsorbed into the ice surface. Debris collecting in surface wide crevasses and depressions at the base of an icefall has also been suggested as a method for band ogive formation by Tutton (1927) and Streiff-Becker (1943).

3.2.8.2 Wave Ogives

Wave ogives differ from band ogives, in that they may not exhibit a contrast between light and dark or clean and dirty ice. The banding seen in wave ogives is the result of a transverse ridge and trough system thought to be caused by differential ablation and accumulation within an icefall at varying times of the year. Fisher (1962) suggested that the seasonal variation of ice flow through an icefall produced differential thermal conductivity of white bubbly ice compared to darker fine ice. In essence, stretched, thinning ice travelling through the icefall during summer loses mass due to ablation, whereas ice travelling through the icefall during winter gains mass due to precipitation. As the ice slows beneath the icefall in a state of longitudinal compression, the bands of ice (marking summer flow) that have lost mass resemble a trough, whilst the areas that

have gained mass (winter flow) produce a ridge as the mass gains represent a net increase in volume.

Fisher (1947) termed wave ogives as ‘Alaskan bands’, and suggested they originate from stratification in the névé, under climatic conditions which produce a particularly large amount of melt water during the ablation season. Fisher (1947) proposed that any apparent discolouration is due to a more solid ice matrix inherited from ablation season surfaces of ‘soggy’ ice.

Differential melt rates are not the only explanation for wave ogives. Rhythmic compression and pressure waves, along with the ablation plastic-stretching mechanism have been suggested to explain wave ogive formation (Goodsell and others, 2002). Haeferli (1957, 1951) proposed a relationship between increased flow velocity during the summer ablation season and the formation of pressure waves. As the ice velocity increases during summer (due to increased melt water at the bed) and slows down during the winter, the plastic deformation of the ice may cause the waves that may be recognisable as ogives. This proposition leads on to another important point considered by Ives and King (1954) and King and Ives (1954) who note that the pressure wave relationship may suggest that ogives are not necessarily annual. Any steep slope in profile can cause sufficient pressure wave to produce ogive banding.

3.2.8.3 Faulting Theory

In addition to dirty/clean ice and ridge/trough theories of ogive formation, Leighton (1951) suggested debris which was originally basal may, by up thrusting and ablation, become the surface manifestation of an ogive (Figure 3.11). Posamentier (1978) built on this by suggesting discolouration may be due to large-crystal, bubble free ice which has been transported from the glacier base towards surface by the processes discussed by Leighton (1951), whilst lighter bands represent relatively small-crystal, bubble rich near surface ice. Goodsell *et al.*, (2002) used ground-penetrating radar to identify fault planes causing up thrust related to ogive structures on Bas Glacier d’Arolla, Switzerland.

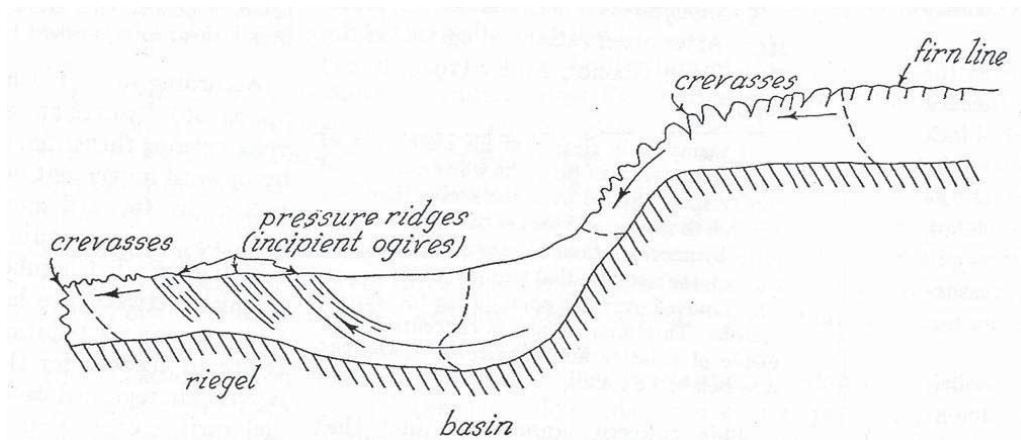


Figure 3.11: The flow of a glacier through an icefall causes primary stratification to become rotated and allows basally derived material to be exposed at the surface due to fracture and thrust planes within the body of the ice (from Leighton, 1951).

3.2.8.4 Other Considerations

In some situations it may be possible that the band and wave ogive hypotheses are not necessarily exclusive, with both systems occurring on the same glacier. Work by Yamaguchi *et al.*, (2007) on Bilchenok Glacier, Kamchatka, described how variations in debris thickness cause differential ablation, causing ridges under areas of thicker debris, and troughs in areas of lesser debris. A regular frequency of ridge/trough pairs was observed, the origin of which being suggested as surging behaviour and the pressure wave hypothesis.

As has been suggested, not all icefalls produce ogives (Waddington, 1986), and not all ogives are caused by icefalls (Ives & King, 1954). In addition to this, Atherton (1963) identifies a difference in ogive formation systems between temperate glaciers and polar glaciers.

King and Lewis (1961) built on the palynology work of Vareschi (1942) and Godwin (1949) to support their theory that the dark ice of a Forbes band travels through the icefall in summer. They suggested that more debris falls onto the ice surface from rock walls during summer as higher temperatures cause a destabilisation of material that would be otherwise held in place by ice or snow during the winter. King and Lewis

(1961) also support Nye's (1958) belief that one pair of light and dark bands represents a year's ice movement through an icefall.

3.2.9 Moulins

Surface-derived melt water, and the means by which it is transferred through the glacier system, is a critical component in glacier hydrological systems modulating basal motion (Gulley, 2009, Gulley and others, 2009) and sediment transfer (Benn & Evans, 1998). Supraglacial water, the result of melting or precipitation, flows across the glacier surface in a dendritic pattern of either regular meanders (Knighton, 1972), or uniform, straight lines that follow structural features such as crevasses or foliation (Sugden & John, 1976). Often the water will infiltrate the glacier, down steeply dipping or vertical conduits called moulins (Figure 3.12). Exploiting structural weaknesses, moulins form when surface slope directs water flow towards an open crevasse or when a crevasse opens across the line of a supraglacial stream (Stenborg, 1969). It is supposed that stress conditions in water-filled crevasses can allow propagation of fractures to the glacier bed, initiating moulins that permeate the full depth of the glacier (Röthlisberger & Lang, 1987, Robin, 1974). Moulins are the most significant means of transferring supraglacial water to an englacial or subglacial position. However, recently a cut-and-closure system has been suggested (Gulley and others, 2009), whereby flowing water incises supraglacial stream channels, the top of which are then closed by ice deformation, transforming a supraglacial stream into an englacial conduit.

Moulins can become isolated from the supraglacial hydrology system that formed them through upstream crevasse formation (Holmlund, 1988) or deformation of the ice surface diverting channels by means of a change in surface slope aspect. At depth moulins are usually water-filled, whereas at the surface the moulin is rarely filled with water except at peak flow (Benn & Evans, 1998). Occasionally a moulin may become blocked through deformation of the ice at depth or through closure of the conduit by freezing. At these times the surface depression in which the moulin is observed can form a supraglacial pond of deep, clear water or shallow, slushy ice (Figure 3.13).



Figure 3.12: Moulin and supraglacial streams on the surface of Fox Glacier. (Photo: M. Brook)



Figure 3.13: Supraglacial pond formed from a closed Moulin on the surface of Fox Glacier. (Photo: S. Winkler)

3.2.10 Boudinage

When stretched in zones of extending glacier flow, layers of fine grained or debris-rich ice may separate into discrete discontinuous lenses (Figure 3.14) termed boudins (Hambrey, 1994, Hambrey & Milnes, 1975, Hubbard & Sharp, 1989). This process of boudinage is analogous to that in rocks (e.g. Arslan and others, 2008).

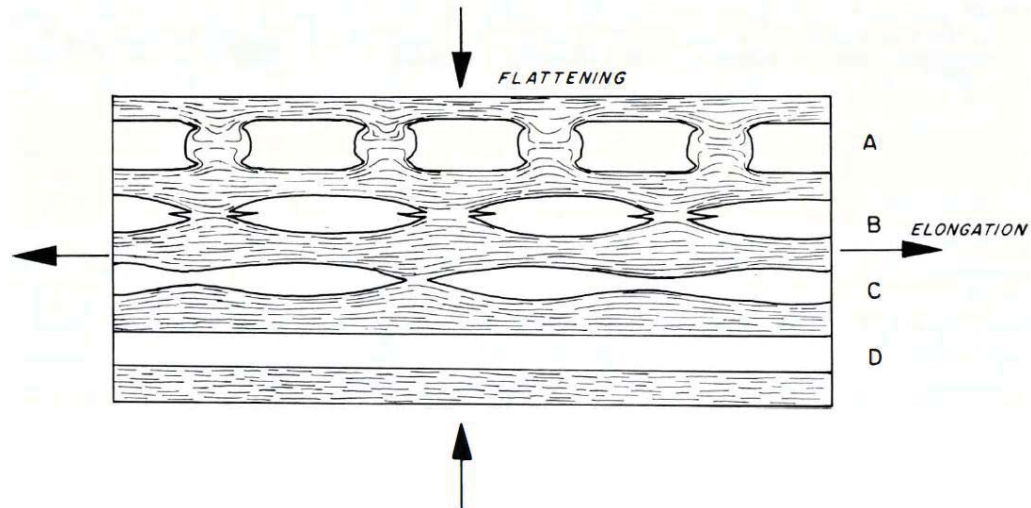


Figure 3.14: Boudins produced from stratified layers within stretched glacier ice in areas of extending flow. Competence of boudinage increases from D (discrete layer) to A (discrete boudin) (from Hambrey & Milnes, 1975).

Hambrey and Lawson (2000) identify two general types of boudinage observable in glacier ice: Foliation boudinage and competence contrast boudinage. Foliation boudinage commonly occurs in association with longitudinal foliation and extension, whereby shear zones or fractures displace ice sideways forming an acute angle at the boudin neck. Competence contrast boudinage occurs where boudins of debris-free ice become isolated in debris-rich basally-derived ice, or when fine-grained ice becomes attenuated within foliated coarse bubbly ice.

Boudinage structures are commonly observed at scales of a few centimetres to several metres (Hambrey & Milnes, 1975, Lawson and others, 1994) although ‘mega-boudins’, two orders of magnitude larger, have been observed on satellite images of the Lambert Glacier, Antarctica (Hambrey & Dowdeswell, 1994).

3.2.11 The Ice and Rock Deformation Analogy

It has been noted (e.g. Hambrey & Lawson, 2000, Allen and others, 1960) that the manner in which glacier ice deforms, producing a variety of ductile and brittle structures, resembles that in rock. When viewed as a metamorphic monomineralic rock, structures in glacier ice can be considered in much the same way as those in structural geology, with many of the same features such as thrust faults, folds, and stratification (Ragan, 1969, Herbst and others, 2006). Primary stratification is developed through annual accumulation of precipitation, before experiencing metamorphic change through the actions of pressure and temperature, in a similar way to sedimentary rocks. Deformation in a typical alpine glacier, however, is thought to take place at a rate of six orders of magnitude faster than the deformation of sediments in Alpine orogenic belts (Hambrey & Milnes, 1977).

The relatively fast deformation rate of ice has led to the suggestion that the study of structural deformation in ice can be a quick and accurate measure of how rocks behave in similar conditions, allowing an understanding of geological processes over a period not normally associated with geological time (Herbst & Neubauer, 2000). In addition, laboratory-based investigations, in which the processes of deformation can be replicated under controlled conditions, are possible: something not possible with geological research (Karato and others, 1998). Ragan (1969) suggests flowing ice is an attractive structural model having advantages of experimental models whilst avoiding the drawbacks.

3.2.12 Review of Previous Structural Evolution Studies

A number of researchers have considered the structural evolution or temporal change in structures seen on glaciers over similar time periods. Most of these studies make use of historical and contemporary topographic maps, aerial photographs and satellite images.

Herbst, *et al.* (2006) examined historic and contemporary topographical maps of Pasterzenkees Glacier, Austria from 1887 to 1997, to identify the development of brittle structures on the ice surface. As with this study, Herbst, *et al.* (2006) concluded that the distribution of brittle structures appears to be sensitive to variations in mass balance.

Three dimensional recreations of historic glacier positions are also possible, with Herbst, *et al.* (2002) developing a model using aerial photographs, topographic maps and digital elevation models to recreate ice thickness and terminus position of Pasterze Glacier, Austria between 1887 and 2001. Over a shorter time period (1948 to 1983), Lawson (1996) studied vertical aerial photographs to determine the structural evolution of Variegated Glacier, Alaska during surge phases. Early maps and recent satellite images of Pasterze Glacier along with Kleines Fleißkees Glacier, also in Austria, between 1893 and 2001 were used by Hall *et al.* (2003) in a discussion of the difficulties found in identifying the terminus position of Alpine Glaciers from the study of historical records; the difficulties coming from the resolution of remotely sensed images and the issues of differentiating debris-covered ice from lateral and terminal moraine.

In addition to studies on alpine glaciers, the evolution of structures in the Arctic and Antarctic has been considered to a limited extent. For example Glasser, *et al.* (2009) used satellite imagery to analyse surface morphology of the Larsen C ice shelf between 1963 and 2007, whilst Hambrey, *et al.* (2005) studied the changing dynamics of Midre Lovénbreen, a polythermal valley glacier in Svalbard, over the 20th century.

3.3 Methods of Structural Investigation

Several methods have been employed in this study to investigate the structural glaciology of Fox Glacier. These include field observations and measurements of surface structures, analysis of historical and contemporary maps, aerial photographs and satellite images, debris analysis, and the analysis of isotopic fractionation. In addition, ground-penetrating radar has been used with the hope of gleaning information with regard to the internal structures of the glacier. The ground-penetrating radar investigation is presented in *Chapter Four*.

3.3.1 Mapping of Surface Structures

The surface structure of Fox Glacier is identified and mapped using two techniques: surface structure identification using remotely sensed images (aerial photographs and satellite images), and structural maps made from observations in the field. Results from the two techniques have been combined to map the location of surface features at a variety of scales.

3.3.1.1 Remote Sensing

Remote sensing allows mapping of large-scale glacier features not possible with ground observations (König and others, 2001), and is often the only method available for studying remote or inaccessible areas. In addition to the mapping of structures being the ultimate goal of research, features observed from remotely sensed images can aid in the understanding of other processes occurring. Hambrey & Dowdeswell (1994) for example, used surface features including foliation and crevasses identified from Landsat images to derive flow directions of Antarctic ice shelves. Aerial photographs and satellite images have been used to map the surface features of Fox Glacier.

3.3.1.2 Aerial Photography

Vertical frame aerial photographs tend to have the finest spatial resolution of remotely sensed images owing to the low flight height and long focal length of aerial cameras (Gao & Liu, 2001) allowing detailed mapping of medium-scale features including foliation. Surface features are recognised and recorded according to their relative orientation, size, relation to other structures and location on the glaciers surface, using the criteria as described by Goodsell *et al.*, (2005c) (Table 3.2). Aerial photographs are scanned into a digital format which is then used in ArcGIS to produce a line map of the glacier surface.

3.3.1.3 Satellite Imagery

As with aerial photographs, satellite images are used to map surface features in ArcGIS, however, the medium spatial resolution of satellite imagery restricts their applications to

the mapping and monitoring of glacial features at a broader scale (Gao & Liu, 2001) such as arcuate bands, crevasses and flow unit boundaries.

3.3.1.4 Field Mapping

As with remotely sensed images, structures were recorded and recognised according to their orientation, size, relation to other structures, and location on the glacier surface, using criteria as described by Goodsell, *et al.* (2005c) along with standard structural geology mapping techniques (Barnes, 1997, McClay, 1997).

Transect lines were walked from side to side of the glacier repeatedly along the length of the three study areas (Fox Névé, Victoria Flat, and Lower Fox Glacier), with large-scale features such as crevasses being recorded on a predefined outline of Fox Glacier, produced from tracings of a topographical map. The locations of smaller features were recorded using a hand-held Garmin Global Positioning System (GPS) unit and these features were then transposed onto the base map. Transect lines were walked in approximately straight lines to ensure uniformity of ground cover, although this was not always possible due to topographical constraints of the glacier surface.

Features such as primary stratification, foliation, and crevasse traces were mapped using techniques adopted from structural geology, namely strike and dip orientation. Strike represents the orientation in degrees from North, across the plane of the feature, with dip perpendicular to the strike line representing the angle down-plane in degrees from the vertical (McClay, 1997). Commonly referred to as ‘the right hand rule’, strike and dip can be quickly identified in the field with strike following the direction in which the index finger points, whilst dip is in the direction of the thumb (Barnes, 1997).

Table 3.2: Descriptive criteria for identification of glacial structures identified from aerial photographs and field observations (Adapted from Goodsell and others, 2005c).

Nongenetic name	Interpretation	Identification on aerial photography	Identification in the field
Systematic layering	Primary stratification	parallel layering usually found in the upper glacier basin, sometimes parallel to snowline.	Thin darker layers between thicker lighter layers of firn often found parallel to receding snowline in late summer.
Discontinuities in layering	Unconformity	A break in the normal systematic layering of the primary stratification.	Difficult to observe close-up. Can be identified as a break in the normal layering when viewed from a distance.
Structural discontinuity	Flow unit boundary	A junction that separates structures rotated in one orientation from structures rotated in a different orientation.	Difficult to identify close-up, but can sometimes be recognised by structures oriented at different angles on either side of an area of intense foliation.
Crevasses	Crevasses	Either as straight white lines (snow filled) or straight dark lines (non-snow filled or water filled), with cross-cut features.	A crack with a visible opening.
Transverse/arcuate structures	Crevasse traces	First found in areas of crevassing as straight dark lines, can be followed downglacier as deforming dark lines, cross-cutting previously formed structures.	Linear or arcuate features, usually <0.2m width, which can be followed for tens of meters.
Steeply dipping longitudinal	Longitudinal foliation	Long linear pervasive layered structure parallel to ice movement, which can be traced discontinuously for several hundred meters.	Alternating, discontinuous layers of bubble-rich and bubble-free white and blue ice, parallel or sub-parallel to surface ice movement.
Folding	Folding	Large-scale folding is identified as curves in linear features which do not follow surface topography.	Isolated folds are identified by linear features which can be followed in one direction before turning through an angle and being followed in a different direction.
Prominent arcuate structures near snout	Thrusts	Not observed on aerial photographs.	A step in the glacier surface, parallel to crevasse traces near the snout of the glacier. Displacement of marker horizons. Associated with basal debris.

3.3.1.5 Presentation of Surface Mapping Results

Field maps were converted into a digital format and used with QuickBird Satellite imagery acquired during 2006 and 2007 (available from Digital Globe (DigitalGlobe, 2010) and Google Earth) to produce a map of the surface structure of Fox Glacier in ArcGIS, according to the conventional methods as used by Hambrey and Lawson (2000) (Figure 3.15). Feature types have been allocated specific symbols or line types and were labelled according to structural notation (S_0 , S_1 , S_2 ...etc). In addition, the orientation of structures according to their strike and dip, have been presented graphically.

Strike and dip orientation data of structures and clast macrofabric are conventionally displayed using a Schmidt equal-area stereonet polar plot. The stereonet allows data to be viewed in three dimensions by plotting strike orientation in degrees from North, shown at the top of the circle, and dip angle in degrees from horizontal, where 90° is represented by the centre of the circle, and 0° is at the outside of the circle.

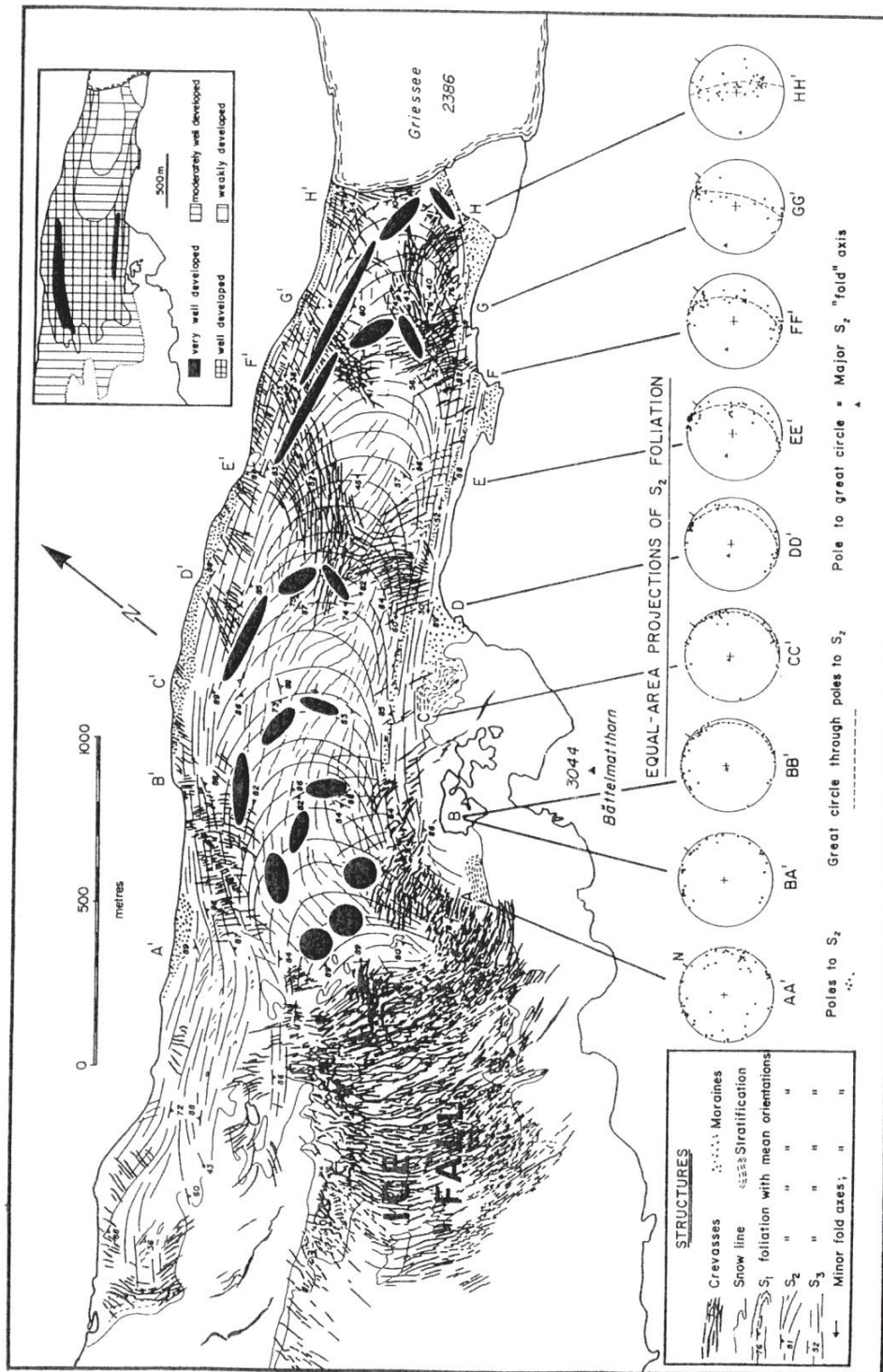


Figure 3.15: Structural map of Griesgletscher, Switzerland, constructed using standard structural mapping techniques including structural notation (S_0, S_1, S_2, \dots etc), and equal-area stereonet projections of feature orientation (from Hambrey & Lawson, 2000).

3.3.2 Isotopic Fractionation

The preferential isotopic fractionation of regelation ice has proved useful in studies of the origin of basal ice facies because a bivariate plot of the ratios of D and ^{18}O isotopes (Figure 3.16) will yield a slightly different slope depending on whether the ice has refrozen at the bed or not (Hubbard & Glasser, 2005). The relationship between δD and $\delta^{18}\text{O}$ potentially represents a powerful analytical tool in glaciology (Glasser & Hambrey, 2002b) allowing investigations into the effects of climate and meteorology on: (1) stable-isotope signals in alpine snowpacks (Neumann & Waddington, 2004, Sinclair & Marshall, 2009, Sinclair & Marshall, 2008, Moran and others, 2007, He and others, 2005, Vimeux and others, 2001, Liebming and others, 2006); (2) the interpretation of the thermal history of ice and snow (Jouzel & Souchez, 1982, Souchez & De Groot, 1985, Souchez & Jouzel, 1984, Souchez and others, 2004, Hubbard & Sharp, 1993, Hubbard & Sharp, 1995, Gordon and others, 1988, Citterio and others, 2004, Stichler and others, 2001); and (3) the study of debris entrainment (Hubbard and others, 2004, Sugden and others, 1987, Glasser and others, 2003, Swift and others, 2006).

The difference in isotopic signature between regelation ice and parent ice provides a means of identifying the provenance and transport mechanism of allocthonous ice such as may be found in thrust planes at the glacier surface. Determining the presence of basal-origin regelation ice in an elevated position gives clues as to the structural and dynamic nature of the ice body (Hubbard and others, 2004).

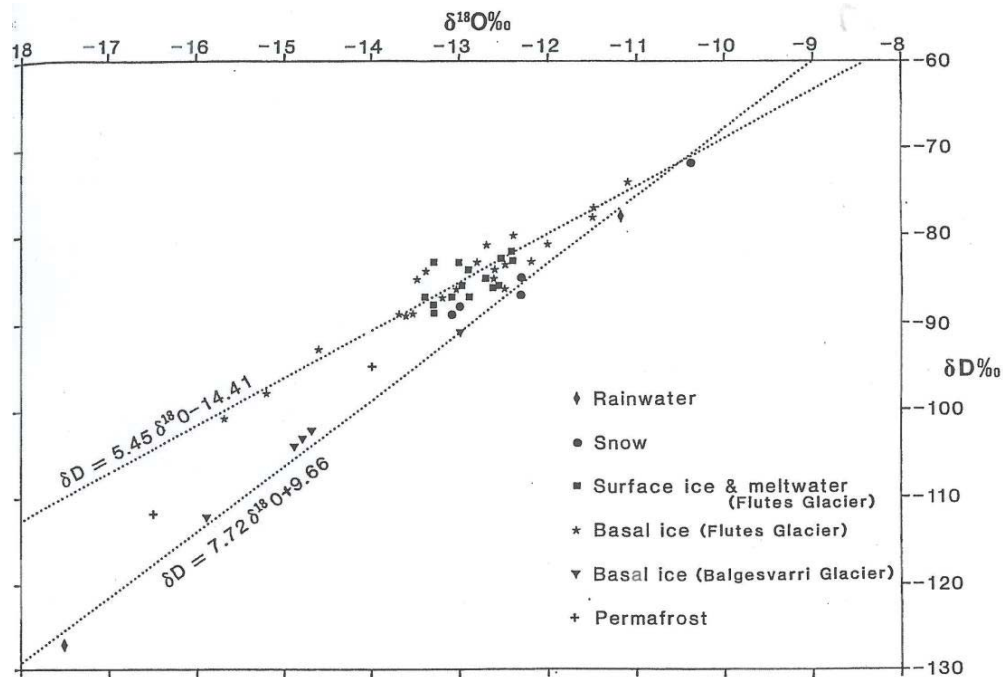


Figure 3.16: Co-isotopic plots of ice, snow and precipitation samples from Flutes and Balgesvarri Glaciers, Lyngen, Norway (from Gordon and others, 1988).

3.3.2.1 Isotope Analysis of Glacier Ice

The process of regelation or refreezing of melt water at the glacier-bed interface involved in glacier sliding results in isotopic fractionation. Preferential bonding of heavier isotopes in re-forming ice crystals, namely δD Deuterium (2H) and $\delta^{18}O$ Oxygen creates compositional banding, with each freezing cycle exhibiting isotopically lighter ice (Figure 3.17). If some of the isotopically lighter water is able to drain away prior to refreezing, the bulk composition of regelation ice will be isotopically heavier than the parent ice (Benn & Evans, 1998).

The mass balance of preferential incorporation of heavy isotopes has been modelled by Jouzel and Souchez (1982), Souchez and Jouzel (1984), and Souchez and De Groot (1985), who examined the concentration of δD and $\delta^{18}O$ in parts per thousand (‰) compared to a reference standard. The reference standard now most commonly used is Vienna Standard Mean Ocean Water (VSMOW) as defined by the International Atomic Energy Agency (IAEA).

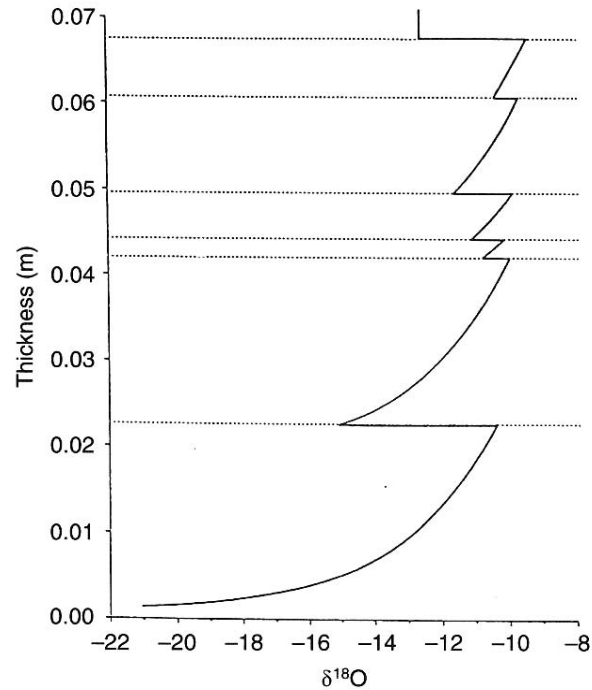


Figure 3.17: Modelled isotopic variation in regelation ice, resulting from the preferential incorporation of heavy isotopes in the first ice to form in each cycle (after Benn & Evans, 1998, Hubbard & Sharp, 1993).

3.3.2.2 Collection of Isotope Samples

Samples were collected along a centre-line longitudinal transect to determine altitudinal variations in isotopic signature of surface snow and ice, along with north-south transverse transects across the névé to determine any latitudinal variations. In addition, samples were collected from specific sites of interest including basal ice and thrust regelation ice to determine the provenance of this ice when compared to the longitudinal transect samples.

Samples were collected according to the methods described by Glasser and Hambrey (2002b) and Glasser *et al.* (2003), over a two day period during February 2011. At each sample site, surface snow or ice was removed from the glacier surface and samples were collected at 5 - 20 cm depth to avoid any surface melt, using a 10 mm diameter ice screw. Snow and ice samples were melted and stored in airtight plastic sample bottles to prevent evaporation. Altitude and location of each sample point on the glacier was

determined using a *Garmin eTrex Vista HCx* hand-held GPS unit calibrated daily at sea level. A note was made regarding the characteristics of the ice facies from which the samples were collected.

3.3.2.3 Isotope Sample Analysis

Water samples produced from melted snow and ice were analysed at the University of Canterbury using a *Thermo Scientific Finnigan* thermal combustion elemental analyser coupled to a *Thermo Scientific Delta V Plus* isotope ratio mass spectrometer via a *Conflo III* gas distribution system. Operating conditions for the thermal combustion elemental analyser were:

- Reactor temperature @ 1420°C
- Gas chromatography column temperature @ 40°C
- 99.999% He continuous flow at a rate of ~110 ml/min.

Each sample, including each 'duplicate analysis', was analysed 4 times. The first analysis for each sample was discarded due to memory effects in the thermal combustion elemental analyser reactor and gas chromatography column. Reported mean delta values and standard deviations were calculated for the last 3 analyses of each sample. All data were corrected using a 2 point normalisation (i.e. stretch and shift) to the SMOW-SLAP scale based on replicate (~40) analyses of International Atomic Energy Agency (I.A.E.A) standard mean oxygen water (SMOW) and standard light Arctic precipitation (SLAP) certified reference waters.

Using this process, the δD values are accurate to <1.0‰ and the $\delta^{18}O$ values are accurate to <0.2‰. The external (i.e. sample collection) precision is indicated by the standard deviations for the replicate analyses, and the internal precision (i.e. the mass-spectrometry itself) is better than 0.5‰ (δD) and 0.1‰ ($\delta^{18}O$) based on standard one-off tests (i.e. zero enrichment tests).

3.3.2.4 Isotope Data Presentation

Results of isotope analysis are presented as statistical data tables detailing regression analysis results, 95% confidence ranges, r^2 , F and p figures, standard deviation and bivariate co-isotopic plots of δD versus $\delta^{18}O$ (Figure 3.22).

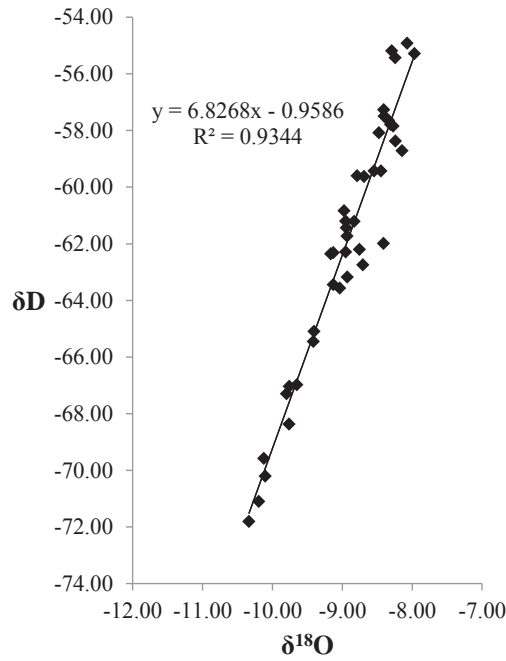


Figure 3.18: An example of a bivariate co-isotopic plot ($\delta D/\delta^{18}O$) of a glacier ice sampled on Fox Glacier.

Chapter 4 : The Historical and Contemporary Structural Glaciology of Fox Glacier

4.1 Introduction

Chapter Four is concerned with the historical and contemporary structural glaciology of Fox Glacier. It presents the results of this historic and contemporary study of the surface structures of Fox Glacier gleaned from the study of contemporary and historic remotely sensed images and maps, along with the field and laboratory techniques described in *Chapter Three*. Finally, the chapter provides a discussion on the contemporary and historical structural glaciology of Fox Glacier.

4.2 The Historical Evolution of Structures at Fox Glacier

The continuous fluctuation in mass balance of alpine glaciers repeatedly alters their gradient, velocity and, in turn contributes to cyclic patterns of advance or retreat, all of which have an effect on the brittle structures present in ice bodies undergoing extensive and compressive flow regimes. Fox Glacier, the advance and retreat of which is discussed in *Chapter Two*, theoretically could exhibit dramatic changes in its structure and length due to the steep gradient and extremely high ratio of collection area to constricted valley tongue.

The aim is to document such changes over as long a period as possible, using information derived from a range of historical sources. This has resulted in the generation of a long-term (110 year) record of Fox Glacier's length, thickness, and surface structures, compiled using information derived from historical maps & sketches, aerial photographs, satellite images, and exploration reports. This record is displayed in a time series of maps depicting glacier length and structural features visible on the glacier surface,

Another key part of this chapter will involve examining this record of temporal evolution with respect to the potential response of the Glacier to external climatic cycles

such as the Interdecadal Pacific Oscillation (IPO) and Southern Oscillation Index (SOI). Such climatic cycles have been shown to influence glacier length (and by inference structural features) at other glaciers in New Zealand (Chinn, 1996, Fitzharris and others, 1997). If the glacier is found to respond to such climate cycles, then this may help to further account for the geomorphic and glaciological features of Fox Glacier and landforms on the proglacial foreland. This will in turn help to predict the future structure and stability of Fox Glacier with continued advance and retreat driven by atmospheric circulation (Chinn and others, 2005c, Purdie and others, 2008a, Salinger and others, 2001).

4.2.1 Structural Changes to Fox Glacier 1896-2006

Data for the structural temporal evolution of Fox Glacier have been collected from a range of sources including maps, photographs, reports and observations on a range of scales spanning 110 years (Figure 4.1). The earliest data source is a map produced by Douglas, Harper, and Wilson in 1896 (Douglas & Wilson, 1896), while the most recent is Quickbird satellite imagery from DigitalGlobe acquired in 2006. These maps, vertical and oblique aerial photographs and satellite images have been used to create a time series of structural maps identifying features visible on the glacier surface, with the aim of determining or recognising trends in structural development and distribution over time.

The early hand-drawn maps produced from field observations such as that by Douglas and Wilson (1896) are limited in detail with regard to small-scale structures. Nevertheless, they give sufficient detail to determine the terminus position of Fox Glacier and the location and relative size of large-scale brittle structures (e.g. crevasses and flow unit boundaries). In addition, the hand drawn maps are accompanied by detailed reports from the cartographers, giving information from which the type and locations of specific structural features can be inferred.

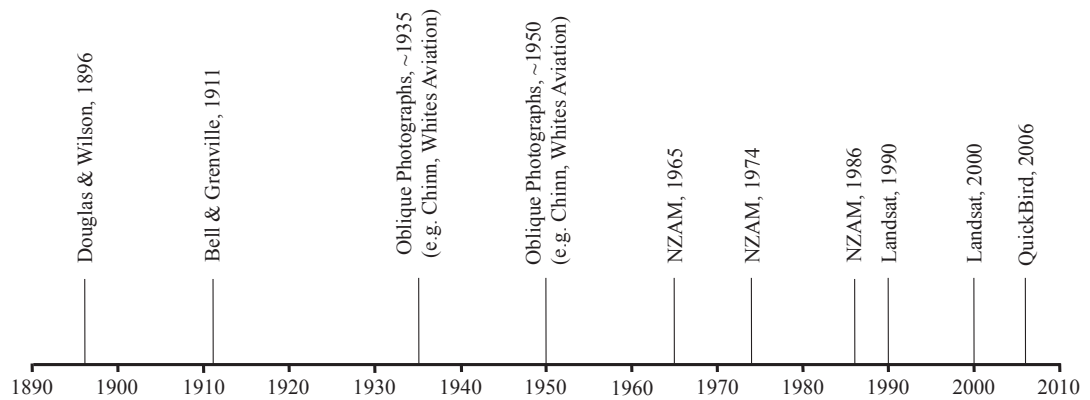


Figure 4.1: Source and date of imagery used for reconstruction of structural temporal evolution of Fox Glacier (A selection of these images is reproduced in *Appendix One*).

4.2.1.1 1896

From the 1896 map (Figure 4.2 a), Fox Glacier terminates approximately 500 m down-valley of Cone Rock (area 1) with the terminal face at approximately 225 m asl. The terminus was given to be 700 feet (213 m asl) the year before (Anonymous, 1895). This is a similar altitude (213 m asl) to that recorded by Von Haast in 1870 and Cox (201 m asl) in 1876 (Cox, 1876). The lower 1000 m of ice immediately above the terminus is covered by supraglacial debris, which is the only supraglacial debris identified on the map. Wilson (1896, p.109) describes the glacier as being “remarkably free from debris” apart from the “half mile” (800 m) up-glacier from the snout. Above this area the ice surface undergoes a transition from moderate crevassing through smooth and undulating ice, to an intensely crevassed area identified as the (present-day) Lower Icefall (area 2). No evidence (either from maps or reports) is available for the presence of the Icefall during this period, although it is reasonable to assume that this major feature was present.

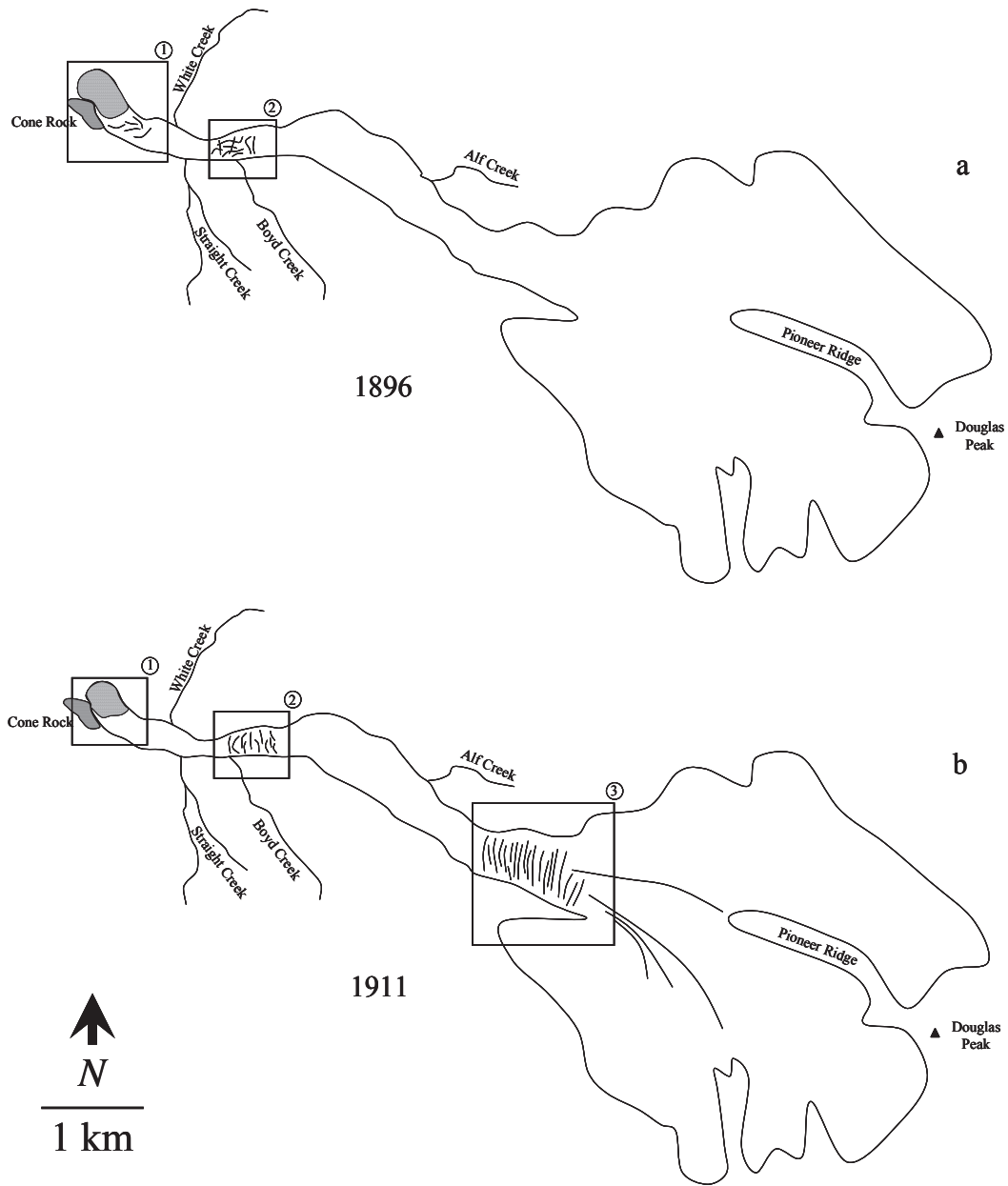


Figure 4.2: Structural interpretations from a) 1896 showing (1) debris-covered terminus down-valley of Cone Rock, and (2) chaotic crevassing in Lower Icefall; and b) 1911 showing (1) terminus close to Cone Rock, (2) Lower Icefall, and (3) Upper Icefall.

In the névé, flow convergence of tributary glaciers can be seen below Pioneer Ridge although no distinct flow boundaries are apparent. No crevassing is identified in the névé from the 1896 map. This may be due to snow cover during the mapping period, although the 1896 map was compiled between 1894 and 1896 with no specific dates indicated, so it is not known if the névé was mapped during summer or winter. In 1896 the Fox River exited from two portals, one being on the true left of the terminus at the distal end of Cone Rock, and the other at the centre of the terminus. Immediately down-valley of the terminus, the two portals form a confluence with Mills Creek which flows into the main Fox Valley from the South West side of Cone Rock.

4.2.1.2 1911

In 1911 (Figure 4.2 b), as in 1896, the terminus of Fox Glacier was still approximately 500 m down-valley of Cone Rock (area 1) although supraglacial debris now only covered the lower 500 m of ice. Intense crevassing is once again identified in the Icefall (area 2) and the Upper Icefall (area 3). Distinct flow unit boundaries separating the Explorer and Albert Glaciers, the main tributary glaciers, are apparent in the névé converging between the lower end of Pioneer Ridge and the top of the Upper Icefall. Only one portal can be identified from the 1911 maps. This portal is in a similar position to the one identified in 1896 at the centre of the terminus. Once again, a confluence is formed immediately down-valley of the terminus, between the Fox River and Mills Creek.

4.2.1.3 1935

Comparison between the 1911 map and 1935 oblique photographs (an example of which is given in Figure 4.3) suggest the terminus has retreated from its 1911 position, and now sits level with the distal end of Cone Rock at approximately 260 m asl. Newton (1939) placed the snout of the glacier at an altitude of approximately 756 feet (230 m asl). Harper (1934) suggested Fox Glacier had altered little from 1894 with the terminus undergoing a slight overall un-quantified retreat between 1894 and 1934, and the main body of the ice up valley from Cone Rock appearing unchanged. Comparing the 1896 map by Douglas, *et al.* (1896) with field observations, Speight (1934) estimated a retreat of ~100 m by 1934. Speight (1934) suggested that the subtle recession since

1896 had been punctuated by a small advance in 1934 as river bed material has been lifted and pushed forward immediately in front of the terminus, although the advance was not quantified. Speight (1934) went on to suggest that the general appearance of the 1934 terminus suggested that the glacier was still experiencing advance, although down-wasting of the area immediately up-valley of the terminus suggested an impending retreat. From the 1935 imagery, chevron and transverse crevasses are identified at the terminus with part of the crevassed area covered by supraglacial debris. Approximately 500 m up valley of the terminus, arcuate bands are observed on the true left of the glacier (Figure 4.4 a, area 1). These arcuate bands are accompanied by an area of crevassing on the true right of the glacier, halfway between the terminus and the foot of the Lower Icefall. Further up-valley, supraglacial debris is restricted to an area on the true left of the glacier, immediately above the Lower Icefall; the icefall is limited at this time in its spatial coverage compared to later years (Figure 4.4 a area 2). The only 1935 photographs available of the glacier up-valley of Victoria Flat show crevassing of the Upper Icefall, whilst structures in the névé are not identifiable, although Gardiner (1934) described Pioneer Ridge during the previous year as “a remote spot with deeply crevassed surrounding glaciers”, suggesting zones of extension on the Albert and Explorer Glaciers.



Figure 4.3: Photograph of lower Fox Glacier acquired in 1935 from Cone Rock. Chancellor Shelf can be seen at the centre left of the photograph with Douglas peak on the right of the skyline (Photo courtesy of T. Chinn).

4.2.1.4 1950

A relatively small retreat occurred between 1935 and 1950 (Figure 4.4 b) with the terminus now at the proximal end of Cone Rock, still below 300 m asl (Suggate, 1950). Speight (1941) commented on the limited change in condition and position of the terminus compared to a visit in 1934, but noted that the lower area has “collapsed” and the ice surface elevation has fallen by approximately 45 m. The area immediately above the terminus is characterised by longitudinal crevassing and heavy supraglacial debris cover on the true right of the glacier. Again, crevassing and arcuate bands can be seen in the area between the terminus and Lower Icefall (Figure 4.4 b, areas 1 & 2; Figure 4.5).

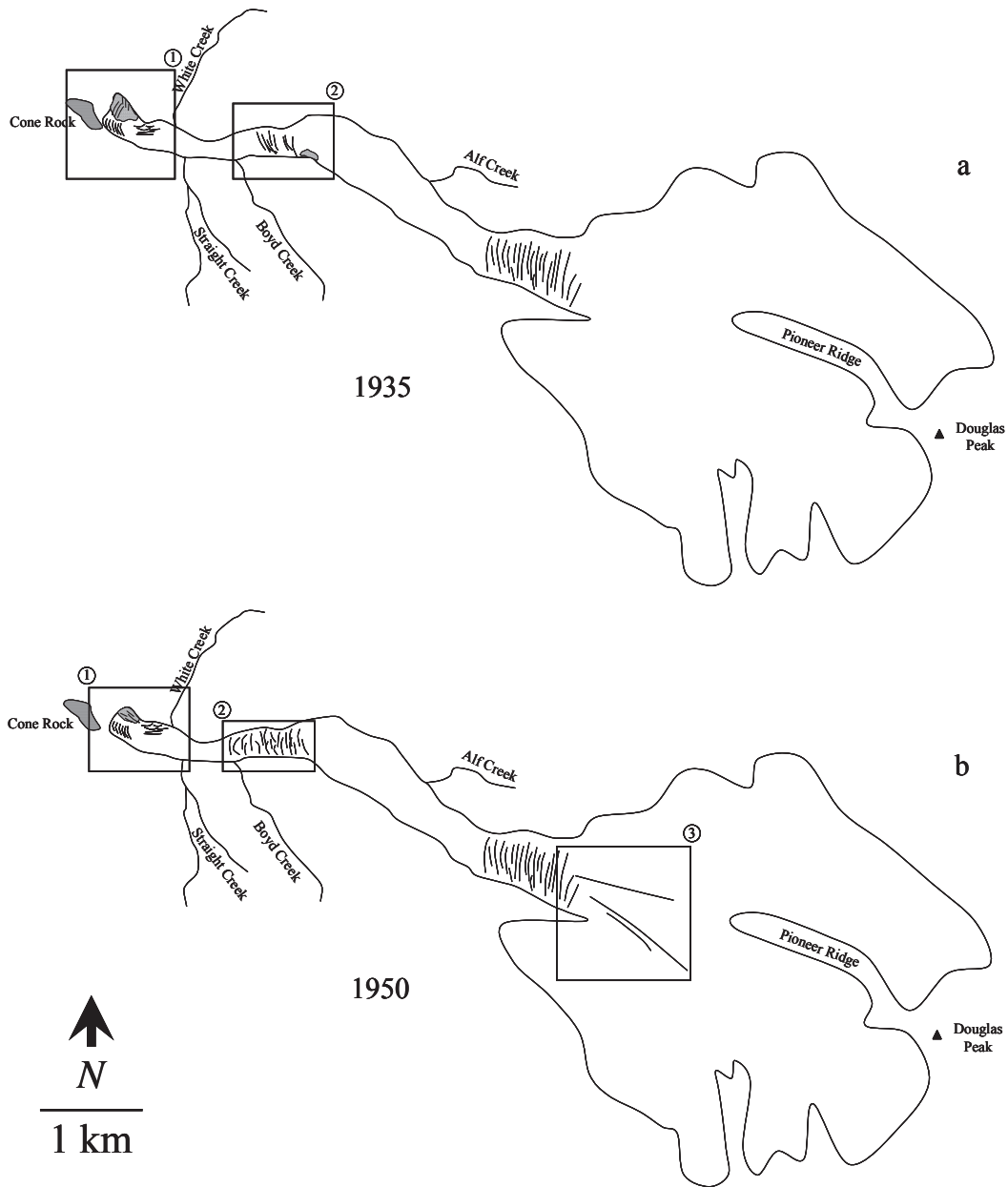


Figure 4.4: Structural interpretations from a) 1935 showing (1) crevassed and debris-covered terminus level with Cone Rock, and (2) crevassing and debris in Lower Icefall; and b) 1950 showing (1) terminus up-valley of Cone Rock, (2) Lower Icefall, and (3) flow boundaries in névé.



Figure 4.5: Oblique aerial photograph of Fox Glacier acquired ~1950 with Cone Rock in the lower right corner and Douglas Peak on the skyline at the head of the glacier (Photo courtesy of T. Chinn).

Intriguingly, the Lower Icefall has expanded longitudinally since 1935 and now occupies a greater length (~1000 m) of the glacier surface from the lowest part of Victoria Flat to Boyd Creek on the true left (Figure 4.4 b, area 2) possibly indicating a shallower surface gradient in the area of the icefall. Whilst travelling up the glacier from the Fox Glacier Road to Chancellor Hut, Lockwood (1949) reported that “owing to recent decay and retreat...pinnacles make up practically the whole of the trunk”, suggesting much of the lower part of the glacier between the terminus and Victoria Flat was characterised by a broken surface, rather than just the Lower Icefall area of present. The Upper Icefall consists of transverse crevasses and seracs pervading the full width of the glacier at the point which the névé is funnelled into the main valley. The area above Victoria Flat during this period was described by Lockwood (1949) as “cascading down in a splintered mass”, confirming the continued presence of the Upper Icefall. Flow boundaries are evident in the area immediately above the Upper Icefall (Figure 4.4 b area 3), although the extent to which they persist into the névé is not known due to the limited coverage of available imagery.

4.2.1.5 1965

In 1965 (Figure 4.6 a), a transition from transverse to longitudinal crevassing is observable below the Lower Icefall (Figure 4.6 a, area 1), with further longitudinal crevassing close to the terminus which at this time sits at approximately 280 m asl, between 1500 m and 2000 m up-valley of Cone Rock. The Fox River emanated from a portal at the true left of the terminus from an area of collapsed ice. The glacier's flow regime changed from longitudinal extension through the Lower Icefall to lateral extension as the ice spread out at the wider part of the valley between Straight Creek and White Creek; a pattern likely to have occurred in previous years, although this is the first visual record. A distinct area of supraglacial debris can be seen on the true left of Victoria Flat, continuing through the Lower Icefall, ending close to the terminus (Figure 4.7). This is the first time an almost continuous line of supraglacial debris is identified on Fox Glacier, as no debris has been recorded on the 1896 (Douglas & Wilson, 1896) or 1911 (Bell & Grenville, 1911) maps, and the oblique angle of the 1935 and 1950 images do not provide a sufficient view of the position of the 1965 supraglacial debris. Supraglacial debris was also evident on the true right of the terminus area of the glacier. Cross-cutting crevasses were present immediately above the Upper Icefall (Figure 4.6 a, area 2) at the point at which the broad névé is concentrated into the much narrower Fox valley.

An area of extensive crevassing can be seen on the Explorer Glacier close to the point at which it flows past the lower end of Pioneer Ridge (Figure 4.6 a, area 3). Comparable crevassing can be seen in a similar location at the true left of Pioneer Ridge on the Albert Glacier, although the crevasses appear less pronounced and not as deep.

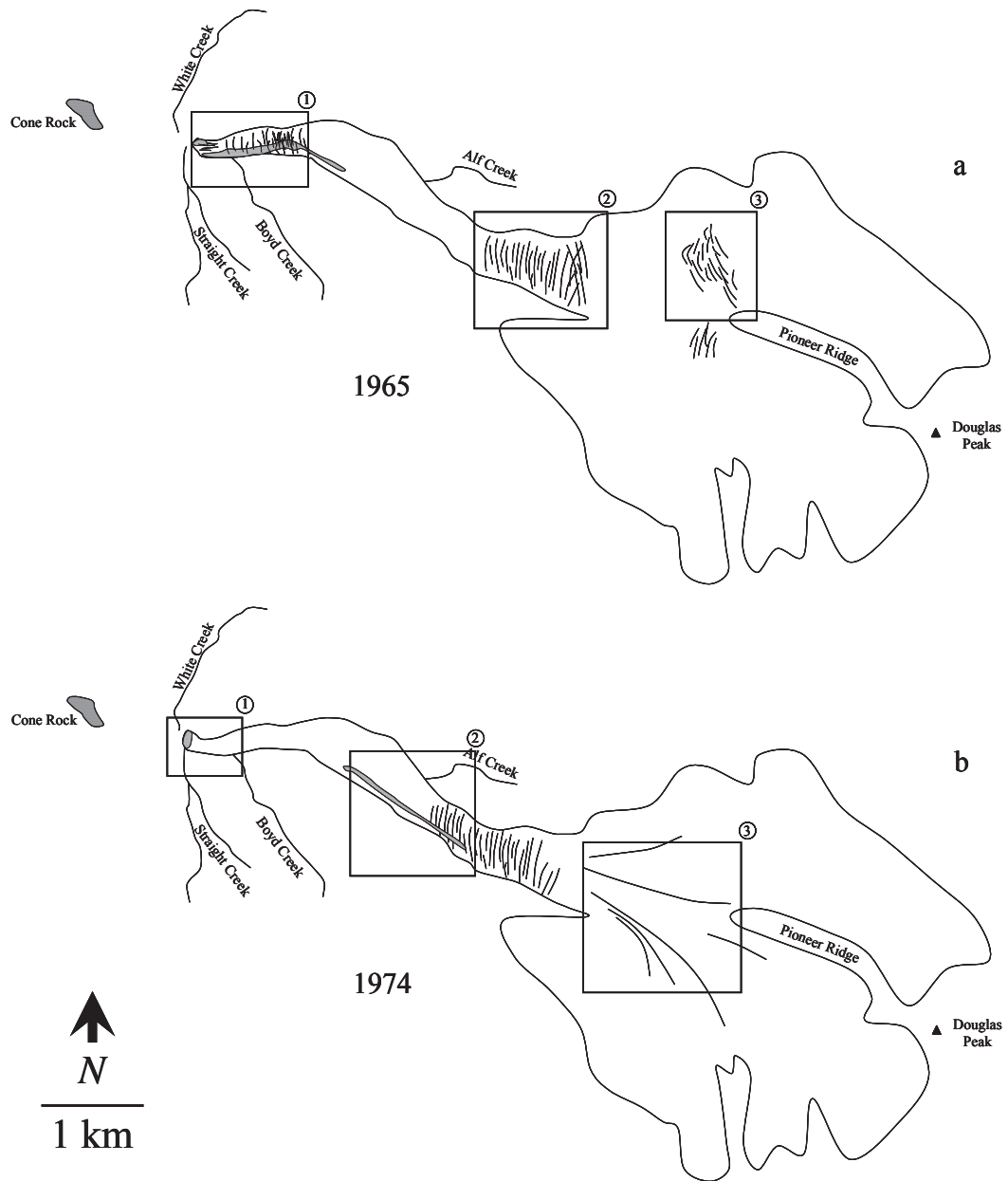


Figure 4.6: Structural interpretations from a) 1965 showing (1) crevassing and debris on the lower glacier, (2) chaotic crevassing in Upper Icefall, and (3) crevassing in the névé; and b) 1974 showing (1) terminus 1 km up-valley of Cone Rock, (2) debris on Victoria Flat, and (3) flow boundaries in névé.

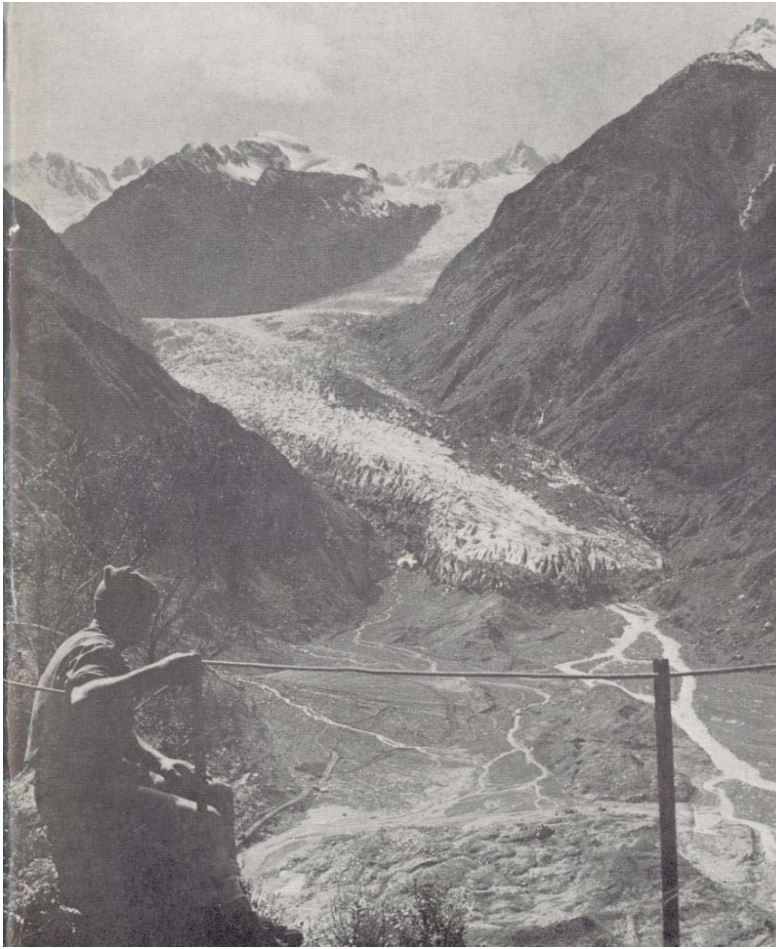


Figure 4.7: Fox Glacier from Cone Rock, November 1966 (from Sara, 1970).

4.2.1.6 1974

The 1974 aerial photograph shows the terminus to be in an advanced position compared to 1965 (Figure 4.6 a), with the front of the ice located close to White Creek (Figure 4.6 b, area 1). Immediately in front of the terminus, the Fox River, at this time flowing from the true right of the snout, is confluent with White Creek and Boyd Creek, the latter of which flows across the face of the terminus from true left to true right. Wardle (1973) identified an advance beginning in 1966, followed by a retreat which was then interrupted by a small advance in 1971. Limited supraglacial debris is evident on the lower section of Fox Glacier with just the end of the snout being covered in material. During this period, the most striking feature on the glacier surface was a narrow, distinct area of supraglacial debris located to the true left of the glacier's centre. This

moraine was approximately 2000 m long, extending from half way up the Upper Icefall to approximately half way down Victoria Flat (Figure 4.6 b, area 2). Approximately six poorly pronounced flow boundaries were evident at the confluence of the Explorer and Albert Glaciers. Chevron crevasses could be seen for almost the full length of both the true left and true right of the glacier caused by friction between the ice body and valley sides, with transverse crevassing at the upper part of both the Upper and Lower Icefalls as velocity rapidly increases causing longitudinal expansion of the glacier.

4.2.1.7 1986

Fox Glacier is at its point of greatest retreat in 1986 (Figure 4.8 a), with the terminus (Figure 4.8 a, area 1) located approximately 2000 m up-valley from the proximal end of Cone Rock, at an altitude of approximately 300 m asl. A portal can be seen at the extreme true right of the terminus, almost bounded by the valley side. Chevron and transverse crevasses were discernible in this area, although they were partially covered by supraglacial debris extending from the terminus through the Icefall on to the lower areas of Victoria Flat. Chevron crevasses were also visible on the true right of the lower part of Victoria Flat. Below the Lower Icefall this debris covered almost the entire width of the glacier (~800 m), whereas approximately half the width of the glacier (~1200 m) was covered on Victoria Flat. Arcuate bands are visible below the intensely crevassed Upper Icefall on Victoria Flat (Figure 4.8 a, area 2) with their wavelength and curvature increasing down-glacier. Prominent flow boundaries (Figure 4.8 a, area 3) are identified in the névé separating the major tributary glaciers. Approximately five flow boundaries converge on the true left of the glacier in the area between the top of the Upper Icefall and base of Pioneer Ridge. A distinct flow boundary can be seen emanating from Pioneer Ridge, terminating at the centre of the glacier in the Upper Icefall.

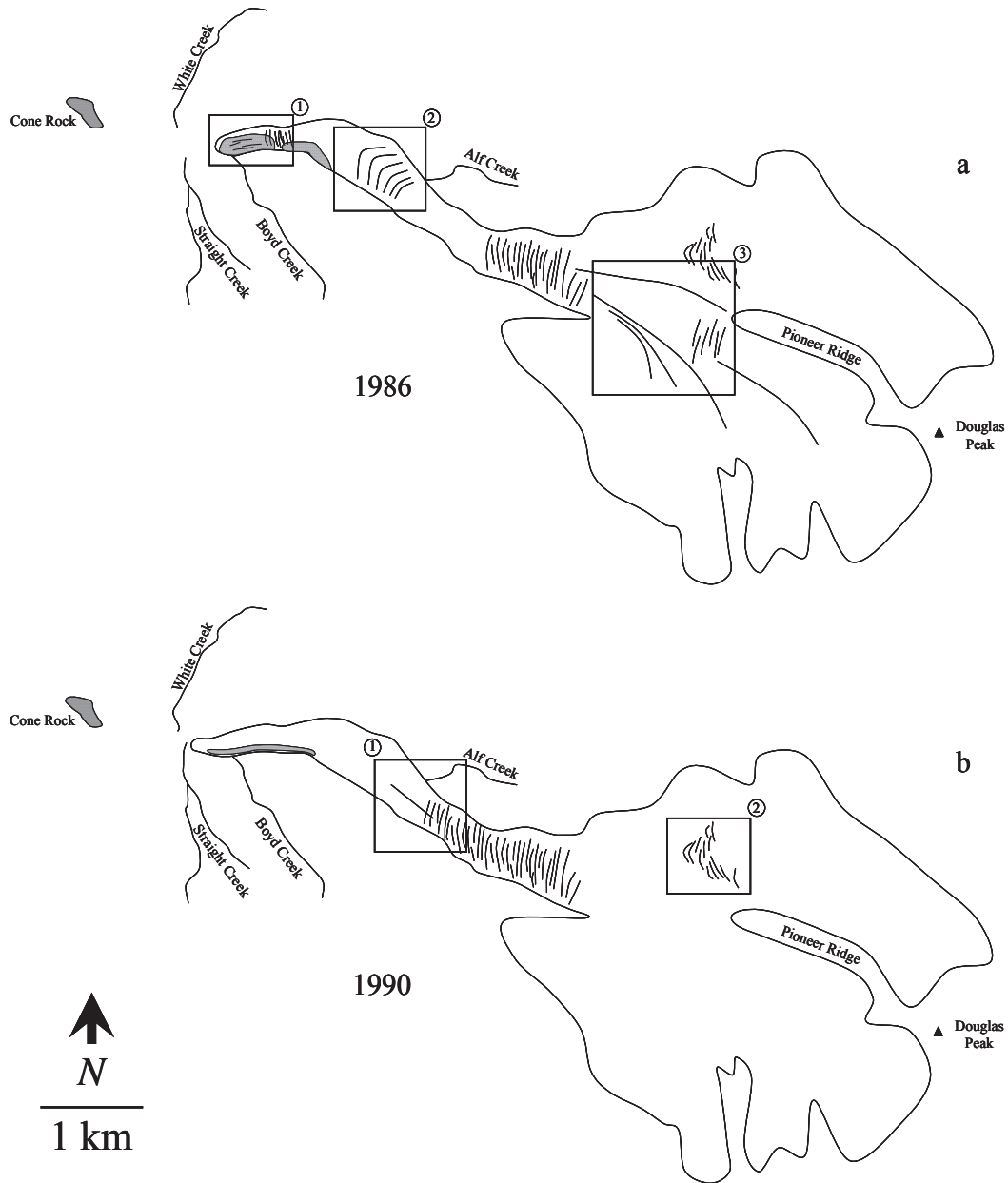


Figure 4.8: Structural interpretations from a) 1986 showing (1) terminus at its position of greatest retreat, (2) arcuate bands on Victoria Flat, and (3) flow boundaries in the névé; and b) 1990 showing (1) longitudinal structure emanating from Upper Icefall, and (2) crevassing of Explorer Glacier.

4.2.1.8 1990

By 1990 (Figure 4.8 b) the terminus had advanced ~300 m from its 1986 position to be almost level with Straight Creek at approximately 270 m asl. Supraglacial debris remained present on the true left of the lower part of Fox Glacier continuing through the Lower Icefall as the glacier turns from a northwest to westerly aspect. Chaotic crevassing was obvious in the Upper Icefall, whilst a longitudinal structure can be identified pervading from the base of the Upper Icefall for approximately 1 km down the centre of Victoria Flat (Figure 4.8 b, area 1). This longitudinal feature is interpreted as the continuation of a flow boundary from the névé, or a narrow band of supraglacial debris indicating a medial moraine. Resolution of the 1990 Landsat image is insufficient to accurately define detail of this structure. The resolution also provides limited detail of the névé area, although large scale features such as an area of crevassing on the true right of Pioneer Ridge above the Explorer and Albert Glacier confluence (Figure 4.8 b, area 2) were identifiable.

4.2.1.9 2000

In 2000 (Figure 4.9 a), the terminus of Fox Glacier was in a similar position to that of 1990, although shadow from the north side of Fox Valley's north side hides much of the lower glacier. Supraglacial debris formed a discontinuous line from half-way along Victoria Flat through the Lower Icefall to the lower glacier (Figure 4.9 a, area 1). Most of the debris was towards the true left of the glacier below the Lower Icefall, although it appears to be closer to the midpoint of Victoria Flat. As in 1990, a longitudinal feature can be identified on Victoria Flat, again pervading from the base of the Upper Icefall to the centre of Victoria Flat, although the feature was reduced in length from 1 km in the previous imagery, to 500 m in 2000. Obvious flow boundaries converge at the top of the Upper Icefall, in an area of chaotic crevassing (Figure 4.9 a, area 2). The crevasses in this area converge, as with flow boundaries, merging from the Albert Glacier on the true left, and an area beneath Chancellor Dome on the true right. Longitudinal features not previously identified can be seen in the true left of the Albert Glacier (Figure 4.9 a, area 3), although cloud cover prevented an accurate assessment of their provenance and spatial extent.

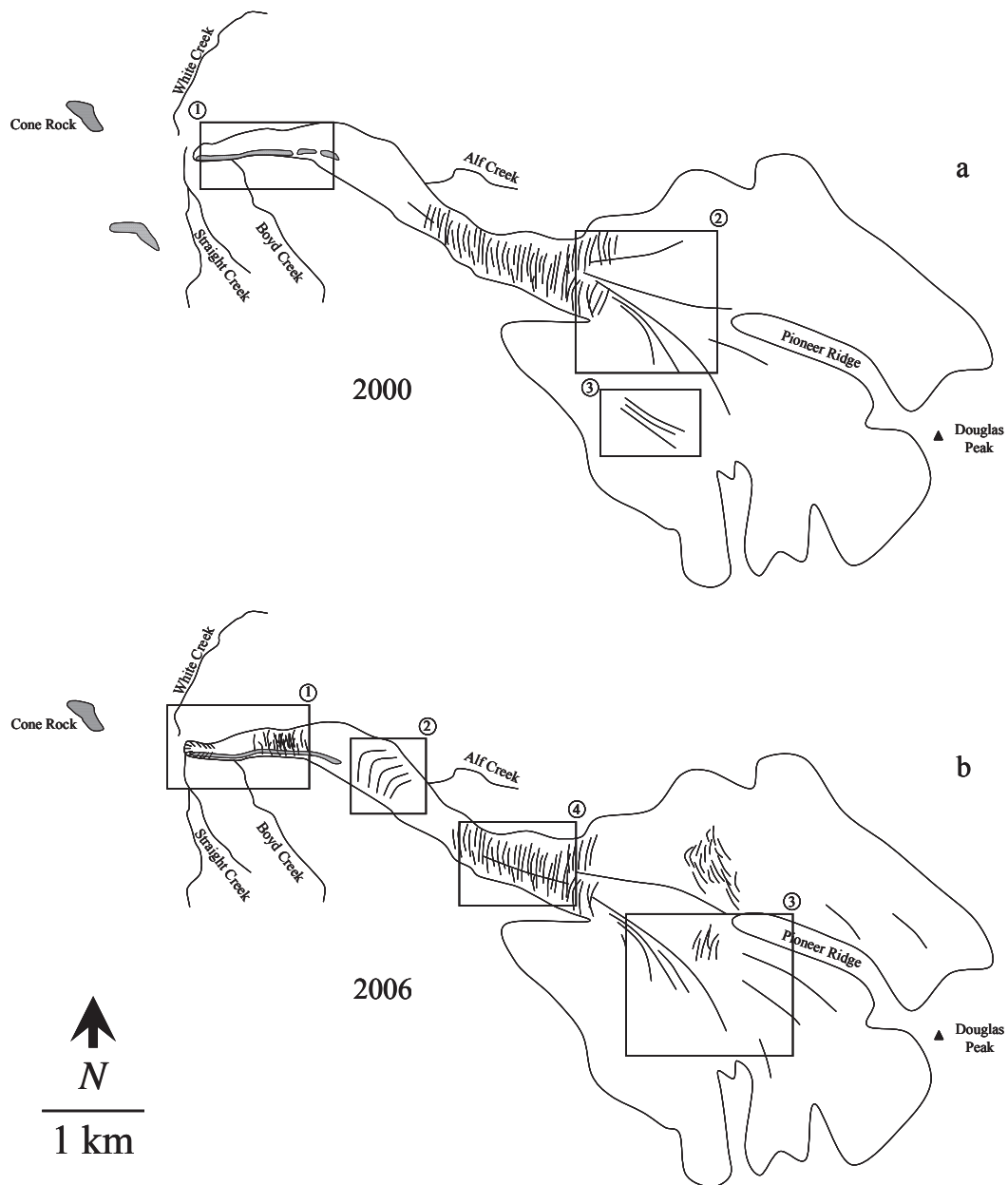


Figure 4.9: Structural interpretations from a) 2000 showing (1) moraine continuing from Victoria Flat to lower glacier, (2) flow boundaries, and (3) longitudinal structures of unknown origin; and b) 2006 showing (1) terminus crevassed lower glacier, (2) arcuate bands on Victoria Flat, and (3) flow boundaries in névé.

4.2.1.10 2006

The 2006 (Figure 4.9 b) QuickBird imagery is currently the highest resolution image available (0.61 m Pan/ 2.4 m MS) for this study and gives excellent detail of both small and large-scale features. The terminus currently sits approximately in line with White Creek on the true right and Straight Creek on the true left with the Fox River exiting from a portal at the true right of the terminus. Splaying and chevron crevasses were present in the lower glacier (Figure 4.9 b, area 1) along with supraglacial debris which formed a continuous line through the Lower Icefall onto the true left of Victoria Flat. Arcuate bands were once again present on Victoria Flat with curvature increasing down-valley (Figure 4.9 b, area 2). The Upper Icefall was characterised by chaotic crevassing, and very limited areas of the névé are crevasse free. A very prominent flow boundary can be seen running from the distal end of Pioneer Ridge to the top of the Upper Icefall. In addition, approximately 8 flow boundaries can be identified on the surface of the Albert Glacier, with 2 on the Explorer Glacier (Figure 4.9 b, area 3). A longitudinal structure that may indicate a possible flow boundary was identifiable through the Upper Icefall (Figure 4.9 b, area 4). The 2006 QuickBird imagery was used in the construction of contemporary maps of the surface features of Fox Glacier provided in *Section 4.3*, below.

4.2.1.11 Relative Changes in Ice Surface Elevation

In addition to temporal variations in surficial structures and terminus position at Fox Glacier, ice thickness also changes in response to fluctuations in mass balance and ice volume. No absolute ice surface elevations have been recorded except for those of Douglas and Wilson (1896) who gave 1894 ice surface elevations of 273 m asl at the snout, 396 m asl in the area immediately adjacent to Cone Rock, and 829 m asl at the confluence of the Victoria Glacier and Fox Glacier half-way down Victoria Flat, however, the work of Sara (1968, 1970) and Purdie (2005), along with field observations of trim lines, has allowed for the analysis of relative glacier surface elevations (Figure 4.10).

The greatest change in ice surface elevation occurs between 1950 and 1965 (~150 m); a change coinciding with the period of greatest terminus retreat (~1250 m). Prior to this, during the period 1896 to 1935, the surface height of Fox Glacier was continuously

reducing but at a much lower rate than after 1950. Since 1965, the ice surface elevation has been concomitant with the regular fluctuation pattern similar to that observed occurring with the terminus position. However, Chinn *et al.* (2002) note that the position of the terminus does not necessarily relate to changes in ice volume, as a glacier may gain or lose volume without a change in the terminus position. This is supported by the fact that there is often a time lag (~8 years for Fox Glacier (Purdie and others, 2008a, Purdie and others, 2008b)) between an increase or decrease in mass balance/glacier volume and the subsequent response at the terminus (i.e. advance or retreat) (Johannesson and others, 1989). At Fox Glacier, relative changes in ice surface height were particularly pronounced, following even small changes in mass balance or ice volume, due to confinement of the ice body by steep valley sides.

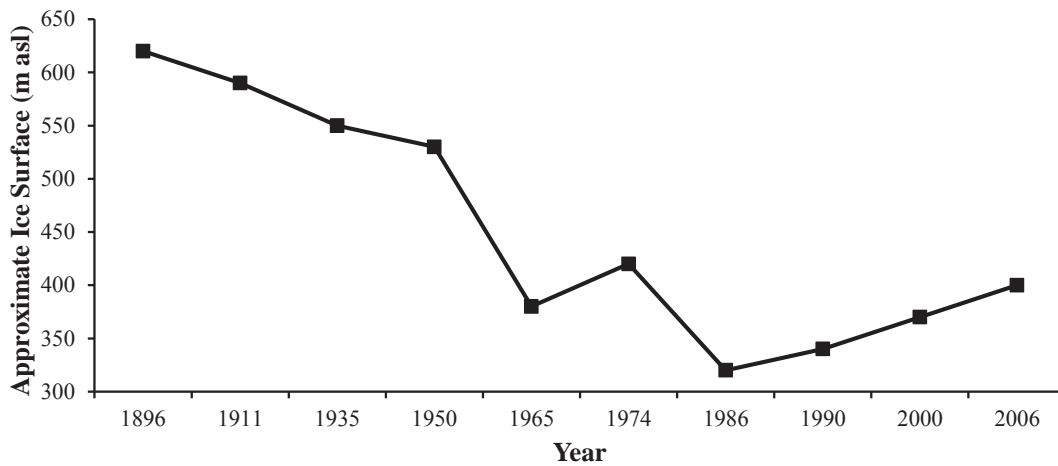


Figure 4.10: Change in approximate ice surface elevation between 1896 and 2006 measured approximately at the 1986 terminus position; the time at which Fox Glacier was at its position of greatest retreat (Developed from Sara (1968, 1970) and Purdie (2005)).

4.3 The Contemporary Structure of Fox Glacier

The contemporary surface structural glaciology of Fox Glacier has been determined through analysis of satellite images (Figure 4.11) and field observations, using the techniques described in *Section 3.5*. Areas of particular structural interest are shown in large-scale maps whilst the overall surface structure is shown in a smaller-scale map. Planar structures are classified using standard structural glaciological notation (e.g. Hambrey & Milnes, 1977, Goodsell and others, 2005c), according to a hierarchy of ‘structural levels’ based on structural geology (e.g. Ramsay & Huber, 1987). Thus, structures are denoted as S_0 , S_1 , S_2 , etc., with primary stratification S_0 .

4.3.1 Structural Domains

Fox Glacier can be broadly divided into three structural domains (Figure 4.12): Fox Glacier Névé; Victoria Flat; and the Lower Fox Glacier. Each domain has distinct structural and topographic characteristics although continuity of some structures means some structures pervade across the domain boundaries.

Fox Glacier névé is characterised by a mixture of gently-sloping snow ramps, deep crevasses and areas of outcropping rock (Figure 4.13). No hard glacier ice is visible in the névé due to permanent snow and firn cover. The lower boundary of the névé domain can be considered approximately the same as the equilibrium line altitude (ELA) (~1800 m; Appleby and others, 2010).

Victoria Flat has the lowest gradient ($<5^\circ$) of any part of the glacier, with a continuously gentle topography broken only occasionally by crevasses, moulins and supraglacial drainage systems. The upper part of Victoria Flat, constituting the lower end of the Upper Icefall, is steeper, with a stepped pattern of transverse ridges and troughs.

The lower glacier (Figure 4.14) between the Lower Icefall and the terminus is characterised by a steeper slope ($15\text{--}20^\circ$) and a more complex topography. Longitudinal ridges and crevasses are typical, with a long ribbon (~1000 m) of supraglacial debris covering almost the entire length of the true left of the lower glacier.



Figure 4.11: Composite satellite image of Fox Glacier used for determining surface structural glaciology. The imagery was acquired in 2006 and 2007 using the QuickBird Satellite owned by DigitalGlobe.

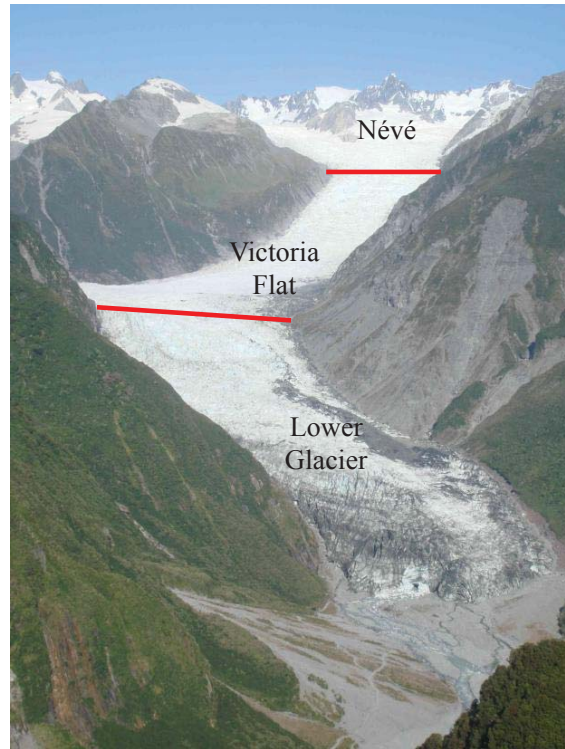


Figure 4.12: Structural domains identified on Fox Glacier. The three domains comprise the Névé, Victoria Flat and the Lower glacier. (Photo: J. Appleby, January, 2009)



Figure 4.13: View looking northeast from Pioneer Ridge towards Mt's Mallory and Barnicoat, which separate the Fox Glacier and Franz Josef Glacier névés. The photograph displays many of the characteristic features of Fox Glacier névé including prominent rock buttresses, deep crevasses and undulating snow slopes. (Photo: J. Appleby, January, 2011)



Figure 4.14: Composite panoramic image of part of the lower Fox Glacier showing many of the features typical of this structural domain. Viewed from the true left of the glacier, ice flow is from right to left. (Photo: J. Appleby, January, 2010)

4.3.2 Contemporary Structural Features of Fox Glacier

Field observations and analysis of satellite images has facilitated the compilation of an interpretive map of the surface structural glaciology (Figure 4.15). This map details the location, relative size and orientation of the structural features which are visible on the glacier surface.

The structures identified on the interpretive map are described in more detail in the following sections, progressing from macro-scale features of structural significance such as icefalls to micro and intermediate-scale features such as folds. Further discussion and interpretation of the presence and location of these structural features is covered in *Section 4.4*.

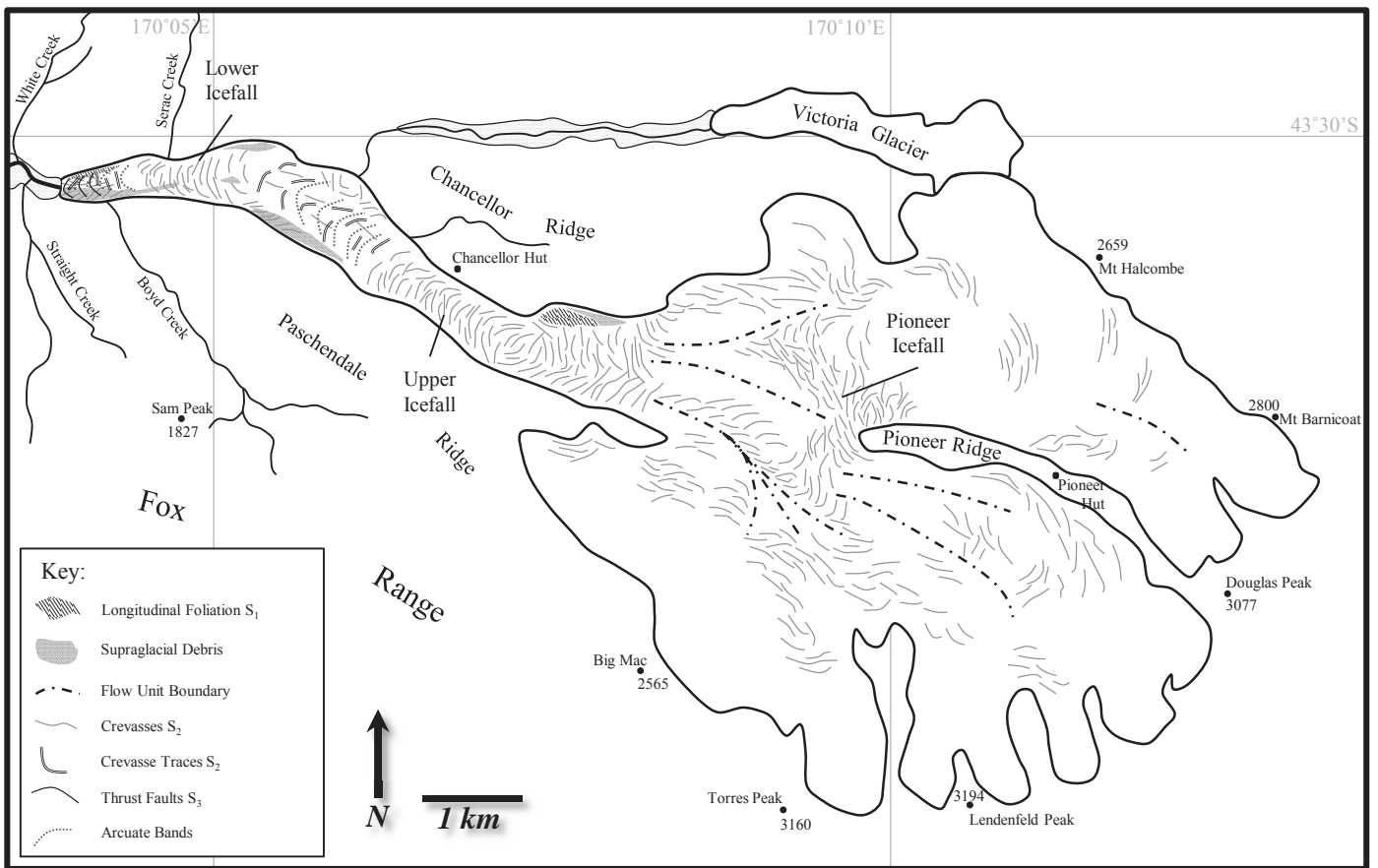


Figure 4.15: Structural glaciological interpretation of Fox Glacier surface features identified through field observations and satellite image analysis.

4.3.2.1 Icefalls

Previous research (e.g. Appleby and others, 2010, Purdie and others, 2008a, b) has defined two icefalls at Fox Glacier, the Upper and Lower Icefalls (Figure 4.16). However, in this work a third icefall is recognised at the distal end of Pioneer Ridge, based on observable topography and surface structures (Figure 4.17). Each of the three icefalls is characterised by chaotic transverse crevassing in zones of extensional flow, due to an increase in surface gradient in the bedrock surface below the glacier (Figure 4.18).

The step in topography associated with the Lower Icefall is interpreted to have formed due to over-deepening of the valley long profile at the confluence of the Victoria and Fox Glaciers. This over-deepening is partly caused by increased basal erosion rates as ice discharge increases (e.g. Harbor and others, 1988) assuming erosion rates are proportional to ice discharge per unit valley width (Anderson and others, 2006b). A full interpretation of the causes of over-deepening is provided in *Section 4.4.2.1*.

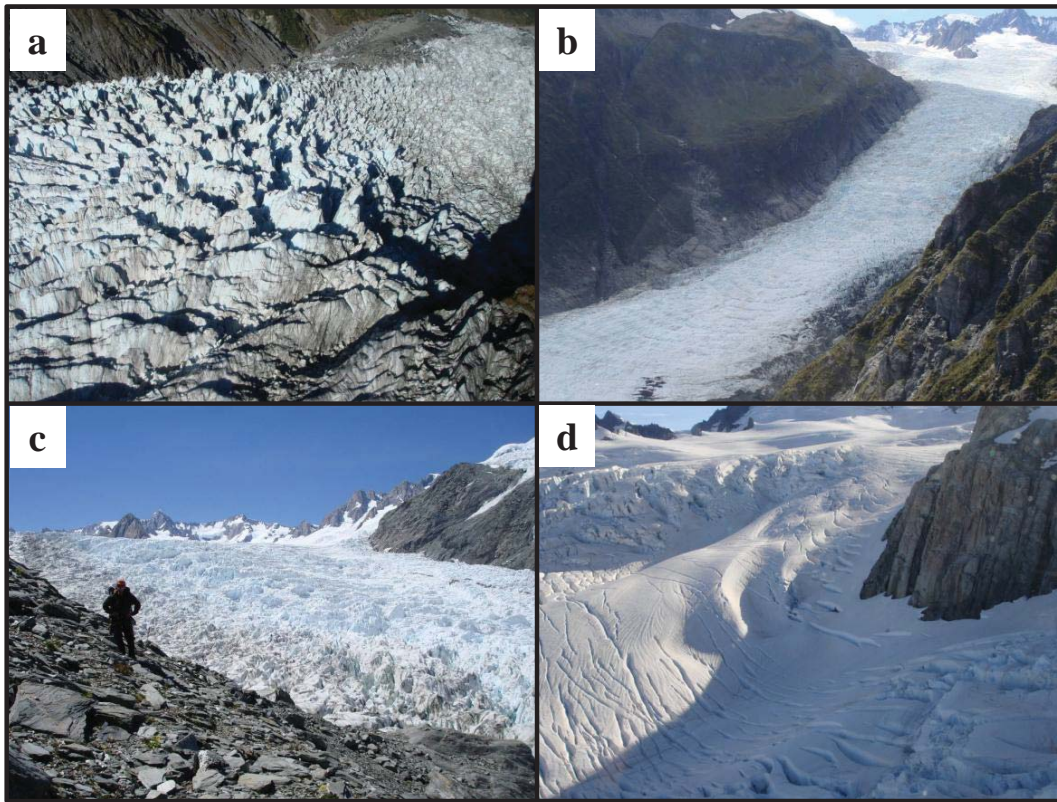


Figure 4.16: Icefalls of Fox Glacier: a) Aerial view of the Lower Icefall looking towards the terminus (ice flow from left to right); b) Aerial view of the Upper Icefall and upper part of Victoria Flat (Chancellor shelf is the grassy area above the true-right of the glacier); c) Upper Icefall viewed from Chancellor shelf; and d) Aerial view of part of the Pioneer Icefall viewed from above the Albert Glacier (ice flow from right to left). The prominent rock buttress at the right of the photograph marks the lower end of Pioneer Ridge. (Photos: J. Appleby)



Figure 4.17: Composite image of the Pioneer Icefall viewed towards the southeast from beneath Chancellor Dome. The distal end of Pioneer Ridge is visible as the rock buttress at the centre of the photograph. Mount Tasman (3497 m) is the prominent, snow-capped peak to the right of the photograph. (Photo: J. Appleby, January, 2011)



Figure 4.18: View of the Lower Icefall looking up glacier. A step in the valley profile has been caused by over-deepening down-valley of the Fox Glacier-Victoria Glacier confluence. (Photo: J. Appleby, February, 2010)

4.3.2.2 Primary Stratification (S_0)

Primary stratification of glacial ice is difficult to observe from aerial photographs, but very apparent in the field. Thus (the majority of) information on primary stratification presented here is based on field observations. Within the névé distinct layering is obvious in the walls of open crevasses (Figure 4.19), with layers becoming increasingly dense as depth increases, in response to the removal of gas bubbles by pressure. In many cases, boundaries between individual layers are highlighted through the incorporation of wind-blown dust. Stratification in the névé has a low-gradient average dip angle of $\sim 2^\circ$.

Primary stratification can also be observed in crevasse walls in the lower glacier and Victoria Flat, although stratification is most prominent at the glacier margins of these structural domains, and in séracs in the Upper and Lower Icefalls (Figure 4.20). Orientation of primary stratification varies considerably throughout the glacier with layers in some areas undergoing rotation from horizontal to near-vertical, and most displaying a high angle of dip (subvertical) in the lower glacier and Victoria Flat (Figure 4.21).



Figure 4.19: Primary stratification exposed in a crevasse wall in the névé. Layers of wind-blown dust are interspersed between layers of clean snow and firn. (Photo: J. Appleby, January, 2011)



Figure 4.20: Primary stratification visible as dirt layers in séracs at the true right of the Lower Icefall, rotated to almost 90°. The icefall is viewed up-valley from the lower glacier. (Photo: J. Appleby, January, 2011)

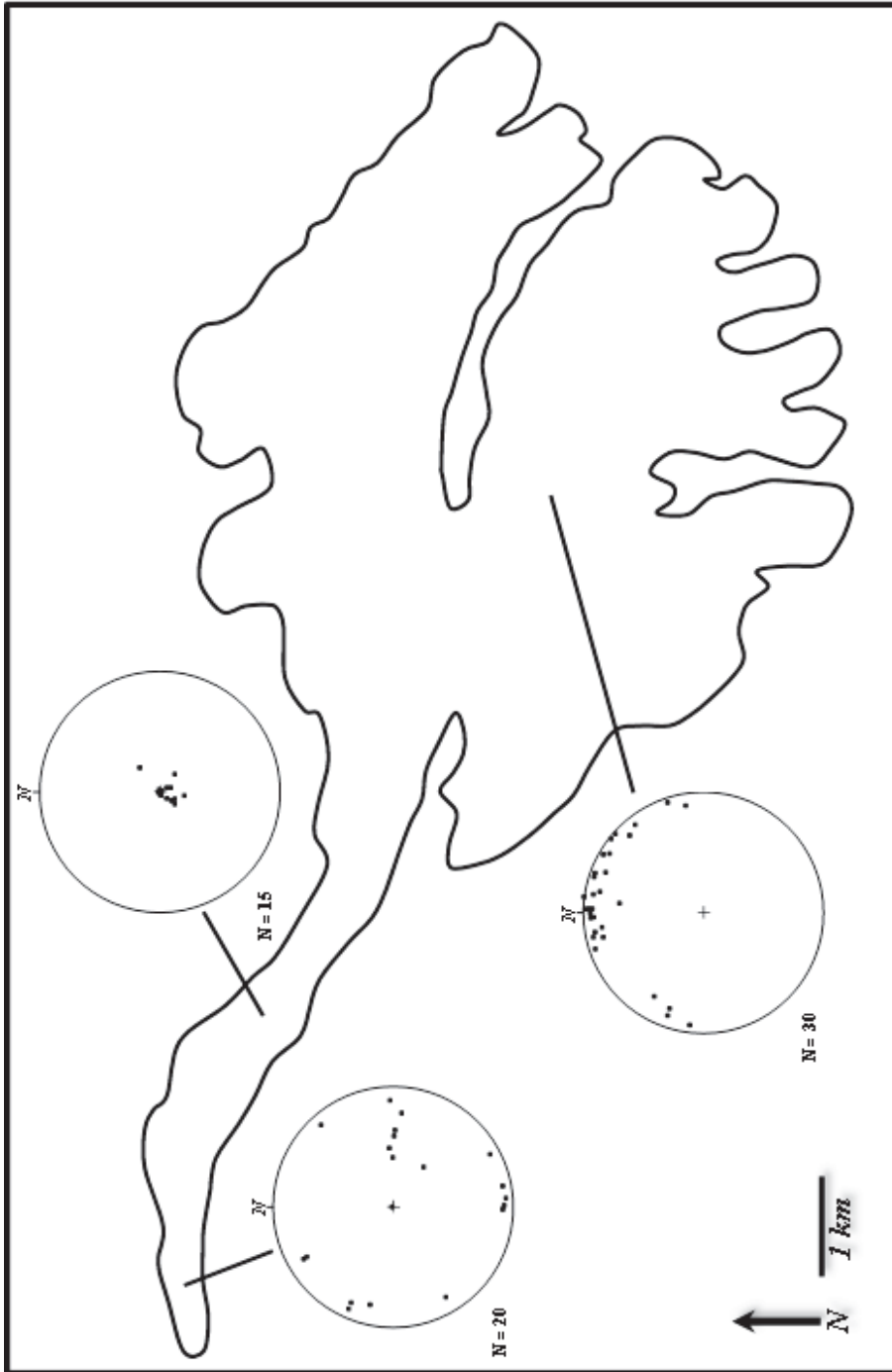


Figure 4.21: Field measurements of primary stratification (S_0). Strike and dip of primary stratification measurements are represented by three-dimensional equal area stereographic projections, where the centre of the circle and the circle itself represent a dip of 90° and 0° respectively. Strike is recorded according to degrees from north.

Accumulation and firnification of snow into glacier ice is assumed to occur across the whole of the névé as this area is entirely above the ELA of ~1800 m (Appleby and others, 2010). However, the spatial distribution of accumulation is uneven across the névé due to topography and synoptic conditions (Purdie and others, 2011a). While many areas of the névé surface are continuous, with few if any crevasses, other areas are characterised by incipient and well-developed crevasses that have exposed primary stratification in their walls. The boundary between some of these stratifications is more visible in some locations due to the presence of dark, wind-blown dust. The repetitive primary stratification can be seen in crevasse walls and areas of exposed ice throughout Fox Glacier, although is most prominent in the névé.

In some areas of the glacier, layers can be categorised as one of two main types: coarse-grained bubbly white ice, and hard blue smooth ice. The coarse-grained ice is likely to have formed from winter snowfall accumulation in the upper part of the accumulation area, whilst the harder blue ice is characteristic of summer ablation ice and superimposed ice caused by the refreezing of melt water (cf. Paterson, 2000).

Layers that are initially sub-horizontal in the névé are slowly deformed and rotated as the glacier flows down-valley, producing the high angles of dip seen in the lower part of the study area, especially visible in the Lower Icefall as limbs of steeply dipping folded ice. Hooke and Huddleston (1978) suggest that primary stratification can be transposed by high strains and rotation to form foliation (S_1 , below). This is suggested as the main process of foliation formation in Fox Glacier.

4.3.2.3 Foliation (S_1)

Longitudinal foliation, presumably developed from rotated primary stratification (Hambrey & Lawson, 2000), is evident at the true right margin of the lower glacier (Figure 4.22) and strikes approximately parallel to the direction of ice flow and dips toward the true left at a high angle between approximately 65° to 90°.



Figure 4.22: Modified primary stratification (S_0) forming longitudinal foliation (S_1), observed in the true right margin of the lower glacier. The proglacial sandur can be seen in the distance. (Photo: J. Appleby, January, 2011)

On Victoria Flat, the foliation identified is mainly of an arcuate nature in plan-form (Figure 4.23). The layers of coarse-grained bubbly ice form arcs similar in appearance to ogives, with a convex, down-valley morphology in plan-form. Common to glaciers with icefalls or areas of extensive transverse crevassing (Hambrey, 1977), arcuate foliation may develop with a purely transverse morphology at its source, becoming curved as a result of differential cross-glacier flow rates. This is a likely scenario on Fox Glacier due to the extensive Upper Icefall and high velocities, which increase toward the centre of the glacier (e.g. Purdie and others, 2008a, Purdie and others, 2008b, Ruddell, 1995), with high strain rates immediately below the icefall in a zone of longitudinal compressive flow. At the true right margin of Victoria Flat, in the area immediately below and down-glacier of the former Fox Glacier/Victoria Glacier confluence, an isolated zone of longitudinal foliation can be observed. This longitudinal

foliation is interpreted as the remnant ‘ends’ of the previously discussed transverse foliae, which have become arcuate in plan-form due to ice flow. Thus, they form large-scale folds with fold limbs dipping parallel to the direction of glacier flow.



Figure 4.23: Transverse foliation observed on Victoria Flat. Clear blue ice is interbedded with coarse white ice. Direction of ice flow is from right to left. (Photo: J. Appleby, June, 2010)

4.3.2.4 Crevasses and Crevasses Traces (S_2)

Crevasses are highly significant features which exert an influence on the dynamics of temperate valley glaciers because they provide a pathway for surficial water to penetrate to the subglacial zone (e.g. Fountain & Walder, 1998, Clason and others, 2012). Flowing water within glaciers in turn profoundly affects glacier movement by influencing the stress distribution at the glacier bed and thereby the rate at which the ice

slides over the bed. This process is especially important in temperate alpine glaciers (e.g. Iken & Bindshadler, 1986, Purdie and others, 2008a).

Crevasses and crevasse traces are the most ubiquitous structural features on the surface of Fox Glacier with a multitude of different types present in various orientations, although some general patterns can be identified. They are observable in various forms (Figure 4.24) throughout each of the structural domains; however, some crevasse types are only present in certain areas, whilst others occur from the highest points in the névé all the way down-glacier right up to the glacier snout. Although crevasse locations are easily identifiable in the field, the overall pattern of crevassing is more easily detected from above, via aerial and oblique photographs, and satellite images.

Transverse crevasses are the most common and most easily recognised type of crevasse on Fox Glacier. This is because the glacier is steep and generally fast-flowing. Transverse crevasses are a common feature in the three icefalls. These areas of extensional flow are characterised by transverse crevasses pervading almost the entire width of the glacier. Many transverse crevasses increase in width down-glacier through the Upper Icefall as gradient and extensional flow increases.

Transverse crevasses are also prominent in the névé (4.24 c) towards the down-glacier end of Pioneer Ridge, and in areas closer to the névé headwall, associated with a drop in altitude. Transverse crevasses are also present at the boundary of the névé and Victoria Flat domains as ice begins to accelerate into the Upper Icefall. Such crevasses pervade the entire length of the Upper Icefall to Victoria Flat, at which point they close and are no longer apparent. A similar relationship between crevasse pattern and surface gradient is observable at the lower end of Victoria Flat where, once again transverse crevasses develop in association with the region where ice velocity increases at the top of the Lower Icefall (Figure 4.24 b).

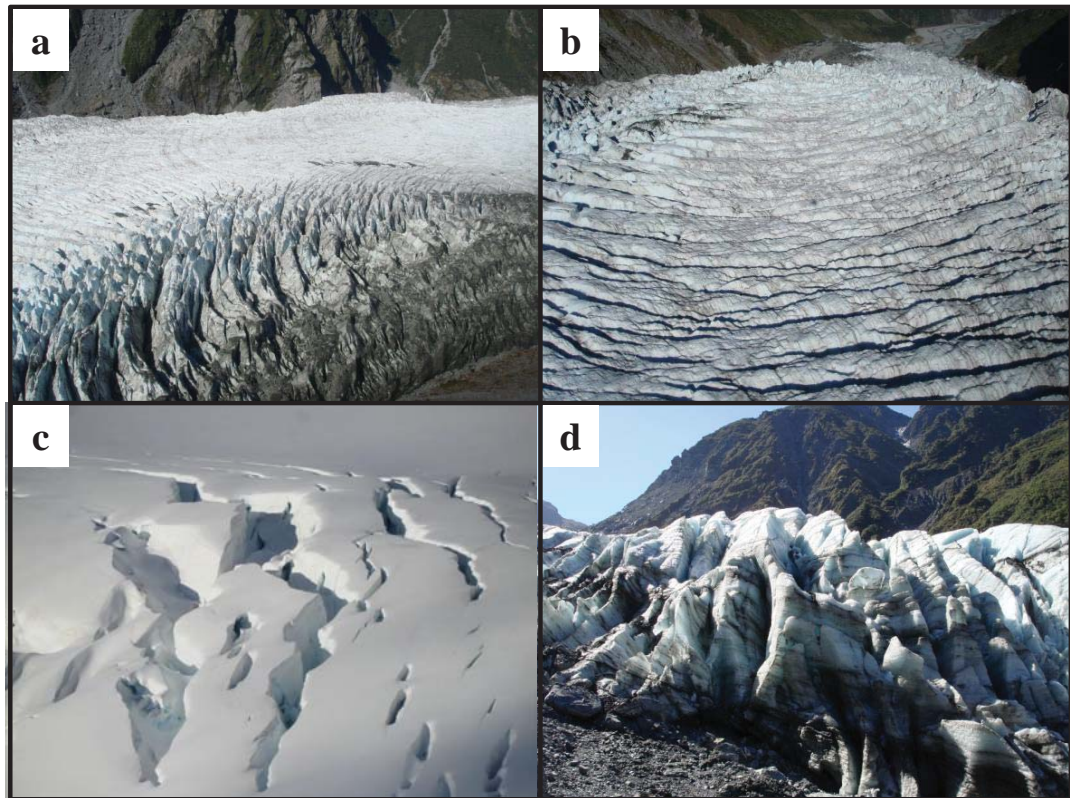


Figure 4.24: A selection of crevasse types observable on Fox Glacier: a) Chevron Crevasses on the true left of Victoria Flat caused by friction between flowing ice and the valley side (flow is from right to left); b) Transverse crevasses in the zone of longitudinal extension as ice flows from Victoria flat into the Lower Icefall; c) Transverse crevasses in the snow-pack of Fox Glacier névé; and d) Splaying crevasses seen in the true-right of the snout, viewed from the proglacial sandur. (Photos: J. Appleby)

Chevron crevasses are present along both the true-right and true-left margins of Victoria Flat and the lower glacier, at the interface between the ice and the valley sides. These are most prominent at the true left margin of Victoria Flat immediately above the Lower Icefall (Figure 4.24 a). Such crevasse forms continue into the lower glacier but are largely obscured by supraglacial debris cover on the true-left.

At the glacier terminus, splaying crevasses become prominent (Figure 4.24 d) as the glacier laterally expands into a wider part of the valley and increased ablation causes unloading and expansion of the ice at the margins. Splaying crevasses in this area radiate towards the true-left, the true-right and towards the snout. Such crevasses likely penetrate the full-depth of the glacier, as is evident at the terminal face (e.g. Fig 4.24 d).

In some areas it is possible to observe the process of crevasse formation, where ice units are ‘close to crevassing’ (Hambrey & Lawson, 2000). In the névé, these incipient crevasses (Figure 4.25) can be followed as narrow traces on the glacier surface for distances in excess of 100 m. Most of these are oriented transverse to flow and appear to be the initial stage of transverse crevasse formation (Figure 4.26), with many forming an en echelon pattern as the ice surface separates.



Figure 4.25: An incipient transverse crevasse forming in the névé. The crevasse has formed an en echelon pattern as the surface has ruptured. Direction of ice flow is from left to right. (Photo: J. Appleby, January, 2011)



Figure 4.26: Incipient crevasse forming transverse to flow on the lower part of Victoria Flat. At this stage the crevasse is <math><0.15\text{ m}</math> wide. Flow is from right to left. (Photo: J. Appleby, June, 2010)

Crevasse traces (Figure 4.27) are present over much of the surface of Victoria Flat and the lower glacier, as observed from both field observations and remotely-sensed images. However, no crevasse traces were identified in the névé. Crevasse traces are present in the lower structural domain, with many persisting across almost the entire width of the glacier.

Crevasse traces measured on Victoria Flat generally have a very steep up-valley dip (80 to 90°), whilst those measured in the lower glacier tend to have a lower dip angle (45 to 85°) (Figure 4.28). A pattern in crevasse trace orientation is not discernible from field observations or remotely-sensed images. The number crevasse traces observed in the field increases with increasing distance down-glacier from the Upper Icefall to the glacier terminus.



Figure 4.27: Intersecting, cross-cutting crevasse traces observed on the lower glacier. Crevasse traces in this area persist for almost the entire width of the glacier. Ice flow is from right to left. (Photo: J. Appleby, January, 2009)

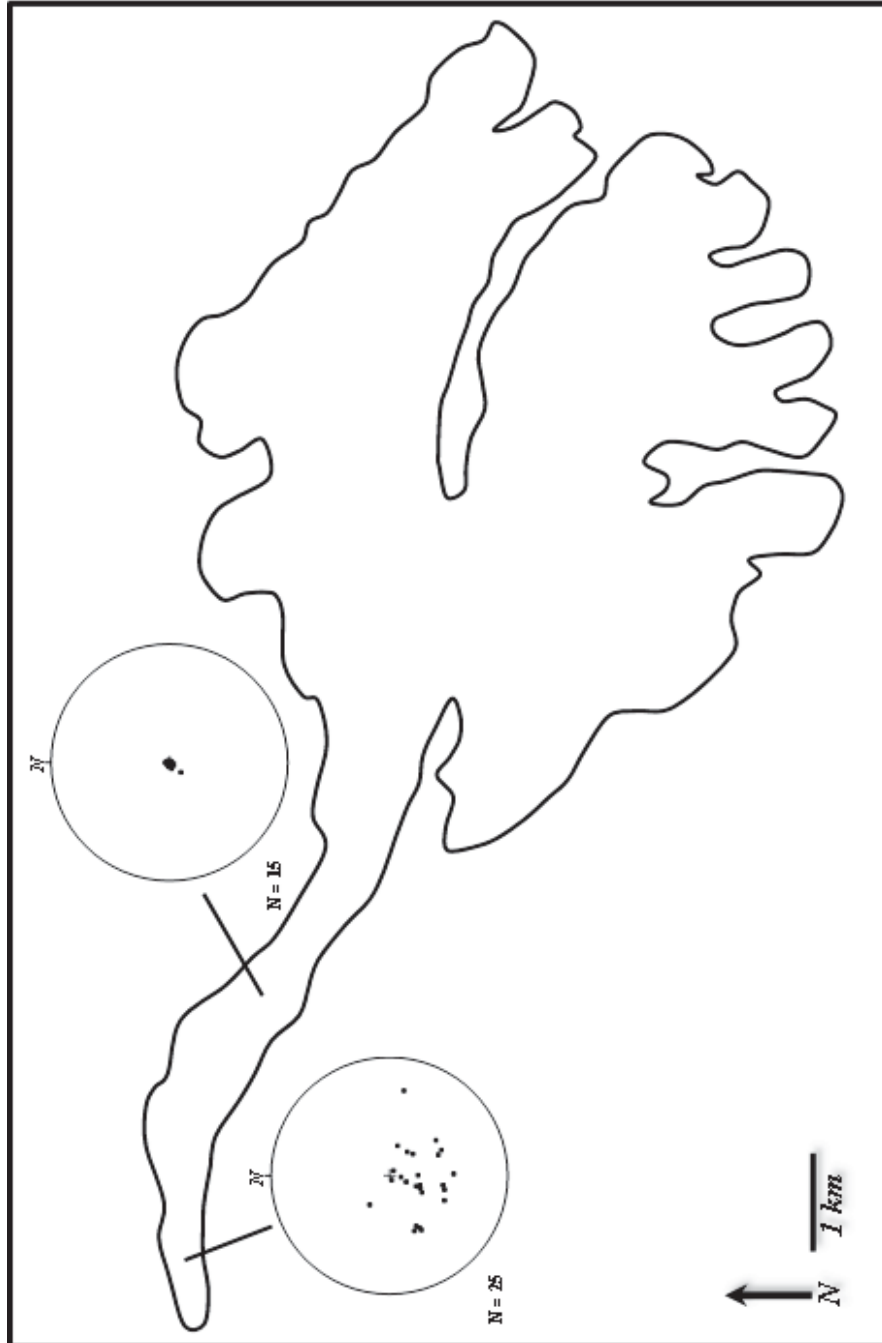


Figure 4.28: Field measurements of transverse arcuate structures (crevasse traces) (S_2). Strike and dip of crevasse trace measurements are represented by three-dimensional equal area stereographic projections, where the centre of the circle and the circle itself represent a dip of 90° and 0° respectively. Strike is recorded according to degrees from north.

4.3.2.5 Thrust and Reverse Faults (S_3)

Prominent features of the lower glacier immediately up-glacier from the snout are arcuate features interpreted as thrust faults (Figure 4.29). In this region, longitudinally compressive flow has resulted in large-scale fracturing/faulting of the ice, followed by the hanging-wall block subsequently over-riding the foot wall. The curved profile and concave-upward surface of the thrust planes creates a listric shape, with dip angle decreasing with depth. The curvature of these thrust planes observable at the glacier surface suggests a 'nested spoon' pattern often seen in foliation (e.g. Hooke & Hudleston, 1978, Hambrey, 1994, Paterson, 2000, Allen and others, 1960).

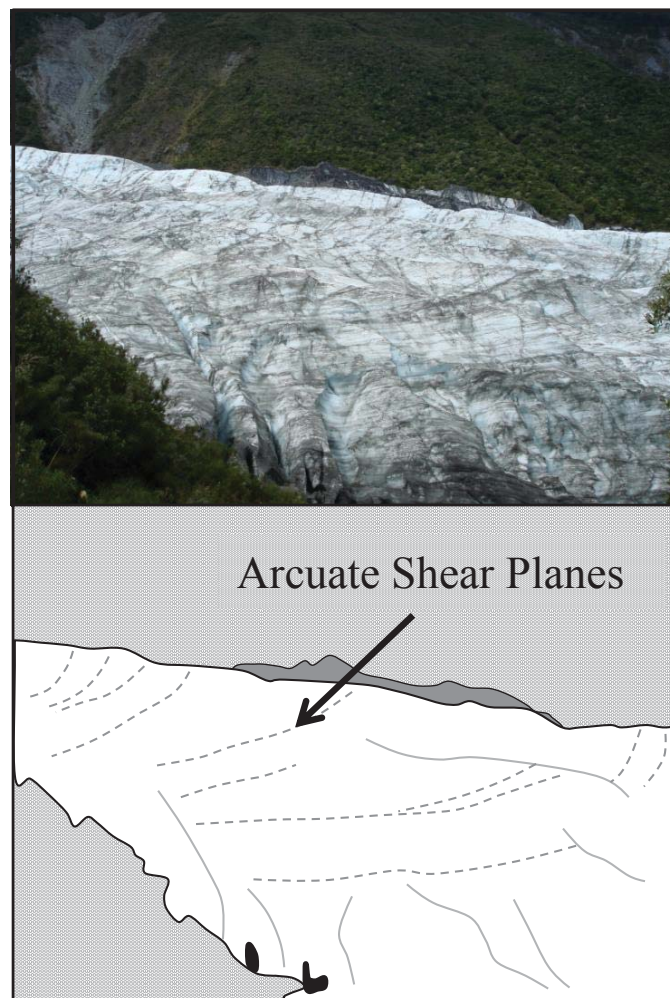


Figure 4.29: View of the true-right side of the lower glacier close to the terminus showing up-glacier dipping planar structures, which are interpreted as thrust planes.

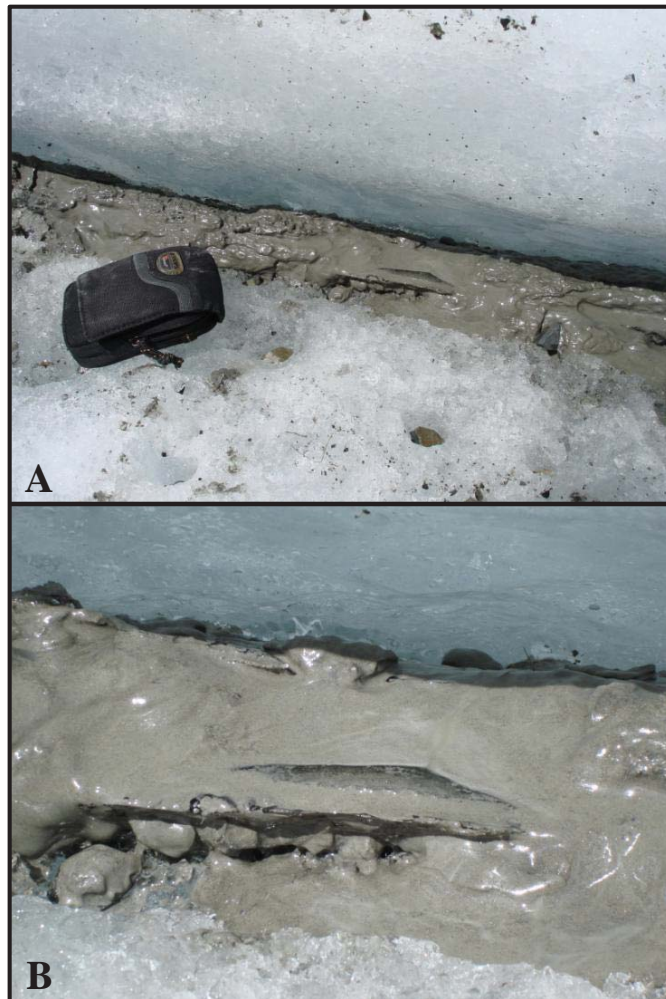


Figure 4.30: A) Surface expression of thrust fault close to the glacier snout; and B) Close up of the thrust fault showing clear, bubble-free regelation ice and fine subglacial material that has been thrust to the surface. (Photos: J. Appleby, January, 2011)

The surface expressions of thrusts are thin (0.1-0.2 m) fault lines that contain clear, bubble free regelation ice (Figure 4.30). Suspended within this regelation ice, can be found lenses of fine sediment that eventually melts out and collects in the depression created by the fault-line, similar to that identified by Hambrey *et al.*, (1996). Grain-size analysis of this fine sediment has been undertaken to determine its provenance and transport history through the glacier system (*refer Chapter Five*). In addition, isotopic fractionation of D-O¹⁸ has been measured in the regelation ice, to determine the altitudinal provenance and transfer history (*refer Section 4.3.3*) of the ice. As water

undergoes isotopic fractionation on freezing, combined δD and $\delta^{18}O$ measurements make it possible to distinguish between isotopically-unmodified surface ice and isotopically modified basal ice. Hence, δD - $\delta^{18}O$ relationships have previously been used to interpret the thermal history of glacier ice and to determine whether basal melting and refreezing has occurred in a given sample of ice (Arnason, 1969, Souchez & De Groot, 1985, Glasser & Hambrey, 2002b).

4.3.2.6 Folding (F_1) and Faulting

Few intact fold structures are present on the surface of Fox Glacier. Most evidence of folding can be seen immediately below the Upper Icefall on the surface of Victoria Flat and to the true-left side of both Victoria Flat and the lower glacier, with less pronounced folding closer to the centre of the glacier. Most folds were found in isolation whilst some were found in a repeating pattern along the length of a crevasse wall, with occasional parasitic folds in these areas. No folds were observed at the ice-bed interface accessible at the true-right margin of the lower glacier and true right section of the terminus.

Recumbent folding has not been identified on Fox Glacier as most folds are identified on the ice surface (Figure 4.31) and are expressed with an axial plane normal to the surface. The folds present on the true left surface of the lower glacier can be classified as isoclinal, as they have an inter-limb angle of less than 10° . The limbs of these folds are essentially parallel with one another.

Areas in which folding has been observed also often display evidence of faulting, highlighted through displacement of existing structures such as primary stratification (S_0). Offset primary stratification can be observed on the glacier surface in the upper part of Victoria Flat and in crevasse walls in the lower glacier structural domain. Offset on most faults is less than 0.2 m, whilst some faults occur in pairs (Figure 4.32), creating distinct fault-blocks.



Figure 4.31: Folding on the surface of Victoria Flat. The axial plane is normal to the surface when viewed from above. (Photo: J. Appleby, June, 2010)



Figure 4.32: Offset primary stratification observed on the surface of Victoria Flat close to the base of the Upper Icefall. The parallel faults have created a distinct fault-block. The primary stratification is oriented approximately transverse to ice flow with flow being from bottom right to top left of photograph. (Photo: J. Appleby, June, 2010)

4.3.2.7 Arcuate Bands (Ogives)

Upper Icefall arcuate bands take the form of ridges and troughs across the glacier surface (Figure 4.33). These features run from the lower half of the Upper Icefall down to the upper end of Victoria Flat. These ridge and trough pairs have peak-to-peak amplitudes of up to 4 m and wavelengths varying from 10 m to >100 m (Figure 4.34). They are suggested to be the product of rhythmic compression, whereby changes in velocity due to a change in gradient produce pressure waves and troughs at the base of an icefall (Haeflerli, 1957, Atherton, 1963).



Figure 4.33: Wave and trough arcuate bands at the base of the Upper Icefall. The person is standing in a trough with the lower slope of a ridge immediately to their right. Ice flow is from left to right. (Photo: J. Appleby, June, 2010)

At the lower end of Victoria Flat, arcuate bands are formed from alternating light and dark arcuate features that can be followed for almost the entire width of the glacier (Figure 4.35). These bands are convex down-glacier, with the degree of curvature of each band increasing down-valley. Light and dark arcuate bands are also observable on the lower glacier beneath the Lower Icefall. Again, these bands are convex down-glacier with degree of curvature increasing with distance down-glacier. These light and dark ‘Forbes bands’ (e.g. Hambrey & Lawson, 2000) are suggested to be the surface

expression of shear planes produced during longitudinal compressive flow, with the dark bands being representative of debris-laden thrusts. No surface topographical expression is associated with the light and dark bands of the lower glacier and the lower end of Victoria Flat, while no arcuate bands are observable in the névé, below the Pioneer Icefall.

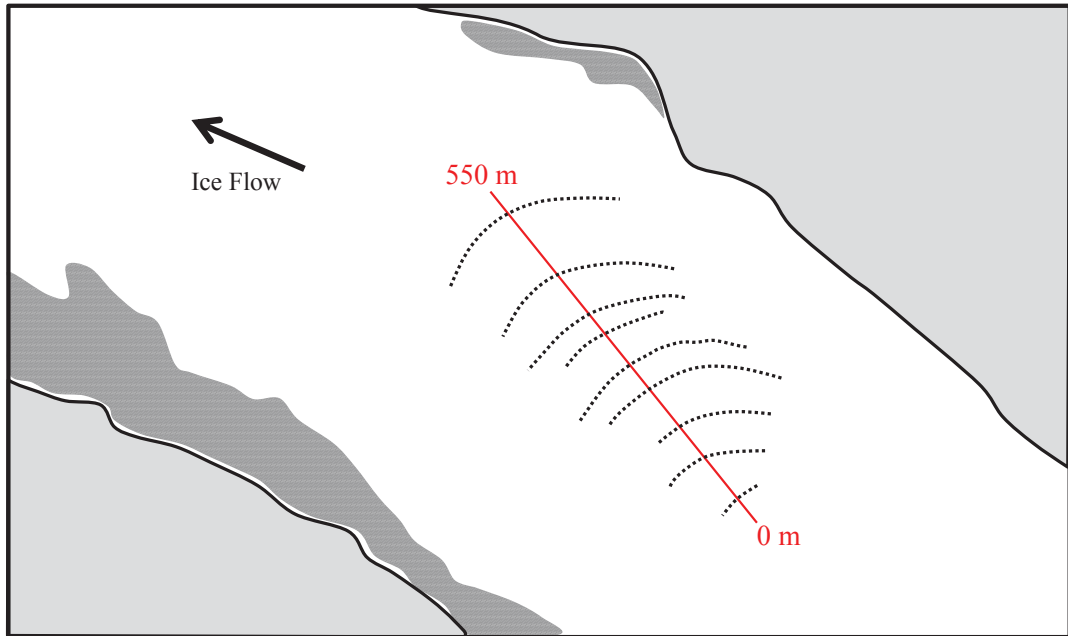


Figure 4.34: Map showing a 550 m longitudinal section of ridge and trough ogives on the upper part of Victoria Flat at the base of the Upper Icefall, identified from satellite imagery. Ice flow is from bottom right to top left. Supraglacial debris on the true left and true right in this area is also mapped (stippled area).



Figure 4.35: Weak dark and light arcuate band ogives at the lower end of Victoria Flat looking south from above the true right valley side of the Fox Glacier valley. Ice flow is from left to right. Curvature of the bands can be seen to increase down valley. (Photo: J. Appleby, January, 2009)

4.3.2.8 Flow-Unit Boundaries

A number of flow-unit boundaries can be seen in the névé delineating individual flow units within the glacier. The most prominent flow unit boundary is that associated with the confluence of the Albert and Explorer Glaciers at the distal end of Pioneer Ridge (Figure 4.36). Flow-unit boundaries are characterised by longitudinally linear depressions in the glacier surface surrounded for approximately 10 m on either side by clean, unbroken snow and ice.

Flow-unit boundaries converge immediately above the Upper Icefall (Figure 4.37) where the ice flow becomes constrained in the narrow valley. Flow-unit boundaries do not persist to within or below the Upper Icefall. Most of the flow boundaries in the névé are seen down glacier of spurs or rock buttresses that form part of the Main Divide. No ice-stream interaction (ISI) medial moraines have been formed at these flow boundaries in the névé, as might be expected from what has been observed at other glacier confluences such as Breiðarmerkurjökull, Iceland (Evans & Twigg, 2002).

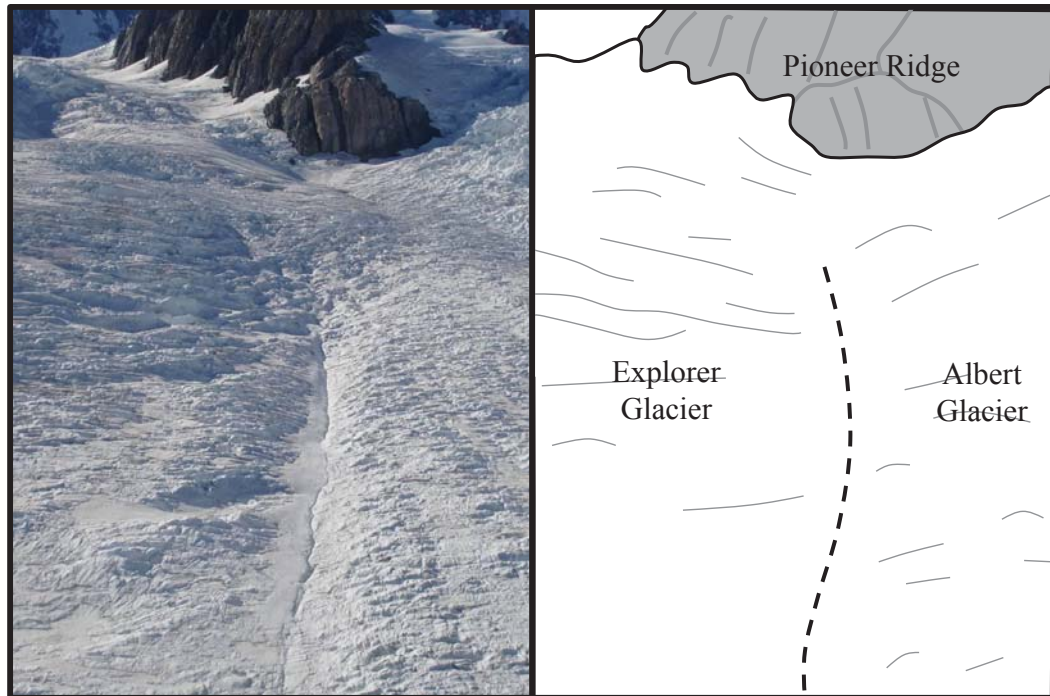


Figure 4.36: Flow-unit boundary (dashed line) delineating the confluence of the Albert and Explorer Glaciers immediately below the distal end of Pioneer Ridge. Flow is towards the camera.

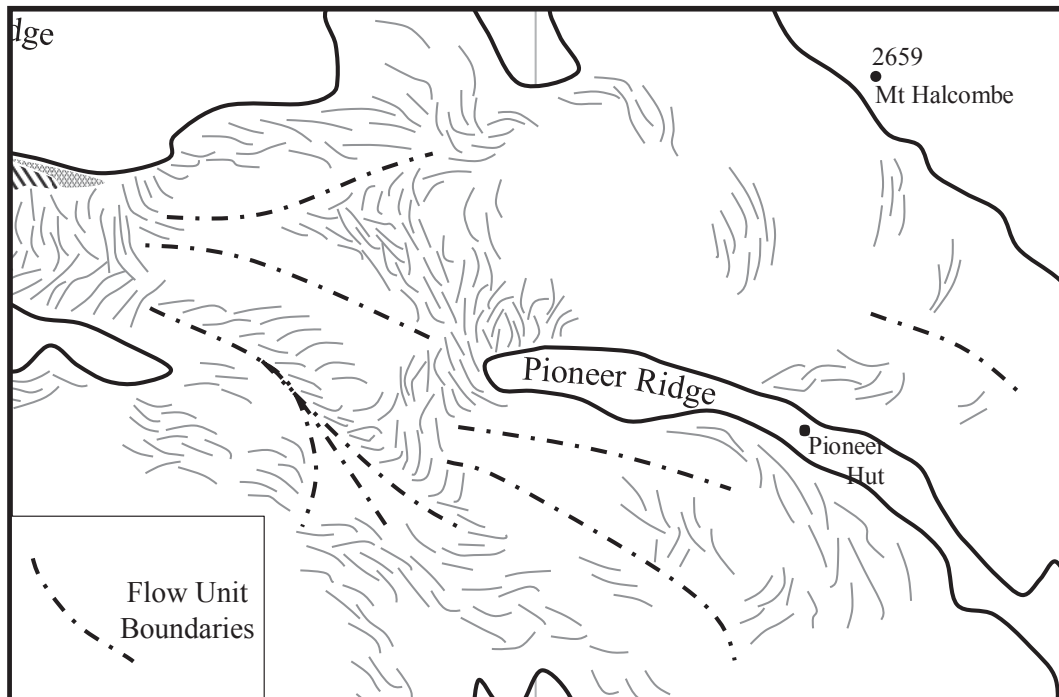


Figure 4.37: Map of flow-unit boundaries in the Fox Glacier névé identified from satellite images and field observations. Flow-unit boundaries down-glacier of Pioneer Ridge converge immediately above the Upper Icefall as flow is constrained in the narrow valley.

4.3.2.9 Supraglacial Drainage Networks

High volumes of meltwater and rainfall enable the formation of well-developed supraglacial drainage networks over the surface of Victoria Flat and the lower glacier. These networks constitute dendritic channel forms, moulins and ultimately, englacial conduits. Many segments of the supraglacial drainage network appear to be ephemeral, being activated during periods of heavy rainfall or on warm summer days when solar radiation and surface ablation are at their highest. A substantial diurnal flow regime is evident in the more regular channels, with rates of flow increasing throughout the day and then decreasing or stopping completely during the night.

In some locations, drainage networks have been altered either by changes in surface topography or englacial structures which have blocked moulins or englacial conduits, causing pooling of water on the surface (Figure 4.38).



Figure 4.38: Pooling of water on the surface of Fox Glacier due to the closure of part of the glacier drainage system. (Photo: S. Winkler)

4.3.2.9.1 Moulins

Moulins are present on the surface of both Victoria Flat and the lower glacier. The largest and most well developed moulins occur on Victoria Flat and are fed by extensive

supraglacial channel networks. The less broken, lower gradient surface in this area prevents supraglacial water from draining via crevasses and so causes pooling of water which in turn creates these larger moulin. Moulins in the lower glacier are smaller with less well developed surface drainage channels. Most moulins have a continuous flow of meltwater whilst some only became active after periods of heavy rainfall, or particularly warm days where surface melt is increased. During the winter, the entrance to moulins can become frozen over (Figure 4.39) causing ponding of surface water.



Figure 4.39: Meltwater from the previous day has frozen over night at the surface opening of a moulin on Victoria Flat. The photograph was taken early morning during winter fieldwork. (Photo: J. Appleby, June, 2010)

The majority of moulins on the lower glacier observed during the course of this work have diameters of <0.4 m, and none measured had a diameter in excess of 1.2 m. The moulins on Victoria Flat had a similar range of diameter, with most >0.6 m, up to a maximum of ~ 1.6 m. Moulins observed on both the lower glacier and Victoria Flat were all close to vertical. Depths were difficult to determine due to limited access.

4.3.2.9.2 Englacial Conduits

Englacial conduits associated with moulins have been exposed in the Victoria Flat study area (Figure 4.40) between the first and second icefalls. They occur towards the centre of the glacier and are mainly found exposed in the walls of crevasses below the Upper Icefall. The conduits have a maximum diameter of 2 m and range in shape from almost circular, to deformed ellipses, with the long axis more than twice the length of the short axis. The conduits plunge into the ice at angles of less than 30° in the down-glacier direction, and are generally aligned longitudinally.

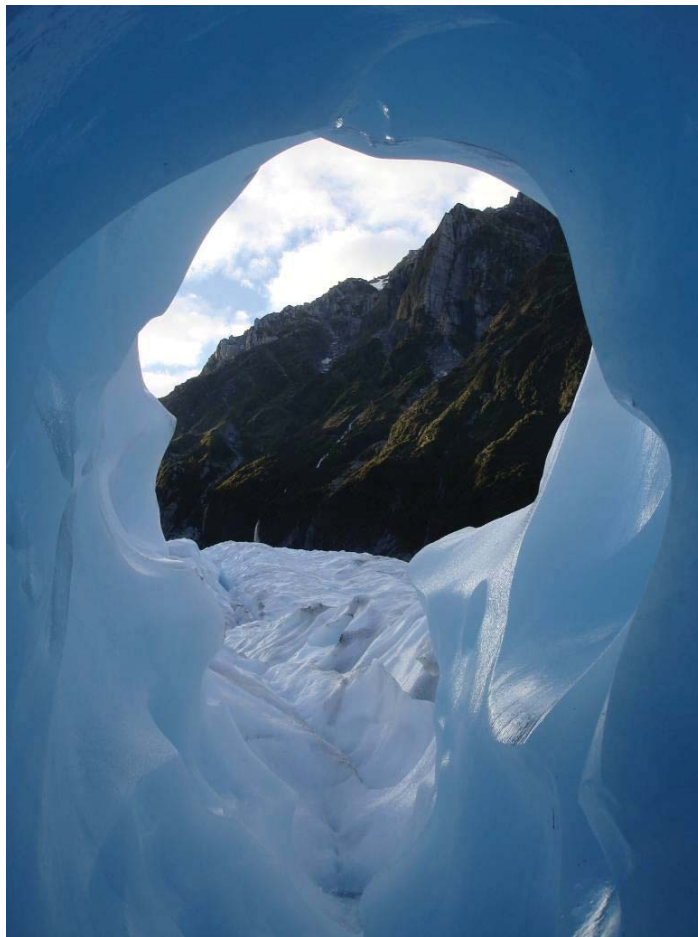


Figure 4.40: Englacial conduit exposed on the surface of Victoria Flat beneath the Upper Icefall. (Photo: J. Appleby, January, 2009)

4.3.2.10 Other Features of Interest

The other main feature of interest is an area known locally as ‘The Trough’, close to the Upper Icefall. This is immediately north of the upper part of the Upper Icefall, between

the icefall and lower slopes of Chancellor Dome, and is a particularly flat area (Figure 4.41). The area is characterised by gently sloping ($<5^\circ$) coarse ice, the surface of which has a dirty appearance. Longitudinal foliation is present for the length of the trough, along with transverse crevasse traces which form a very gentle ridge and trough pattern (Figure 4.42).



Figure 4.41: ‘The Trough’ viewed from the up-valley end of Chancellor Shelf looking west towards the Main Divide. The upper part of the Upper Icefall is visible at the right of the photograph with the lower slopes of Chancellor Dome visible on the left. Flow separation has caused stagnation of the extreme true right of the Upper Icefall. (Photo: J. Appleby, January, 2011)



Figure 4.42: Longitudinal foliation observable on the surface of ‘The Trough’ looking down-valley towards the narrowest part of the Upper Icefall. The upper end of Chancellor Shelf can be seen on the right of the photograph. (Photo: J. Appleby, January, 2011)

‘The Trough’ is dominated by longitudinal foliation where coarse-grained dirty ice is interspersed with coarse, bubble-free clean ice. This is found at the true right margin of the lower glacier and across the whole surface of ‘The Trough’. This is interpreted as the result of rotation and lateral compression (Hambrey, 1994) of primary stratification causing transposition, and is near-vertically dipping and orientated parallel to the direction of flow. Lateral compression has occurred due to changes in valley geometry, with the topographic constriction at the point at which ice in the névé converges into the main valley, with a similar constriction immediately below Victoria Flat in the lower glacier.

4.3.3 Isotopic Fractionation as an Indicator of Internal Structural Deformation

Isotopic fractionation can potentially provide information on internal structural deformation processes operating within glaciers (cf. *Section 3.3.2*). This section details a small study which applies isotopic fractionation to Fox Glacier in an attempt to better understand in particular the processes of thrust faulting operating within the glacier.

Surface snow and ice samples were collected in each of the three structural domains (névé, Victoria Flat and lower glacier), to provide a long profile of isotope values for the length of Fox Glacier (Figure 4.43). δD - $\delta^{18}\text{O}$ relationships have been used previously to interpret the thermal history of ice. Typically, samples of glacier ice that have not undergone refreezing lie on the same regression line as precipitation (normally with a regression slope of around 8; Glasser & Hambrey, 2002b). In contrast, ice that has undergone refreezing produces a regression line with a lower slope, which actually depends on the initial δ values of the melted ice at the onset of freezing (Glasser & Hambrey, 2002b). In addition basal ice and thrust ice were also sampled to determine any significant differences between those and the longitudinal surface ice samples. Characteristics and associated mean δD and $\delta^{18}\text{O}$ values are summarised in Table 4.1. Each facies, with the exception of Victoria Flat and the lower glacier, vary in their characteristics, ranging from coarse-crystalline snow in the névé, to coarse-bubbly ice in the lower glacier. For bivariate isotope analysis to prove useful in determining the structural evolution of Fox Glacier, the results must show statistically significant differences in values at the 95% confidence intervals of the different ice facies sampled (e.g. Hubbard & Sharp, 1993, Glasser & Hambrey, 2002b, Gordon and others, 1988, Souchez & De Groote, 1985).

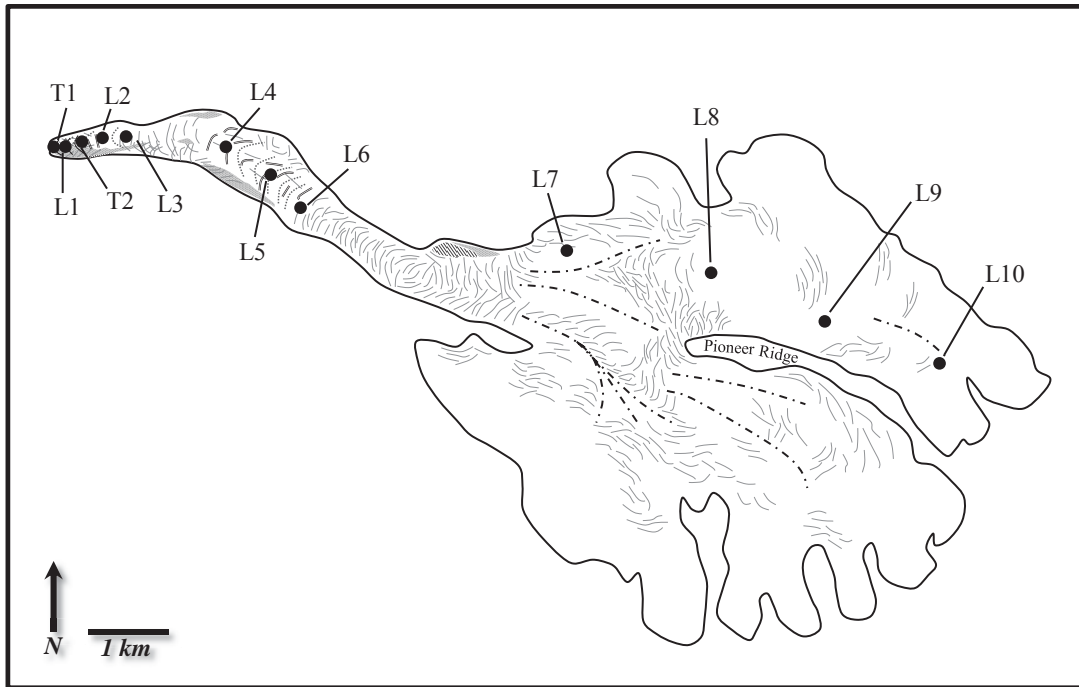


Figure 4.43: Longitudinal (L1 to L10) and thrust regelation ice (T1 & T2) isotope sample locations on Fox Glacier.

Table 4.1: Ice facies sampled for isotope analysis on Fox Glacier, with descriptive characteristics and associated mean δD and $\delta^{18}O$ values relative to Vienna Standard Mean Ocean Water (VSMOW).

Facies	Characteristics	$\delta^{18}O$ ‰ VSMOW	δD ‰ VSMOW
Basal Ice	Coarse-clear ice with debris	-8.95	-61.68
Thrust Ice	Coarse-clear ice with mud clots	-9.41	-64.32
Névé	Coarse-crystalline snow	-8.48	-58.78
Victoria Flat	Coarse-bubbly ice	-8.70	-60.62
Lower Glacier	Coarse-bubbly ice	-9.74	-67.30

Table 4.2: Statistics for best-fit linear regression relationships between δD and $\delta^{18}O$. The 95% range for b_1 ($\delta^{18}O$) coefficient is calculated as the mean \pm 2 standard errors of the estimate. p is the significance level at which r^2 and F are significant.

Sample Facies	Regression Model	b_1 (95% Range)	r^2	F	p
Basal Ice	$\delta D = -5.0138 + 6.3301 \delta^{18}O$	6.3431 5.304-7.381	0.93	212.69	<0.001
Thrusted Ice	$\delta D = 10.1561 + 7.9171 \delta^{18}O$	8.25 5.665-10.834	0.74	40.171	<0.001
Névé	$\delta D = 7.9859 + 7.8691 \delta^{18}O$	7.9744 5.366-10.597	0.76	45.91	<0.001
Victoria Flat	$\delta D = -16.5475 + 5.0651 \delta^{18}O$	4.7254 2.331-7.119	0.68	21.97	<0.001
Lower Glacier	$\delta D = 7.3921 + 7.6715 \delta^{18}O$	7.745 6.788-8.701	0.97	373.61	<0.001

Regression relationships (Table 4.2) for the basal ice, thrusted ice, névé, Victoria Flat, and lower glacier facies show strong, statistically significant relationships between δD and $\delta^{18}O$, as indicated by the high r^2 and F statistics, and very low p -values, all <0.001. The 95% confidence ranges in b_1 ($\delta^{18}O$) coefficients for thrusted ice and the lower glacier can be compared and used qualitatively to determine whether significantly different regression relationships exist as a function of melting, refreezing, and thrusting of basal ice.

4.3.3.1 δD and $\delta^{18}O$ Relationships

Mean and standard deviations of δD and $\delta^{18}O$ for each of the sample facies have been calculated and are presented in Figure 4.44. δD values for sample facies on Fox Glacier range between -54.92 and -71.83 ‰, with a mean of -62.54 ‰. $\delta^{18}O$ values range between -7.97 and -10.33 ‰, with a mean of -9.06 ‰. For both δD and $\delta^{18}O$, the lower glacier facies displays the highest mean ($\delta^{18}O = -9.74$; $\delta D = -67.30$), whilst the N v  displays the lowest mean ($\delta^{18}O = -8.48$; $\delta D = -58.78$).

Bivariate co-isotopic plots have been produced (Figure 4.45) to graphically compare least-squares regression lines and r^2 values of each of the five ice facies sampled, along with the least-squares regression line and r^2 value for the averaged data obtained from the Fox Glacier long profile. The regression lines of the different facies range from $y = 5.0651x - 16.548$ (Victoria Flat) to $y = 7.9172x + 10.156$ (thrust ice), with r^2 values ranging from $r^2 = 0.6872$ (Victoria Flat) and $r^2 = 0.9739$ (lower glacier). The bivariate co-isotopic plot least-squares regression line $\delta D = 6.8268 \delta^{18}O - 0.9586$ ($r^2 = 0.93$) of the longitudinal sample transect (Figure 4.45 F) approximates the regional monthly IAEA data least-squares regression line $\delta D = -7.892 \delta^{18}O + 9.663$ ($r^2 = 0.91$) displayed in Figure 4.46, although the Invercargill IAEA data have a much greater range ($\delta D = -15.7$ to -76.3 ‰; $\delta^{18}O = -3.19$ to -10.33 ‰) and lower means ($\delta D = -43.88$ ‰; $\delta^{18}O = -6.78$ ‰) compared to the results from Fox Glacier. As Invercargill is the closest location to Fox Glacier with recorded GNIP data (IAEA, 2006), this suggests either a geographic and synoptic effect on isotopes, or that the surface ice of Fox Glacier has undergone significant isotopic modification during transformation from precipitation to glacier ice.

Some variation in δD and $\delta^{18}O$ along the length of the glacier is apparent with changing altitude (Figure 4.47). Although despite the observed differences in mean and range between the n v  and lower glacier, there is no clearly defined trend in the observed variation. The lack of any strong trend supports the notion that snow does not become isotopically lighter with increasing altitude on Fox Glacier, despite the ~ 2500 m altitudinal range of the glacier.

The overlap in b_1 values between the different ice facies (Table 4.2), the δD and $\delta^{18}O$ relationships do not vary due to ice facies type. Despite this, subtle but discernible differences may be used to assist in interpreting structures, for example determining the provenance of the allocthonous, coarse-clear thrust ice facies, inter-bedded with the coarse-bubbly ice of the lower glacier.

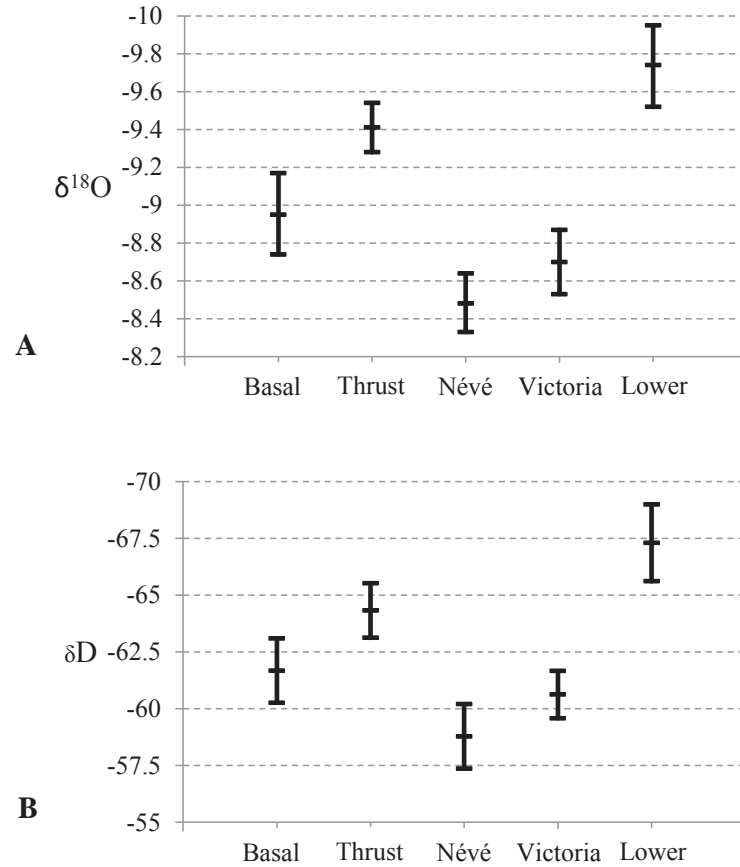


Figure 4.44: Mean and standard deviation of A) $\delta^{18}O$, and B) δD in snow and ice facies identified on Fox Glacier.

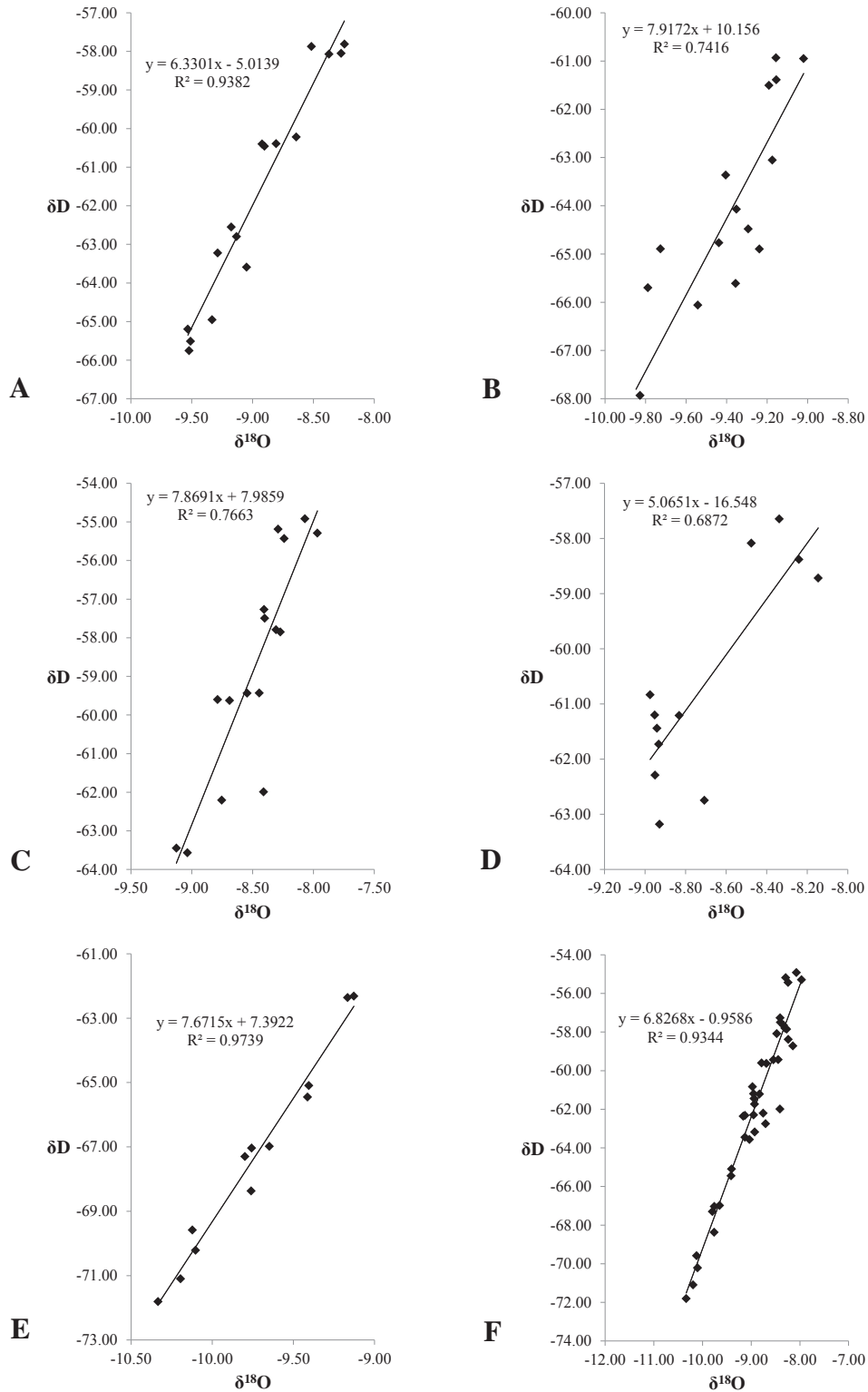


Figure 4.45: Bivariate co-isotopic plots ($\delta D/\delta^{18}O$) of sample facies identified on Fox Glacier: A) basal ice; B) thrustured ice; C) névé; D) Victoria Flat; E) lower glacier, and; F) All longitudinal surface samples constituted of névé, Victoria Flat and lower glacier, showing y-intercept and r^2 value.

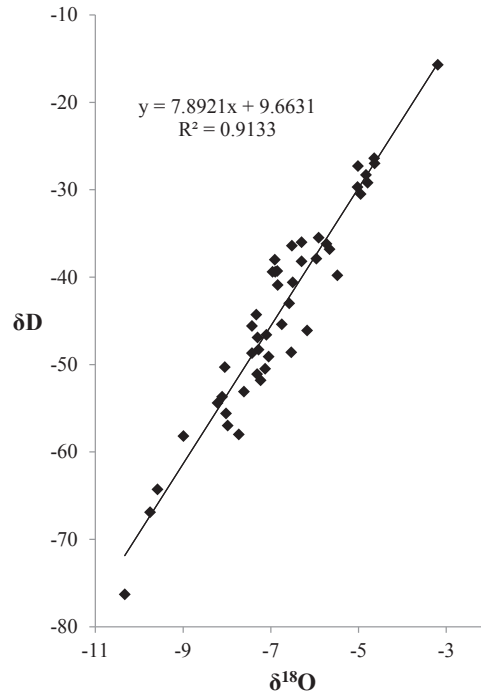


Figure 4.46: Bivariate co-isotopic plot of $\delta\text{D}/\delta^{18}\text{O}$ measured at Invercargill, New Zealand, between 2005 and 2008, as part of the Global Network of Isotopes in Precipitation (GNIP) database. Invercargill is the closest location to Fox Glacier with recorded GNIP data (IAEA, 2006).

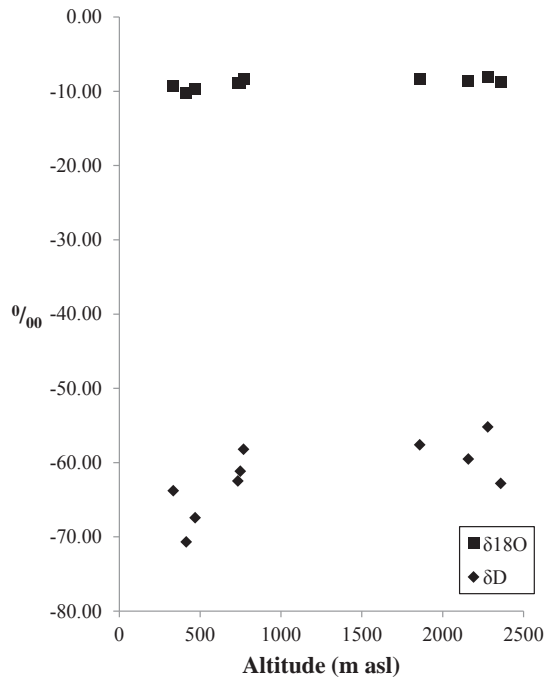


Figure 4.47: Altitudinal variation in mean δD and $\delta^{18}\text{O}$ for sample locations along a longitudinal section of Fox Glacier.

4.4 Discussion on the Structural Glaciology of Fox Glacier

Discussion and interpretation of the surface structures of particular interest is provided; the aim of which is to identify the processes that have produced the structures and compare these processes with existing theories on the formation of the surface features on temperate maritime glaciers of New Zealand's Southern Alps.

4.4.1 Historical Structural Glaciology

The surface morphology of Fox Glacier has varied markedly during the period 1896 to 2006. Many structural features remain constant although their precise locations vary in time and space. The changes observed are those identified from hand drawn maps, aerial photographs or satellite images, and so may not be an exact representation of the spatio-temporal distribution of features observable in the field at the specific times the maps represent. In addition, the whole length of the glacier is not covered by every historical source and so a complete representation of the structure is not possible for all periods.

As well as the changing structural glaciology of Fox Glacier over the ~110 year period described, fluctuations in terminus position are also addressed and the relationship these have to climate trends over a similar period is considered.

4.4.1.1 Structural Features

Crevassing seen in the Lower and Upper Icefalls is constant throughout the period covered by the photos. However, the longitudinal spatial extent varies over time, possibly due to variations in mass balance causing changes in surface gradient and ice thickness at the steepest parts of the glacier's profile (Sugden & John, 1976, Benn & Evans, 1998). Crevassing observed in the upper and Lower Icefalls is chaotic with no clear orientation evident, apart from some transverse crevassing at the top of the Upper Icefall. Few crevasses are recorded on early maps although the broken nature of the ice surface is referred to by a number of early observers (e.g. Gardiner, 1934, Newton, 1939, Porter, 1934, Lockwood, 1949).

Flow unit boundaries are not recorded on every map or apparent on every satellite image or aerial photograph due to resolution or spatial coverage of the images, although their position is the same on each of the sources on which they do appear. The exception is the longitudinal structure that may indicate a flow line in the Upper Icefall on the 2006 structural interpretation. The number and extent of boundaries that are identifiable varies over time, which may be due to the spatial resolution of the image and also the snow conditions at the time the image was produced. Flow boundaries may be less pronounced when covered by winter snowfall, and more pronounced at the height of the summer ablation season. This is supported when the acquisition dates of the images with the most obvious flow boundaries are considered, for example February 1986, March 1974 and March 1990, and May 2006. All of these are close to the end of the Austral summer.

Supraglacial debris is evident on all maps and remotely sensed images, although distribution varies during each of the study periods. This is likely due to variations in debris supply and coupling between the supply and glacier, along with variations in rates of accumulation incorporating debris and rates of ablation exhuming debris at the glacier surface. Debris is only observed below the Upper Icefall and on the glacier surface between the terminus and the Lower Icefall. No debris is observable on the surface of the névé due to incorporation of material at the head of the névé.

During 1896 and 1911 a large part of the snout was completely covered in debris (from the terminus to ~500 m up-valley), whereas later years have a larger proportion of 'clean' ice below the Lower Icefall. A consistent medial moraine can be seen, usually towards the true left of the glacier centreline, on all of the aerial photographs and satellite images (1965 to 2006). However, no debris was recorded on the 1896 and 1911 maps, or is observable on the 1935 and 1950 oblique photographs, possibly due to the angle at which the photographs were acquired. This medial moraine usually forms a continuous or semi-continuous line running through the Lower Icefall from the lower end of Victoria Flat to the lower glacier between the Lower Icefall and terminus. The 1974 structural interpretation places the moraine higher up on Victoria Flat, continuing into the Upper Icefall; this is the only year during which supraglacial debris is observed this far up-glacier. Supraglacial debris in this area suggests either (1) debris has been supplied to the ice surface at a location further down-valley than debris which is

exhumed below the Upper Icefall and so does not get incorporated into firn within the névé; (2) ablation rates are sufficiently greater than accumulation rates at this time, preventing deep burial of material and promoting quick exposure higher up-valley; or (3) particularly large rock falls have occurred in the névé in the preceding years and this material has been transported from these source areas. A combination of (2) and (3) is the most probable cause of the observed supraglacial debris.

Arcuate bands (weak band ogives) are identified in aerial photographs (1965 to 1986) and the 2006 satellite image on Victoria Flat. These arcuate bands are of a wave and trough type, and are most likely caused by the extension and compression of the ice as it flows through the Upper Icefall, as described further in *Section 4.4.2.5*. Curvature and wave length of the arcuate bands identified increased as they move down-valley away from the base of the Upper Icefall. Some dark and light bands (Forbes Bands) have been identified from oblique photographs (1935 and 1950) on the lower true left of the glacier between the Lower Icefall and terminus. These dark and light bands have been identified in as the surface expression of thrust faults, and foliation due to exposure of stratification at the terminus.

4.4.1.2 Terminus Position

The terminus position of Fox Glacier is the most obvious feature to undergo considerable change during the period 1896 to 2006 (Figure 4.48). The period 1950 to 1965 saw the most dramatic retreat, after which the terminus remained relatively steady between 1965 and 2006 with only small magnitude fluctuations of advance and retreat. 1985 saw the terminus at its position of greatest retreat. A similar pattern was identified for the terminus of the Franz Josef Glacier by Chinn (1999), however, the changes appear to precede those on Fox Glacier with a rapid retreat from the mid-1930s to the mid-1970s, and the period of greatest retreat occurring in approximately 1984.

Difficulty in determining the exact pattern of terminus position change has been experienced during this study for a variety of reasons. First, the rate of retreat has not been uniform across the width of the terminus due to the action of subglacial water emanating from a glacial portal continuously present at the snout. On a large scale, the position of the exit portal at the snout (which fluctuates over time), along with water

flowing from Straight Creek and Boyd Creek which reaches the valley floor close to the glacier terminus, controls the precise geometry of the terminal face. This water in conjunction with high ablation rates, regularly causes collapse of the R-channel roof at the exit portal on one side of the snout rather than the other (Purdie and others, 2008a). At a smaller scale, the exposure of longitudinal and/or splaying crevasses at the terminus creates a crenulated terminal face. For these reasons, a general frontal position (an approximate line of the average snout position from one side of the valley to the other) of the terminus is used as a measure of its deviation. Second, the temporal resolution of this study may have led to the exclusion of some distinct advances and retreats in the periods between years examined for structural interpretation.

Attempts have been made to correlate frontal position fluctuations at other glaciers with precipitation and temperature (e.g. Suggate, 1950, Hessel, 1983, Gellatly & Norton, 1984), however, Chinn (1996) found results to be ambiguous. Greater success has been achieved relating glacier length variations in New Zealand's Southern Alps with variations in atmospheric circulation such as the Interdecadal Pacific Oscillation (IPO) and Southern Oscillation Index (SOI) (e.g. Fitzharris and others, 1992, Hooker & Fitzharris, 1999) with a strong link between climate and terminus position being determined (Chinn, 1996, Fitzharris and others, 1997). In relation to this, an attempt has been made to identify relationships between terminus positions of Fox Glacier and atmospheric circulation.

No clear correlation is immediately apparent between either the Southern Oscillation Index (SOI) or Interdecadal Pacific Oscillation (IPO) and terminus position deviation of Fox Glacier in Figure 4.48. A general decrease in mean SOI sea surface air pressure bringing a more consistent El Niño trend can be identified after ~1980. El Niño conditions bring an increase in precipitation to the South Westland region from strong westerly winds during summer whilst cold southerly winds predominate during winter, increasing accumulation rates in the Fox Glacier névé and allowing for a greater volume of snow to survive through the ablation season. This increase in mass balance leads to an advance in terminus position following a lag period (Chinn, 1996).

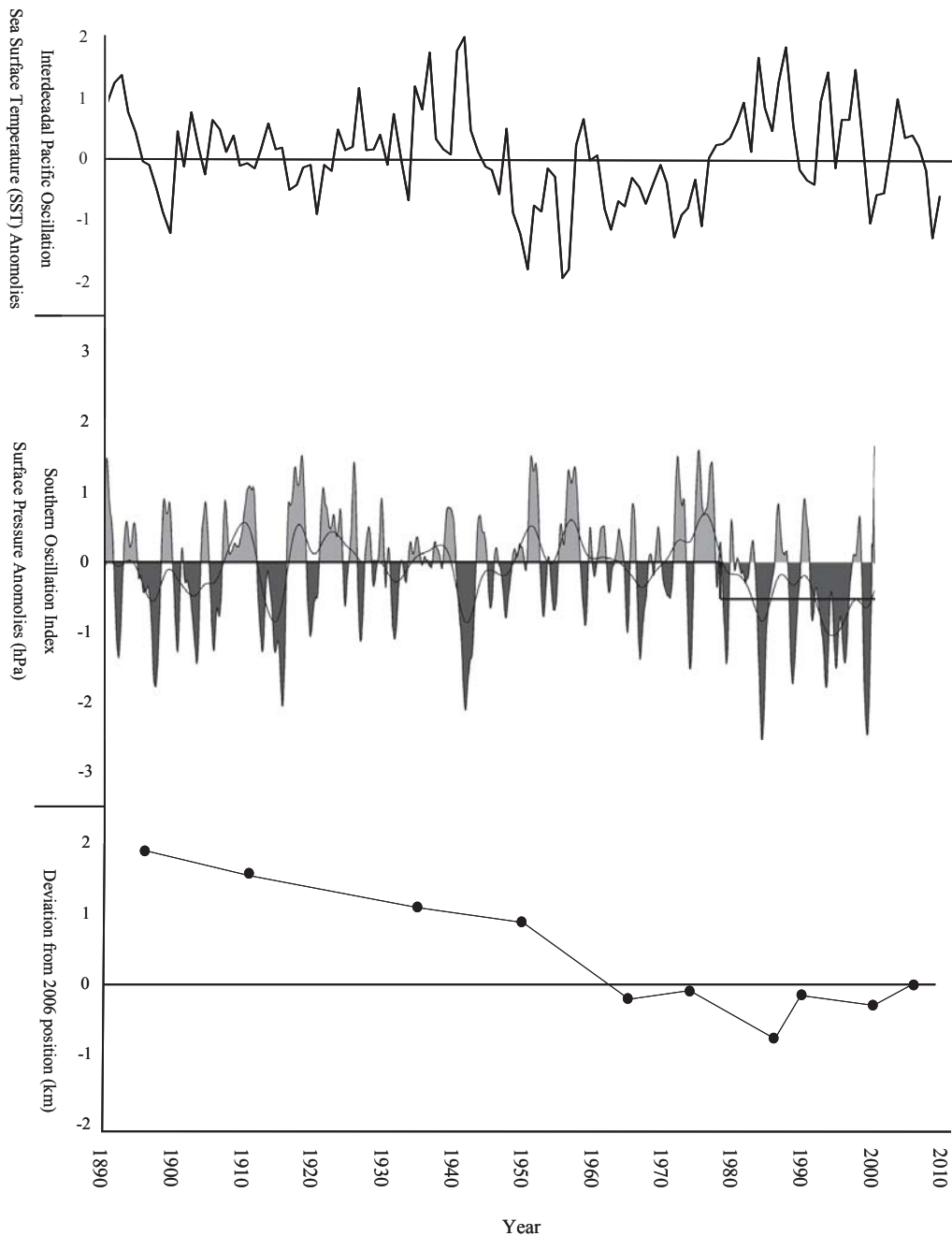


Figure 4.48: Deviation of terminus position between 1896 and 2006 (bottom) relative to 2006 position showing steady retreat from 1896 to 1950, followed by rapid retreat to 1965, and then a pattern of cyclic advance and retreat 1965 to 2006. Terminus position is compared to Southern Oscillation Index (SOI) (middle) showing annual fluctuations in sea surface air pressure between Darwin and Tahiti from 1890 to 2000 (negative values represent El Niño conditions whilst positive values represent a La Niña year), and Interdecadal Pacific Oscillation (IPO) (top) showing annual mean fluctuations in sea surface temperature (SST) between 1890 and 2009 (Developed from Biondi and others, 2001, JISAO, 2010).

With regard to the Interdecadal Pacific Oscillation, a decrease in IPO sea-surface temperatures seems to coincide with the rapid change in glacier frontal position observed between 1940 and 1990 along with a slight recovery in frontal position during a return to a positive IPO after 1986. However, the recovery in frontal position post-1986 is not as dramatic as the increase in sea surface temperatures observed during this period. The more consistent pattern of advance and retreat since the late 1980s is possibly due to the accumulation effects of regular El Niño years opposing the increase in global temperatures. It should be considered that the temporal resolution of terminus position measurements may be insufficiently fine to identify inter-annual trends that may more closely match the fluctuations of the Southern Oscillation.

Throughout the 20th Century there has been limited change in the overall area of Fox Glacier, other than variations in terminus position which has undergone a general retreat since 1896. This lack of areal change is due to the constraining effect of the narrow, steep-sided main valley and the steep peaks at the head of the Fox névé, both of which prevent lateral expansion of the ice. A much greater reduction in ice volume would be required to see a significant contraction of glacierised area in the névé for the same reasons. This change could be expected due to significant decreases in precipitation and increases in temperature. The general terminus retreat has been accompanied by an overall reduction in ice thickness since 1896, with only small variations over the last 40 years.

The upper and Lower Icefalls constantly demonstrate intense crevassing in a similar location on each of the structural interpretations, with the only variation being that of longitudinal extent which varies as the surface slope of the glacier changes. The ongoing presence of the two icefalls in combination with the generally crevassed ice surface identified from the reports published with the 1896 and 1911 maps, the later aerial photographs and satellite images all allude to the steep surface profile of Fox Glacier remaining relatively constant, reflecting the underlying bedrock long-profile.

In general, the types of structural feature identified on the surface of Fox Glacier remains reasonably constant during the period 1896 to 2006 with the only observable changes being those in spatial extent and location of the individual features.

4.4.2 Contemporary Structural Glaciology

4.4.2.1 Icefalls and Valley Over-Deepening

Between the upper and Lower Icefalls, an over-deepening in the bedrock long-profile appears to have occurred in the area immediately down-valley of Victoria Flat, explaining the presence of the Lower Icefall. Lloyd *et al.* (2012) suggest a strong correlation between over-deepening and the presence of glacial confluences in alpine mountain belts. Gudmundsson *et al.* (1997) suggested that such a correlation is strongest where confluence-geometry indicates ice-flow speed-up. This confluence-diffuence theory has been debated for many years (e.g. Sugden & John, 1976, Holtedahl, 1967). The lower end of Victoria Flat was once the confluence of Victoria Glacier and Fox Glacier and would therefore theoretically have experienced an increase in ice volume, velocity and erosion rates (e.g. Harbor and others, 1988). Hence, it follows that the former confluence is the primary cause of the valley overdeepening and location of the Lower Icefall. Geological maps of the area (Cox & Barrell, 2007) indicate that the Victoria Glacier valley is crossed by faults trending sub-parallel to the range-bounding Alpine Fault. Therefore underlying bedrock structure may have exerted control over the location of the valley in which Victoria Glacier formed, and so has influenced the location of the confluence. This control is inherited as fluvial valleys formed in response to structural weaknesses have been transformed and modified into glacial valleys. Moreover, further investigation suggests that all three of the icefalls identified on Fox Glacier are coincident with inactive faults crossing the valley axis (Figure 4.49).

Fault A runs approximately across the top of the Lower Icefall and along the Victoria Glacier valley where it terminates against another fault running transverse to the Victoria Glacier. At the upper end of Victoria Flat, Fault B runs perpendicular to Fox Glacier valley axis, crossing the valley coincident with the lower section of the Upper Icefall, terminating against Fault A in the Victoria Glacier valley. The top of the Upper Icefall coincides with Fault C. At this location, a reduction in valley width occurs, forming the lower part of 'The Trough' and the upper part of Chancellor Shelf. Finally, Fault D is aligned across the Pioneer icefall, at the distal end of Pioneer Ridge.

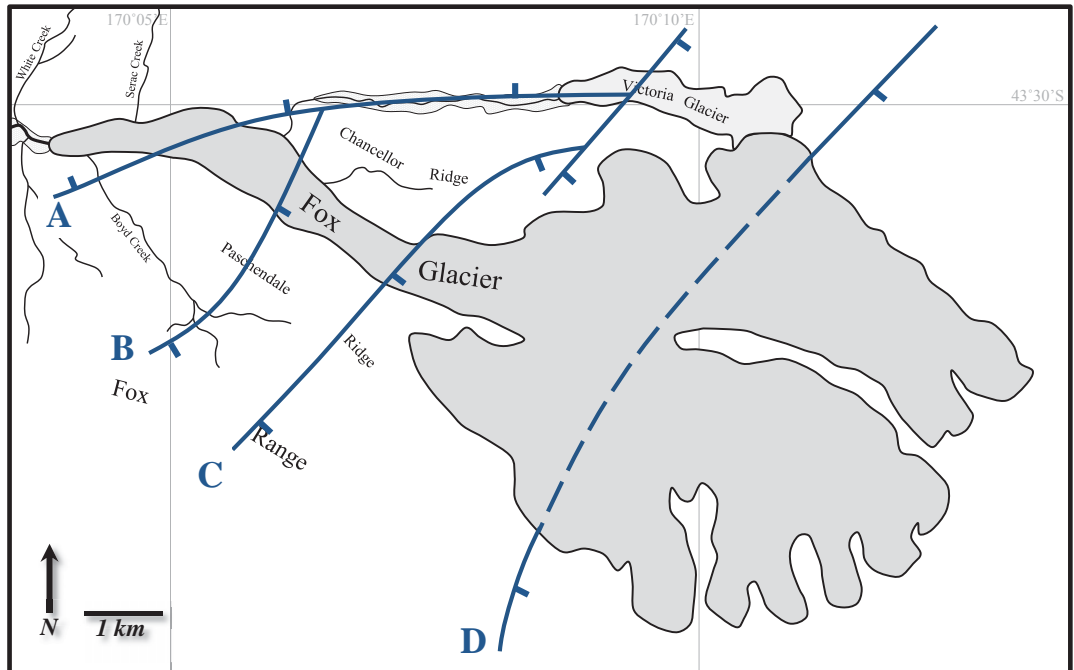


Figure 4.49: Location of faults bisecting the Fox Glacier Valley and névé (ticks on downthrown side of fault). Fault A is located at the top of the Lower Icefall; Faults B and C are located at the bottom and top of the Upper Icefall respectively; Fault D is extrapolated (dashed line) across the névé from confirmed locations north and south, and runs approximately parallel to the location of the Pioneer Icefall (Developed from Cox & Barrell, 2007)).

Lloyd *et al.* (2012) concluded that over-deepening is most efficacious where fractured bedrock enables efficient quarrying, and suggested that the magnitude of the increase in ice-flow velocity correlates with over-deepening depth only for confluences situated in or near major geological fault-zones. Gonzalez and Aydin (2008) infer that over-deepening's occur in areas of concentrated erosion at faults zones. They also suggest valley-widening occurs as a result of these fault zones. This appears to be the case at Fox Glacier, because the valley widens from ~500 m within the Upper Icefall to ~1 km on Victoria Flat. A similar trend is seen in the neighbouring Franz Josef Glacier where widening occurs in the main glacier valley at the point where the valley is bisected by fault lines (e.g. Cox & Barrell, 2007).

Thus faulting is suggested to have determined the location of over-deepening in the Fox Glacier valley. This has produced a stepped bedrock longitudinal profile, with icefalls located in the steeper parts of the profile. This is most marked at the former confluence

of Victoria and Fox Glacier. The weakening of rock in these fault zones has a further effect, namely, that highly fractured rock on steep slopes, such as at Paschendale Ridge, is a ready source of supraglacial debris.

4.4.2.2 Foliation (S_1)

The steep orientation angles of foliations on the surface of Fox Glacier are indicative of high strain rates in the ice. This is supported by Gunn (1964), who associated transverse foliation in Fox Glacier with a high strain rate in ice under compression. Originally formed approximately parallel to the ice surface as primary stratification (S_0) in the accumulation area, the foliations develop steep dip angles by the time the ice has flowed from the névé through the icefalls, and undergone high strain (both longitudinal and compressional) and rotation by glacier flow (Goodsell and others, 2005c, Lawson and others, 1994).

In some areas of the lower glacier, cross-cutting relationships between primary stratification and foliation are visible. This suggests that an alternative explanation for foliation evolution may be appropriate too. Meier (1960) proposed foliation in ice as a uniquely metamorphic structure produced entirely from high strain rates and ice flow, and therefore not originating from primary stratification. Hence the cross-cutting relationships indicate that this model of foliation development may also be applied to Fox Glacier. However, given the much more limited extent of cross-cutting S_0/S_1 relationships observed, transposition of primary stratification (e.g. Goodsell and others, 2005c), is most probably the primary mode of formation for the majority of foliation at Fox Glacier.

4.4.2.3 Crevasses and Crevasse Traces (S_2)

At the very upper limit of Fox Glacier, randclufts and bergshrunds have formed in areas where the glacier has pulled away from the head walls surrounding the névé. This represents a detachment of the glacier from the rock buttresses of the main divide, along with crevassing in areas where, as shown by fracture of the glacier surface, sections of snow and ice remain frozen to the headwall. Further down-glacier within the névé, transverse crevasses are prominent in areas of extending flow where a change in

subglacial topography occurs. This is most apparent on the southern side of Pioneer Ridge, the area between the locations of the Albert and Pioneer strain networks (*refer Chapter Seven*) and the areas immediately above and below the Pioneer Icefall. Indeed, above the Pioneer Icefall, crevasses are confined to areas of steep topography, whereas below the icefall the entire surface is crevassed due to the acceleration of ice down the Upper Icefall into the main valley channel.

The Victoria Flat study area between the Lower and Upper Icefalls is characterised mainly by transverse crevasses. These crevasses are the product of shear stress and longitudinal tensile stress, the principal stress of which is parallel to flow causing transverse crevasses oriented normal to the glacier centreline. As ice flows down the Upper Icefall, velocity increases causing longitudinal extension of ice immediately up-glacier of Victoria Flat. This rapid extension causes fracturing of the ice, as represented by some of the continuous, glacier-wide fractures. Some of these transverse crevasses persist as ice moves through Victoria Flat whilst others close to form transverse arcuate structures identified as crevasse traces. At the lower end of Victoria Flat immediately above the Lower Icefall, some of these crevasse traces are reactivated. Also, new crevasses are formed as ice velocity once again increases as ice begins to accelerate at the top of the Lower Icefall. A complex pattern of crevassing is developed in this area as cross-cutting of existing crevasses and crevasse traces occurs as new surface fractures open. This trend continues as ice flows through the Lower Icefall, with longitudinal tensile stress producing transverse crevassing characteristic of icefalls, as per the Pioneer and Upper Icefalls.

At the snout of the glacier, longitudinal crevasses are dominant. Due to high rates of surface ablation (Purdie and others, 2008a, Purdie and others, 2008b), and a widening of the valley geometry, pressure is unloaded from the glacier tongue causing lateral expansion of the ice. During the process of ice expansion, fracture occurs producing deep (>20m) crevasses which pervade from the surface of the glacier toward the subglacial zone close to the terminus. This loss of ice volume and subsequent loss of lateral confining pressures has also resulted in the formation of a splaying crevasse at the snout of the glacier. Hence, in the lower glacier, above the snout, the glacier surface topography is deeply-entrenched.

Along both the true left and true right of the glacier in the lower glacier domain and Victoria Flat, chevron crevasses can be seen, aligned obliquely up-valley from the margins toward the centreline. These are symptomatic of frictional and shear stress exerted by the valley walls. As the glacier flows more rapidly at the centre than at the margins, tensile stresses pull the ice down-valley away from these margins and in towards the centre, opening up the ice surface at approximately 45° . However, the production of chevron crevasses at Fox Glacier appears asymmetric, with chevron crevasses appearing to be more characteristic of the true left of the glacier. This may be because of shear stress produced by frictional resistance of the valley wall below Paschendale Ridge on Victoria Flat and the lower slopes of Sam Peak in the lower glacier.

At the true left of Victoria Flat, the shear stress producing chevron crevassing acts in conjunction with a longitudinal compressive stress produced by a 45° re-orientation of the glacier following the valley topography (the valley axis changes from a northwest orientation to a westerly orientation). Together, these two factors appear to have produced en echelon crevasses whereby simple shear and rotation has caused deformation of pre-existing linear fractures. This contrasts with the true right side of Victoria Flat, where there is limited or no longitudinal compressive stress, and no en echelon crevasses have been observed in this region.

As some crevasses formed by tensile stress have subsequently closed due to compressive flow or rotation, crevasse traces have been formed. These linear features are omnipresent over almost all of the lower glacier and Victoria Flat, whilst none are observable in the névé. The absence of crevasse traces in the névé is likely the result of the lack of compressive flow in this area in combination with the absence of hard ice, meaning limited crevasse closure, until firn reaches the base of the Pioneer Icefall, and a zone of longitudinal compression is encountered by advected ice.

Various formation mechanisms have been suggested for crevasse traces observed on the surface of Fox Glacier. Their visibility is obvious, due to differences in density and ice colour, with some being constructed of very white, coarse ice, and others being of hard, blue ice. Most of the crevasse traces seen in the lower part of the study area are apparent by the dirt and debris trapped within them. In contrast, in some other crevasse traces,

dirt or debris is completely absent, suggesting these traces did not form from open crevasses. Rather, the implication is that they formed in an area of expanding ice which has then compressed before reaching the threshold of fracture.

Crevasse traces filled with dirt and debris in the lower glacier may represent once open crevasses further up-glacier that have since closed due to transfer through a zone of compressive flow. Fine debris was visible in the ablation area and Upper and Lower Icefalls during the summer when the concentration of wind-blown material is at its greatest and fine debris is deposited whilst the crevasse is open and subaerially exposed.

Further up-glacier on Victoria Flat, crevasse traces have a cleaner, less 'dirty' appearance. They are constructed of layered white, coarse-bubbly ice, most probably the result of crevasses that were open above the ELA, and were snow-filled at the time of closing, before being transported through the Upper Icefall onto Victoria Flat.

Cross-cutting relationships of some crevasse traces with others in the lower glacier especially, suggest this ice has undergone at least two phases of deformation. Tensile stress causes ice to extend, the crevasse then closes as compressive stress is encountered. Crevasses may then be opened up by subsequent tensile stress, which are then later closed by a further phase of compression. It should be noted, however, that some of these traces may never have been open crevasses, and may represent the extension of ice below its fracture threshold. In this way, the crevasse traces actually represent narrow tensional 'veins', as are often seen in rock (e.g. Fossen, 2010, Twiss & Moores, 2007). Hence, the cross-cutting crevasse traces actually indicate two cycles of deformation which may relate to ice in the lower part of the study area having passed through both the Upper and Lower Icefalls. Furthermore, it appears that at the terminus of Fox Glacier, where longitudinal compression occurs, some of these crevasse traces are reactivated as thrust faults.

4.4.2.4 Arcuate Features (Thrust Faults) (S₃)

Hambrey *et al.* (1999) detailed five criteria for recognizing thrust faults within glaciers: (1) evidence for truncation of older structures resulting from over-riding along the thrust plane; (2) zones of mylonitized ice (fine ice with microshears); (3) sharply defined

zones of coarse-clear ice (0.01–0.5 m wide), representing recrystallization after thrust formation; (4) clean fractures with debris-rich basal ice or frozen subglacial sediment above the fracture; and, (5) direct measurements of displacements in active ice. As outlined by Hambrey *et al.* (1999), it is rare for all these criteria to be met, although if one or two structures show these features and numerous other structures display a similar morphometry, then the implication is that these similar structures are formed by thrusting. The analysis of fine sediments (*refer Chapter Five*) and isotopic signatures (*refer Section 4.3.3*), coupled with surface observations of arcuate shear fractures (S_3) on the lower section of Fox Glacier therefore accord with features (1) and (4) as described by Hambrey *et al.* (1999). This indicates that these features are thrust planes caused by longitudinal compression below the Lower Icefall (Figure 4.50) as ice decelerates and pushes into the proglacial sandur.

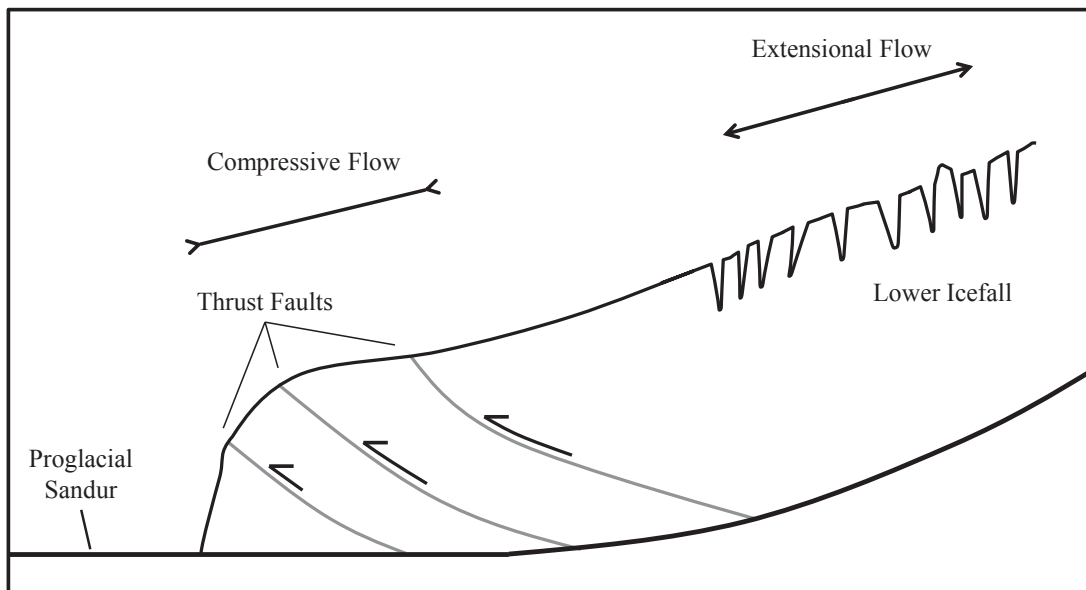


Figure 4.50: Simplified schematic diagram describing the thrusting of subglacial sediments along arcuate shear planes from the bed to the glacier surface.

Although thrust planes are common in polythermal and cold-based glaciers where marginal ice is frozen to the bed (Hambrey & Huddart, 1995), generating compressive stresses, the process-origin of thrusting at the snout of mid-latitude alpine glaciers is not as well-recognised (Glasser & Hambrey, 2002a, Herbst and others, 2006, Roberson, 2008). Thrusting occurs where up-glacier units of ice ('hanging walls') override down-

glacier ice units beneath ('footwalls'). Upward displacement of ice along thrusts has been identified in Svalbard at Bakaninbreen (Murray and others, 2000b), Hessbreen (Hambrey & Dowdeswell, 1997), and Kongsvegen (Glasser and others, 1998). However, some features that were originally described as thrusts by Glasser *et al.* (1998) have been re-reinterpreted as basal crevasse-fill structures by Woodward *et al.* (2002). Nye (1951) proposed that thrusting may occur along pre-existing structural weaknesses (e.g. crevasse traces). In one of only a few studies of the structural features of a mid-latitude alpine glacier, Goodsell *et al.* (2005b) invoked reactivation of crevasse traces as a facilitator of thrust faulting at the terminus of Haut Glacier d'Arolla, Switzerland. The longitudinal compression thought to be responsible for such thrusting may be in response to flow against a reverse slope (e.g. Sharp and others, 1993), a zone of thick proglacial foreland sediments, or an advancing ice margin causing increase in surface velocity (e.g. Herbst and others, 2006).

A thrusting origin for the structures close to the terminus of Fox Glacier is consistent with observations of Gunn (1964) and the hypothesis of Hambrey and Ehrmann (2004). Gunn (1964) proposed a zone of longitudinal compression on the lower section of Fox Glacier, which would presumably be accommodated by thrusting. Although Hambrey and Ehrmann (2004) presented only a photograph to support the hypothesis of thrusting at the lower Fox Glacier, they proposed that thrusting in this zone of the glacier was sufficient to entrain and elevate subglacial material from the bed. Thus, the weight of evidence points to thrusting at Fox Glacier, but the high ablation rates on the lower glacier of up to 13 cm d^{-1} (Purdie and others, 2008a) mean it is difficult to demonstrate large displacements along these features at the surface due to the surface melt. Nevertheless, as Fox Glacier has been advancing since the mid-1980s until the late 2000's into a proglacial foreland (Purdie and others, 2008a), a combination of both the reverse slope effects (e.g. Sharp and others, 1993) and advance effects (e.g. Herbst and others, 2006) would appear a likely scenario.

4.4.2.5 Arcuate Bands (Ogives)

Various theories exist to explain the formation of arcuate bands or ogives on glaciers, though no single theory has gained universal acceptance (Goodsell and others, 2002) (*refer Section 3.2.8*). The observations of ogives made during this research allow for a

comparison with the summer versus winter passage hypothesis, the shearing hypothesis, and the rhythmic compression hypothesis. From these observations, a number of specific features of the ogives identified on Fox Glacier are salient: (1) thrust planes have been observed on the surface of Fox Glacier, but not in the most obvious zone of band-ogives on the surface of Victoria Flat between the Lower and Upper Icefalls; (2) band-ogive width is typically 30–40 m, whilst the Upper Icefall is very long (c. 2.5 km); and (3) the band-ogives appear weak, with a more subtle contrast between the light and dark bands than has been described at other glaciers, such as Mer de Glace (e.g. Washburn, 1935) and Bas Glacier d’Arolla (e.g. Goodsell and others, 2002). On this basis, delineating a precise mechanism of band-ogive formation at Fox Glacier is problematic.

Given the narrow band-ogive width (~30–40 m) and long Upper Icefall (~2.5 km), and typical surface velocities of up to 1 m d^{-1} (Purdie and others, 2008a), each band-ogive pair cannot represent one year’s passage through the Upper Icefall, as suggested by Nye (1958, 1959), King and Lewis (1961) and Fisher (1962). This is because the Upper Icefall is too long for a transverse crevasse to transit through the entire length of the icefall within one year. Furthermore, the main problem with applying Posamentier’s (1978) shearing model is that clearly defined thrust planes would be visible on the glacier surface, but at Fox Glacier they are not present at Victoria Flat. Potentially, Posamentier’s (1978) model may be better applied if multiple small-scale faults transfer basal debris to the surface (e.g. Goodsell and others, 2002), rather than one discrete thrust plane being associated with each band-ogive. In addition, Goodsell *et al.* (2005) suggested a variation on Posamentier’s (1978) model whereby enhanced shear at the base of the icefall creates heavily foliated ice which is then thrust to the surface. This would explain the lack of large-scale transverse arcuate shear planes and the discordance between the narrow band-ogive width, relative to the length of the Upper Icefall and surface velocity. The ogives immediately beneath the Upper Icefall have a wave-type morphology and are suggested to have formed according to the rhythmic compression hypothesis proposed by Haeflerli (1951, 1957) and Atherton (1963). No variation in ice type is observable between that constituting the ‘wave’ or ‘trough’ portion of the wave-type ogives, and no obvious shear plane is apparent.

Chapter 5 : Sedimentology of Fox Glacier

5.1 Introduction

Chapter Five is concerned with the sedimentology of Fox Glacier. Analysis of supraglacial, englacial, subglacial and proglacial sediments has been undertaken using field-mapping of debris distribution and *in situ* measurements of clast *a*-axis orientations. In addition, the morphology of clasts has been examined to investigate the transport history and provenance of debris. The provenance and transport history of glacial debris can reflect the type and location of structures within the glacier system, as structural development processes can control the spatial distribution of sediment facies within a glacier (e.g. Bennett and others, 1996), and can also control the delivery of sediments to glacier margins and in turn influence sediment-landform associations (Roberson, 2008).

5.2 Glacial Debris Transport

The precise relationships between debris and structures within glaciers have not been rigorously defined (Hambrey & Glasser, 2003). Nevertheless, debris provides an indication of the dynamic processes occurring in a glacial system (Hambrey and others, 1999). Many glacial structures (e.g. arcuate bands, foliation, thrust planes, and folding) are, in some situations, only identifiable due to the debris which they contain.

Transport of material through the glacial system imparts characteristic signals on the morphology or form of individual clasts (Hambrey & Ehrmann, 2004) which give information about the likely mode of transport of the material (Boulton, 1978, Benn & Ballantyne, 1994). Indeed, clasts in different depositional environments commonly exhibit contrasting morphologies as a result of their erosional, transport and depositional histories (Reheis, 1975, Evans & Benn, 2003) giving an indication of their origin (Figure 5.1). Work by Glasser and Hambrey (2002a) showed how supraglacial debris incorporated on the ice surface controlled both the distribution of sedimentary facies on the forefield and moraine ridge morphology of Soler Glacier, Patagonia.

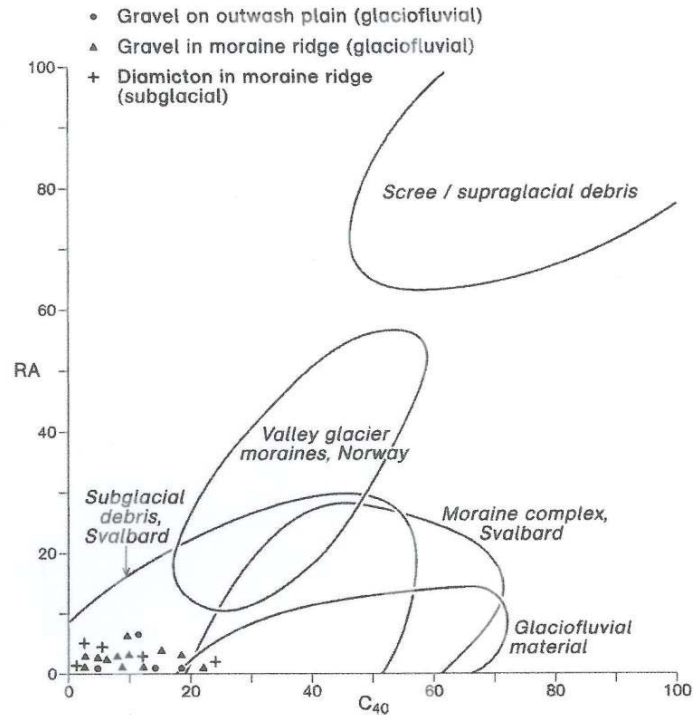


Figure 5.1: Covariant plot of RA index (percentage of angular and very angular clasts) against C₄₀ (percentage of clasts with c/a ratio ≤ 0.4) for lithofacies in the Laguna San Rafael, Chile, compared with facies envelopes based on data from Benn and Ballantyne (1994) and Bennett *et al.* (1997) giving an indication of clast provenance (from Bennett and others, 1999).

According to Boulton (1978), transport of material can be divided into active or passive transport. Active transport takes place at the glacier sole, and involves the interaction between particles or between particles and immobile objects, resulting in progressive debris modification through abrasion and crushing. Debris carried in an englacial or supraglacial position can be considered as undergoing passive transport, and is relatively unmodified in its transfer down-glacier, unlike active transport.

5.2.1 Subglacial Transport

Most theories of basal or subglacial debris entrainment involve some mechanism of regelation (Kirkbride, 2002) and include one of two main processes: abrasion and quarrying. Abrasion is regarded as the process whereby bedrock is scored by debris-laden basal ice (Sugden & John, 1976) as it flows over the bed and includes striation and polishing, the effectiveness of abrasion being dependent on the downward force

acting on basally-entrained clasts. Two models have been proposed to address the effective force acting on these clasts. The *Coulomb friction model* suggests that contact forces depend mainly on the weight of the overlying ice mass minus the effect of ‘jacking up’ by high pressure melt water at the bed (Boulton, 1974). In contrast, the *Hallet friction model* states that contact force is more dependent on the buoyant weight of particles and the rate of ice flow towards the bed (Hallet, 1979, Hallet, 1981).

Quarrying involves the fracture of large fragments (≥ 1 cm) from the bed by propagation of pre-existing or new cracks by high pressure melt water from basal ice at the pressure melting point. This can occur via the hydraulic effect of high pressure water within a crack or via the pressure difference between a high-pressure up-stream side of a bed unconformity and a lee-side low-pressure cavity. A heat-pump effect has been proposed (Robin, 1976, Röthlisberger & Iken, 1981) to explain transport of clasts fractured by quarrying whereby basal ice locally freezes to the bed as part of the regelation sliding process. As melt water moves through the subglacial system, water pressure, and therefore pressure melting point, changes (e.g. in the lee of an obstacle) allowing cold patches to develop causing the glacier sole to freeze to the bed adhering the fractured clasts to the sliding ice body. These clasts may then become the agents of abrasion as they are carried down-valley by the sliding ice.

In addition to abrasion and quarrying, overriding and inclusion of existing debris-rich ice has been suggested (Sharp, 1985b) as a method of subglacial debris entrainment and transport. Surging glaciers may override debris rich down-valley deposits of ice which then coalesce by means of regelation to the overlying ice.

5.2.2 Supraglacial and Englacial Transport

The addition of debris to valley glacier surfaces is dominated by rockfall and avalanching from mountain faces (Kirkbride, 2002, Gordon & Birnie, 1986, Boulton & Eyles, 1979), with material being made available by frost shattering of weakly jointed rocks, or de-buttressing of moraines and valley sides due to glacial retreat (Blair, 1994). In addition, mass movement of adjacent mountain slopes in tectonically active areas along with transport of debris by rivers from ice free tributaries and hanging valleys, and wind-blown dust all add mass to the glacier debris system. Where supraglacial slopes are rare or absent (e.g. ice caps and ice sheets) tephra can provide a major debris

input to the system (e.g. Richardson & Brook, 2010), as can localised inputs from nunataks (Benn & Evans, 1998).

Rockfall is a continuously occurring process during diurnal and seasonal cycles of freezing and melting on high mountain slopes. Occasional high magnitude catastrophic rockfalls may occur such as the 1991 *Aoraki*/Mount Cook rock avalanche which supplied an estimated 14 million m³ of rock onto the Hochstetter Icefall and Tasman Glacier, reducing the height of *Aoraki*/Mount Cook by ~20 m (Hambrey, 1994, Kirkbride & Sugden, 1992, Chinn and others, 1992). It has been suggested that catastrophic rockfalls may have considerable effects on glacier advance and retreat cycles (Shulmeister and others, 2009, Singer and others, 1998), through altering both a glacier's self-weight and its mass balance.

The point in the glacier system at which debris is supplied to the ice surface influences whether passive or active transport occurs. Rockfall in the accumulation area means debris will be buried by winter snowfall and become englacial. This debris may then become supraglacial as it emerges below the firn-line (Boulton, 1978) or may migrate to a subglacial position through ice deformation or transport along englacial conduits or crevasses. Debris reaching the ice surface in the ablation area will both stay on the glacier surface and remain unmodified (except for subaerial weathering) until it reaches the terminus, or will fall down open crevasses or be washed down moulins to englacial or subglacial positions. Actively transported debris may be elevated from the bed by basal freezing or thrusting and may enter passive englacial and supraglacial transport (Boulton, 1978). Debris may also pass between passive and active transport paths via englacial meltwater conduits (Kirkbride & Spedding, 1996). The path of supraglacial debris can often be followed for many kilometres on large Himalayan or polar glaciers as lateral or medial moraines. In general, supraglacial and englacial debris retains the morphological characteristics of parent material (Benn & Evans, 1998).

5.3 Analysis of Glacial Sediments

Supraglacial debris analysis has been used to differentiate provenance and transport histories of debris deposits in varying locations within the Fox Glacier system. Some of

these locations contain clasts of known origins and transport histories (e.g. rock fall deposits on Victoria Flat) whilst some are of unknown origins (e.g. a medial moraine on Victoria Flat). In addition, grain size analysis by way of particle size distribution has been undertaken to determine the provenance of fine sediments found in the surface expression of thrust faults on the surface of the lower glacier.

5.3.1 Collection of Samples

Clast samples were collected and analysed in various locations along the length of the glacier including Victoria Flat, the lower glacier and the proglacial sandur in the area immediately down valley of the terminus. Each sample population consists of 50 clasts to gain a representative sample of the Supraglacial debris in each of the areas.

The collection of clasts from a variety of locations throughout the glacier system allows for the comparison between clasts from different areas with regard to lithology and degree of working. This will help determine provenance and transport pathways of each of the sample populations.

Fine sediments were collected from lenses within regelation ice layers of thrust faults on the surface of the lower glacier. These samples were bagged, labelled and taken for laboratory analysis.

5.3.2 Clast Analysis

Supraglacial debris has been classified on Fox Glacier according to C_{40} index (percentage of clasts with a c/a ratio ≤ 0.4) and RA index (percentage of angular and very angular clasts) according to the methods described by Benn and Ballantyne (1994, 1993). A visual analysis and classification of lithology was also undertaken to determine rock type of each clast.

A number of researchers (e.g. Kirkbride & Spedding, 1996, Vere & Benn, 1989, Benn & Ballantyne, 1994) have suggested that it is possible to determine the mode of glacial transport of a clast by means of co-variate analysis of clast roundness and shape. Indeed, transport histories have been classified according to C_{40} index (percentage of clasts with

a c/a ratio ≤ 0.4) and RA index (percentage of angular and very angular clasts) according to Benn and Ballantyne (1994).

The dimensions of a clast (clast shape) are determined by the length of the three orthogonal axes of the clast: a (long), b (intermediate), and c (short). ‘Blocky’ clasts have been shown to indicate active transport in the basal transport zone, whilst ‘slabby’ clasts indicate passive transport either englacially or supraglacially (Benn & Ballantyne, 1994, Benn & Ballantyne, 1993).

The amount of wear exhibited by a clast is classified according to its roundness, and is quantified by assigning the clast to one of a number of roundness categories (e.g. Krumbein, 1941). In glaciology, a standard set of six roundness categories has been adopted from Benn and Ballantyne (1994) and range from very angular (VA) to well rounded (WR), with each category representing a greater amount of active transport as sharp edges are eroded as clasts are transported through the glacier system.

Although analysis of RA represents a standardised, widely-used system, ambiguities in roundness categories can arise due to the subjective nature of clast description. Varying lithologies (different jointing, layering and hardness) may also affect how well-worked a clast appears (cf. Brook & Lukas, 2012). A softer, more jointed parent material may become more rounded than a more resistant parent material even though both may have experienced the same level of active transport. Advancing glaciers may incorporate material that has previously been worked by a prior advance, glaciofluvial erosion in the glacier hydrological system, or fluvially-modified sediments on a sandur plain.

5.3.2.1 Clast Data Presentation

Results are presented using histograms to show the frequency of clast shape class along with ternary diagrams showing RA & C_{40} data (Figure 5.2). RA values are determined from the frequency histograms and show the percentage of clasts displaying an angular (A) or very angular (VA) shape. Ternary diagrams were first proposed by Sneed and Folk (1958) and plot each clast according to the ratio of its a , b , and c axes. The C_{40} value identifies the percentage of clasts with a c/a axial ratio of ≤ 0.4 , an indication of passive transport.

In addition to the individual RA histograms and C_{40} diagrams, a co-variance plot of RA against C_{40} is used to provide a more accurate measure of variation in clast transport history (e.g. Graham & Midgley, 2001).

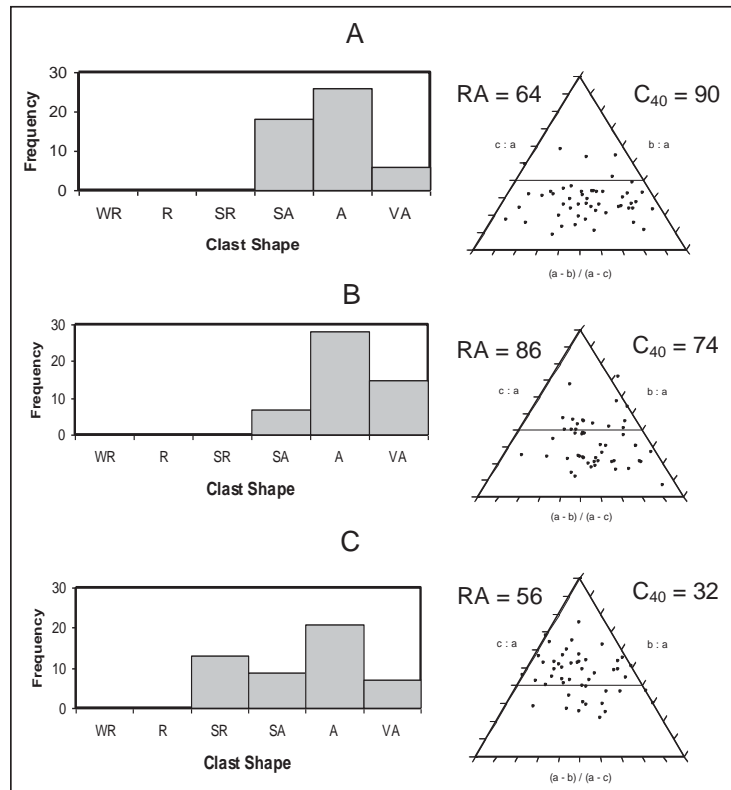


Figure 5.2: Examples of clast shape and morphology of surficial debris data presentation for clasts collected on the lower Fox Glacier. Frequency histograms show the frequency of clast shape (well rounded, rounded, sub-rounded, sub-angular, angular, and very angular), with the proportion of angular and very angular clasts represented by RA (%) values. Clast morphology is represented by ternary diagrams and C_{40} values.

5.3.3 Grain Size Analysis

Particle size distribution was undertaken using a *Horiba Partica LA-590* laser particle size analyser which uses two beams of light of different wavelengths (LED: $\lambda = 405$ nm; Laser: $\lambda = 650$ nm) to determine the distribution of grain-size classes (within the range of 10 nm to 3 mm) in fluid-solid dispersions. A double array of sensors detects light rays either passing through or being scattered by solid particles of a specific refractive index in relation to deionised water.

5.3.3.1 Refractive Index

As the laser particle size analyser uses scattered light intensity to determine particle size distributions, a refractive index is required for analysis of samples. The refractive index (RI) characterises the optical properties (refraction) of a specific mineralogical phase (crystal, glass, etc.) and is determined according to the mineralogy of the material being analysed. The mineralogy of a known parent material is derived from published literature or the use of x-ray diffraction (XRD) or x-ray fluorescence (XRF).

5.3.3.2 Calculation of Fractal Dimensions

Fractal dimensions of sediment grains are calculated to determine whether these grains have been modified by crushing and abrasion in the subglacial zone and are based on the methods described by Benn and Gemmell (2002), Hooke and Iverson (1995), Iverson *et al.* (1996) and Kjær (1999), and are given by the formula:

$$N(d) = N_0 \left(\frac{d}{d_0} \right)^{-m}, \quad (5.1)$$

whereby N is the number of particles of diameter d and m is the fractal dimension. N_0 is the number of particles of a reference size d_0 , whilst $-m$ is given by the gradient of double log-plot distribution. A complete description of the mathematical calculation of fractal dimensions is given by Benn and Gemmell (2002).

5.3.3.3 Grain Size Data Presentation

Grain size analysis results are presented as size distribution histograms and double logarithmic plots of particle size versus particle number (Figure 5.3). Size distributions are presented as the frequency (%) of grains within a size category measured in either micrometres (μm) & millimetres (mm), or phi (ϕ). Double logarithmic plots display particle size (d) in micrometres or millimetres versus particle number (N) per nominal particle diameter, assuming that all grains are spherical, with a constant density (Hooke & Iverson, 1995, Benn & Gemmell, 2002).

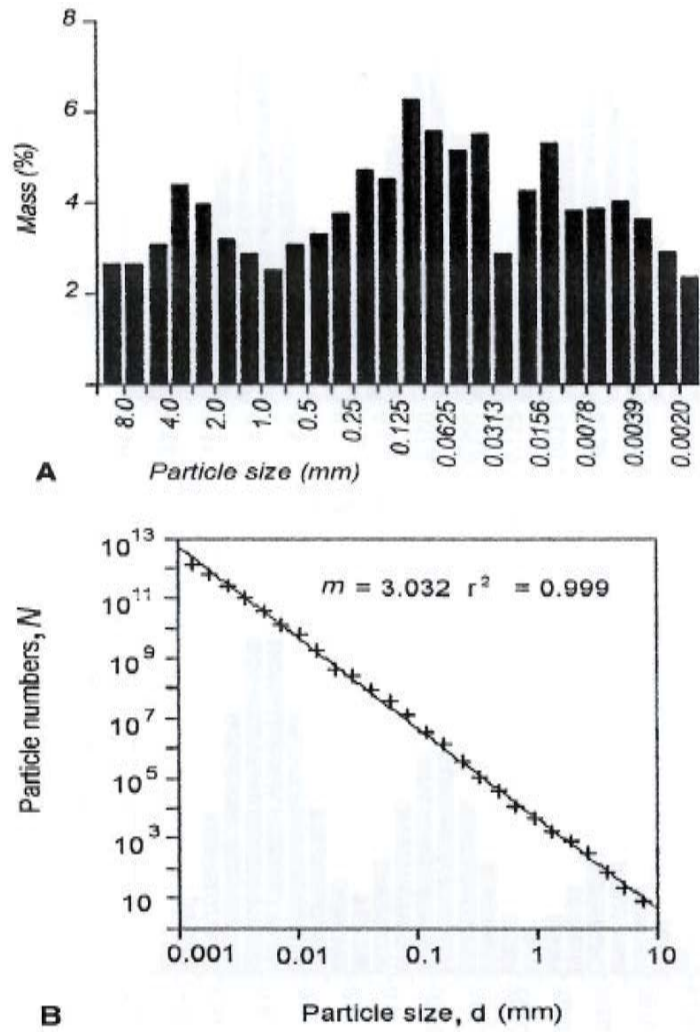


Figure 5.3: Particle size distribution (A) and double logarithmic ($\log d$ versus $\log N$) plot (B) of basal till from a Patagonian glacier (from Benn & Gemmell, 2002).

5.4 Contemporary Sedimentology of Fox Glacier

5.4.1 Supraglacial Debris

The spatial distribution of supraglacial debris has been determined using field-mapping and analysis of remotely-sensed images. The most extensive area of supraglacial debris (nearly all of which is a mixture of argillite and greywacke) occurs on the true-left of the lower glacier and Victoria Flat (Figure 5.4). On the surface of Victoria Flat, a separate zone of supraglacial debris distinct from that on the true left valley side persists from immediately beneath the Upper Icefall to immediately above the Lower Icefall at the point where the glacier turns to a westerly aspect. Below the Lower Icefall, supraglacial debris forms a distinctive ribbon of medial moraine, disconnected from the valley side (Figure 5.5). This moraine persists to the glacier snout, and increases in supra-glacial thickness down-glacier (Figure 5.6). A distinct boundary can be seen between the darker argillite and greywacke rocks of the supraglacial debris of the medial moraine, and the lighter coloured schist derived from rock falls off the southern valley side (Figure 5.7).

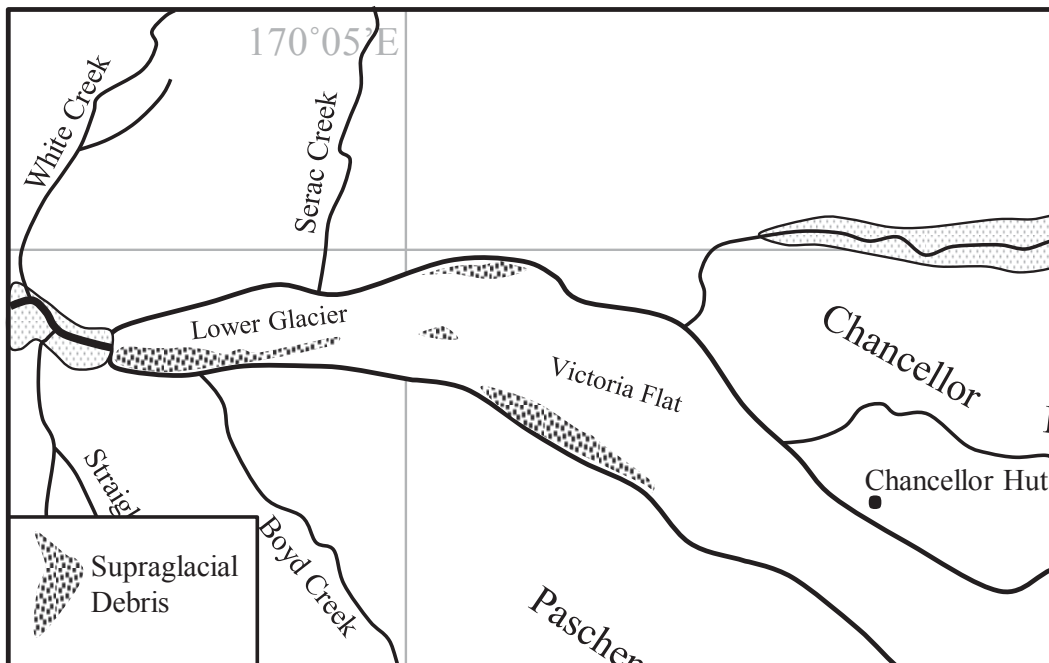


Figure 5.4: Map of the distribution of supraglacial debris on the lower glacier and Victoria Flat.



Figure 5.5: Composite image of the medial moraine located towards the true left of the lower area of Fox Glacier. The view is towards the true left valley side. (Photo: J. Appleby, January, 2010)

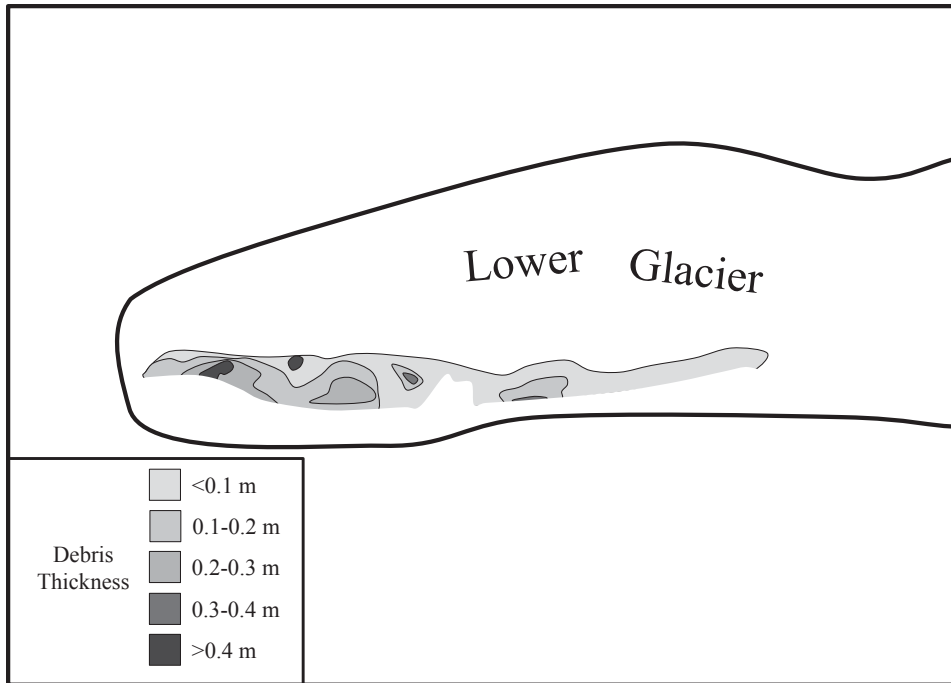


Figure 5.6: Contour map of supraglacial debris measured on the surface of the lower glacier. Debris thickness increases down-glacier. Steep topography and crevassing prevented debris thickness measurements of the true-left of the moraine.



Figure 5.7: Lower glacier medial moraine viewed from below the Lower Icefall looking down-glacier. A distinct boundary can be seen (denoted by dashed line) between darker, supraglacial argillite and greywacke (right) and lighter schist (left) produced by rock fall from Paschendale Ridge. (Photo: J. Appleby, January, 2011)

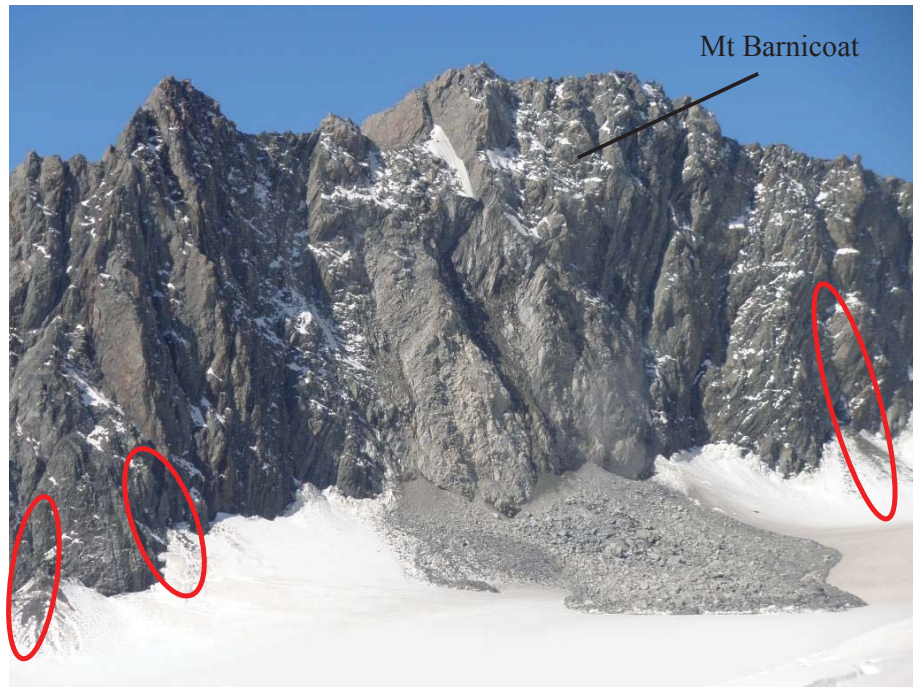


Figure 5.8: A large supraglacial debris deposit on the surface of the Explorer Glacier in the Fox Glacier névé, produced during a rock fall from Mt Barnicoat (2800 m), photographed in 2011. Numerous other debris sources have also been identified in this area (circled), all contributing material to the glacier sedimentary system. (Photo: E. Hawke)



Figure 5.9: Large-scale (~6 m high) mega-clast of schist, observed immediately beneath the Lower Icefall. No other individual clasts of this scale were identified on the glacier surface. (Photo: J. Appleby, January, 2011)

Little supraglacial debris is present on the surface of the névé, with only sporadic debris cones visible close to the headwall of the névé and along the ridges and buttresses that protrude into the névé from the Main Divide. High frequency, low magnitude rockfall events seem to be the main contributor to these cones (Figure 5.8).

Supraglacial debris on Victoria Flat and the lower glacier varies in size from <0.01 m to >10 m for individual clasts (Figure 5.9). The largest sized clasts are generally greywacke whilst the smallest sized clasts are argillite. A small amount of schist is observable in the lower glacier medial moraine.

Immediately below the Lower Icefall, a ribbon of medial moraine emerges, the point at which (Figure 5.10) supraglacial debris is first observable on the lower glacier. At this point, clasts of various sizes melt-out of the ice. *In situ* orientation measurements of clast *a*-axis azimuths show that long axes generally parallel ice flow (Figure 5.11). Dip of individual clasts is difficult to determine as once enough of the clast is exposed to make measurements possible, heat conduction to the margins of the clast causes preferential melting beneath the clast and so effectively increases the dip angle by undermining the clast.



Figure 5.10: Point of exhumation of englacial debris below the Lower Icefall. This is the point at which supraglacial debris first appears in the lower glacier structural domain. (Photo: J. Appleby, January, 2011)



Figure 5.11: In-situ orientation measurement of a clast being exhumed below the Lower Icefall. The clast *a*-axis azimuth is approximately parallel to the ice flow direction. (Photo: J. Appleby, January, 2011)

5.4.2 Subglacial Debris

At the true-right margin of the lower glacier and Victoria Flat immediately beneath Chancellor Shelf, it is possible to access subglacial tunnels and ice caves (Figure 5.12) formed by subglacial water channels and the deformation of ice as the glacier over-rides subglacial obstacles. Access to these subglacial areas has been made possible by the recession of the glacier away from the valley sides, which has been taking place since 2008.

The floor of these tunnels and ice-caves is characterised by relatively poorly sorted glaciofluvial deposits of schistose sediments (Figure 5.13) interspersed with small fragments of argillite and greywacke. Layers of fine sediment and entrained clasts are observable in the roofs of these caves. Measurement of *a* axes in some of the larger clasts exposed shows an orientation (Figure 5.14) generally parallel to the direction of ice flow.



Figure 5.12: Collecting ice and sediment samples from the entrance of a subglacial tunnel and cave formed by subglacial water action and ice over-riding a bed obstacle at the true-right margin of the lower glacier. (Photo: J. Appleby, January, 2011)



Figure 5.13: Poorly-sorted glaciofluvial debris constituting the floor of subglacial tunnels and caves exposed beneath the true right margin of the lower glacier and Victoria Flat. (Photo: J. Appleby, January, 2011)

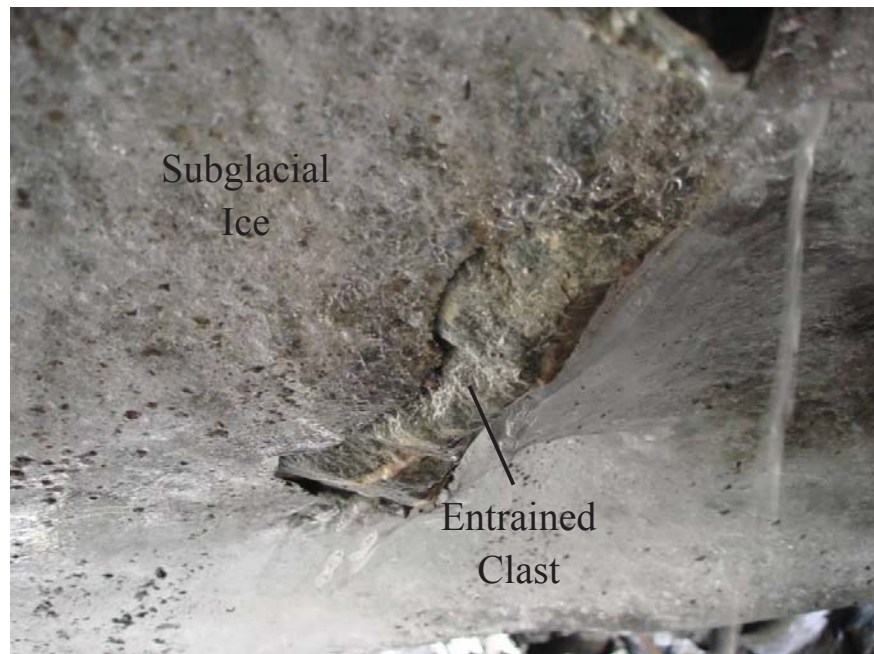


Figure 5.14: Entrained clast exposed in a subglacial cave roof at the true-right margin of the lower glacier. The clast a -axis is approximately 0.3 m long and aligned with glacier flow. (Photo: J. Appleby, January, 2011)

5.4.3 Proglacial Sediments

Sedimentary deposits are a common feature of the proglacial sandur immediately in front of the true right of the glacier snout. Deposits in this area typically comprise mounds or ridges (Figure 5.15) of a diamicton of poorly-sorted sediments of a dominantly schistose lithology. Most mounds and ridges are between 1 m and 2 m high. Towards the valley centre, transverse debris ridges parallel the terminal face. This orientation suggests formation via dumping of material from the snout. Whilst at the true-right valley side, ridges with their axes parallel to ice flow occur. These are similar to seasonal flutes as described by van der Meer (1997) at the Turtmann Glacier, Switzerland.



Figure 5.15: Ridge of proglacial debris (ridge crest denoted by dashed line) approximately 1.5 m high observed immediately in front of the true-right of the glacier snout. The ridge axis is approximately 10 m in length and parallel to glacier flow, forming a feature similar to seasonal flutes as described by van der Meer (1997). The debris in the background is part of the true right lateral moraine bounding the proglacial zone. (Photo: J. Appleby, January, 2011)

5.4.4 Morphological Analysis of Glacial Sediments

Debris was sampled from 11 locations in the lower glacier and Victoria Flat structural domains (Figure 5.16). Sample sites 1 and 2 are located on the proglacial sandur, sites 3-6 are located on the lower glacier medial moraine, sites 7 and 8 are on the true right of Victoria Flat, and sites 9-11 are on the true left of Victoria Flat. At each location, 50 clasts were measured for clast shape (RA) and morphology (C_{40}), according to methods outlined by Benn and Ballantyne (1993, Benn & Ballantyne, 1994) and discussed in *Section 5.3.2*. Clast shape and morphology can provide information on the transport mechanism (active or passive) experienced by sediments and so can give an indication of both clast provenance and the dynamic forces responsible for depositing the sediment in its current position.

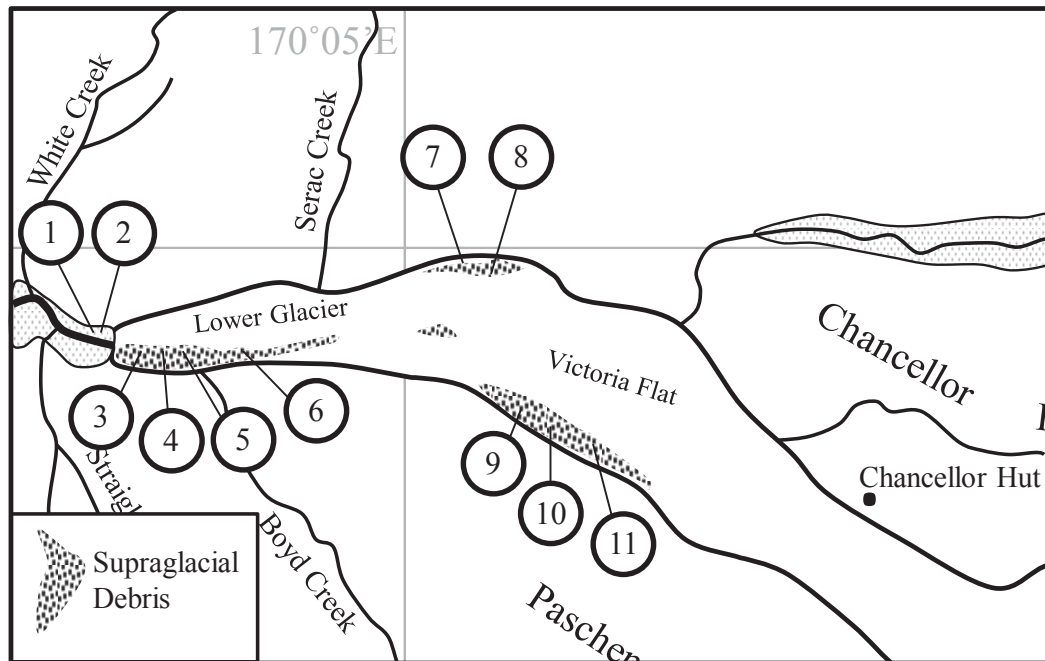


Figure 5.16: Map of the location of clast analysis samples. Sample location numbers relate to frequency histograms and ternary diagrams in Figures 5.17, 5.18, 5.19 and 5.20.

5.4.4.1 Proglacial Clast Analysis

Sediment samples 1 and 2 (all of which had a schistose lithology) in the proglacial area have relatively low RA and C_{40} values. Location 1 has measured RA and C_{40} values of 58% and 64% respectively, whilst location 2 has measured values of 20% and 60% (Figure 5.17). These clasts have a range of shapes from very angular to rounded.

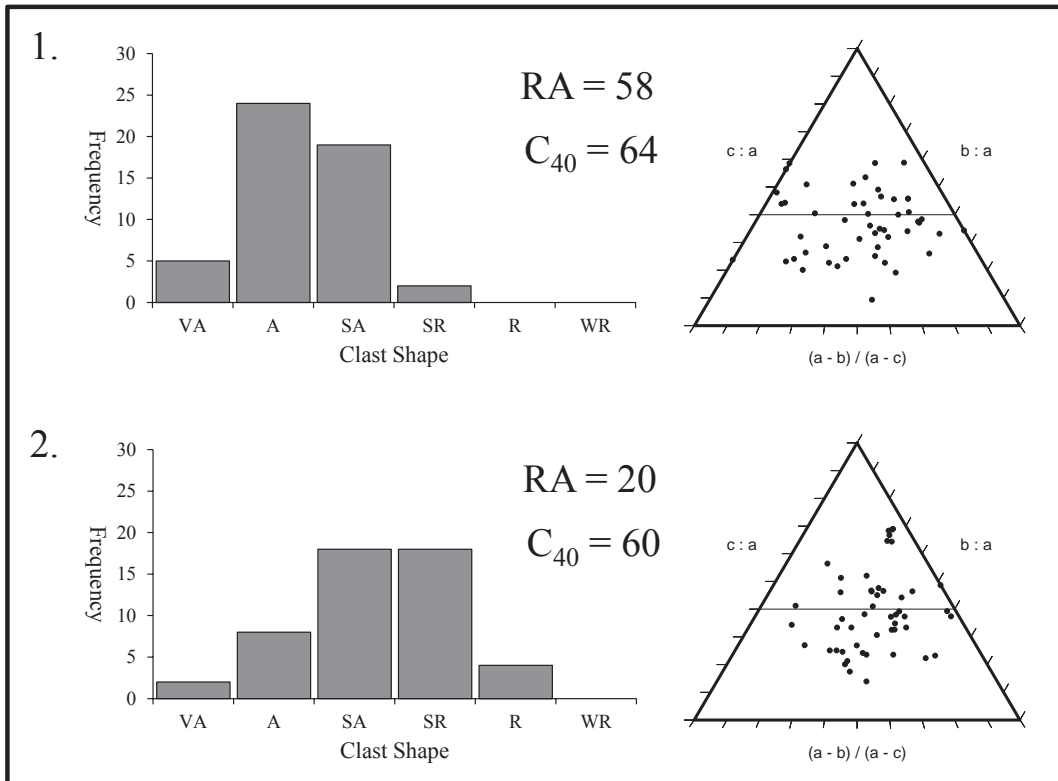


Figure 5.17: Clast shape (RA) and morphology (C_{40}) of debris measured on the proglacial sandur immediately in front of the true right of the glacier snout. Frequency histograms show the frequency of clast shape (Very Angular, Angular, Sub-Angular, Sub-Rounded, Rounded and Well Rounded), with the proportion of angular and very angular clasts represented by RA (%) values. Clast morphology is represented by ternary diagram and C_{40} value.

5.4.4.2 Lower Glacier Clast Analysis

Sediment samples 3 to 6 measured on the lower glacier medial moraine have higher RA and C_{40} values than those observed in the proglacial area (Figure 5.18). Measured clast shapes (RA) in this area range from 60% to 84% with all clasts falling into the very angular to sub-angular range of shapes. Clasts have a morphology value (C_{40}) ranging from 72% to 90%

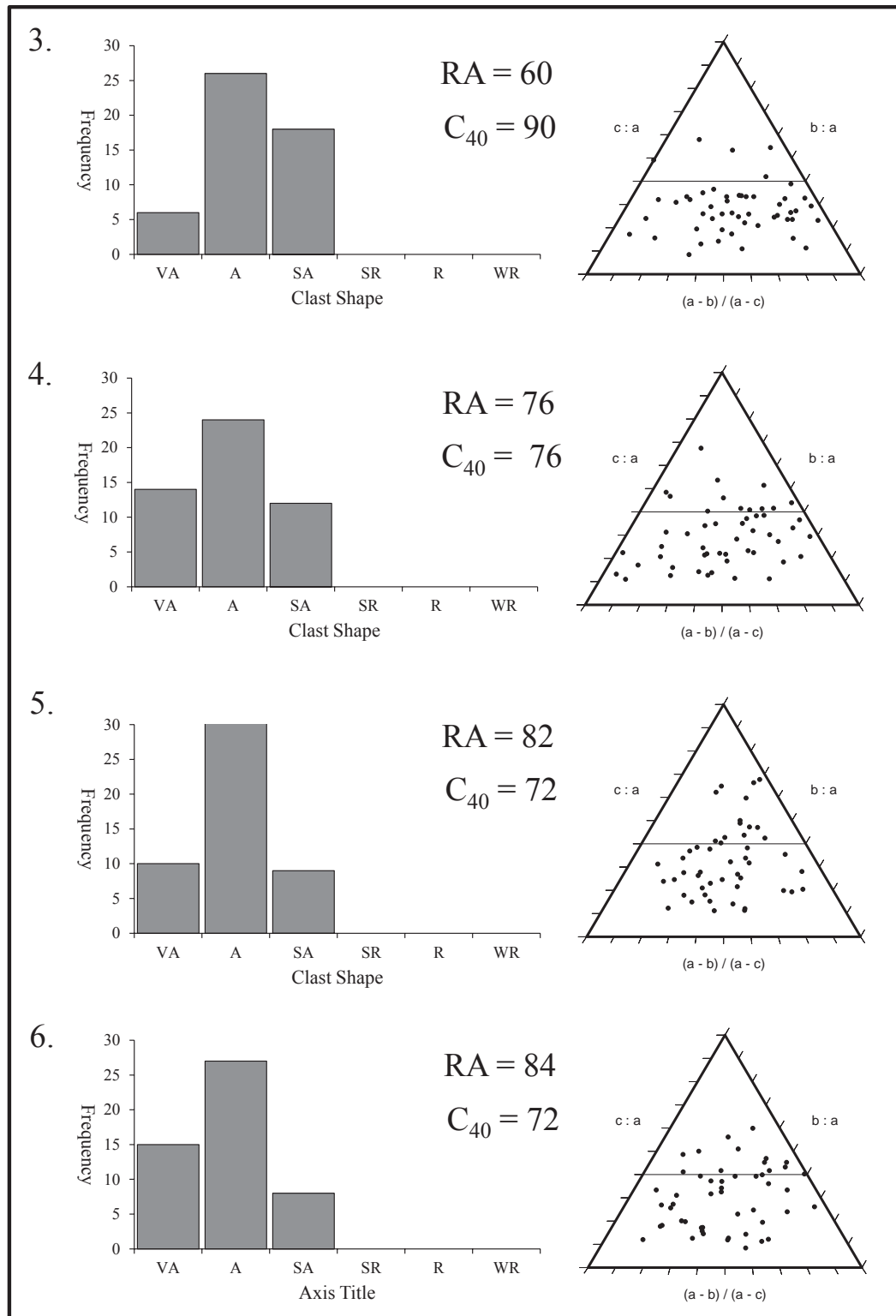


Figure 5.18: Clast shape (RA) and morphology (C_{40}) of debris measured on the true lower glacier medial moraine. Frequency histograms show the frequency of clast shape (Very Angular, Angular, Sub-Angular, Sub-Rounded, Rounded and Well Rounded), with the proportion of angular and very angular clasts represented by RA (%) values. Clast morphology is represented by ternary diagram and C_{40} value.

5.4.4.3 Victoria Flat Clast Analysis

Samples were collected from two areas of Victoria Flat. Sites 7 and 8 are situated on the true right of Victoria Flat with sites 9-11 on the true left. Data from sites 7 and 8 (Figure 5.19) varies markedly between one and other. Clasts from site 7 have relatively high RA and C_{40} values of 86% and 68%, respectively. In contrast, clasts from site 8 have much lower values of 56% and 30%, with a large proportion of clast shapes in the sub-angular and sub-rounded range.

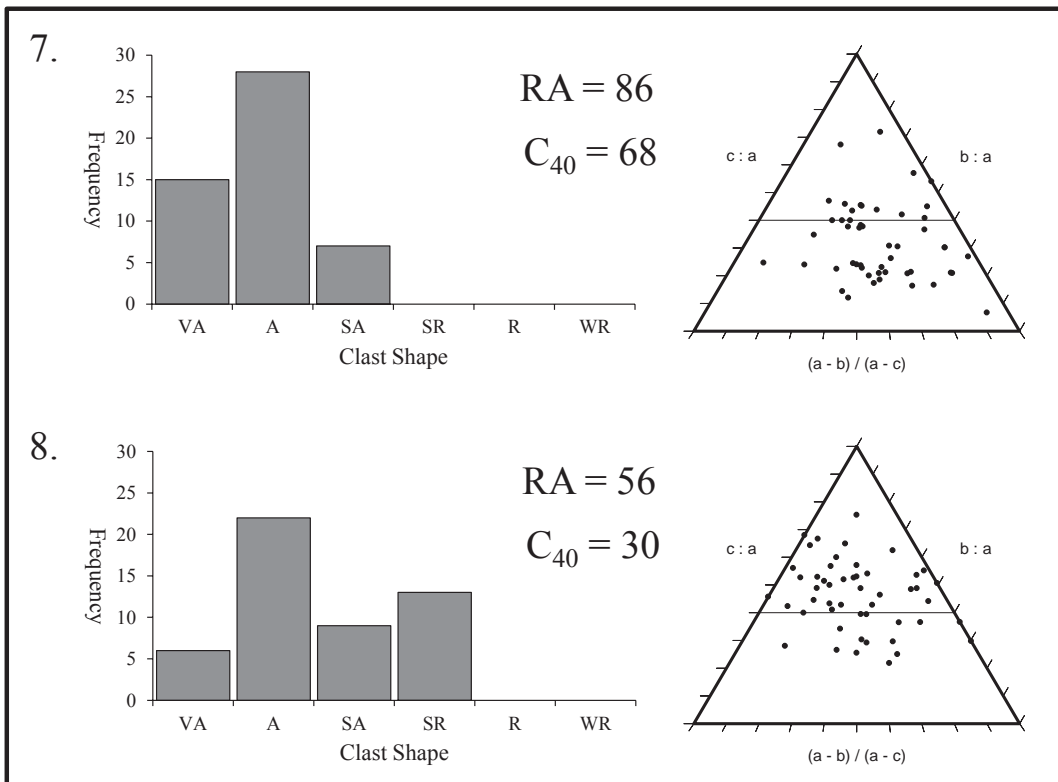


Figure 5.19: Clast shape (RA) and morphology (C_{40}) of debris measured on the true right of Victoria Flat. Frequency histograms show the frequency of clast shape (Very Angular, Angular, Sub-Angular, Sub-Rounded, Rounded and Well Rounded as defined by Benn and Ballantyne (1994)), with the proportion of angular and very angular clasts represented by RA (%) values. Clast morphology is represented by ternary diagram and C_{40} value.

Clasts from the true-left sample sites (9-11) (Figure 5.20) show RA and C_{40} values more similar to those recorded on the lower glacier medial moraine than those recorded on the true right of Victoria Flat. RA values here range from 72% to 98%, with C_{40} values of

64% to 82%, and all clasts lie within the very angular to sub angular range, with the majority angular. This suggests passive transport of these clasts despite them being exhumed from the lower part of the Upper Icefall.

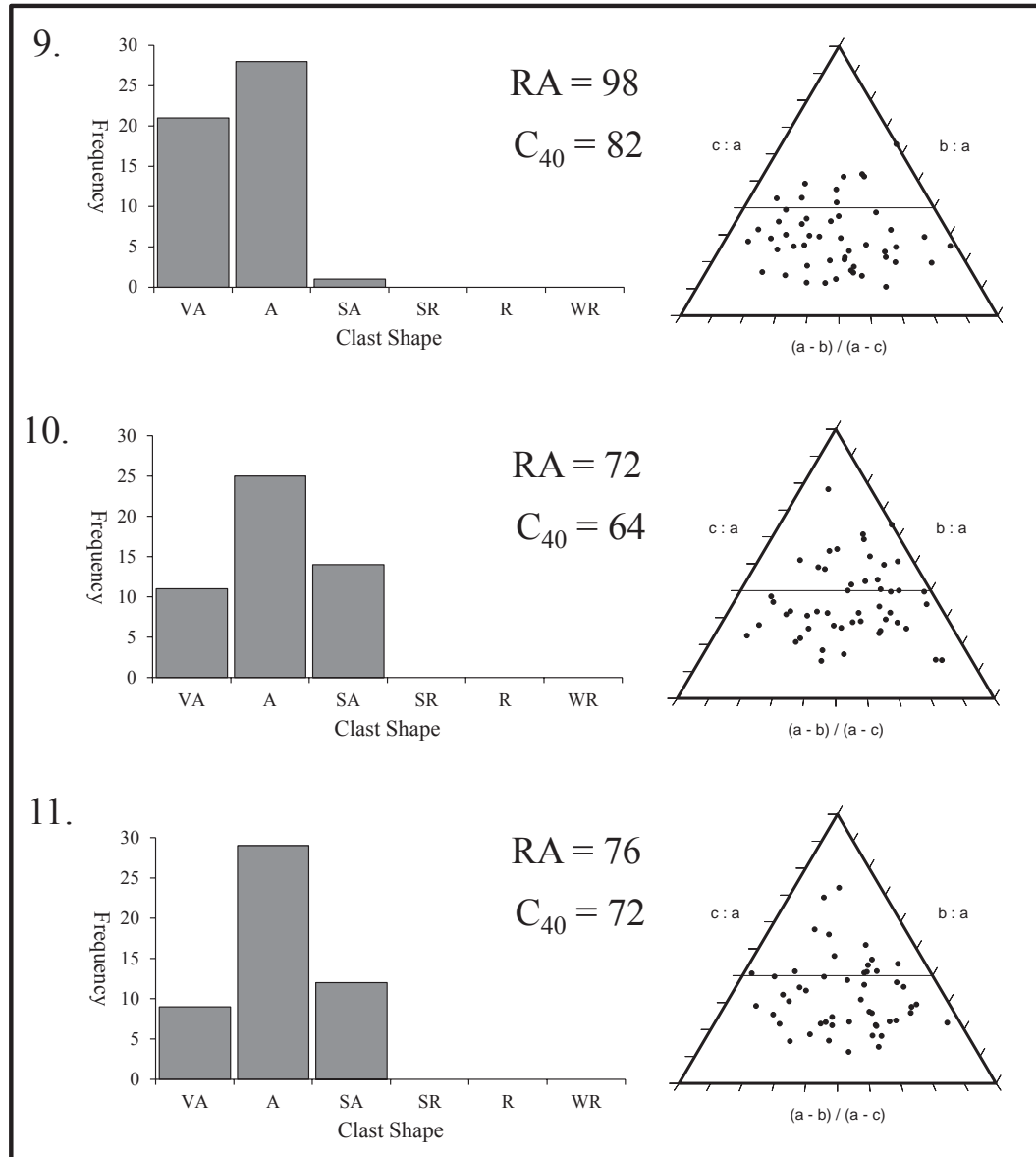


Figure 5.20: Clast shape (RA) and morphology (C_{40}) of debris measured on the true left of Victoria Flat. Frequency histograms show the frequency of clast shape (Very Angular, Angular, Sub-Angular, Sub-Rounded, Rounded and Well Rounded as defined by Benn and Ballantyne (1994)), with the proportion of angular and very angular clasts represented by RA (%) values. Clast morphology is represented by ternary diagram and C_{40} value.

5.4.4.4 Clast Shape and Morphology of Thrust Plane Sediments

At the true-right margin of the lower glacier, thrust planes are exposed in splaying crevasse walls. These exposed thrust planes appear to contain regelation ice and fine sediment as seen on the glacier surface, whilst some also contain larger clasts suspended in the ice (Figure 5.21). At the point of exposure, these thrust planes dip at a high angle (60-90°) and on average, strike 250° from north, approximately parallel to the direction of glacier flow.

Clasts found within the thrust plane are of relatively small size (maximum long axis of 83 mm) with RA = value of 36% and $C_{40} = 50\%$ (Figure 5.22). Clasts with a long axis sufficiently large to measure *in situ* had an azimuth approximately parallel to glacier flow, although the number of exposed clasts suitable for measuring was limited.

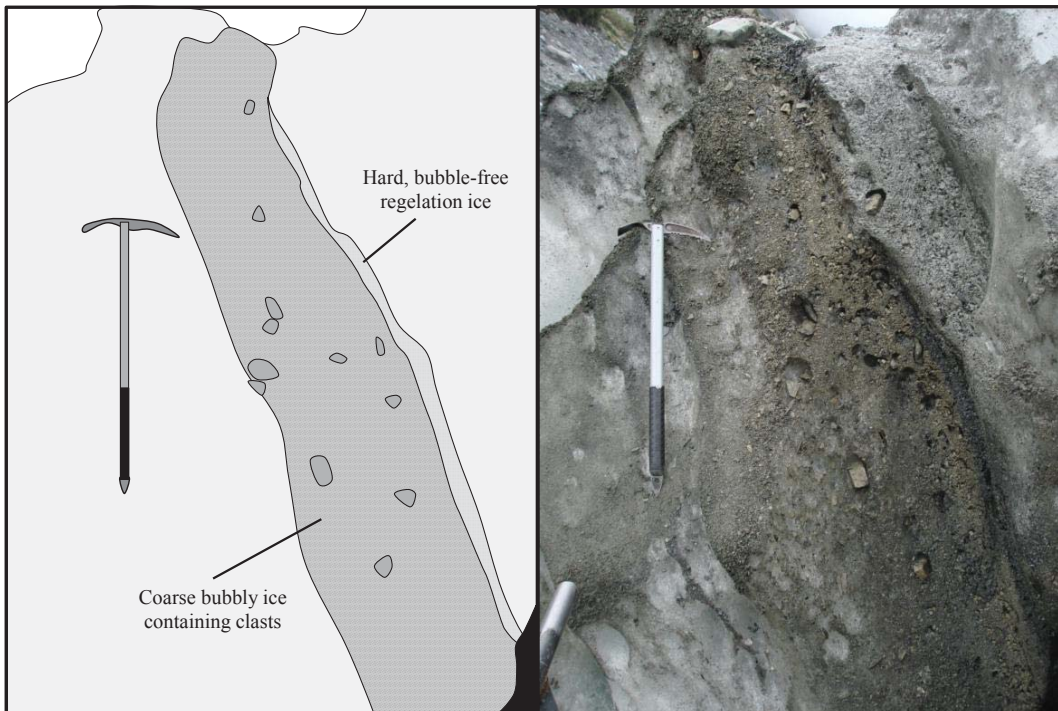


Figure 5.21: Section of a thrust plane exposed in a crevasse wall in the lower glacier. The thrust plain contains a layer of hard, bubble-free regelation ice and a layer of coarse, bubbly clast-rich ice.

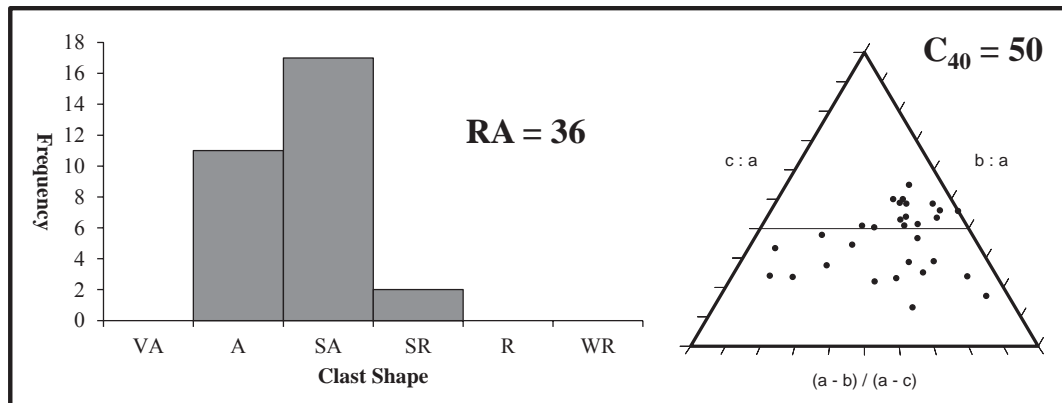


Figure 5.22: Clast shape (RA) and morphology (C_{40}) of material found in a thrust plane exposed in a crevasse wall in the lower glacier structural domain. Frequency histogram shows the frequency of clast shape (Very Angular, Angular, Sub-Angular, Sub-Rounded, Rounded and Well Rounded), with the proportion of angular and very angular clasts represented by RA (%) values. Clast morphology is represented by ternary diagram and C_{40} value. Sample size $n = 30$.

5.4.4.5 Grain-Size Analysis of Thrust Plane Sediments

Grain-size distributions of intra-thrust sediments have been measured to determine if the sediments have been comminuted at the bed before being transported to the glacier surface thrusting. Three thrust planes in the lower glacier zone were sampled at two different points within each plane (Figure 5.23). A laser particle size analyser was used to measure grain-size distribution. A refractive index of 1.54 was applied to the samples during processing due to the type and provenance of the sediment parent material (Möebis, 2012, pers. comm.).

Particle-size distributions of till deposits have long been used to obtain information on processes of glacial transport (Benn & Gemmell, 2002). Double logarithmic plots (Figure 5.24) of grain-size distribution can indicate degree of grain crushing and therefore subglacial transport (Hubbard & Glasser, 2005). Indeed, Boulton (1974) and Iverson *et al.*, (1996) found that comminution by crushing as a result of shear was responsible for significant changes in the grain-size distribution in deforming subglacial till. Hooke and Iverson (1995) compared grain-size distributions of subglacial tills with other common sedimentary environments and found subglacial till size distributions to be fractal, with an excess of fines, whilst the other tills they studied were not. Hooke and Iverson (1995) go on to suggest that it may be possible to use grain-size

distributions to distinguish between tills that have undergone deformation (i.e. subglacially) and those that have not. This was supported by Kjær (1999) who stated that grain-size distribution studies have proven useful as discriminatory tools to reconstruct transport pathways in glaciers. Iverson *et al.* (1996) suggest a grain-size distribution with a fractal dimension greater than 2.6 is probably a necessary condition for determining whether a till has been highly deformed at the glacier base.

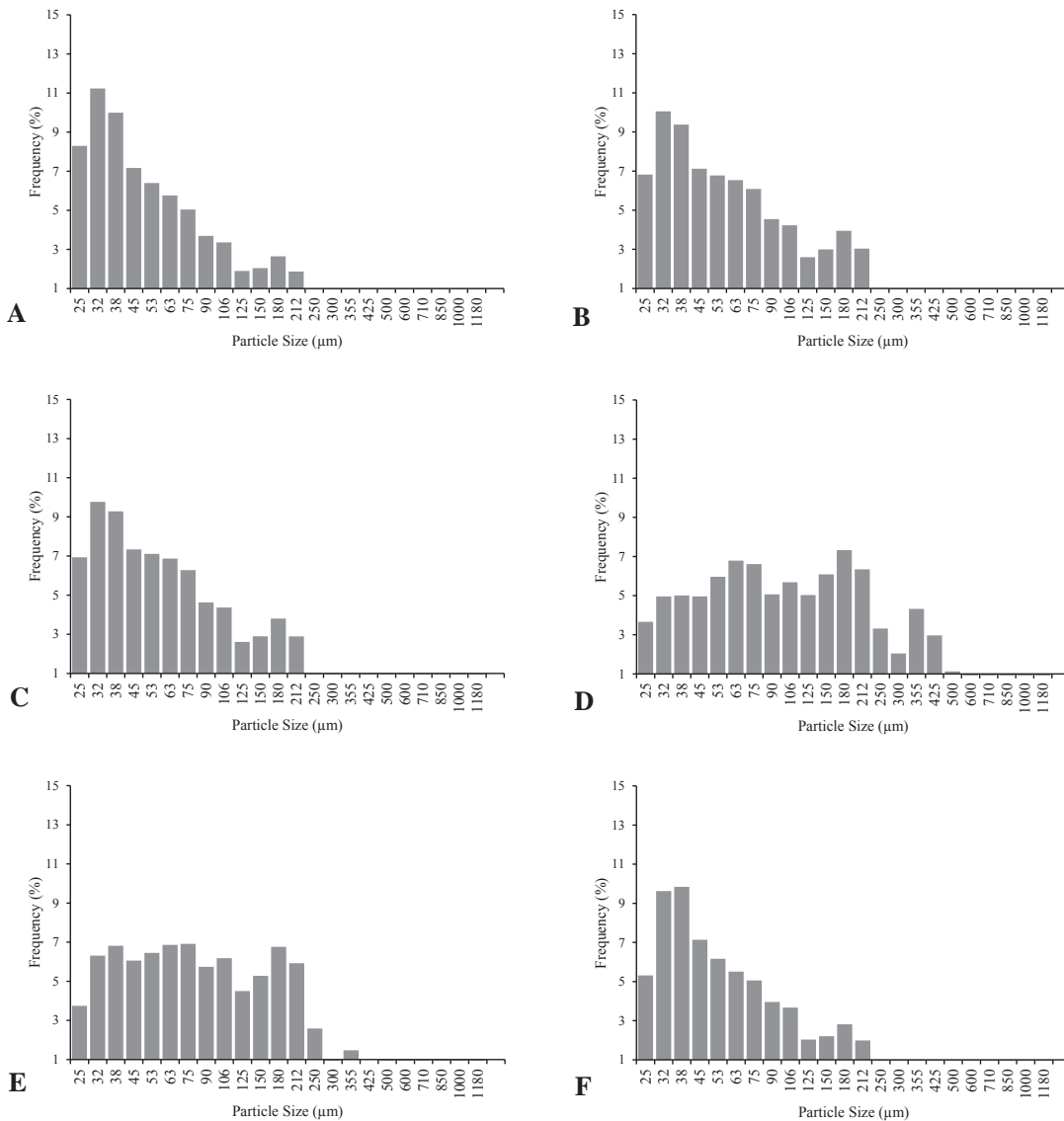


Figure 5.23: Grain-size distribution of sediments sampled from the surface expressions of thrust planes on the lower Fox Glacier. Frequency histograms represent sample locations Thrust 1, Sample A and B (A, B); Thrust 2, Sample A and B (C, D); and Thrust 3, Sample A and B (E, F).

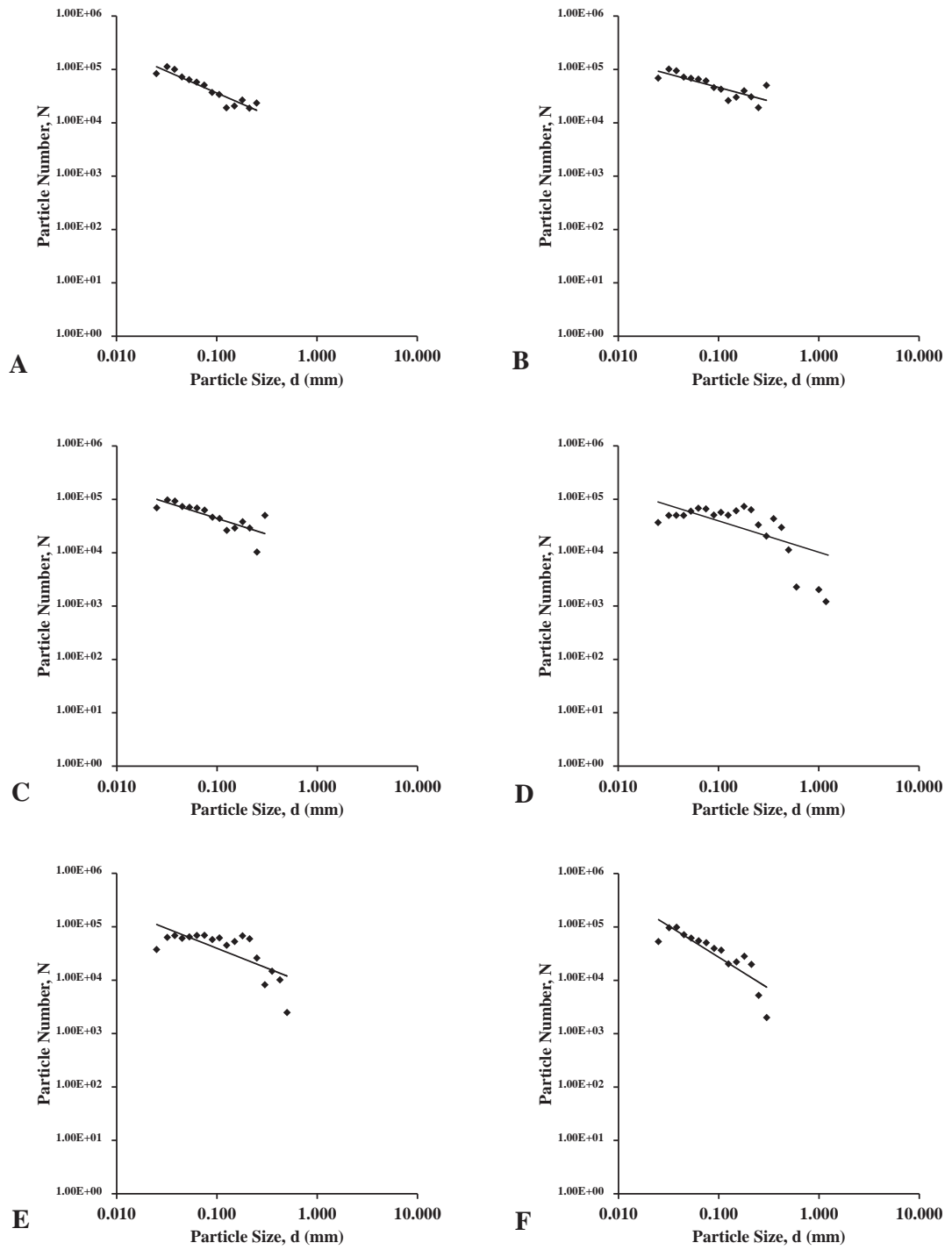


Figure 5.24: Double logarithmic plots of grain size versus grain frequency. Plots represent sample locations Thrust 1, Sample A and B (A, B); Thrust 2, Sample A and B (C, D); and Thrust 3, Sample A and B (E, F).

The majority of sediments from the thrust planes are $<500\ \mu\text{m}$ ($1.0\ \phi$) so can be classed as medium sand or smaller. The dominant size frequency for samples A, B, C and F is between 32 to $38\ \mu\text{m}$ (5.0 to $4.0\ \phi$ - coarse silt), with the smallest measured particle size being $25\ \mu\text{m}$ (6.0 to $5.0\ \phi$ - medium silt). The coarsest grains occurred in sample D with less than 1% of the sample ranging from $600\ \mu\text{m}$ to $1.2\ \text{mm}$ (1.0 to $\sim 0.0\ \phi$) coarse to very coarse sand.

Kjær (1999) suggests that mechanical crushing produces relatively coarse material (i.e. sand), whilst abrasion will produce relatively finer material (i.e. silt) (Boulton, 1978, Sharp & Gomez, 1986). Furthermore Kjær (1999) infers that the ratio of coarse to fine material decreases as sediment is progressively comminuted during transport. The excess of fines in each of the sediments suggests that they have undergone comminution at the bed and are therefore of subglacial origin. In addition, each of the samples has a fractal dimension of ~ 3 , again suggesting an excess of fines (e.g. Hooke & Iverson, 1995) and therefore comminution at the bed.

5.4.5 Trends in glacial sediment morphology along Fox Glacier

The general trend is for a decrease in RA down-glacier, with average RA's decreasing from 83% to 76% to 39% down-glacier from Victoria Flat to the lower glacier to the supraglacial area respectively (Figure 5.25). A general change can be seen from very angular and angular clast shapes on Victoria Flat to more sub-angular, sub-rounded and rounded clast shapes on the proglacial sandur immediately in front of the terminus. Clasts change from a slabby and angular morphology to a more blocky and rounded morphology as they travel through the glacier system, suggesting active transport.

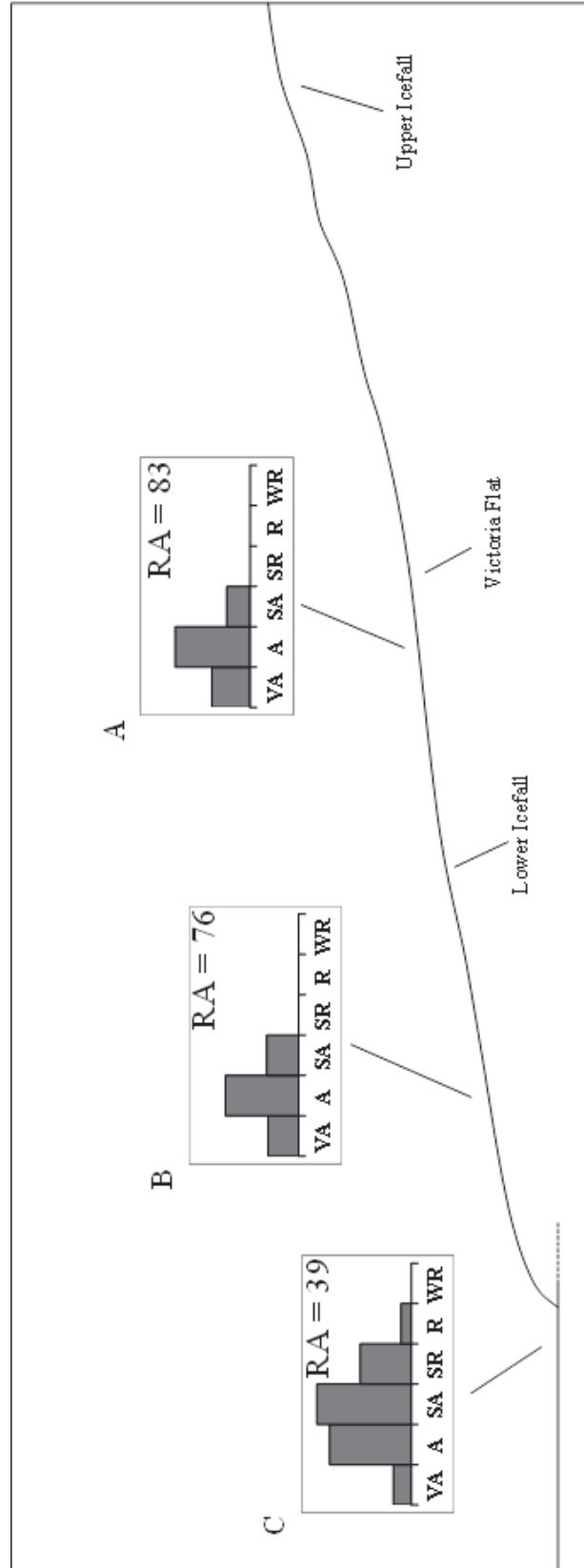


Figure 5.25: Cross profile of the Lower Fox Glacier and Victoria Flat showing results of clast roundness measurements. Frequency histograms A, B, and C represent Victoria Flat, Lower glacier and Proglacial Area sample locations, respectively.

5.4.6 Covariance of Clast Analysis

Measured RA and C_{40} values for each of the 11 sample locations have been compared in a covariance plot (Figure 5.26), to allow direct comparison with facies envelopes describing the process-origin of glacial sediments identified from previous research (Glasser and others, 2006). All clast sample sites except 1 & 2 (proglacial), 3 (lower glacier) and 8 (true right of Victoria Flat) fall within the scree/supraglacial debris envelope of Glasser *et al.* (2006). This is expected for locations 1 and 2 as these will be heavily influenced by the glaciofluvial interaction of the Fox Glacier and River, whereas the other locations have been transported in an englacial position before being exhumed onto the glacier surface below icefalls.

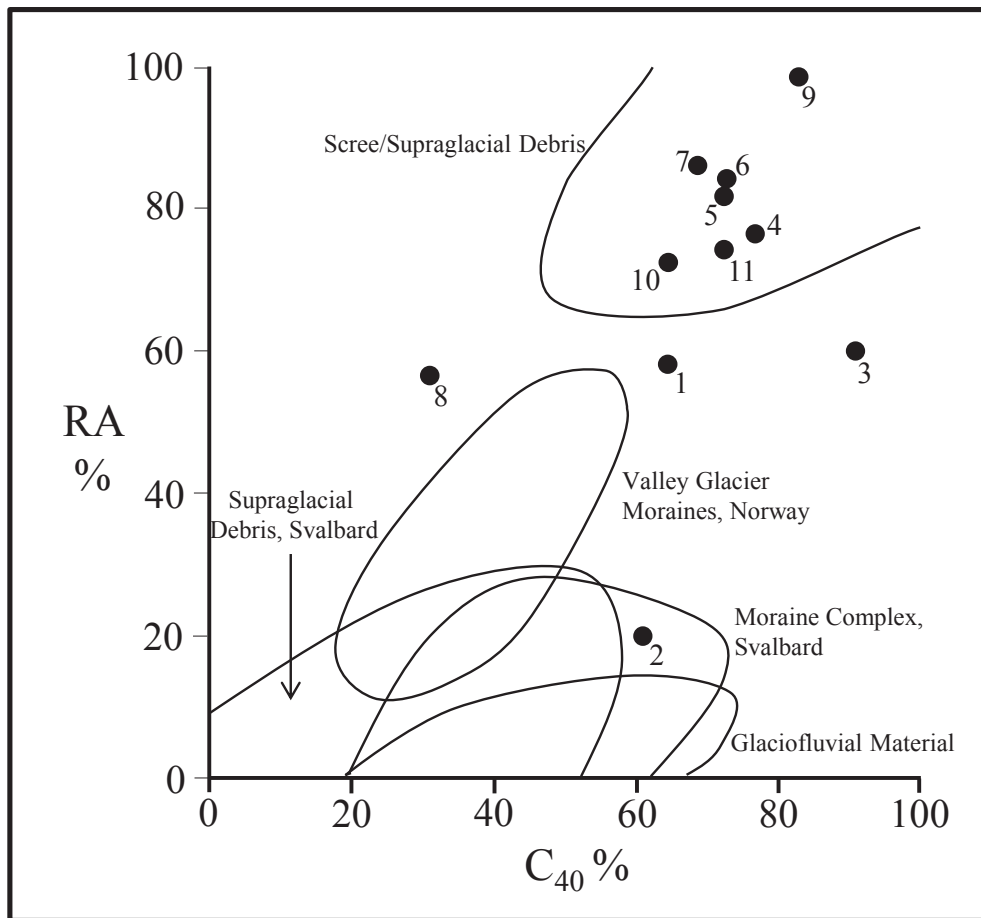


Figure 5.26: Covariance plot of C_{40} against RA for debris measured at sample locations 1 to 11 (refer Figure 5.16). The covariance of each location has been plotted with facies envelopes described by Glasser *et al.* (2006).

5.5 Discussion on the Sedimentology of Fox Glacier

The importance of sedimentology in terms of an understanding of the structural glaciology of Fox Glacier lies in the principal that glacier structures can control the distribution of sediment facies within a glacier (e.g. Bennett and others, 1996), and can control the delivery of sediments to glacier margins and therefore sediment- landform associations (e.g. Roberson, 2008). A deductive analysis of sediment facies (in combination with flow dynamics (*refer Chapter Seven*)), therefore, will help determine the processes occurring by which these facies formed. This is particularly important in terms of understanding the processes by which the lower glacier medial moraine has formed.

5.5.1 Sediment Provenance

The lithology of the supraglacial debris on the surface of the lower glacier consists largely of greywacke and argillite suggesting a provenance high in the Fox Glacier system. Sporadic rockfall from the headwall and rock buttresses of the névé accumulates on the surface and is then covered by snow and firn accumulation, producing dispersed debris bands parallel to primary stratification (Goodsell and others, 2005b). These debris bands become increasingly deformed, rotated and concentrated as ice transits the glacier system and is laterally compressed as it enters the narrow Fox valley. The rock fall-derived debris maintains its angular clast morphology as it is passively transferred through the system, finally being ‘exhumed’ and forming the medial moraine below the Lower Icefall.

In addition to surficial accumulation and incorporation of debris, material may be supplied to the glacier system from the distal ends of the many ridges and rock buttresses that extend into the accumulation area, in particular Pioneer Ridge. Converging flow units at the distal ends of these ridges can cause basal ice to be elevated from the bed creating a medial debris septum (Eyles & Rogerson, 1978, Boulton & Eyles, 1979, Goodsell and others, 2005b, Goodsell and others, 2005c). Benn and Evans (2010) note that if the confluence of flow units occurs in the accumulation zone, the medial septum will not extend to the surface until exposed by ablation lower down the glacier. No evidence for the existence of medial debris septa is presented by

this research, although the possibility of their existence remains. Confirmation of the presence (or absence) of medial debris septa in the Fox Glacier névé may prove a worthwhile future study to accurately identify the transport history and origins of material constituting the lower glacier medial moraine. Some excellent examples of debris septa are observable on the east of the main divide; for example the Tasman/Darwin, and the Murchison/Mannering Glacier confluences.

In the lower glacier and on Victoria Flat, the extreme true left margin of the glacier is mantled by schistose rock derived from Paschendale Ridge which forms the true left valley side. Already weakened by faulting (*refer Section 4.4.2.1*), Paschendale Ridge is undercut by the glacier causing instability and rockfall onto the glacier surface. As the glacier has retreated, the ridge has been further destabilised by de-buttressing effects following ice contraction (e.g. Augustinus, 1995).

5.5.2 Medial Moraine Formation

The true left supraglacial debris on the lower glacier is interpreted as a medial moraine due to the distinct lithology and boundary between it and the true left valley side. Medial moraines are well-defined features of many valley glaciers, often forming at the confluence of two glaciers or downstream of a nunatak (e.g. Vere & Benn, 1989). Early work by Heim (1885) also recognized that medial moraines may be formed in accumulation zones before being ‘exhumed’ down-glacier in zones of ablation. Detailed conceptual models of medial moraine formation have been discussed by Anderson (2000) and Bozhinskiy *et al.* (1986), whilst comprehensive medial moraine classification schemes based on the relationship between sediment supply and morphological development, have been proposed by Eyles and Rogerson (1978). Three models of medial moraine formation have been postulated (e.g. Vere & Benn, 1989). First, ablation-dominant (AD) medial moraines are developed from englacial debris, often of supraglacial origin, and can be of three sub-types: burial of debris in open crevasses below the ELA (AD1), incorporation as part of firm sedimentation above the ELA (AD2), and elevation of debris in the lee of subglacial obstacles such as bedrock knobs (AD3). Second, ice stream interaction (ISI) moraines are formed at the junctions of confluent glaciers, finding immediate surface expression (Gomez & Small, 1985), and increasing in relief down glacier. Third, avalanche-type (AT) moraines can be

identified, originating from persistent supraglacial sources within individual flow units (Vere & Benn, 1989).

An analysis of the lower Fox Glacier medial moraine has been undertaken as part of this research, and three aspects of this can be highlighted. First, the moraine contains material that appears to have been passively transported, based on comparison of clast form (C_{40}) and roundness (RA) with published results from other studies (e.g. Glasser and others, 2006). Second, the moraine is not visible on the glacier surface until below the Lower Icefall, from where the material becomes gradually thicker down-glacier from this point of exhumation. Third, although the in-situ a -axes of emergent clasts in the moraine are aligned down-glacier, they do not appear to parallel any identifiable fold hinges, as has been found elsewhere (e.g. Hambrey & Glasser, 2003, Goodsell and others, 2005b). These characteristics of the moraine strongly indicate that constituent clasts were initially deposited as discrete debris layers (most probably originating from infrequent rockfalls) in the Fox Glacier névé (reinforce with lithology). These supraglacial debris accumulations were then ingested into the glacier by annual snow and firn accumulation above the ELA, and passively transported englacially down-glacier toward the snout. Once in an englacial position, clasts are re-oriented by lateral compression as the surrounding ice exits the ~4.5 km wide névé and is channelled down the <1 km wide Fox valley. Below the Lower Icefall, the material is ‘exhumed’ by rapid surface melt (Purdie and others, 2008a) at a point-source from where the debris then accumulates on the surface to form the medial moraine. On this basis, the medial moraine observable on the lower Fox Glacier can be considered to correspond to the AD2 model proposed by Eyles and Rogerson (1978). The lack of significant positive relief prior to the point of emergence below the icefall reflects the low debris concentrations within the ice along with the discontinuous debris-supply from sporadic rock fall in the névé.

5.5.3 Thrusting and Elevation of Subglacial Sediment

A great deal of debate exists in the literature as to whether debris can be elevated along thrust planes (Glasser & Hambrey, 2003) (*refer Section 3.2.7*), identified as S_3 structures in this study. Benn and Evans (2010) suggest that debris-filled thrust faults are rare on temperate glaciers (such as Fox Glacier). However, Glasser and Hambrey

(2002a) identified basal debris that had been elevated along thrusts at the margins of the temperate Soler Glacier in Patagonia. The excess of fines in supraglacial sediments associated with thrusts close to the terminus of Fox Glacier, along with analysis of clasts identified in exposed thrust planes, points toward elevation of debris from subglacial and englacial positions.

Two main mechanisms have been suggested (e.g. Hambrey and others, 1999) to explain elevation of debris along thrust planes. First, ice slabs over-thrusting static or slower moving down-glacier ice can carry englacial debris to the surface. Alternatively, debris may be transported along a thrust plane by the action of water flow or shearing. The first of these mechanisms may occur at Fox Glacier, as indicated by the longitudinal compression of ice as it flows against the topographical barrier created by the proglacial sandur. The enhanced shearing produced by this compressional flow, coupled with the large volumes of water found in the Fox Glacier system may also be sufficient to produce the conditions required to elevate fine sediments along thrust planes, as suggested by the second mechanism. Hence, it is feasible that a combination of both of these mechanisms is occurring in the lower Fox Glacier. Isotope analysis (*refer Section 4.3.3*) has been used in this study to try and determine which of the two mechanisms is occurring at Fox Glacier. Despite subtle but discernible differences between the isotopic signatures of thrust ice and surface ice, the significance of these differences is not strong; as such results can be considered inconclusive.

5.5.4 Fluted Moraines

The longitudinal ridges of debris oriented parallel to glacier flow present at the true right of the proglacial sandur immediately in front of the snout are interpreted as fluted moraines, also known as flutings or simply, flutes (Boulton, 1976, Rose, 1989, Rose, 1992, Gordon and others, 1992). The most widely accepted model of fluted moraine formation suggests them as being the product of subglacial sediment deformation and accumulation in the lee of an obstruction at the glacier bed (Eklund & Hart, 1996, Benn, 1994, Boulton, 1976) due to changes in pressure. The parallel-sided flutings (Benn & Evans, 1996) seen at Fox Glacier, however, are suggested as being formed due to the blockage and filling of subglacial cavities and channels by large clasts which allow water to pass through but catch glaciofluvially-transported material, causing the cavities

to become 'choked' with debris. These flutes have then become exposed on the proglacial sandur due to the retreat of the glacier. This is a similar mechanism to that which has been proposed for the formation of supraglacial eskers (e.g. Kirkbride & Spedding, 1996, Huddart and others, 1999). In contrast to the fine sediments found to constitute fluted moraines elsewhere (e.g. Benn, 1994, van de Meer, 1997), the moraine diamicton seen at Fox Glacier has a higher proportion of large clasts. The glaciofluvial transport mechanism of these clasts is supported by the schistose lithology of the moraine suggesting a relatively local source (within the Fox valley rather than the névé) and the more rounded, blocky morphology of the individual clasts.

Fluted moraines are often short-lived, having a low preservation potential being readily degraded by wind and water (e.g. Evans & Twigg, 2002, Glasser & Hambrey, 2001) and over-riding of ice due to fluctuations of terminus position (e.g. van de Meer, 1997). This is suspected to be the case for Fox Glacier, having a highly dynamic proglacial river planform that changes rapidly, as well as being subject to sporadic outburst floods (Carrivick & Rushmer, 2007).

Chapter 6 : Ground-Penetrating Radar

6.1 Introduction

Chapter Six is a ground-penetrating radar investigation into the structural glaciology of Fox Glacier. It begins with a review of existing literature describing the use of geophysics in glaciology, then goes on to describe the methods used in this ground-penetrating radar study, before presenting the results obtained. Finally the chapter provides a discussion on the use of ground-penetrating radar at Fox Glacier and glaciers in other locations.

6.2 A Review of Ground-Penetrating Radar

6.2.1 Introduction

The first published accounts of the use of ground-penetrating radar in glaciology are from Stern (1929, 1930) who undertook surveys to determine ice depth on European alpine glaciers. The technology and method Stern (1929, 1930) developed was then largely forgotten, until the 1950's, when the United States Air force lost a number of aircraft, whilst they attempted to land at a military base in Greenland. According to Waite and Schmidt (1962) and Olhoeft (1996), the radar developed during the second world war, now fitted to military aircraft, 'saw through' the snow and ice to the bedrock below, giving a false reading of altitude as the aircraft approached the runway. As with many new technologies, military applications are a driver in the early stages of development, and so it seems with ground-penetrating radar. For example, Barringer (1965, 1966) investigated ground-penetrating radar for terrain sensing, largely for military use, again mostly over snow and ice. Geophysics over ice was also taken up by a number of research institutes such as the Scott Polar Research Institute at Cambridge (Bailey and others, 1964) and the University of Wisconsin Polar Research Centre (Walford, 1964). Soon after, however, the technique expanded to include more civilian centred aims, such as the detection of ground water reservoirs (Caldecott, 1967) or civil engineering and construction (Morey, 1974).

6.2.2 Principle of Ground-Penetrating Radar

GPR uses electromagnetic fields to probe lossy dielectric materials to detect structures and changes in material properties within the materials (Annan, 2002). Common ground-penetrating radar or radio echo sounding system comprises a signal generator, antenna for transmitting and receiving, and a receiver for recording data whilst in the field (Figure 6.1). In its simplest form, the signal generator causes the transmitter (T_x) to produce a wave train of radio waves that propagate from an antenna into the material or substance to which it is in close proximity. The radio waves are transmitted through the material according to the materials dielectric constant. According to Hubbard and Glasser (2005), radio wave propagation is principally controlled by permittivity, and conductivity of the material. Electrical permittivity (ϵ , m^{-1}) describes the capacity of a material to store an electrical charge, impeding the flow of a current. Permittivity is described relative to that in free space ($8.854 \times 10^{-12} \text{ Fm}^{-1}$) and can therefore be referred to as relative permittivity (ϵ_r) or the dielectric constant.

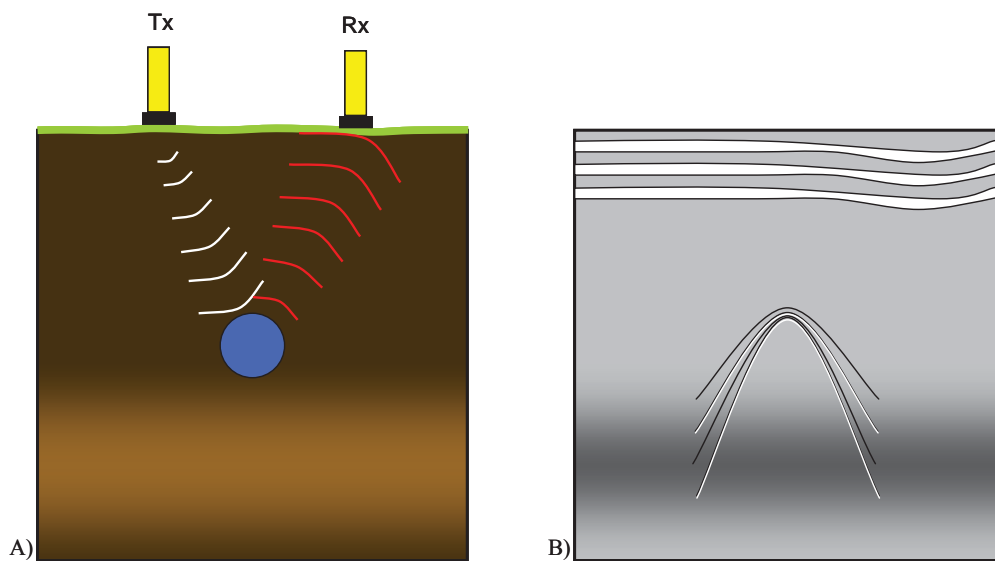


Figure 6.1 A) Transmission of high frequency radio waves from a transmitter T_x , reflected by a feature, and detected by a receiver R_x . B) A simplified, typical profile produced from the feature seen in A).

If the radio waves meet a differential object that varies sufficiently from the host material, they are reflected. The reflected wave train is then detected by the antenna and receiver (R_x). The time taken from the wave train being propagated by the transmitter to when it is detected by the receiver (two-way travel time) gives an indication of the depth of the reflector, when the relative permittivity or dielectric constant of the material is known (Macheret and others, 1993). Both the transmitter and receiver need to be highly accurate to perform this measurement, as the radio waves travel at such high speeds, with two-way travel times often in the range of a few tens to several thousands of nanoseconds (Reynolds, 1997).

6.2.3 Ground-Penetrating Radar in Glaciology

Radar waves have been widely used to investigate the internal and basal properties of ice masses (Plewes & Hubbard, 2001). Indeed, the origins of ground penetrating radar and echo sounding, as previously discussed, lie in investigations of ice and snow depth, with the first published uses of these techniques being ice thickness determination of the Antarctic and Greenland ice sheets in the 1950s and 1960s (e.g. Steenson, 1951, Cook, 1960).

In their review of ground-penetrating radar use on glaciers and frozen materials, Woodward and Burke (2007) suggest significant areas of investigation as;

1. Water content,
2. Route-ways for subglacial/subsurface drainage,
3. Internal structure,
4. Fracturing and deformation of ice, and
5. Inclusions in sediment/ice matrix (e.g. sediment in glacier or ice in frozen ground).

In addition to research in glacierized areas, ground-penetrating radar and radio echo sounding can be used in glaciated areas and areas of permafrost, such as determining the structure of moraines and frozen ground.

6.2.3.1 Depth Profiling

Where radio wave penetration is sufficient, basal reflectors may be recorded, allowing ice or snow thickness to be recorded (Hubbard & Glasser, 2005). Indeed, ice thickness determination is now the most widespread application of radar (Plewes & Hubbard, 2001), with extensive ground-penetrating radar profiling of Antarctica (e.g. Siegert, 1999, Bingham & Siegert, 2007, Horwath and others, 2006, Laird and others, 2010, Cui and others, 2010), Greenland (Steinhage and others, 2005), Svalbard (Nicollin and others, 1992, Taurisano and others, 2006), and North America (Nolan and others, 1996). Reynolds (1997) suggests ice thickness determination by ground-penetrating radar to be accurate to around 1%. This technique has been used to produce baseline information relating to depth and volume of almost all of Earth's major ice bodies (Hubbard & Glasser, 2005). To date, most research has been carried out on ice sheets and ice caps, with limited temperate depth mapping apart from single soundings to determine approximate ice depth of an area being investigated for other research purposes. This is likely due to the higher incidence of meltwater being present in temperate or polythermal glaciers than in the polar ice masses.

Due to the often immense areal scale of GPR surveys undertaken in the Polar and Sub-Polar regions (e.g. Antarctica and Greenland), many use airborne GPR technology (Watts & Wright, 1981, Kennet and others, 1993, Kim and others, 2010). These surveys are capable of collecting data at a sufficient resolution to measure approximate ice and snow depths, but in a much more efficient way than traditional field techniques. These types of study have also been fundamental in the discovery and mapping of sub-glacial Antarctic lakes (Siegert, 2000, Siegert and others, 1996, Siegert, 2005, Gorman & Siegert, 1999). Most small-scale studies are ground-based, using the reflection and common mid-point methods as discussed in *Section 6.2.4*. Often the resolution of detail achieved by airborne ground-penetrating radar and radio echo sounding surveys is not sufficient for the more precise investigations required for structural glaciology.

6.2.3.2 Structural Glaciology

Basal and internal structures in ice sheets and glaciers have been mapped and investigated extensively using ground-penetrating radar. Significant work has been

undertaken in the European Alps (Goodsell and others, 2002, Goodsell and others, 2005b, Goodsell and others, 2005c, Monnier and others, 2008), much of which has concentrated on the mapping of brittle fracture, crevasses and faults in temperate ice. Appleby *et al.* (2010) undertook a small scale structural survey on the lower Fox Glacier, achieving limited success in identifying shear planes. Similar work was carried out by Hambrey *et al.* (2005) on Midre Lovénbreen, Svalbard, whilst Woodward (1999) working on Kongsvegen, also on Svalbard, concentrated on mapping sediment incorporation using geophysical methods. In addition, Maurer and Hauck (2007) and Hausmann *et al.* (2007) studied the internal structure of alpine rock glaciers, whilst Yamamoto *et al.* (2004) used high frequency ground-penetrating radar to investigate the highly detailed internal structure of snow.

Similar structural work has also been widely undertaken in Antarctica (e.g. Taurisano and others, 2006, Camerlenghi and others, 2001, Urbini and others, 2001, Frezzotti and others, 2002a, Frezzotti and others, 2002b, Gogineni and others, 2007), complementing the depth profiling of polar ice caps well.

The investigation of glacial structure using ground-penetrating radar can further be improved by combining it with additional methods. Navarro *et al.* (2005) combined ground-penetrating radar with seismic methods to better understand structure and ice depth in temperate glaciers, whilst Eisen *et al.* (2003) combined ground-penetrating radar with ice cores to further determine structure of alpine ice bodies.

6.2.3.3 Hydrology

Flowing water in glacial environments exerts an important influence on glacier behaviour and geomorphologic processes, and presents both hazards and benefits for human populations (Benn & Evans, 1998, 2010). For these reasons, ground-penetrating radar and radio echo sounding are increasingly being used as a method for investigating glacier hydrology. Methods have been suggested to locate englacial and subglacial waterways (Priscu and others, 2010, Murray and others, 2007a, Kennet, 1989, Lee and others, 2010, Carter and others, 2009) and, once located, to characterise them (Moorman & Michel, 2000) to further understand their behaviour. Longer term hydrological geophysical studies have been undertaken (Catania & Neumann, 2010,

Bjornsson and others, 1996, Irvine-Fynn and others, 2006, Moorman & Michel, 2000), from which, glaciologists have gained a better understanding of the thermal regimes of temperate and polythermal ice bodies.

The high relative permittivity of water makes it an excellent reflector when using ground-penetrating radar or radio echo sounding, allowing water to be located with ease. Unfortunately this high dielectric constant also causes a lot of noise, and can obscure features other than water that may be being studied.

6.2.3.4 Periglacial, Paleoglacial and Permafrost

Geophysics is not limited to glacierized regions in terms of research value. Ground-penetrating radar and radio echo sounding have been used extensively for the investigation of Periglacial and Paleoglacial processes. One of the major uses has been detecting and determining the structure of permafrost (Vonder Muhll and others, 2002, Rossiter and others, 1975, Annan & Davis, 1976, Davis and others, 1976, Moorman and others, 2003, Munroe and others, 2007, Brandt and others, 2007), useful for a variety of reasons from quantifying climate change to the sighting of pipelines or communications.

In addition to mapping the location of, and structures in, permafrost and frozen ground, it is possible to use geophysical techniques to detect the location of ice deposits in otherwise unfrozen ground (De Pascale and others, 2008). This is a useful tool for civil engineering and construction projects in high latitude regions that may not be completely frozen, but are cold enough to have pockets of ice, or ice deposits left behind after a glacial retreat, such as helping to determine the stability of existing buildings and structures (Jorgensen & Andreasen, 2007) and to aid in the siting of new developments.

The architecture, stratigraphy and morphology of glacial deposits such as moraines have also been widely studied using ground-penetrating radar (Lonne & Lauritsen, 1996, Sadura and others, 2006, Burke and others, 2010). Sass (2006) and Sass and Wollny (2001) have extended the technique to study the structure of alpine talus deposits in European Alps related to the sub-aerial processes occurring in temperate glacial regions.

6.2.3.5 Geophysics in New Zealand Glaciology

Very little work has been undertaken using geophysical techniques in New Zealand glaciology. Techniques such as ground-penetrating radar, radio echo sounding, or seismic reflection are currently under-used as research tools by New Zealand based glaciologists and glacial geomorphologists.

A limited amount of research has been done regarding the rapid retreat and down-wasting of calving glaciers in Mount Cook National Park. Ground-penetrating radar was used in conjunction with GPS and gravity data on the Tasman Glacier (Hochstein and others, 1995) and Hooker Glacier (Hochstein and others, 1998) to identify changes in ice thickness over time, and so determine rates of down-wasting and retreat.

Depth profiling, or the measurement of ice thickness, is by far the most common use of geophysics in New Zealand glaciology. Ground-penetrating radar has been used to determine ice depth of Franz Josef Glacier (Jol and others, 2004, Watson, 2008), and Tasman Glacier (Nobes & Owens, 1995), whilst Thomson (2005) undertook work on the Tasman Glacier using radio echo sounding. These studies used ice and snow depths primarily in mass balance models. Along with the Tasman Glacier, Nobes *et al.* (1994) used ground-penetrating radar on the Mueller Glacier to study the geophysics of debris covered ice. As previously noted, Appleby *et al.* (2010) undertook structural glaciology investigations on the lower Fox Glacier, utilising GPR.

Some geophysical techniques and field methods have been tested on New Zealand glaciers. For example, Nobes (1999) looked at the directional dependence of ground-penetrating radar antenna, and the effect their varying orientation had on the observed reflection signals from a small area of the Franz Josef Glacier névé.

6.2.4 Common Survey Methods

There are a limitless number of options for geophysical surveys, all dependent on the type, quality and volume of data required, and also the physical and chemical properties of the material or substance that is to be investigated. However, the majority of research

makes use of a small number of survey methods, the main ones being reflection, common mid-point, and borehole.

6.2.4.1 Reflection/Common Offset

Reflection or Common Offset (CO) is the most commonly used survey method for ground-penetrating radar investigations. This is also the only mode of airborne surveys (Hubbard & Glasser, 2005). Common offset uses a separate transmitter and receiver which are kept at a constant separation, approximately equal to the length of the antenna being used. The two antennae are moved along a survey line at a set step distance (Figure 6.2) determined according to the required resolution of the survey data, with small steps for highly defined surveys and larger step sizes for lower resolution results. Smaller step sizes of course, mean a survey line will take longer to complete and so a balance between survey resolution and available time must be achieved.

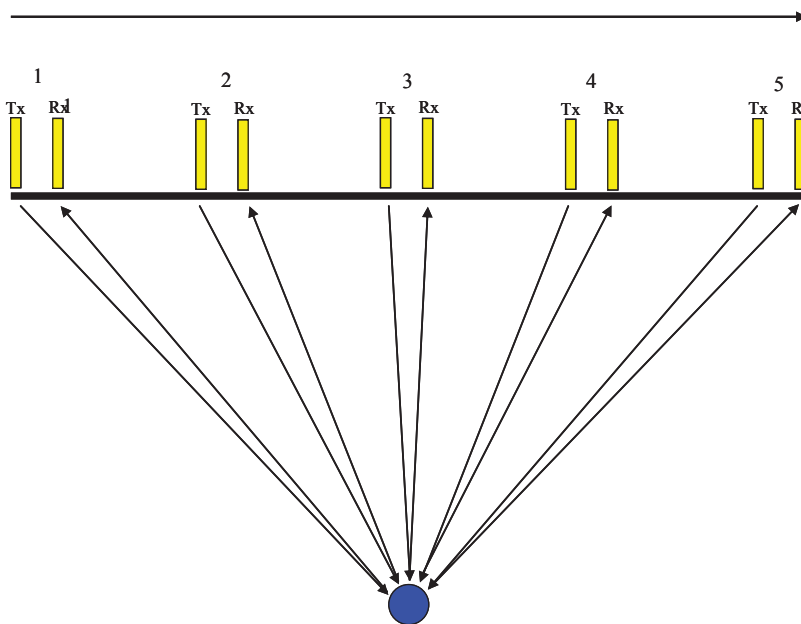


Figure 6.2: Common offset survey in which the transmitter and receiver are kept at a constant separation and moved along the survey line at a constant step size.

6.2.4.2 Common mid-point

Unlike common offset surveys, common mid-point surveys are used to determine radio wave velocity through the study material, rather than determine the depth of a reflector.

For common mid-point surveys, the transmitter and receiver are moved apart at a pre-determined step size above a particular reflector within the study material (Figure 6.3) which acts as a static common mid-point between the two antennae. The changing two way return times for the transmitted radio waves can then be used to determine the average wave velocity. This method is often used to obtain the dielectric constant of a material at the start of a study, so that the depth of reflector can be measured (Eisen and others, 2002).

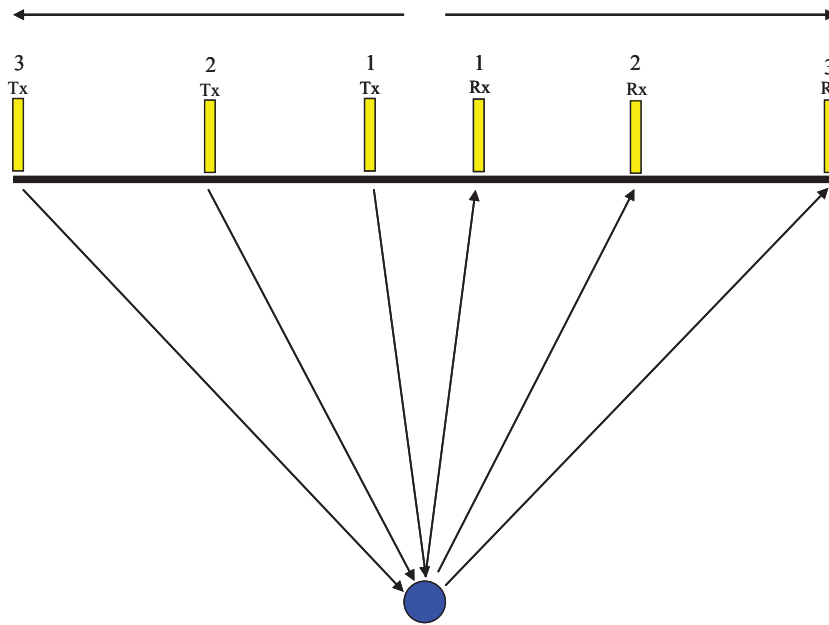


Figure 6.3: Common mid-point survey in which the transmitter and receiver are moved apart at a constant rate to determine the wave velocity through a specified material or substance.

6.2.4.3 Transillumination/Borehole

Transillumination surveys are used to study the transmission properties of a material, and are undertaken by placing the transmitter and receiver on either sides of an object or material. The most common transillumination investigations are borehole surveys. Unlike common offset or common mid-point surveys, bore hole-based investigations use a one-way rather than two-way travel time to identify the dielectric constant of a material or the distance of an object. With borehole surveys, either one antenna is located down the borehole with the other at the surface, or both antennas are located

down boreholes. The one way travel time of radio waves between the two antennas determines the dielectric constant which can then be used to produce a tomogram of the material between either the two bore holes, or the borehole and the surface.

6.2.4.4 Wide Angle Reflection and Refraction

Wide angle reflection and refraction (WARR) surveys are similar to common offset, however the receiving antenna remains in a fixed location, whilst the transmitting antenna is incrementally moved away at a set distance. As with common mid-point, WARR is generally used to determine radar wave velocity through the study material, and so gain an accurate determination of depth.

6.2.4.5 Choice of frequency

Choice of frequency is a trade-off between depth of penetration into the ice by the wave train, and the resolution of the data collected. High frequency antennas collect highly detailed data but penetrate only a short distance, whilst low frequency antennas collect data of a limited detail but penetrate a much greater depth (Table 6.1).

Table 6.1 Approximate depth of penetration and resolution of data detection, according to choice of antenna frequency. This assumes a resolution of $\frac{1}{4}$ the wavelength.

Frequency (MHz)	Depth (m)	Resolution (m)
12.5	50+	6
25	30	3
50	10	1.5
100	5	0.75
200	2	0.375
500	1	0.15
1000	0.5	0.075

The depth of penetration and resolution of detection are only ever approximate, as an almost limitless number of variables effect the behaviour of radio waves in the material. These may include density, water content, temperature, and interference of other

materials. To limit some of the variables, and to gain a broader range of depth and resolution results at the same study site, Matsuoka *et al.* (2002) used a ground-based multi frequency system, which propagates a range of frequencies (one after the other to avoid interference) in rapid succession giving a range of depth and resolution results. Kulesa (2007) has suggested that a change has occurred in the most commonly used range of frequency for ground-penetrating radar investigations, as research moves away from the low frequency depth profiling surveys of Antarctica and Greenland, that first began the use of geophysics in glaciology, to concentrate more on the smaller scale high frequency structural investigations of ice and snow bodies.

6.2.5 Directional Dependence of GPR

It has been noted (Nobes, 1999, Nobes & Owens, 1995, van Overmeeren, 1994) that the type and data of radar reflectivity gained from surveys on temperate glaciers is dependent on the orientation of the antenna relative to the direction of flow of the glacier. Nobes (Nobes, 1999) emphasises the need to consider this directional dependence when planning and undertaking profile data collection, and also when analysing and post-processing the data.

6.3 Methods of Ground-Penetrating Radar Investigation

The quality and validity of results gained from ground-penetrating radar investigations are very much dependent on the quality and type of data gained in the field, and how the data is handled during post processing. Many components of profile interpretation are highly subjective, and so a sound understanding of the ground-penetrating radar technique is required.

6.3.1 Timing of Surveys

GPR surveys were timed to avoid periods of highest ablation and its related meltwater, whilst also avoid excessive snow coverage of the ice surface, which would reduce the depth penetration of the survey by increasing the distance between the transmitting and receiving antennas and the hard-ice structures below. For these reasons, surveys have been completed on Victoria Flat and Fox Glacier terminus area, the lower parts of Fox

Glacier, during July 2009 (Austral winter). Surveys of Fox Glacier Névé were undertaken during January and February 2009 (Austral summer), avoiding winter snowfall.

6.3.2 Survey Type

Reflection surveys were used (Figure 6.4) to acquire ground-penetrating radar data, using the standard method described by *Sensors and Software*, manufacturers of the Pulse EKKO Pro GPR unit. Prior to commencing a reflection survey, the effects of antenna orientation and frequency were investigated according to the variations described by Nobes (1999) and Nobes and Owen (1995), to determine the most appropriate antenna configuration for a reflection survey on Fox Glacier. In addition, a common mid-point (CMP) survey was undertaken to determine an accurate measure of radar velocity for the study areas. The results of the common mid-point survey are used in combination with parabola analysis to determine an accurate measure of depth for features identified in radar profiles.



Figure 6.4: Pulse EKKO Pro ground-penetrating radar unit being used to identify englacial structures on a part of Fox Glacier Névé using common-offset reflection surveys. (Photo: J. Appleby, January, 2009)

6.3.3 GPR Parameters

A Pulse EKKO Pro GPR unit manufactured by *Sensors and Software* was used during ground-penetrating radar investigations into the englacial structure of Fox Glacier. A number of antennae were used, with frequencies ranging from 25 MHz to 100 MHz, each with specific separation and step-size values ranging from 1 m separation and step size of 0.25 m for 100 MHz antennas to 4 m separation with a 1 m step size for 25 MHz antenna. For each antenna a standard set of collection parameters was used. These were: an assumed radar velocity of 0.160 m/ns; a system stacking of 32; a pulser setting of 1000 V Pro; and an AGC gain type. GPS data was set to record with every trace, using a baud rate of 9600.

6.3.4 Post-processing of Data

Post-processing of data was undertaken using *EKKO View Deluxe* software from *Sensors and Software*. Post-processing is done with the aim of clarifying ground-penetrating radar profiles by reducing unwanted ‘noise’, magnifying the reflection signal of structures within the ice, and reducing the distorting effect of scattered hyperbola energy. Most post-processing tools do not change the raw data, but change how it is displayed in the GPR profile.

6.3.4.1 Filtering

Filtering of profile data can help remove unwanted noise that may obscure data from reflections we wish to study. Unwanted noise can be particularly prevalent in temperate glaciers such as Fox Glacier, which often contain large volumes of melt water, scattering radar signals, and providing false reflections. Dewow filtering is the filter type most commonly used in this research. The radar signal transmitted during data collection sometimes induces a low frequency ‘wow’ on the trace caused by the electrical field produced from the relative proximity of the transmitter and receiver, along with the electrical conductivity of the ground. Dewow filtering (or signal

saturation correction) removes unwanted, low frequency noise whilst retaining high frequency signals produced from reflectors.

6.3.4.2 Gain

Signal strength or amplitude of radar signals decreases with increasing distance from the transmitter because of spherical divergence and geometric spreading according to Reynolds (1997). Gain alters the amplitude of the signal to enhance the strength of reflectors from features at depth.

A number of gains are available including constant gain, spreading and exponential compensation (SEC), autogain, and automatic gain control (AGC). Automatic gain control can be selected when setting up GPR parameters and acquisition control at the time of data collection, and attempts to equalize all signals by finding the average amplitude of a number of points along a set length of each trace. AGC has been applied to each trace in this research at the time of data acquisition.

6.3.4.3 Migration

One of the most obvious features of a GPR profile is the presence of hyperbola at the location of reflecting features within the glacier. These hyperbolas represent the distorting effects of diffraction and interference caused by scattering of energy due to the ‘cone-shaped’ radar signal received by a reflector. As the radar signal is refracted around an object or feature, the receiver ‘sees’ the object for an extended length of time rather than at a single point, as the signal passes the object, giving a spatially incorrect or diffuse position, and an incorrect idea of object size. Migrating data reduces the diffusion of a reflectors signal, flattening or completely removing the hyperbola, giving a much more accurate size and location of features.

6.3.4.4 Applying Topography

Topographic data were acquired at the same time as GPR profiles using a Trimble R8 RTK GPS Rover. The Rover was set to output NMEA GGA data strings giving three dimensional x , y , and z data for each trace. For example,

```
$GPGGA,142803,4407.020,S,17233.000,E,1,09,0.6,621.1,M,51.9,M,*46
```

Where:

GGA	Global Positioning System Fix Data
142803	Fix taken at 14:28:03 UTC
4407.020,S	Latitude 44 deg 07.020' S
17233.000,E	Longitude 172 deg 33.000' E
1	Fix quality: 0 = invalid
	1 = GPS fix (SPS)
	2 = DGPS fix
	3 = PPS fix
	4 = Real Time Kinematic
	5 = Float RTK
	6 = Estimated (dead reckoning)
	7 = Manual input mode
	8 = Simulation mode
09	Number of satellites being tracked
0.6	Horizontal dilution of position
621.1,M	Altitude, Meters, above mean sea level
51.9,M	Height of geoid (mean sea level) above WGS84 ellipsoid
*46	Checksum data

During post processing, the GPS data recorded with each trace can be applied to the GPR line data (Figure 6.5) to display the topography of the area being studied. This allows for a better appreciation of the position and size of reflectors relative to other features and the slope of the glacier.

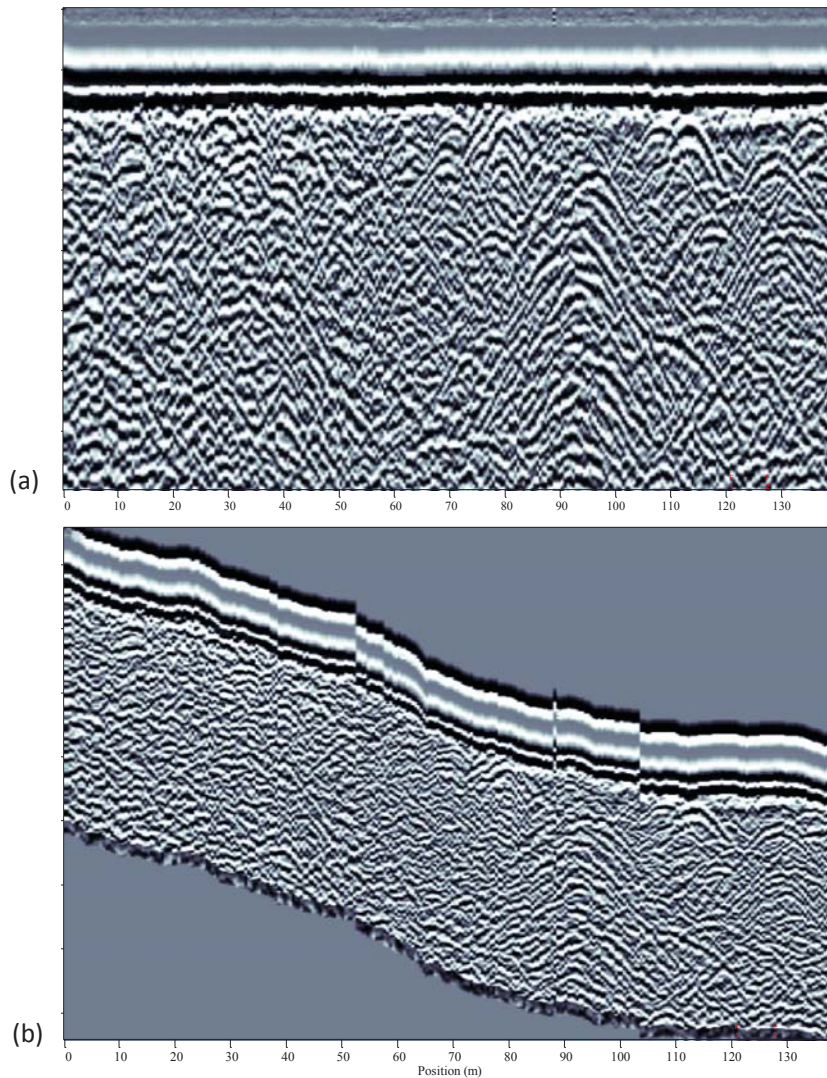


Figure 6.5: (a) Unformatted GPR profile from the lower Fox Glacier and (b) the same profile with GPS derived topographical data applied.

6.3.5 Presentation of Results

Two dimensional profiles are created using EKKO View Deluxe, and are used to display englacial structure derived from ground-penetrating radar investigations. Profiles are conventionally displayed with three axes: Position in meters along the transect; two-way travel time of radio waves in nanoseconds (ns); and depth according to known radar velocity established from common mid-point surveys and parabola analysis. In addition to the EKKO View Deluxe profile, a visual interpretation of the

identified features can be provided to clarify the location and help explain the type of structures present.

6.4 A Ground-Penetrating Radar Survey of Fox Glacier

Structures have been interpreted using a combination of two methods: (1) comparisons with previous GPR analyses of structures in snow and glacier ice (Yamamoto and others, 2004, Machguth and others, 2006, e.g. Goodsell, 2005, Woodward, 1999, Kohler and others, 1997, Goodsell and others, 2005b); and, (2) comparison of GPR radargrams with surface features identified in the vicinity of the GPR transect locations, such as thrust faults and crevasses. For this research, a Sensors & Software *PulseEKKO Pro* GPR unit was used in bistatic mode according to Sensors & Software Inc. (Anonymous, 2003).

6.4.1 Calculation of Radar Velocity

A radar velocity of 0.165 m/ns was applied to the ground-penetrating radar system set-up in the field during data collection. This is the mid-point for standard radar velocities in ice (0.16 to 0.17 m/ns) as determined by *Sensors & Software* (Anonymous, 2003), and is used to gain an approximate measure of reflector depth whilst in the field. This is supported by Hubbard and Glasser (2005) who suggest radar velocities in temperate, wet ice will be slightly lower than their measured average velocity of 0.167 m/ns. In addition, two further techniques were used to determine radar velocity specific to snow and ice conditions in Fox Glacier: (1) common mid-point (CMP) (e.g. Greaves and others, 1996) and, (2) calibration of hyperbola (e.g. Olhoeft, 2002, Schwamborn and others, 2008, Olhoeft, 2000). CMP was used in the field to collect data for determination of radar velocity, whilst calibration using hyperbola was used to determine radar velocity during post processing of data.

6.4.2 Antenna Orientation Effects

In addition to radar velocity, the most appropriate antenna orientation was determined prior to undertaking common offset surveys of Fox Glacier. It has been postulated (e.g. Nobes, 1999, Nobes & Annan, 2000, Lutz and others, 2003) that antenna orientation

can have a considerable influence on the quality of the GPR profiles obtained. To test this hypothesis, a survey was undertaken along a transect using various antenna orientations to determine the potential influence antennae orientation may have on the data collected (Figure 6.6). Each profile was obtained along the same 20 m transect line using the same 100 MHz antenna, with the only variation being the orientation of the antenna.

Although some reflectors are obvious in all of the profiles, the strength of the reflection does appear to vary considerably with antenna orientation. Differences are observable between the two cross-polarisation methods, whereby the electromagnetic poles of the two antennas are oriented at a 90° angle to each other. Whilst there are similar results in terms of identifiable reflectors in the upper part of the two cross-polarisation radargrams, noticeable variation can be observed in the lower parts, where reflectors appear much more defined when the transmitter and receiver are oriented parallel and perpendicular respectively. Higher resolution reflectors were also observed in the lower part of radargrams rather than the upper part by Nobes (1999).

Both of the cross-polarisation methods produce more detail at depth than the two broadside methods, which appear to produce lower resolution images of smaller scale features. In contrast, a number of larger scale features are obvious on the radargrams produced using the broadside methods but are absent on those produced from the cross-polarisation configurations. Travassos and Simões (2004) describe an increase in noise and clutter, severely limiting the effectiveness of radar surveys, when using perpendicular-broadside rather than parallel-broadside, although this has not been observed during this research. All four methods give a depth of penetration to approximately 11 metres, suggesting little or no influence on the depth of penetration achievable from each of the four orientations.

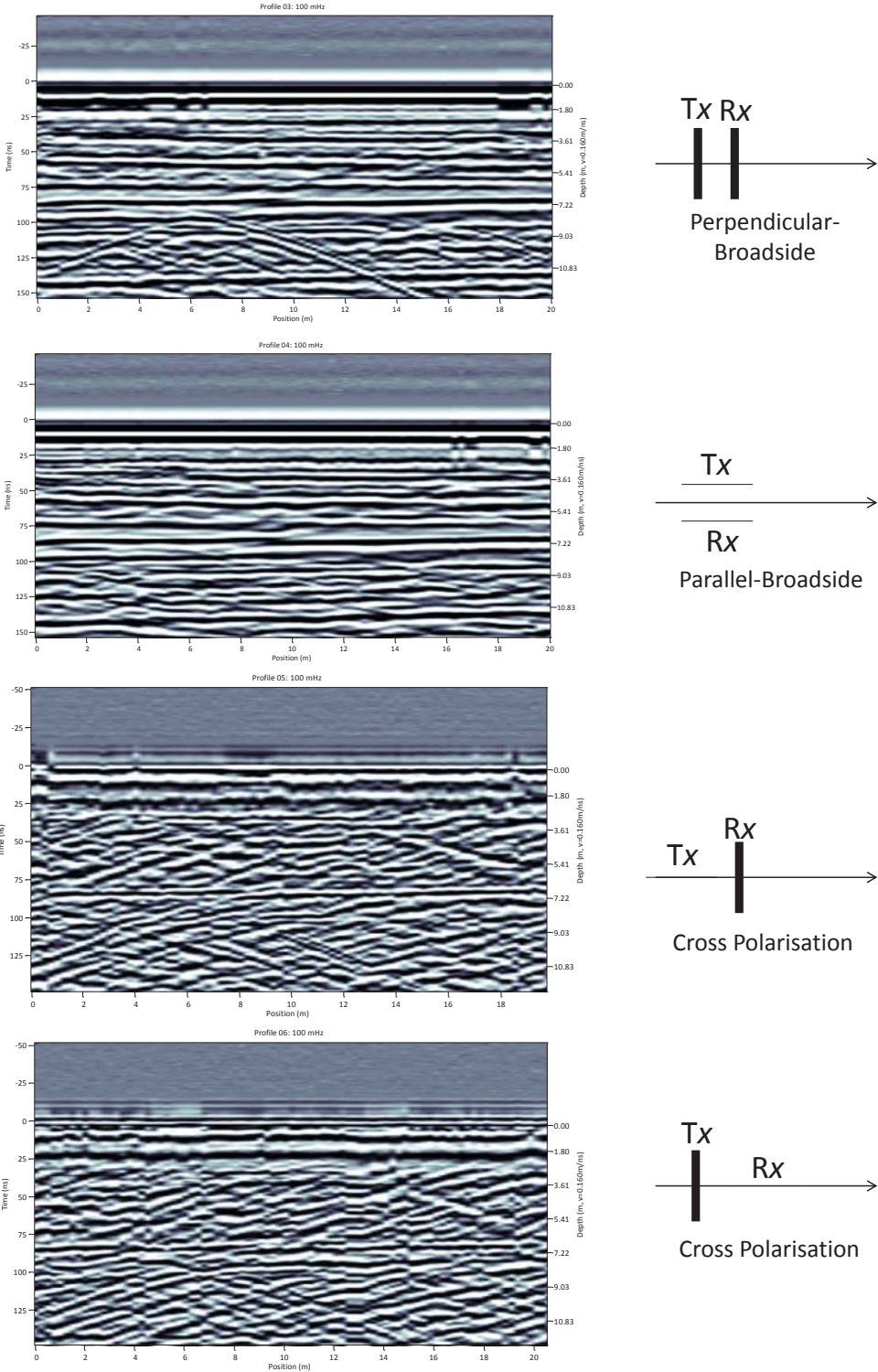


Figure 6.6: Varying profiles produced from the same 20m transect using a 100 MHz antenna, according to antenna orientation. Profile letter (A, B, C or D) relates to the corresponding antenna orientation shown according to relative position along the transect line. Orientation A is the conventional method as described by Sensors & Software Inc. (Anonymous, 2003). Transmitter and receiver are represented by Tx and Rx respectively.

For the following surveys, the conventional perpendicular “broadside” method suggested by Sensors & Software Inc. (Anonymous, 2003) and Jol (1995) was chosen as the most appropriate method to identify major englacial features and produce the most useful data for this research. Broadside antenna orientation provides the most energy in the direction of the survey transect, reducing reflections from targets to the side of the survey line, enabling a ‘clearer picture’ of the englacial features present in the areas of particular interest identified during this study. In addition, Radzevicius *et al.* (2000) suggest that “rotating ideal dipole antennas” (cross polarisation) results in a “polarisation mismatch” and are therefore not commonly used in GPR investigations.

6.4.3 Post-Processing of Data

Before interpretation of GPR profiles was undertaken, post-processing of the raw GPR data was completed to help amplify certain reflectors and remove ‘noise’ by filtering. A combination of processes and recipes was applied to each profile according to the level of noise and the type and quality of reflectors. The specific processes included in the recipes are briefly outlined below.

Dewow, or signal saturation correction filtering was applied to all of the profiles to remove unwanted low frequency interference created by the close proximity of the transmitting and receiving antennae to one another, while preserving high frequency reflections. Dewow filtering is pre-set at an optimized level in the *EKKO View Deluxe* software to produce a ‘compromise’ filter which removes a sufficient amount of interference without losing too much useful data or producing too many unwanted artefacts. In addition to dewow filtering, bandpass filtering has also been used to remove the considerable noise recorded in the profiles. Bandpass filtering allows the enhancement of desired signals (e.g. reflectors) within certain portions of the radio frequency spectrum whilst removing the unwanted noise portion of the spectrum.

Topography shift has been applied to permanently shift traces up and down according to surface topography data acquired using GPS at the time of data collection. This allows for a better understanding of the proper spatial positioning and orientation of radar reflectors. Text files containing topographic data are added to the elevation field of each GPR trace during collection, and then applied during post-processing.

Gains have been applied to boost weaker signals at depth, as ungained data is likely to show little signal except for the stronger near-surface reflectors. The main gain type applied was Automatic Gain Control (AGC) which attempts to equalize all signals (strong and weak) but loses the ability to deduce the strength of one reflector relative to another. In addition, constant gain was also used for some of the profiles, whereby a constant factor is applied to all traces and all data points are multiplied by this factor. This will amplify both strong and weak signals and retains information about the relative strength of each reflector, but can ‘over-gain’ the strongest shallow reflector signals.

Finally, migration has been used to focus scattered signals and concentrate them on their point of origin. This process has been helpful in collapsing some hyperbolic reflectors, effectively converting them into point source reflectors, giving a more accurate indication of the size and location of individual features.

6.4.4 Locations of GPR Profiles

Given the considerable length (~11.5 km) of Fox Glacier, GPR transect locations were chosen to provide a representative sample of the range of englacial structures likely to be present at Fox Glacier, from the névé to the terminus. Surveys were undertaken in key, accessible areas along the length of the glacier (Figure 6.7) from the upper parts of the névé, through Victoria Flat, to the lower tongue of the glacier. The aim here was to identify changes in internal structure as ice descends through the Fox Glacier system. Some areas (e.g. Upper-, Lower-, and Pioneer Icefalls) were unable to be surveyed due to topographic restrictions such as crevassing and steep surface slopes, along with limited access and the risk of rock fall and avalanching in some areas.

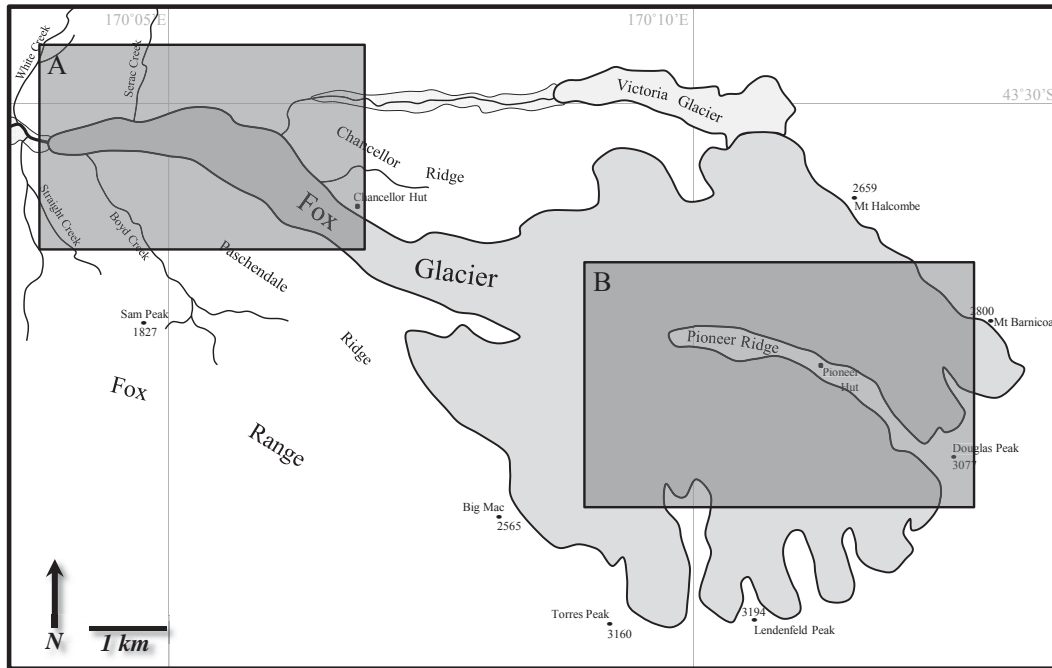


Figure 6.7: Map showing the locations of ground-penetrating radar surveys undertaken on Fox Glacier: A) the Lower Glacier & Victoria Flat, and B) Fox Glacier névé.

6.4.5 Common Offset Surveys

The very distinct black, white and grey banding at the top of each of the profiles is interpreted as an air and ground wave reflection (e.g. Sun & Young, 1995) and so is discounted as a structure of interest. The lower boundary observable in profiles V1-V3, and L1-L3 is interpreted as the maximum depth-of-penetration for the GPR antennas rather than the ice-bed interface. This boundary line is produced during the shifting of topography and is deformed in line with the surface topography. Previous work (e.g. Jacobel and others, 2009, Mottram and others, 2009, Welch and others, 1998) has produced radargrams showing a distinct ice-bed interface with continuing reflectors below this level indicating bedrock or subglacial sediment; this has not been observed on Fox Glacier radargrams.

6.4.5.1 Fox Glacier Névé

GPR surveys were undertaken on the two main tributary glaciers that constitute the Fox Glacier névé: the Explorer Glacier and the Albert Glacier (Figure 6.8). These surveys were undertaken during March 2009 at the end of the Austral summer, so as to avoid winter snowfall in the névé and to increase the depth of penetration into the hard-ice and firn layers of the glacier. The chosen survey locations are characteristic of névé areas where the surface remains mostly unbroken by crevasses (Figure 6.9). Small (<2 m wide) snow-filled crevasses are evident in the area but the surface remains largely structureless.

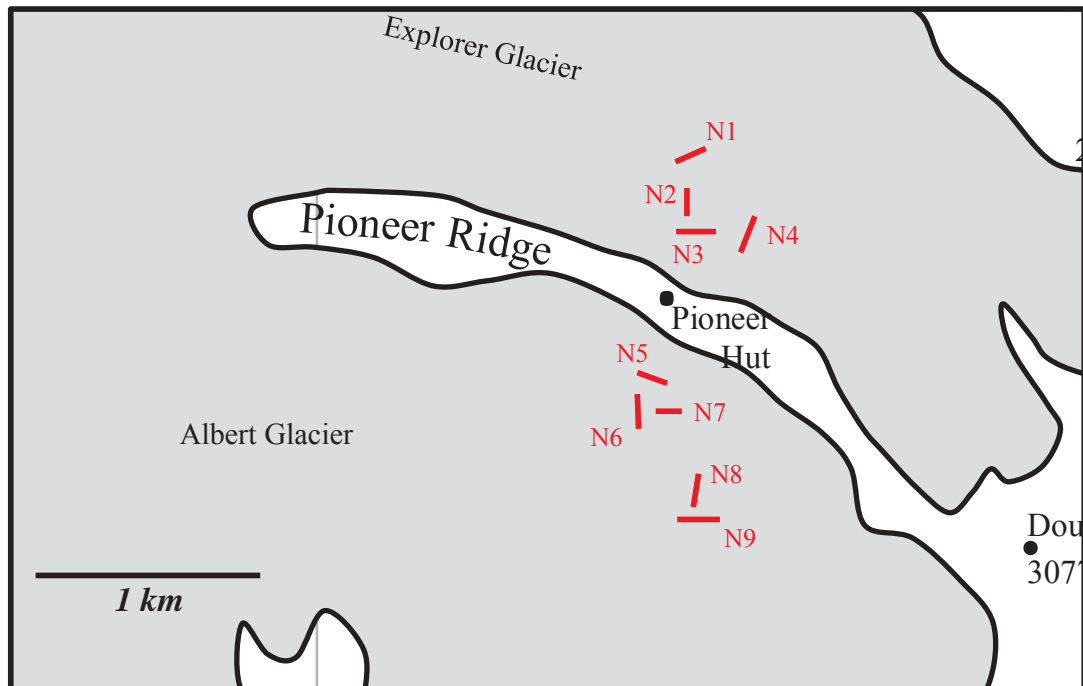


Figure 6.8: Location of GPR Transects undertaken on Fox Glacier Névé. Transect names correspond to profiles N1 to N9 as shown in Figures 8.5 to 8.8.

Profile N1 (Figure 6.10) exhibits a parallel reflector at ~ 7 m depth (a) interpreted as the interface between snowfall events, or seasonal variation in precipitation with a dense summer regelation layer overlain by winter snow, similar to those identified by Machguth *et al.* (2006) on the Findel and Adler Glaciers, Switzerland. Below this parallel reflector, two converging diagonal reflectors (b and c) have been interpreted as the sides of a ~ 3 m deep, snow-filled depression or crevasse.

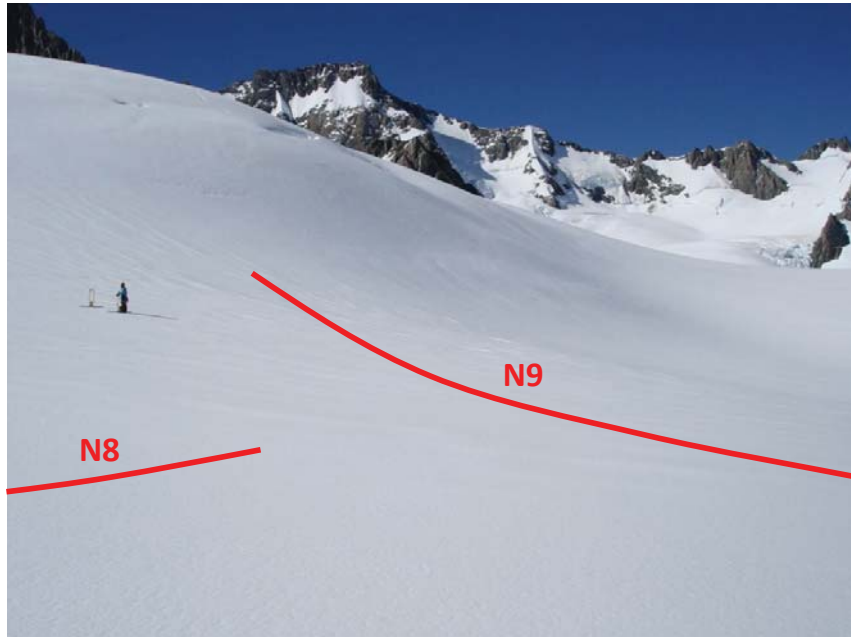


Figure 6.9: Approximate location of transects N8 and N9 as an example of the surface of the Fox Glacier névé (person for scale). The skyline ridge forms part of the Main Divide of the Southern Alps, with the glacier flowing left to right (east-west) across the photograph. (Photo: J. Appleby, January, 2009)

Profile N2 (Figure 6.11) exhibits a parallel reflector at ~7 m depth (a). This reflector is interpreted as the same reflector identified in profile N1, due to the close proximity of the profiles and matching depth. The cross-cutting of dipping reflectors (b) suggest re-working and overlaying of regelation layers and snow event records.

Profile N3 (Figure 6.12) and Profile N4 (Figure 6.13) exhibit a number of parallel reflectors at regularly spaced depths. These parallel reflectors have been interpreted as the interface between snowfall events, or seasonal variation in precipitation with a dense summer regelation layer overlain by winter snow. The lowermost reflector in both profile N3 and N4 shows a break in continuity (a). These breaks may be due to a weakly-reflecting area being removed during noise filtering and post processing, or may be an actual break in the englacial layer.

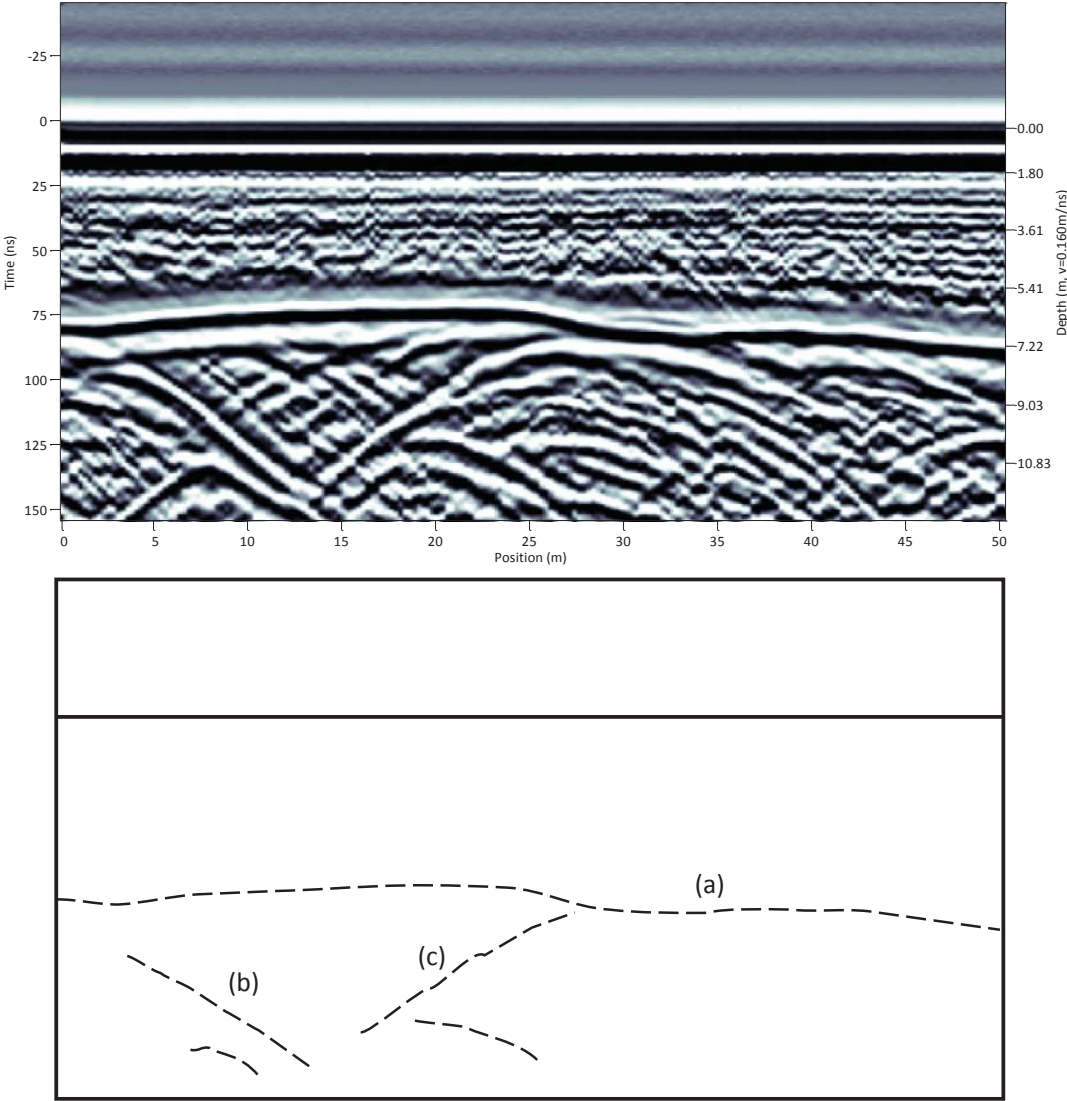


Figure 6.10: Interpreted ground-penetrating radar profiles N1, showing parallel (a) and dipping (b and c) reflectors.

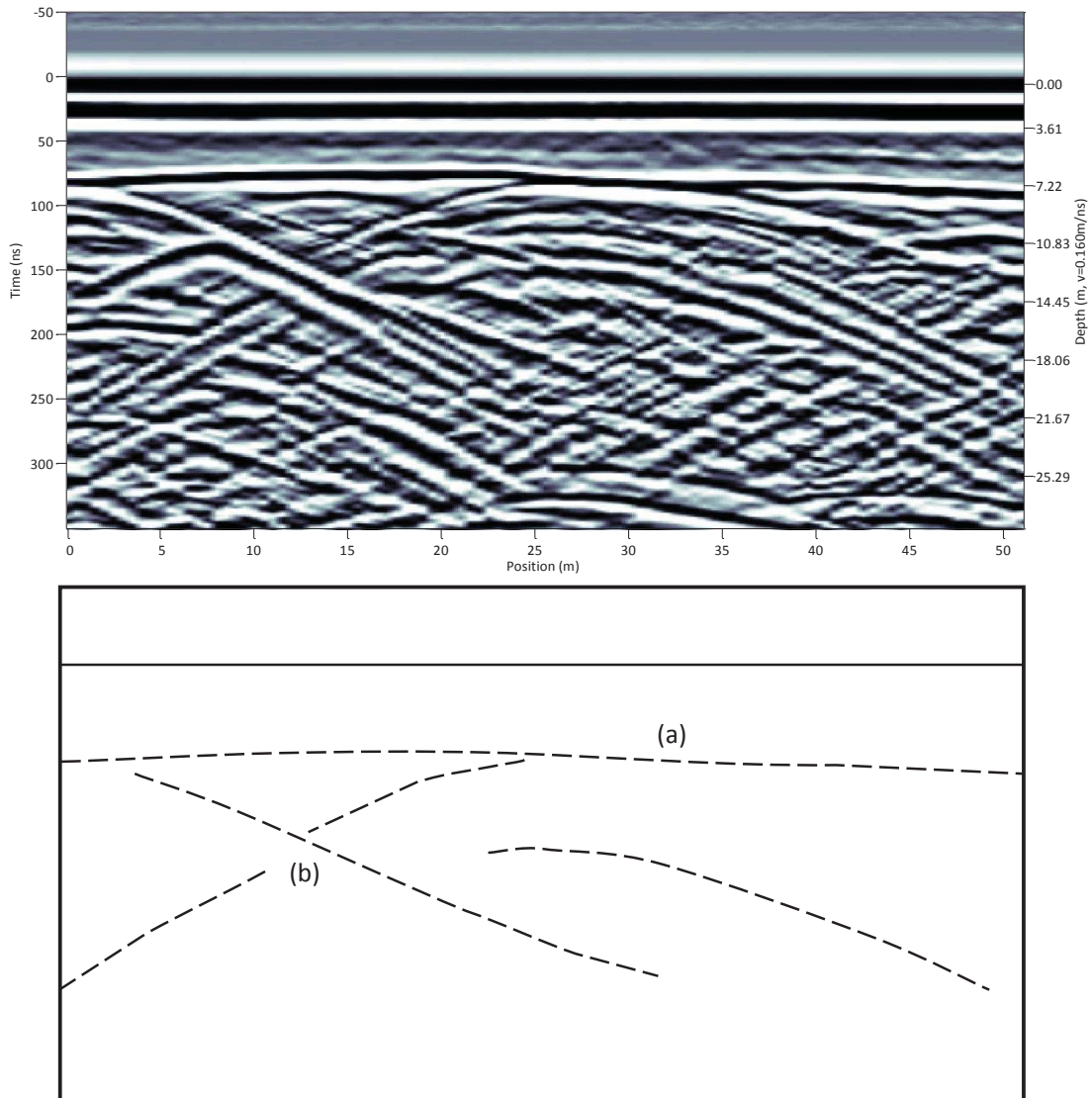


Figure 6.11: Interpreted ground-penetrating radar profiles N2, showing cross-cutting dipping reflectors (b).

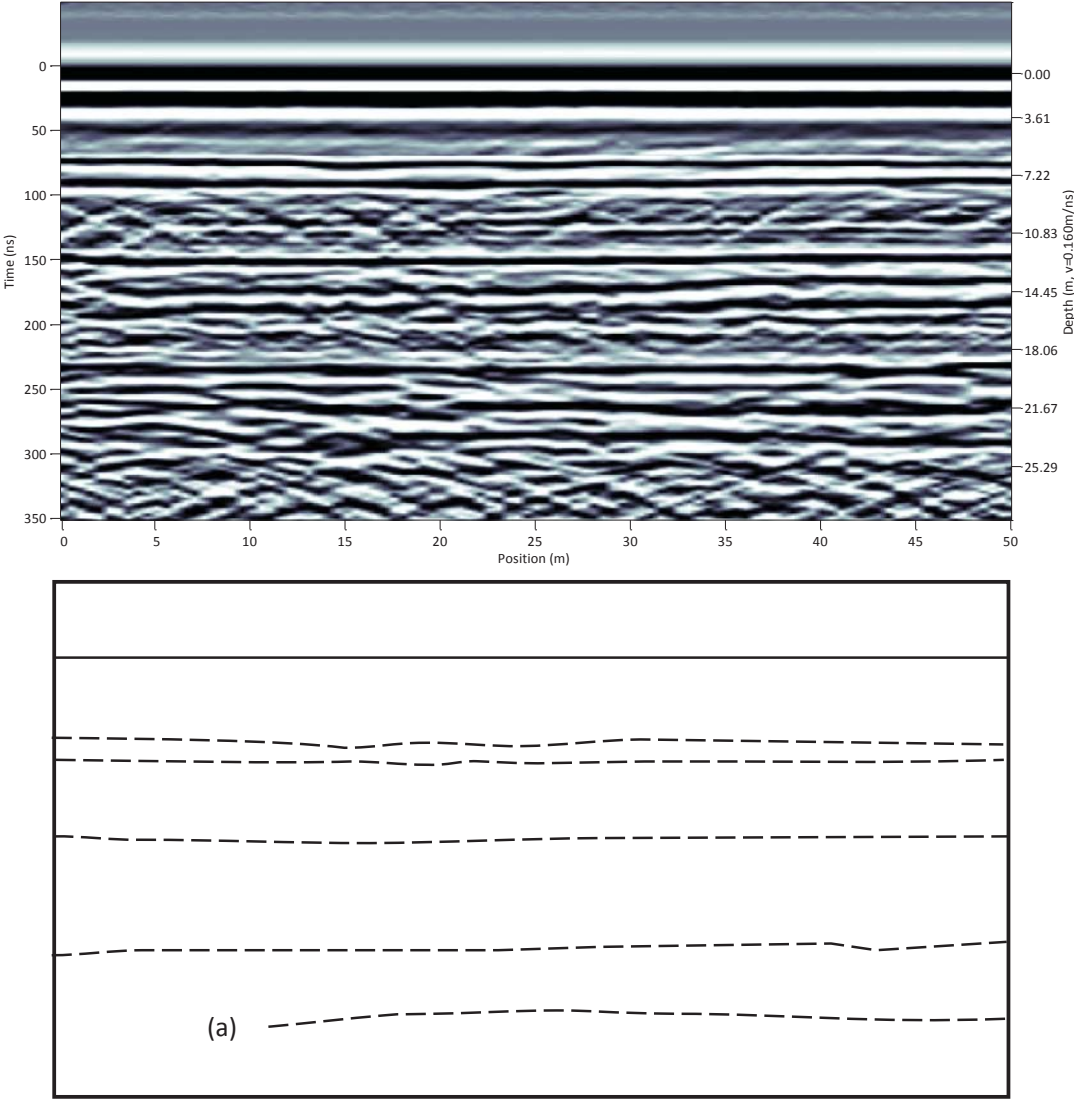


Figure 6.12: Interpreted ground-penetrating radar profiles N3, showing various parallel reflectors.

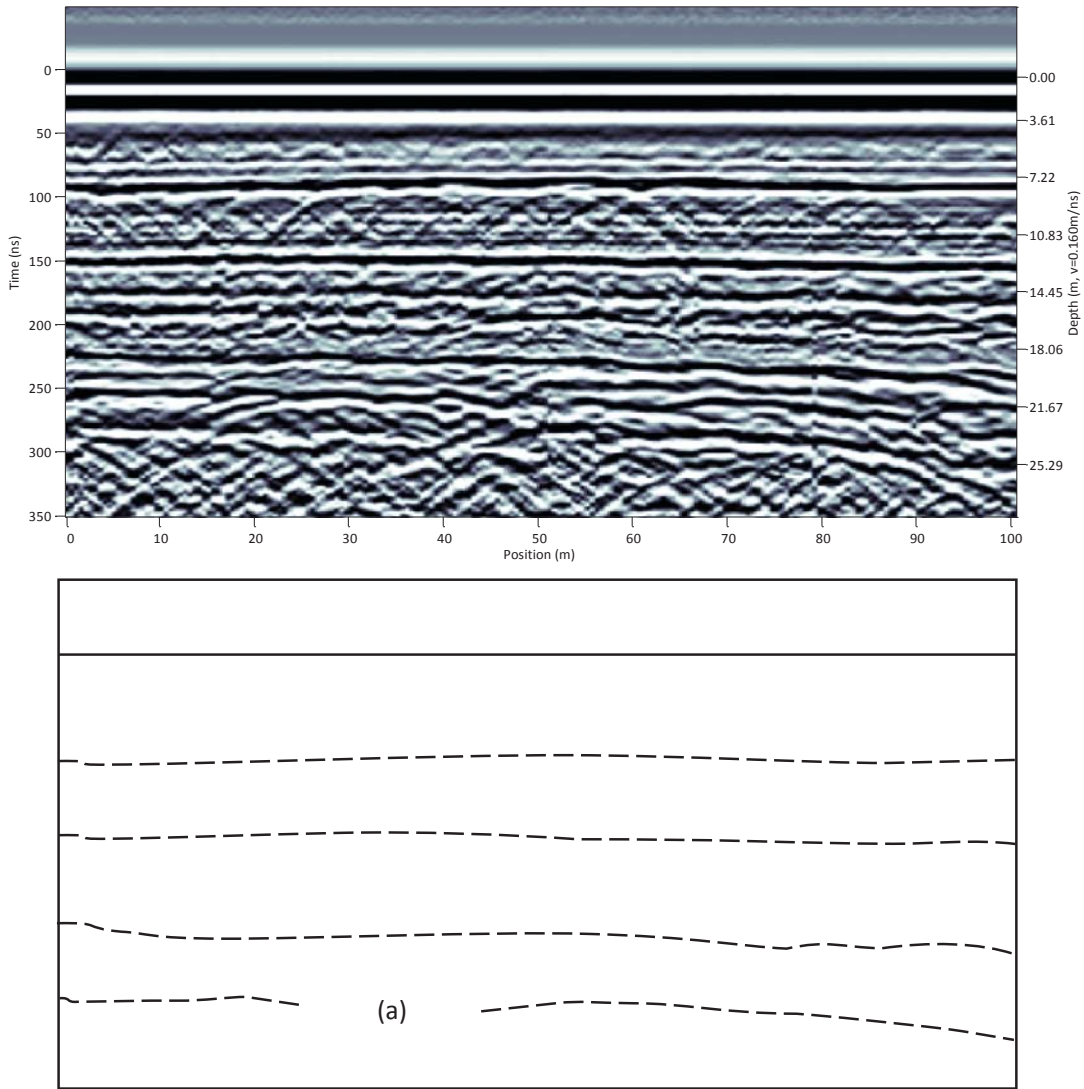


Figure 6.13: Interpreted ground-penetrating radar profiles N4, showing broken parallel reflectors (a).

Profile N5 (Figure 6.14) exhibits closely-spaced parallel reflectors interpreted as annual stratification. A break in reflectors is seen (demarcated by dotted line) (a) running diagonally left from ~18 m depth to below ~25 m depth and can be interpreted as a transverse incipient crevasse, cross-cutting and displacing annual stratification.

Profile N6 (Figure 6.15) shows more widely spaced primary stratification reflectors. A small number of parabolic reflectors (a) are identified immediately beneath the upper layer of primary stratification at ~7 m depth and may be interpreted as distinct reflectors such as clasts of material introduced to the neve surface during rockfall events.

Profile N7 (Figure 6.16) shows parallel reflectors interpreted as primary stratification caused by annual snow layers. Some sections of reflectors are not clearly visible in the radargram, and may be actual disturbances in the stratification or just an artefact of post processing.

Profile N8 (Figure 6.17) shows a strong reflector at ~3 m depth, beneath which is a gap of ~4 m (a) before closely spaced parallel reflectors (b) resume and continue to the deepest part of the profile at ~11 m. This gap in reflectors may represent internal structure caused by a major precipitation event such as a period of heavy snow fall, or a snow avalanche onto the névé surface.

Profile N9 (Figure 4.18) exhibits 3 major parallel reflectors at approximately 2 m, 7 m, and 11 m depth. Between these 3 main reflectors can be seen a number of less obvious parallel reflectors. The reflectors identified in profile N9 are interpreted as primary stratification formed by layering in the snowpack. The stacked reflector at ~50m (a) is interpreted as an incipient crevasse.

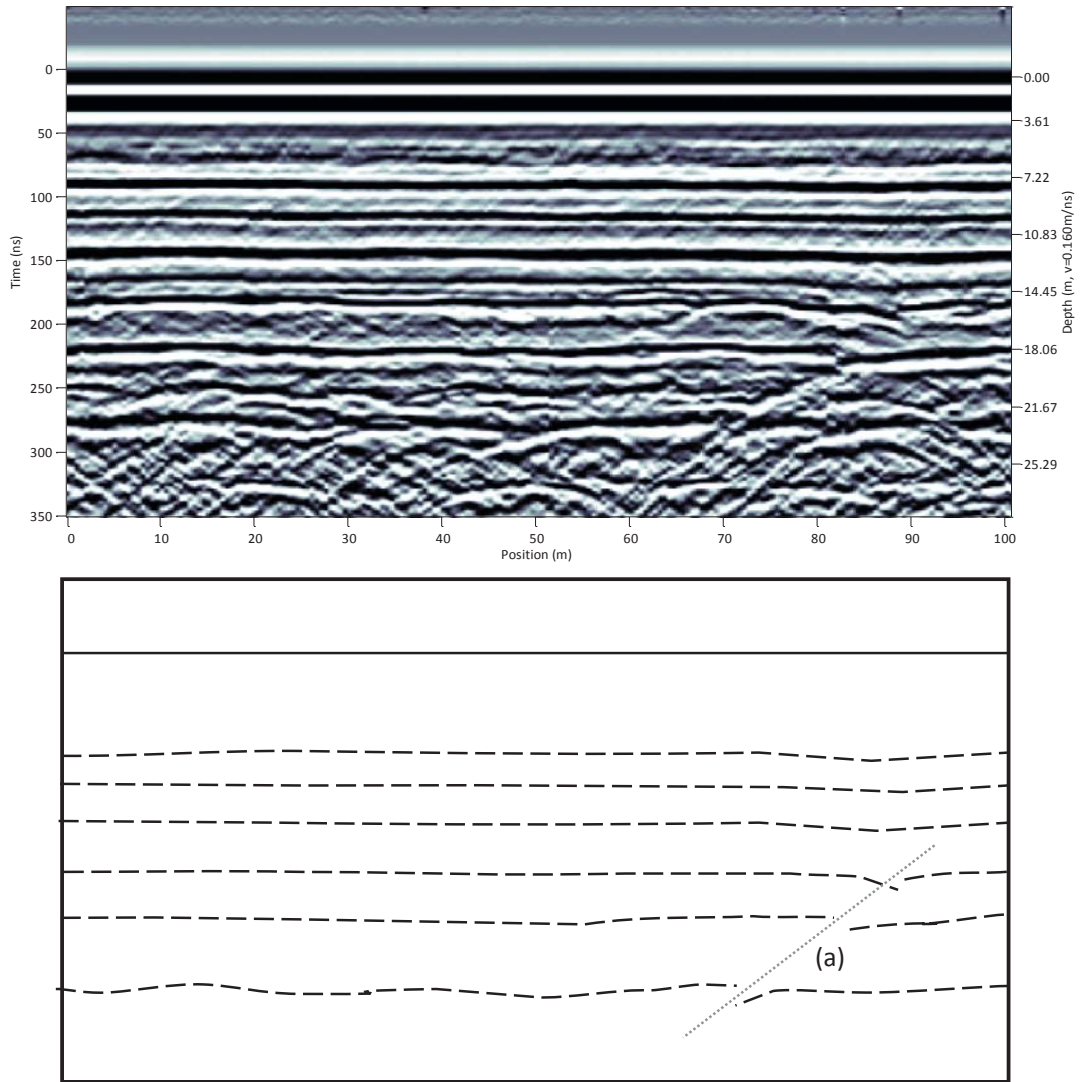


Figure 6.14: Interpreted ground-penetrating radar profiles N5 collected on the Albert Glacier, showing displaced parallel reflectors (a).

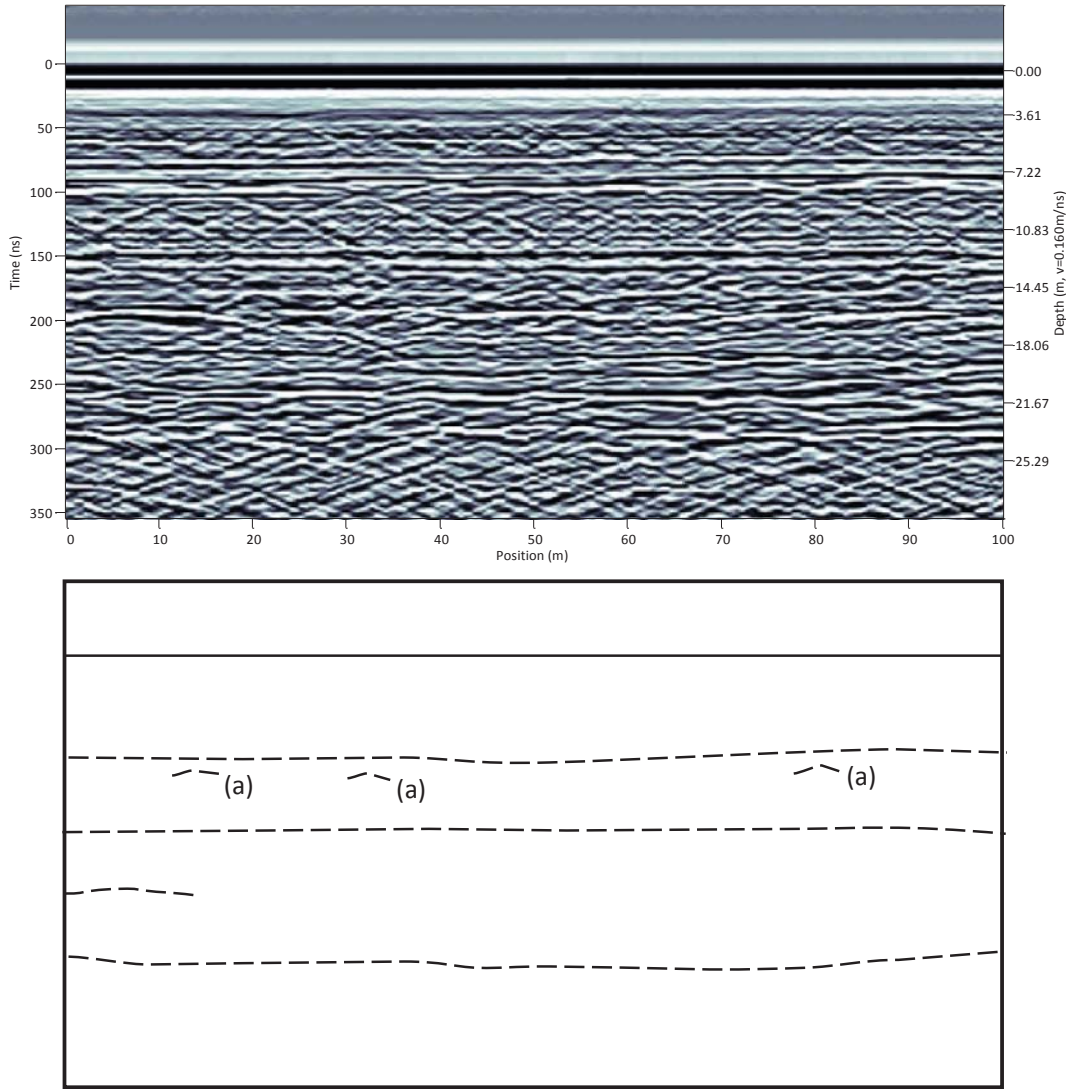


Figure 6.15: Interpreted ground-penetrating radar profiles N6 collected on the Albert Glacier, showing parallel reflectors interspersed with point reflectors (a).

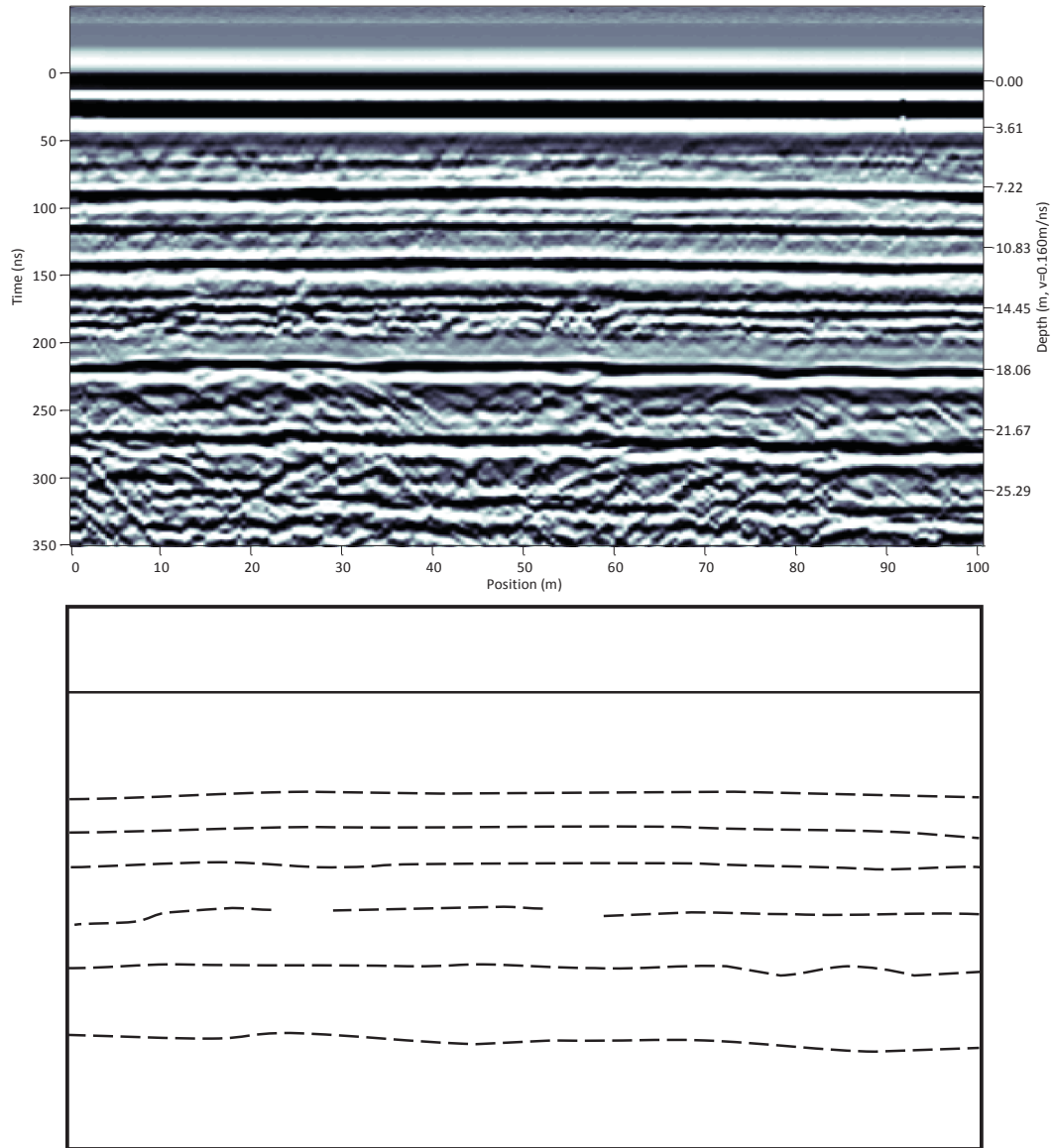


Figure 6.16: Interpretation of ground-penetrating radar profile N7, showing parallel reflectors.

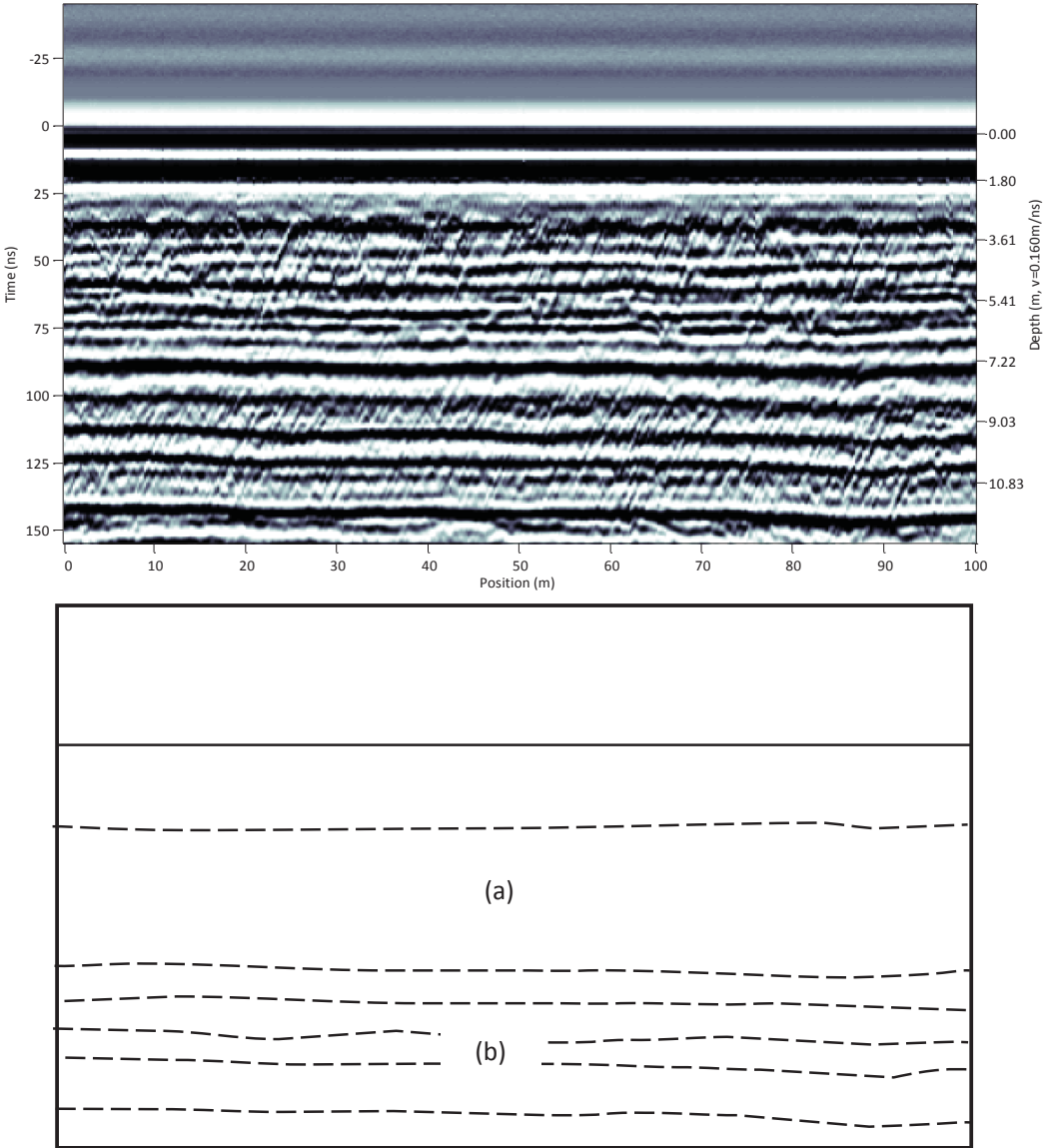


Figure 6.17: Interpretation of ground-penetrating radar profiles N8, showing a large-scale layering event (a), above closely-spaced parallel reflectors (b).

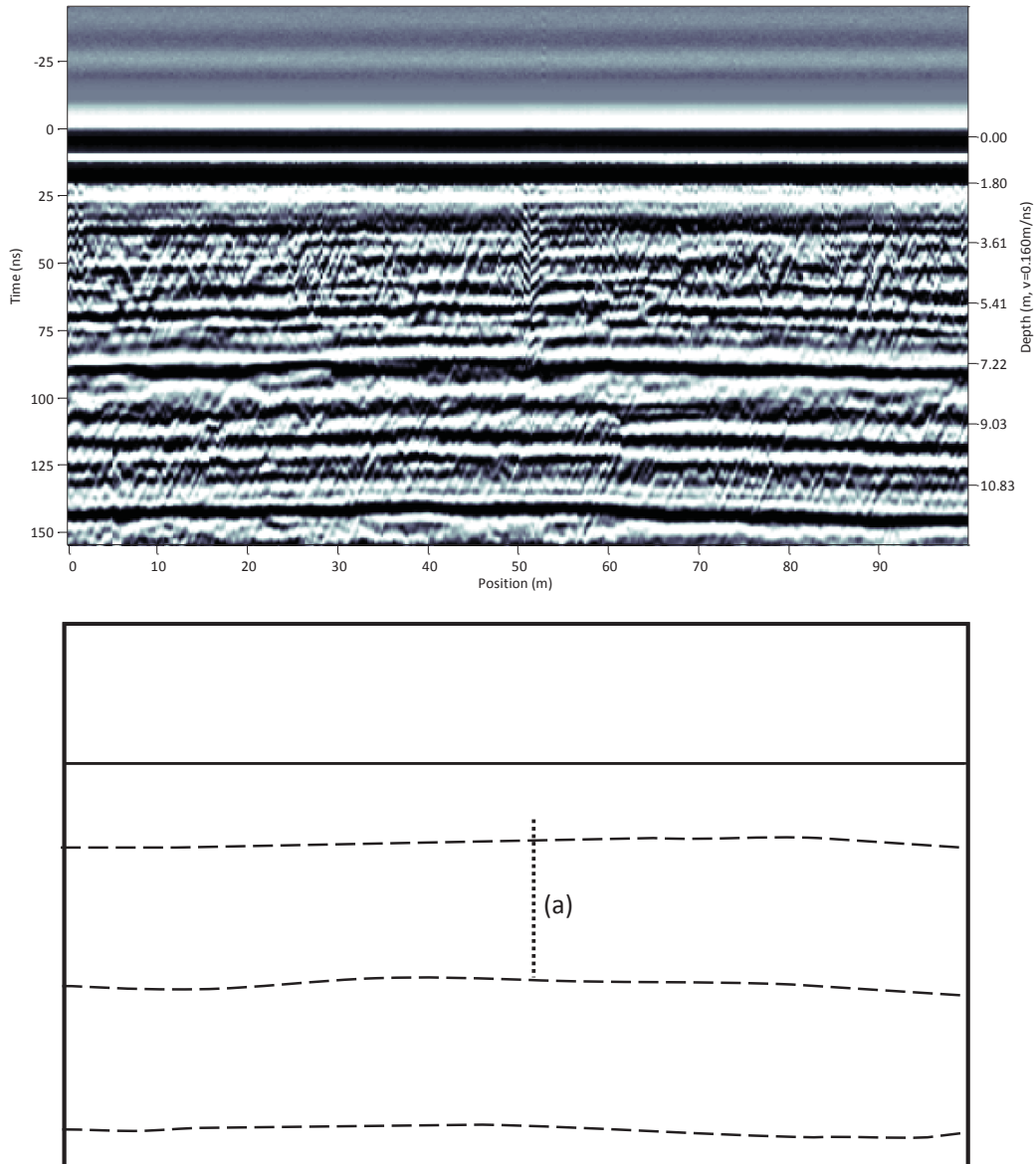


Figure 6.18: Interpretation of ground-penetrating radar profile N9, showing widely-spaced parallel reflectors and an incipient crevasse (a).

The ground-penetrating radar profiles presented above, show that the Fox Glacier névé is characterised by obvious primary stratification in the snowpack with very few disturbances in this layering. The depth between annual layers varies with each radar profile, with distances between layer boundaries ranging from ~ 0.2 m to >1 m. These patterns of marked spatial variation identified in radargrams, and also observed in exposed crevasse walls (Figure 6.19), are supported by Purdie *et al.*, (2011a, 2011b), who describe variations in spatial distribution and annual net accumulation across the névé of neighbouring Franz Josef Glacier, identified from crevasse stratigraphy studies.

The absence of parabolic reflectors within most of the profiles suggests little internal deformation structures such as folding, faulting, crevassing, or the presence of englacial conduits at this elevation (~ 2450 m). This is supported by the subdued surface topography in the survey areas which displays few undulations or disturbances, and a relatively low density of surface structures such as crevasses (Figure 6.20).



Figure 6.19: Primary stratification created by annual layering, observed in exposed crevasse walls in the Fox Glacier névé. (Photo: J. Appleby, January, 2009)



Figure 6.20: Low density, incipient transverse crevasses observed on the glacier surface at the head of the Albert Glacier. These crevasses are identified in GPR radargrams N2 as dipping reflectors. (Photo: J. Appleby, January, 2009)

6.4.5.2 Victoria Flat

GPR surveys were undertaken on Victoria Flat, the area of subdued surface topography between the upper and Lower Icefalls (Figure 6.21). The survey was undertaken in July 2009 during the Austral winter, so as to avoid summer melt water on the surface of the glacier which would potentially interfere with radar signals due to the high electrical conductivity of water (Saarenketo, 1998, Murray and others, 2007b, Farzaneh and others, 2007). Survey locations were chosen to avoid supraglacial ponds (Figure 6.22) formed due to freezing of moulins and englacial conduits during winter. At between 640 and 1040 m asl, Victoria Flat is below the current ELA (~1800 m, Appleby and others, 2010) and so winter snowfall would be less likely to pose any issues during the survey period. The surface of Victoria Flat is characterised by a dense network of crevasses and crevasse traces (Figure 6.23), giving an indication of internal structure and allowing the possibility of ‘ground-truthing’ of radargrams.

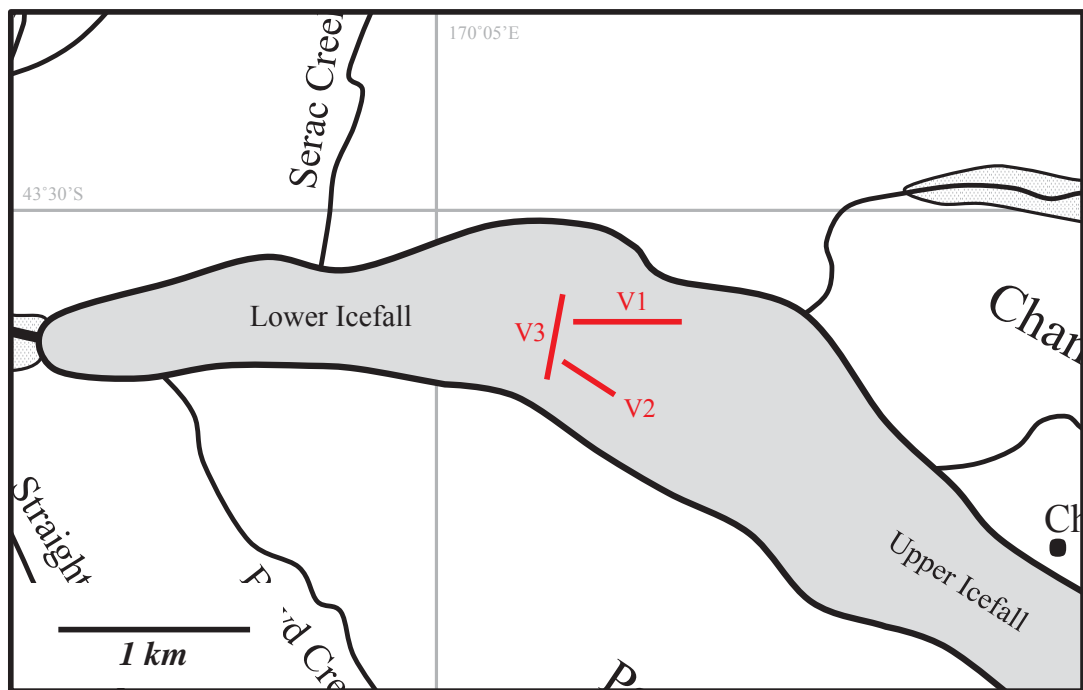


Figure 6.21: Location of GPR Transects undertaken on Victoria Flat. Transect names refer to transects V1 to V3 as shown in figures 6.24 to 6.26.



Figure 6.22: Approximate location of transect V1 (red line) as an example of Victoria Flat GPR study area. The view is towards the true left valley side with the glacier flowing left to right across the photograph. GPR transects were located so as to avoid interference from supraglacial pools and slush ponds such as those pictured. (Photo: J. Appleby, July, 2009)



Figure 6.23: Crevasses and crevasse traces (arrowed) observed on the surface of Victoria Flat. (Photo: J. Appleby, July, 2009)

Profile V1 (Figure 6.24) shows vertically-stacked reflectors (vertical dashed lines) (a) interpreted as crevasses or crevasse traces. A small number of parabolic reflectors (b) are identifiable suggesting the presence of englacial debris clusters or englacial conduits. Irvine-Fynn *et al.* (2006) suggest point source reflectors may be interpreted as either englacial voids, sediment inclusions or conduits running perpendicular to the traverse of the profile.

Profile V2 (Figure 6.25) shows vertically-stacked reflectors (vertical dashed lines) interpreted as crevasses or crevasse traces. A large number of crevasses and crevasse traces were identified in this area, produced during extensional flow in the Upper Icefall. A small number of parabolic reflectors identifiable suggests the presence of englacial conduits or englacial debris layers associated with in-transport debris septa. A cluster of reflectors can be seen just below the surface and approximately 200 m along the profile. This cluster is interpreted as a large englacial conduit or conduit system that may be either flowing, or blocked due to winter freeze.

Very few individual parabolic reflectors are obvious in profile V3 (Figure 6.26), with the most obvious features being stacked parabolas interpreted as crevasses. The profile is a cross-section looking down-valley with the true-left being at 0 m and the true right at ~380 m.

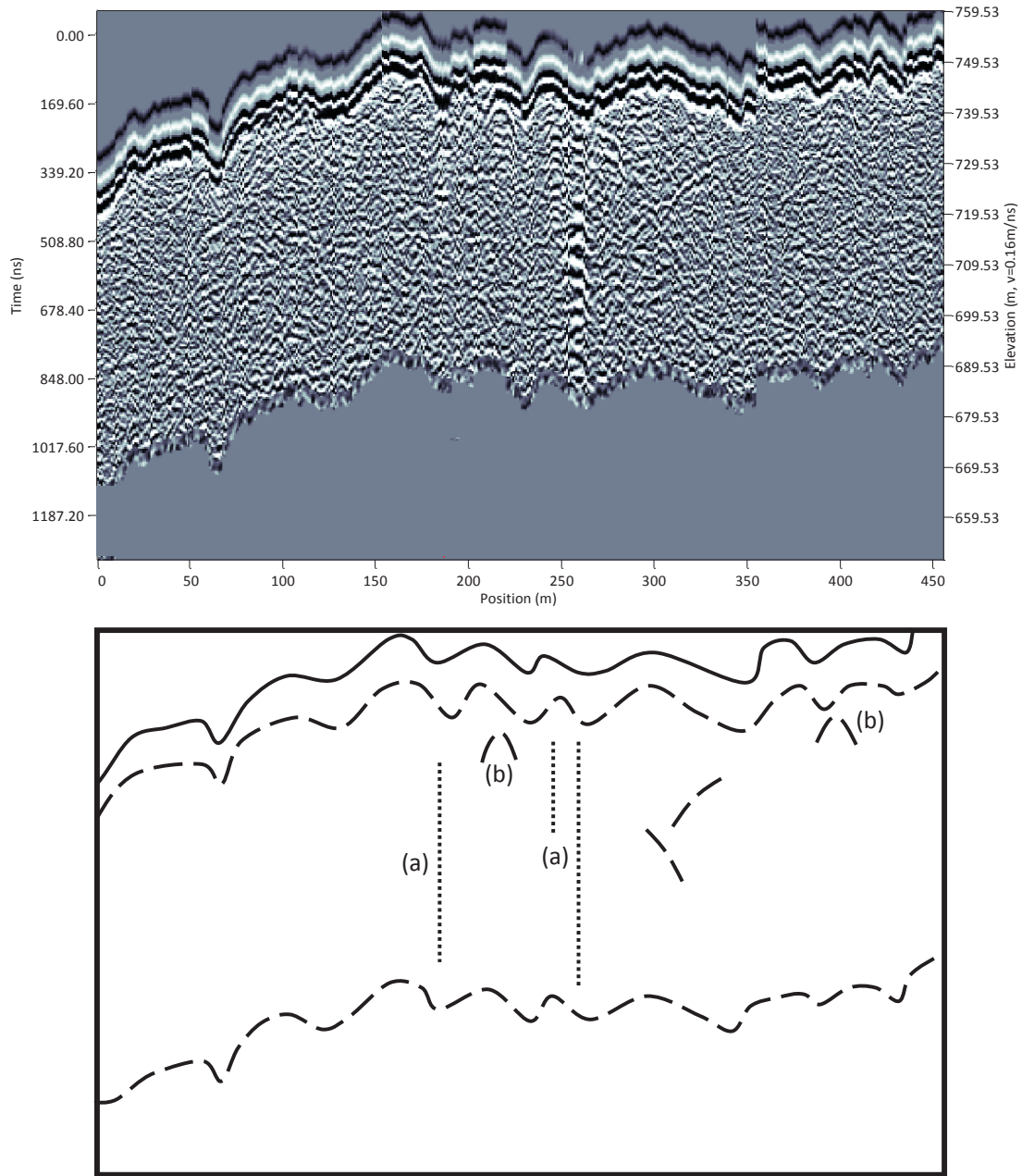


Figure 6.24: Interpretation of ground-penetrating radar profile V1, showing stacked parabolic reflectors (a) and parabolic reflectors (b). Vertical exaggeration = 2.75, depth of penetration = ~60 m.

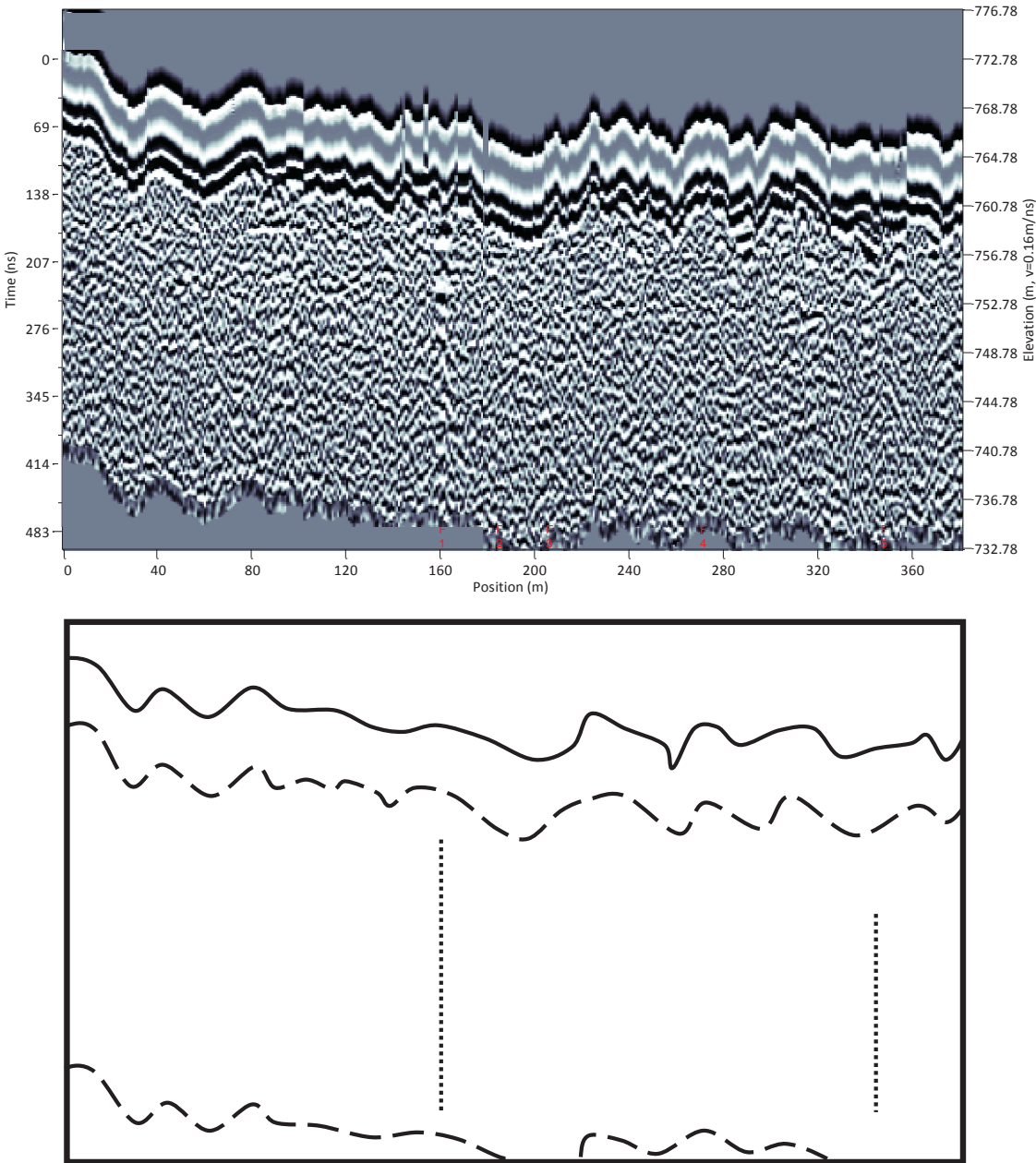


Figure 6.25: Interpretation of ground-penetrating radar profile V2, showing various point reflectors and stacked parabolic reflectors. Vertical exaggeration = 5.5, depth of penetration = ~30 m.

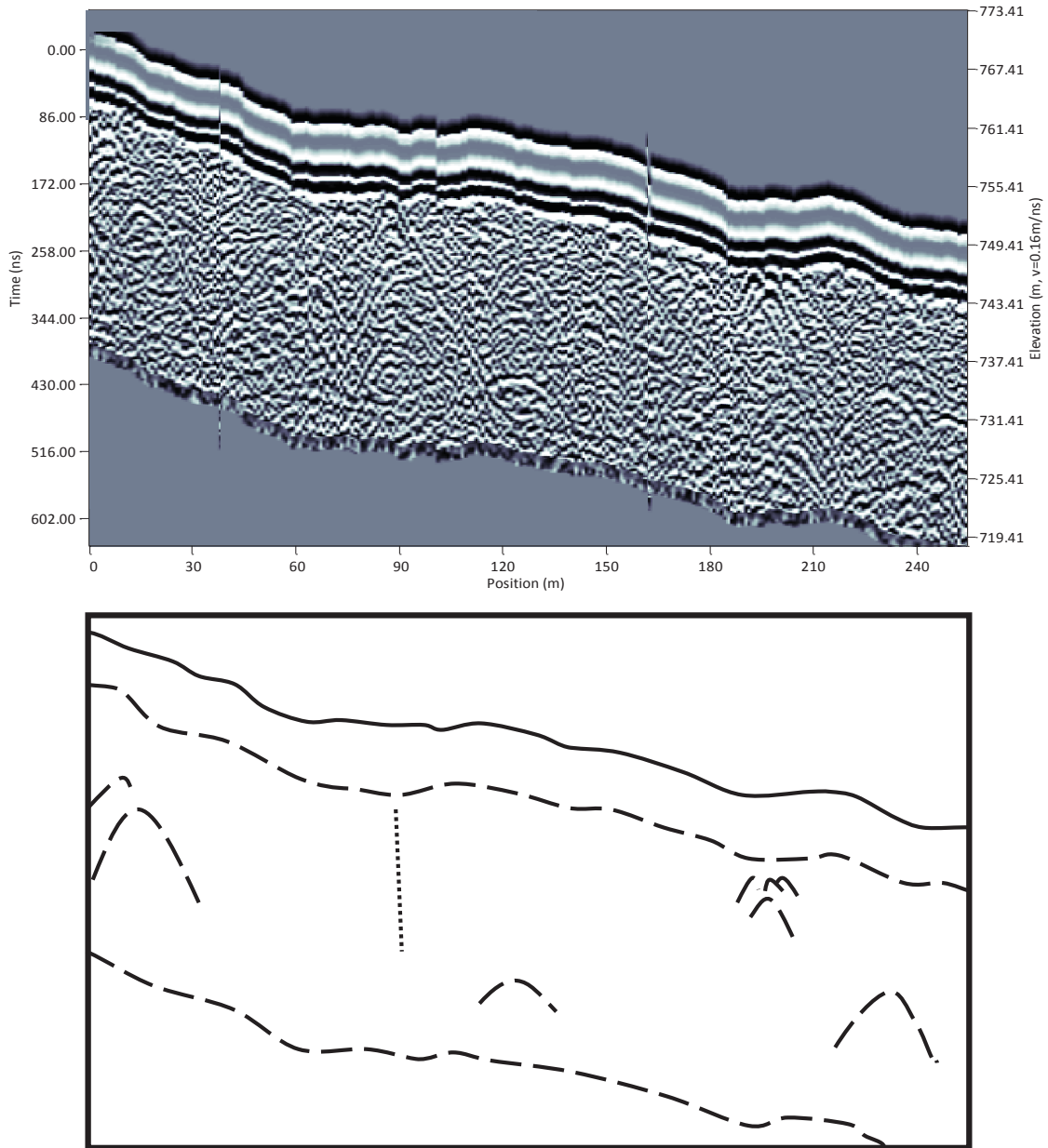


Figure 6.26: Interpretation of ground-penetrating profile V3, showing a large number of point-source reflectors. Vertical exaggeration = 2.7, depth of penetration = ~43 m.

In contrast to the profiles obtained in the Fox Glacier névé, no primary stratification is apparent in the survey profiles obtained from Victoria Flat. The transects in this area are characterised by individual parabolic reflectors spread throughout the profile, with some stacked parabolas indicating the presence of crevasses or crevasse traces, some of which are observable on the glacier surface. In addition, some reflectors are clustered in groups. The presence of supraglacial streams and moulins in the area of the Victoria Flat survey suggests that these highly 'reflective' zones are englacial water conduits that contain either flowing water or stored water that has been prevented from draining from the glacial system by freezing of the englacial drainage network (e.g. Willis and others, 2009). Perched water on the surface of Fox Glacier in the proximity of GPR survey lines suggest the latter as the source of clustered reflectors.

6.4.5.3 Lower Fox Glacier

GPR surveys were undertaken on the lower part of Fox Glacier between the Lower Icefall and the glacier terminus (Figure 6.27) at ~250 m elevation. The survey was undertaken in July 2009 during the Austral winter, avoiding summer melt water on the surface of the glacier which would potentially interfere with radar signals due to the high electrical conductivity of water. Due to the heavily crevassed and high-relief nature of the glacier surface in this zone, survey locations were chosen in areas of the ice surface where topography allowed use of the GPR unit (Figure 6.28). The cross-glacier ridge and trough pattern caused by lateral compression of the glacier causes steep topography making surveys logistically difficult in some areas. Hence, low-relief areas of the lower glacier were chosen so as to allow the possibility of surveying longer, more continuous profiles.

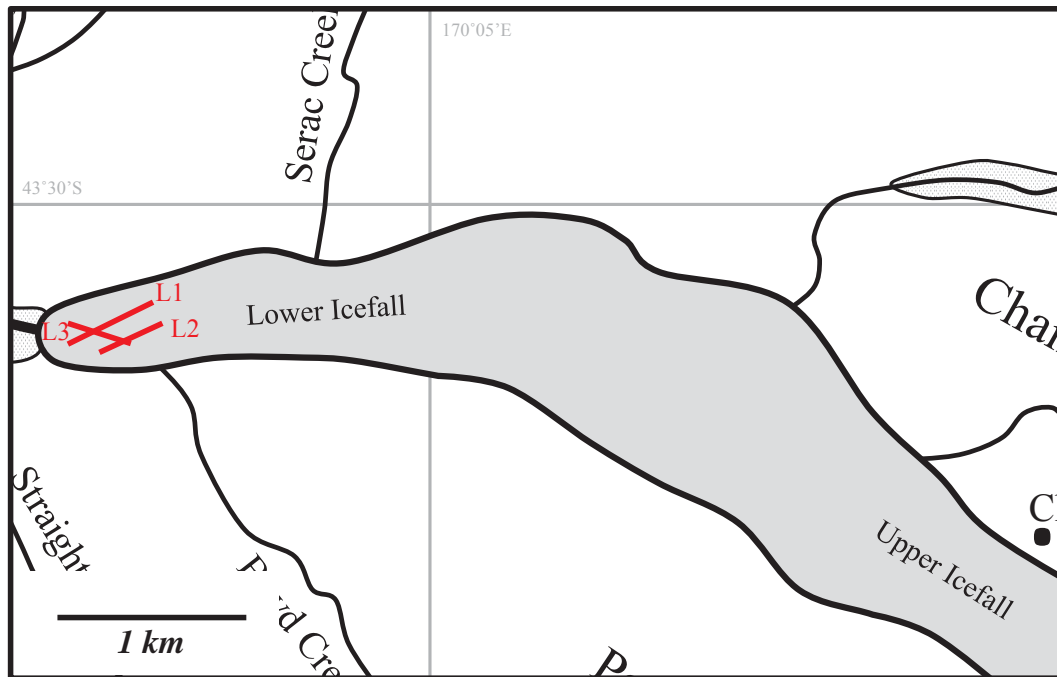


Figure 6.27: Location of GPR Transects undertaken on the lower Fox Glacier. Transect names refer to transects L1 to L3 as shown in figures 6.29 to 6.31.



Figure 6.28: Approximate location of transect L2 (red line) as an example of the lower study area. The view is towards the true right valley side of the Lower Icefall with the glacier flowing diagonally right to left. The break in the ridgeline at centre-right of the photograph is the hanging valley created by the former confluence of the Fox and Victoria Glaciers. (Photo: J. Appleby, July, 2009)

A small number of individual parabolic reflectors are obvious in profile L1 (Figure 6.29), with the most obvious feature being a prominent set of stacked parabolic reflectors at ~145 m (a). This feature is interpreted as a large, splaying crevasse radiating from the centre of the glacier, which has been bisected by the ground-penetrating radar survey.

Profile L2 (Figure 6.30) shows a vertically-stacked reflector interpreted as a crevasse (a). A number of parabolic reflectors (b) are also identifiable, suggesting the presence of englacial debris or englacial conduits.

The cross-valley profile L3 (Figure 6.31), exhibits two distinct parabolic reflector clusters (~30 m and ~80 m) (a), which are interpreted as concentrations of englacial water similar to those described by Zamora *et al.* (2009), possibly in englacial conduits, oriented down-glacier, that have been bisected by the ground-penetrating radar profile. The profile is a cross-section looking approximately up-glacier with the true right at 0 m and the true left at ~150 m.

As with Victoria Flat, no primary stratification is observable in the lower glacier survey area, as is expected given the ~11 km of ice transport through two icefalls. Once again, stacked parabolic reflectors have been identified and interpreted as open crevasses and crevasse traces. As the englacial drainage system has become more developed down-glacier, the clustering of reflectors has become more obvious with a larger volume of water being observed within conduits. This is particularly noticeable in profile L3 as longitudinal englacial channels have been bisected by the radar profile (Figure 6.32).

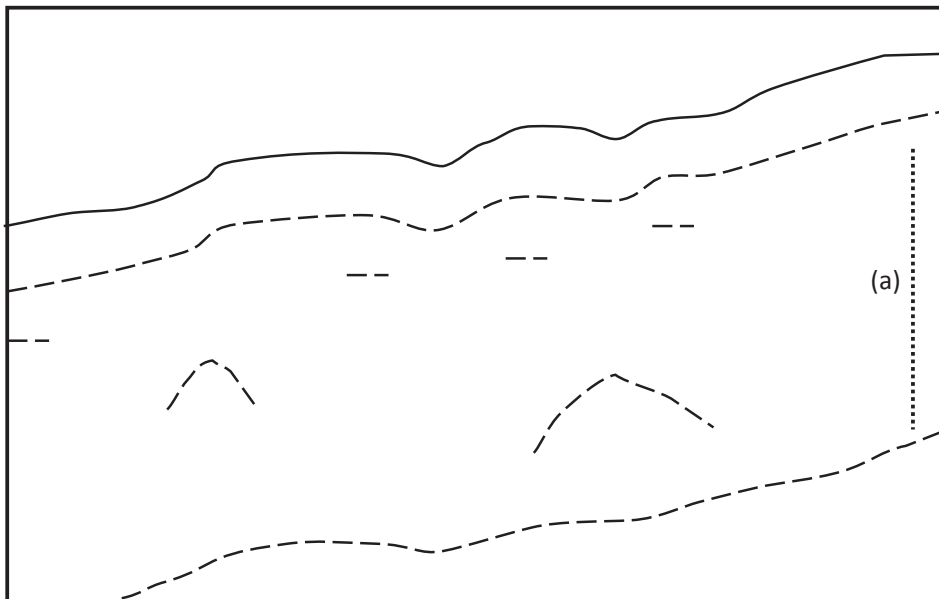
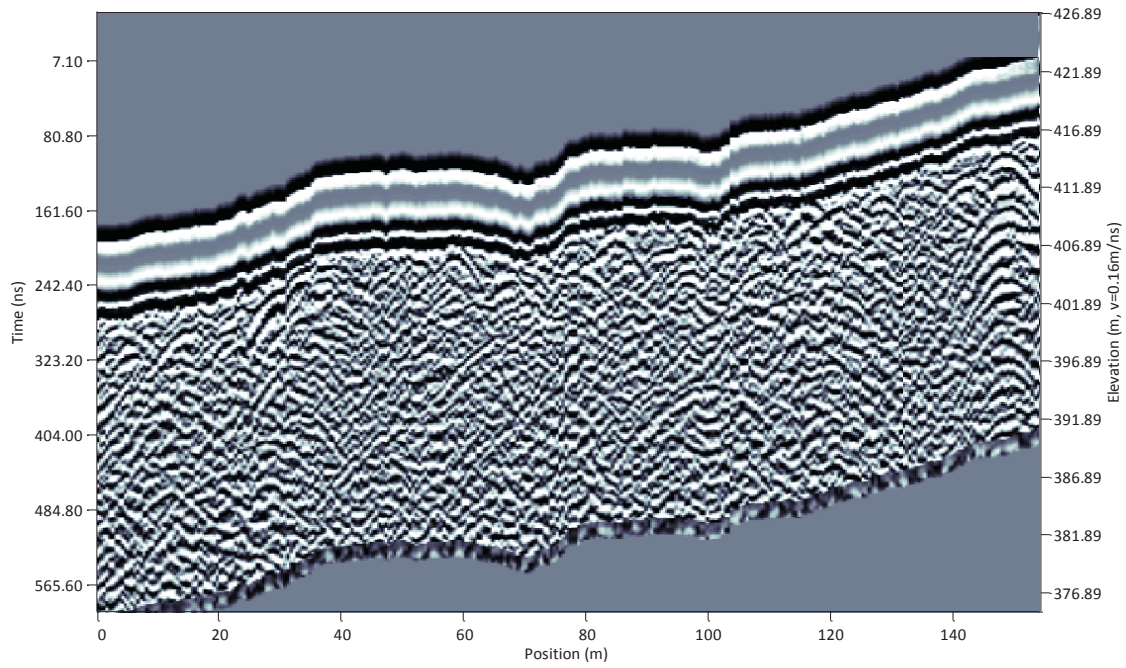


Figure 6.29: Interpretation of ground-penetrating profile L1 showing a prominent stacked hyperbolic reflector (a). Vertical exaggeration = 2.2, depth of penetration = ~30 m.

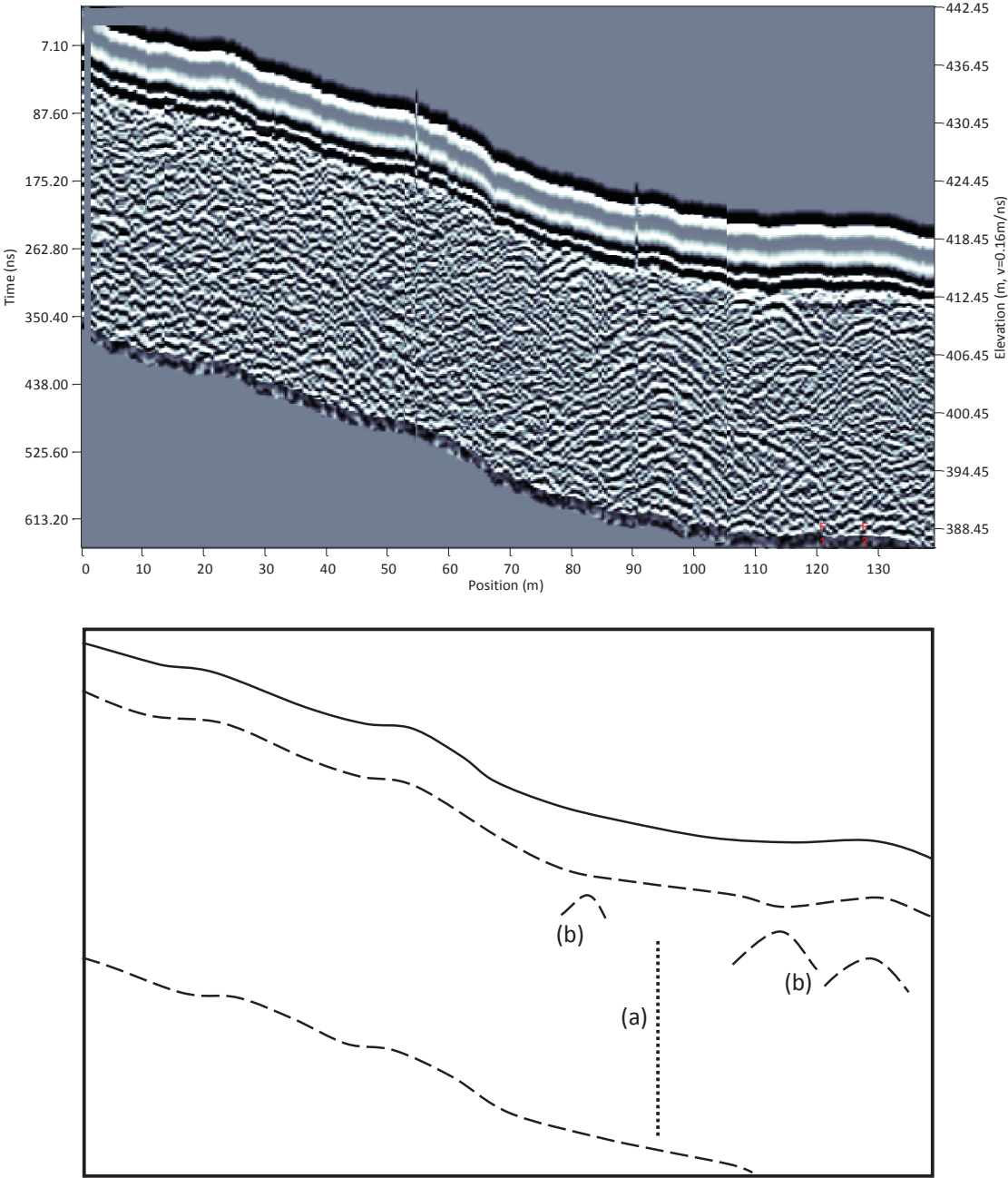


Figure 6.30: Interpretation of ground-penetrating radar profiles L2, showing a steep surface topography. Vertical exaggeration = 1.5, depth of penetration = ~35 m.

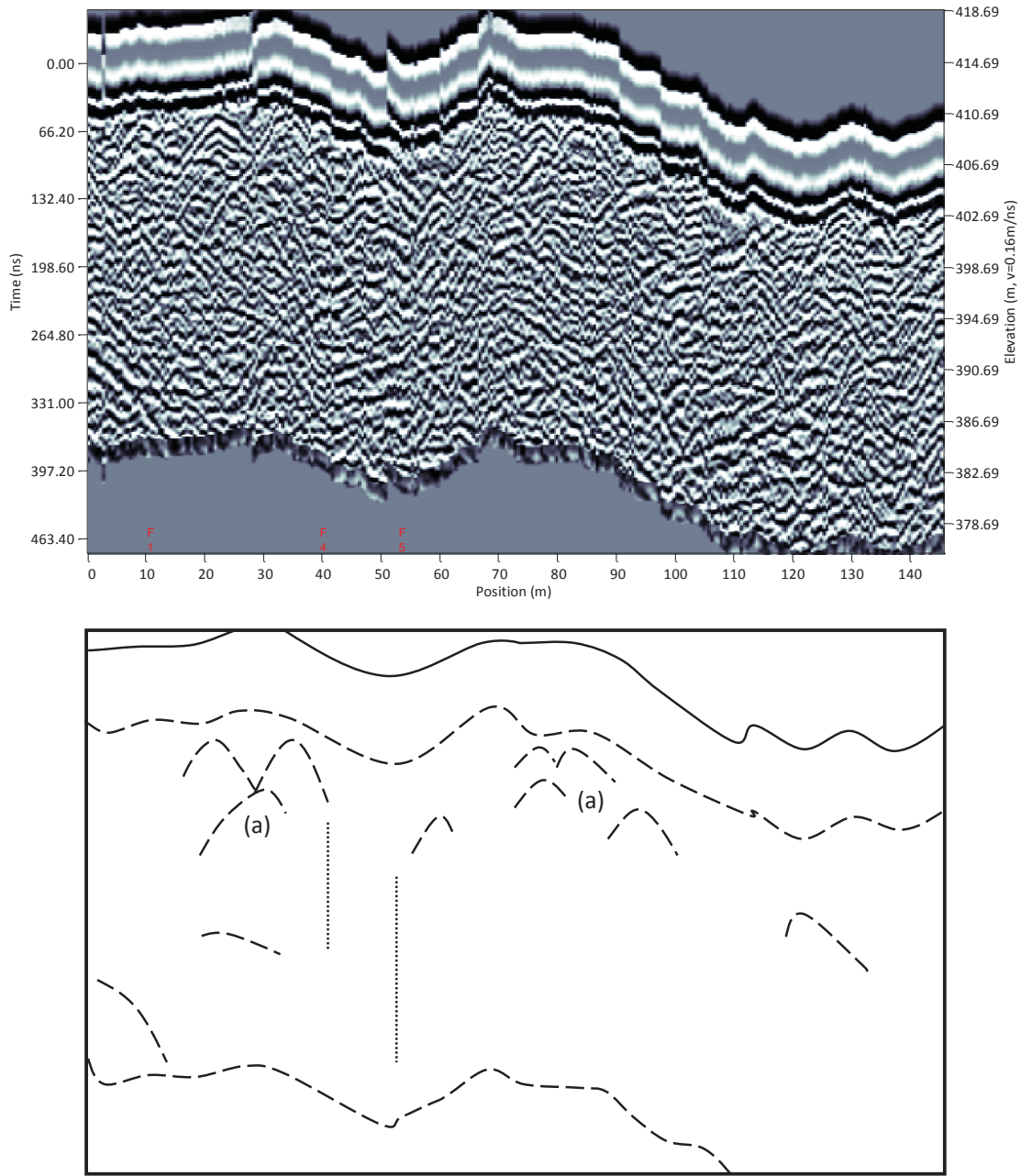


Figure 6.31: Interpretation of ground-penetrating radar profiles L3, showing a large number of parabolic reflectors (a). Vertical exaggeration = 2.25, depth of penetration = ~40 m.



Figure 6.32: Longitudinal englacial channel (arrowed) bisected by radar profile L3. (Photo: J. Appleby, July, 2009)

A large amount of ‘noise’ is present in the lower glacier, making the location and identification of individual features difficult. At this altitude (~300 to ~500 m asl), large volumes of supraglacial and englacial water diffract radio waves, causing scatter, typical of temperate ice (Macheret and others, 2009). In addition, higher concentrations of point-source reflector-creating clasts are found in the lower glacier close to the terminus. This is due to high volumes of rockfall from the steep valley sides, and the concentration of englacial clasts close to the surface and supraglacial sediments on the surface due to ablation and unloading of the ice (*refer Chapter Five*).

This study identified no features interpreted as thrust planes within the ice, as were found by Appleby *et al.* (2010) on the lower Fox Glacier and by Murray *et al.* (1997) within the surge front of Bakaninbreen, Svalbard.

6.5 Discussion on Ground-Penetrating Radar Surveys

A general down-glacier evolution of structures is observable from the ground-penetrating radar survey of Fox Glacier, as low density, parallel reflectors identified as primary stratification (S_0) are progressively destroyed as unique features. Lower down the glacier, the predominant structures become point source or stacked parabolic reflectors, dominated by crevasses and crevasse traces, the product of the passage of ice through two icefalls toward the terminus. The general results of this ground-penetrating radar survey highlight the increasingly deformed nature of Fox Glacier with distance from the névé, in terms of surface and englacial structures.

A great deal of spatial variations in depth and vertical distance between reflectors has been observed in the radargrams obtained from the névé of Fox Glacier, suggesting a strong influence on snow accumulation by topography (e.g. Woodward & King, 2009) and synoptic patterns (e.g. Purdie and others, 2011a). This is supported by previous workers (e.g. Huybrechts and others, 2009, Purdie and others, 2011b, Farinotti and others, 2009, Binder and others, 2009, Purdie and others, 2011a) who showed, using a combination of GPR, crevasse stratigraphy, ice cores and density probes, how accumulation rates and depths of primary stratification can vary. A great deal of spatial variations in depth and vertical distance between reflectors has been observed in the radargrams obtained from the névé of Fox Glacier, suggesting a highly heterogeneous pattern of snow accumulation. This marked heterogeneity may be due to the influence of topography (e.g. Woodward & King, 2009) and/or synoptic climatology (e.g. Purdie and others, 2011a). This is supported by previous workers (e.g. Binder and others, 2009, Farinotti and others, 2009, Huybrechts and others, 2009, Purdie and others, 2011a, Purdie and others, 2011b) who showed, using a combination of GPR, crevasse stratigraphy, ice cores and density probes, how accumulation rates and depths of primary stratification can vary considerably both spatially and temporally. Purdie *et al.* (2011a) suggest increased snow depth in the accumulation area of Franz Josef Glacier is controlled by a combination of higher altitudes, a northwest aspect, and proximity to the Main Divide of the Southern Alps. It is likely that such factors are important controls on the spatial pattern of accumulation in the adjacent Fox Glacier névé, too. However, the limited scope of the present study means extrapolation of data to provide general trends in the Fox Glacier névé is not possible.

Despite the identification of a large number of prominent features in each of the three survey zones (névé, Victoria Flat and lower Glacier), the resolution achieved by the antenna used, may be insufficient to identify all features of interest on Fox Glacier.

6.5.1 GPR in Temperate Glacier Structural Investigations

Ground penetrating radar investigations on temperate (warm-based) glaciers are particularly challenging (e.g. Navarro and others, 2005, Burke and others, 2009, Murray and others, 2000a). Significant amounts of water are found in Fox Glacier, both supraglacially and englacially, causing scatter of electromagnetic waves and making englacial horizon interpretation difficult. This signal attenuation also makes the identification of point-source reflectors representing individual structures problematic, as filtering of noise during post-processing can cause the loss of parabolas of interest.

Despite these issues, some success has been achieved on other temperate glaciers (e.g. Goodsell and others, 2005c, Welch and others, 1998, Eisen and others, 2009, Willis and others, 2009), although these glaciers are mostly at higher altitudes than Fox Glacier. The corollary is that the lower snow and ice temperatures characteristic of higher altitude alpine glaciers are suggested (e.g. Farzaneh and others, 2007) as improving radio-wave conductivity through snow and ice bodies. In addition, the synoptic patterns and geographical setting of Fox Glacier in a maritime climate (Purdie and others, 2008a, Purdie and others, 2008b) allow for a greater quantity of water (from precipitation and ablation) to be present in the Fox Glacier system compared to those temperate glaciers found at intra-continental locations such as the central European Alps.

More success has been achieved using ground-penetrating radar on polythermal (e.g. Murray and others, 1997, Woodward, 1999, Woodward and others, 2003) and cold-based glaciers (e.g. Karlsson and others, 2009, Macheret and others, 2009, Arcone and others, 2005). Despite this, Langley *et al.* (2007) identified very high scattering properties of the upper layers of Kongsvegen Glacier, Svalbard, that precluded layers deeper than approximately 6 m from being imaged in any detail. A more appropriate use for GPR may be for aerial surveys to glean a rapid, broad picture of accumulation in areas with limited access.

In addition to the inherent limitations on the application of GPR to structural investigations of temperate glaciers, in-field limitations also exist. Practical use of the PulseEKKO Pro GPR unit employed in this study is straight forward on subdued areas and gentler slopes of Fox Glacier névé and Victoria Flat. However, the steeper topography of the lower glacier and the areas immediately above and below the three icefalls prevents unfettered access, making long, continuous survey lines impossible.

For the reasons above, ground-penetrating radar is currently of somewhat limited use for structural investigations on the glaciers of New Zealand's South Westland Region, and may prove a more appropriate technique when applied to cold-based, polythermal and higher altitude glaciers, along with the 'dryer' glaciers east of the main divide (e.g. Purdie and others, 2011b).

Chapter 7 : Dynamics of Fox Glacier

7.1 Introduction

Chapter Seven considers the dynamic behaviour of Fox Glacier. It begins with a review of existing literature describing the dynamics of glaciers, then goes on to describe the methods used to quantify the dynamics of Fox Glacier, before presenting the results obtained. Finally the chapter provides an interpretation and discussion on the flow dynamics of Fox Glacier and compares its behaviour with glaciers in other locations globally.

7.2 Review of Glacial Dynamics

7.2.1 Introduction

One of the most fundamental characteristics of glaciers is their ability to flow (Benn & Evans, 1998, 2010), although until the mid-nineteenth century, the fact that glaciers moved at all was unknown to the scientific community (Hambrey & Alean, 2004). Many processes and properties of the surrounding environment influence glacier movement (Benn & Evans, 1998) including thermal regime, substrate composition, ice thickness and glacier hydrology. This movement, in turn, influences the type and occurrence of supraglacial, englacial and subglacial structures including crevasses, foliation, folding and faulting. In addition, the dynamics and deformation of glaciers has an important role in determining glacial debris entrainment, transport and deposition.

7.2.2 Processes of Glacier Motion

Glacier motion can be seen as a result of strain of the ice in response to an applied stress (Benn & Evans, 1998), and can occur by three main mechanisms (Figure 7.1); a) Deformation of the ice; b) Sliding of the glacier, and; c) Deformation of the bed.

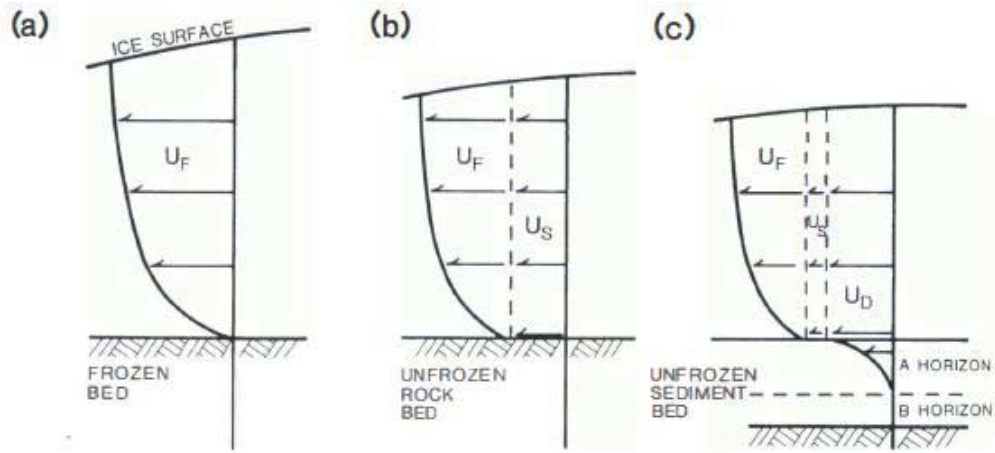


Figure 7.1: Modes of glacier motion showing (a) a glacier frozen to the bed flowing due to deformation of ice (U_F); (b) a glacier resting on an unfrozen bed flowing due to deformation of ice (U_F) and basal sliding (U_S), and; (b) a glacier resting on a sediment layer at the ice-bed interface flowing due to a combination of deformation of ice (U_F), basal sliding (U_S), and deformation of subglacial sediments (U_D) (from Boulton, 1996).

In the case of glaciers, the applied stress causing motion is acceleration due to gravity acting on the mass of ice which has potential energy by virtue of its elevated position. The inherent instability of glaciers caused by mass balance gradients (Figure 7.2), causes down-slope ice movement as the glacier attempts to obtain a position of equilibrium. The *wedge model* of glacier flow described by Sugden and John (1976) describes how over-steepening of the ice surface by thickening in the accumulation area and thinning in the ablation area requires the transfer of mass through the equilibrium line to rectify the loss of the ablation wedge and maintain a steady state. The mass balance gradient has been used by a number of authors (e.g. Meier & Tangbourn, 1965, Meier, 1961, Pelto, 1988) as a proxy for the energy of glacier activity. Regional trends in mass balance gradients indicate that glaciers in humid, maritime areas should flow faster than glaciers in arid, cold climates, and that glacier activity decreases with increasing latitude and greater continentality (Benn & Evans, 1998), although this doesn't take account of surge phases in surge-type glaciers. Fox Glacier, along with other West Coast Glaciers, is likely to have one of the steepest mass balance gradients of any glacier globally due to its unique ablation area ratio, and high levels of both annual accumulation and ablation.

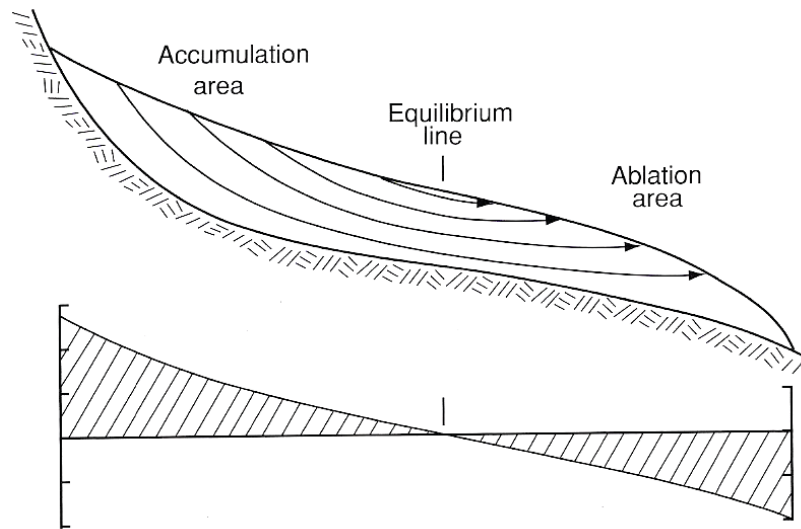


Figure 7.2: Longitudinal cross section of a valley glacier showing schematic representations of mass balance and gradient (from Hooke, 2005).

7.2.2.1 Deformation of Ice

Deformation of ice can consist of either creep or fracture, and refers to the permanent change in shape of the ice as a result of an applied stress (Alley, 1992). Creep occurs by the movement between individual crystals either by change in shape of the crystals or recrystallisation at grain boundaries, or by movement within crystals by gliding along cleavage planes or crystal defects. The most commonly used explanation, or flow law, of the relationship between applied stress and the response of ice is Glen's Flow Law (Glen, 1955), which has been adapted for use in glaciology by Nye (1957). Glen's flow law can be written as

$$\dot{\epsilon} = A \tau^n, \quad (7.1)$$

where $\dot{\epsilon}$ represents strain rate, A and n are constants (A is determined by ice temperature; n is usually ~ 3), and τ represents the shear stress. When ice cannot creep fast enough to change shape according to an applied stress, fracture occurs. Once a critical strain is reached, beyond which ice cannot deform, the ice breaks apart

demonstrating features such as crevasses, which pervade down through the brittle upper part of the glacier to the plastic zone below where creep rates are higher.

7.2.2.2 Deformation of the Bed

In some situations, deformation of the bed occurs rather than deformation of the ice. Subglacial deformation accounts for a substantial share of the forward movement of some glaciers (Benn & Evans, 1998) and occurs in a similar way to deformation of ice, as subglacial sediments experience permanent strain in response to an applied stress; in this case stress applied by the overlying ice. Changes in basal motion may be the result of changes in water pressure at the ice-bed interface having a lubricating effect on till (Weertman & Birchfield, 1983, Kamb, 1987) or the result of deformation of the till itself (Clarke, 1987, Boulton & Hindmarsh, 1987, Truffer and others, 2000). In addition to movement of the ice mass, deformation of subglacial material has an important role in the rate of subglacial erosion and deposition (Boulton, 1996).

7.2.2.3 Basal Sliding

Thirdly, movement may occur without deformation of either the bed or ice. In warm-based glaciers, where basal temperatures are above the pressure melting point, a wet ice surface resting on a low friction subglacial material such as till or bedrock allows for slip between the glacier and its bed at the ice/bed interface. Willis (1995) postulates the assumption that basal sliding is the most important mechanism causing variations in glacier motion at an intra-annual timescale. Weertman (1957, 1964) first developed a law of basal sliding, incorporating theories on regelation and enhanced plastic flow, whereby intermediate sized bed unconformities act as 'controlling obstacles' which determine overall basal-sliding velocities. These theories were adapted and developed by Nye (1969, 1970) and Kamb (1970) who demonstrated a transition wavelength of bed obstacles in the order of ~ 0.5 m. Unconformities smaller than this allow sliding of ice by regelation, whereas larger unconformities require plastic flow for the ice body to slide.

Subglacial water is recognised as having a profound influence on ice velocity (Hubbard & Nienow, 1997) and glacier stability. Sliding and bed deformation rates are related to variations in subglacial water pressure (Willis, 1995, Mair and others, 2001), with

drainage type having important implications for controlling water pressure at the bed. Changing water pressure affects sliding by submergence of bed unconformities, increased plastic deformation, and hydraulic ‘jacking’. Small-scale (~mm scale) bed roughness can be submerged by a thin film of water creating a smooth bed surface over which the ice can slide freely. Larger scale bed roughness is reduced by pressurized water in cavities that, as a non-compressible medium, transfers the force of the overlying ice to crests and stoss sides of unconformities not covered by water, reducing the pressure melting point and increasing regelation and plastic deformation. Pressurized water in cavities also has the effect of ‘jacking-up’ the glacier by exerting a down-glacier force on the up-glacier face of the subglacial cavity.

A strong association has been identified between an increase in subglacial water pressure and increased glacial velocity (Mair and others, 2001, MacGregor and others, 2005, Kavanaugh & Clarke, 2001, Meier and others, 1994). In contrast, Magnusson *et al.*, (2010) describe reduced sliding rates of a Vatnajökull outlet glacier due to persistent drainage of a subglacial lake.

7.2.2.4 Stress and Strain of Glacier Ice

Stress is a measure of the force acting on an object or material, whereas strain is a measure of the amount of deformation that the material experiences. The two components interlink with stress being directly proportional to strain according to a relationship described as Hookes Law (Cutnell & Johnson, 2012).

Ice masses experience moderate or low stresses for tens or hundreds of years and surface features such as crevassing are thought to be a product of these long stress histories (Vaughan, 1993), although much higher stresses acting over a shorter time would be expected in a glacier flowing as rapidly (~ 0.9 m/day) as Fox Glacier (Purdie and others, 2008b, Purdie and others, 2008a). At higher stresses, according to Jaeger and Cook (1979), ice becomes brittle and its ability to resist load decreases with increasing deformation.

Strain can be considered as a total or cumulative value describing the total strain experienced by a material due to the stress applied. It is more commonly expressed as a

dimensionless ratio of the difference between initial length and final length, describing the rate at which the body of ice deforms in response to the applied stress (termed strain-rate) and is expressed in units of $time^{-1}$ (Hubbard & Glasser, 2005).

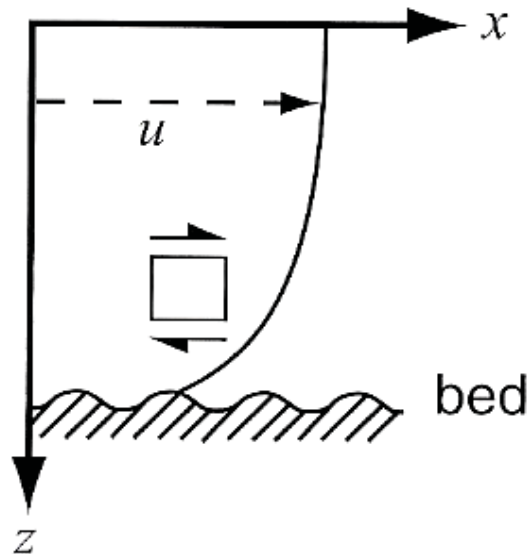


Figure 7.3: Normal force due to mass of ice z , and shear-stress force x , of a body of ice. Horizontal velocity is defined u , whilst perceived shear stress is demonstrated by the arrowed-box (Hooke, 2005).

Stresses are tensor quantities, meaning they have both magnitude and direction (Hooke, 2005). Stresses that are directed normal to the surface on which they are acting are called normal stresses; in this case, the mass of the ice causing a downward stress on the glacier bed. Those stresses acting parallel to the shear surface are shear stresses. This is the force of the ice moving down-valley under the influence of its mass and gravity (Figure 7.3). The parallel shear stress acting on a body of ice is largely controlled by ice thickness and surface slope (Echelmeyer & Kamb, 1986), which in turn can be greatly influenced by the mass balance gradient of the glacier.

7.3 Methods for Determining the Dynamic Behaviour of Fox Glacier

Data on the dynamic behaviour of Fox Glacier were collected and analysed according to the methods described by Nye (1959), Wu and Christensen (1964), Milnes and Hambrey (1976), Vaughan (1993), Goodsell *et al.* (2005c) and Appleby *et al.* (2010). For this research, triangles were used to avoid complexity whilst still allowing accurate measurements of strain. Five transects were located at various positions on the glacier surface: below the Lower Icefall; below the Upper Icefall on Victoria Flat; and on and around the Albert Glacier in the Fox Név . Transects were constructed of ten 25 mm diameter plastic ablation stakes drilled into the ice surface using a Kovac ice auger (Figure 7.4). The position of each of the stakes was recorded using a Trimble R8 Real-Time-Kinematic (RTK) Global Positioning System at the start of the study period and then again at the end. Transects in Fox Glacier N v  were measured over four weeks in February and March 2010. Transects on Victoria Flat and the lower part of Fox Glacier were measured over four weeks in January and February 2011.



Figure 7.4: 25 mm plastic ablation stakes drilled into the glacier surface using a Kovac ice auger used for measurement of surface strain (Photo: M. Brook).

7.3.1 Measuring Ice Deformation

Ideally, deformation polygons should be formed by perfect squares, diamonds or triangles (Figure 7.5) with a y -axis representing the down-glacier direction, and an x -axis representing the across-glacier direction (Nye, 1959, Hambrey & Müller, 1978). A z -axis can be used to represent a component normal to the glaciers surface (Wu & Christensen, 1964), however this research is only concerned with deformation measurements in two dimensions and so the z -axis has been dispensed with. As far as topography would allow, strain polygons were laid-out with a y -axis between A-A, and an x -axis between C-B.

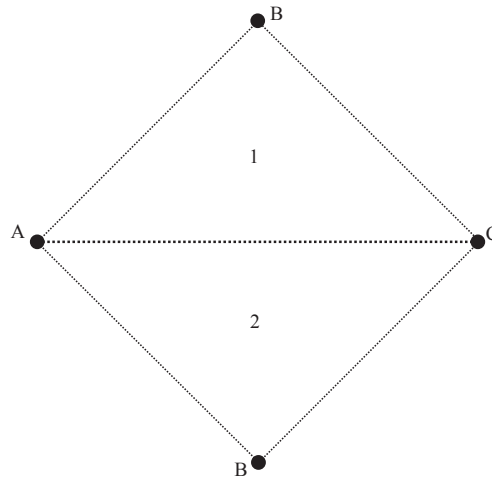


Figure 7.5: Idealised polygon for measurement of strain rate on the surface of a glacier. Each strain diamond is divided into two triangles (1 and 2) with corners A, B, and C. The changing distance between the corners allows for the calculation of strain rate and cumulative strain.

The distance d between two points in a plane of known co-ordinates (i.e. point A = (x_1, y_1) and point B = (x_2, y_2)) is given by

$$d = \sqrt{(x_2 - x_1)^2 + (y_2 - y_1)^2} \quad (7.2)$$

Equation 7.2 was used to determine the initial distance between two ablation stakes at the start of the study period and then again at the end of the study period, allowing the change in distance or deformation in shape of the polygons to be calculated.

7.3.2 Calculating Strain

Strain calculations were done using software created in *BBC BASIC* by Williams and Knight (1987) and developed for use in *Microsoft Excel* by Goodsell (2005). The program requires the input of the initial (A-B, B-C, C-A) and final (A'-B', B'-C', C'-A') triangle side lengths and the length of time in days over which the study was undertaken. From these inputs, the program outputs maximum and minimum principal strains with positive values for extensional strain and negative values for compressive strain. In addition, maximum principal strain orientation relative to line A-B, magnitude of maximum shear strain, and rate of change of triangle area are also output. *Appendix 2* gives a break-down of the mathematical methods of producing strain results if a program is not available.

Strain can be measured cumulatively or as strain rate. Cumulative strain is the total amount of strain (or total change in triangle side length) experienced over the study period and is not described relative to time. Most glaciological literature makes use of strain rate, a measure of cumulative or total strain divided by the study period to give an indication of the strain experienced per unit of time (usually 1 year). For this reason, all results from this research are extrapolated to give annual strain rates, for ease of comparison with other research.

7.3.3 Presentation of Results

The relative positions of the stakes in each transect at the beginning and end of the study period can be graphed by simply inputting the co-ordinates to GIS software such as *ArcGIS* or *Surfer*. This produces a polygon pattern as for that produced by Boyce *et al.*, (2007) (Figure 7.6). Any change in geometry between the primary and secondary transects can then easily be seen. Overlain on these, can be the magnitude and orientation of the extensional or compressive strains experienced at the centre of the triangle.

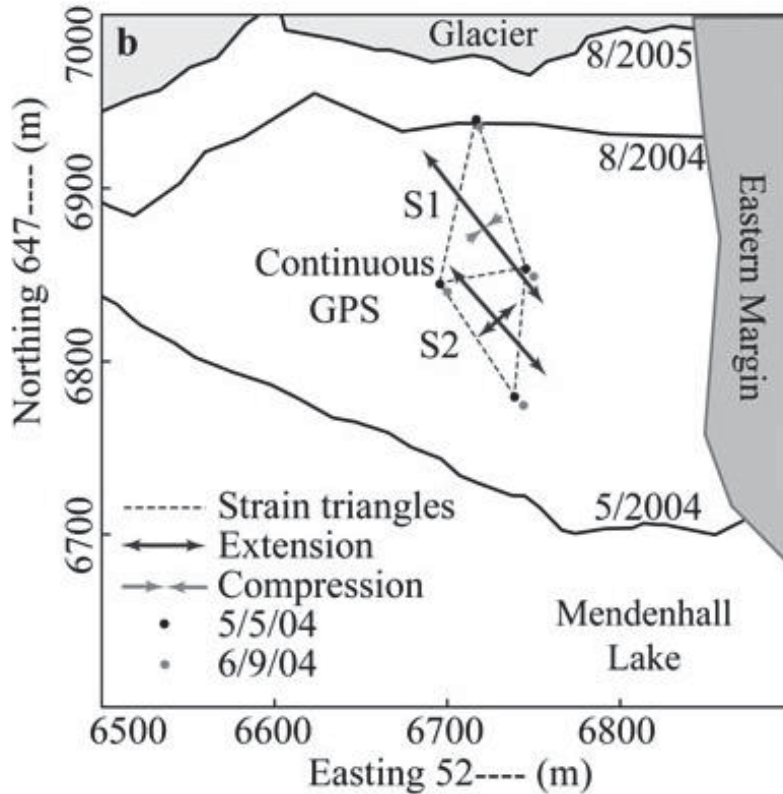


Figure 7.6: An example of the graphical representation of extensional and compressive strain rates mapped on the surface of Mendenhall Glacier, Alaska (from Boyce and others, 2007).

7.4 Dynamics of Fox Glacier

Strain measurements were undertaken in three areas: the lower Fox Glacier, Victoria Flat and Fox névé. These areas were chosen on the basis of where topography and surface structure would allow ready access, and so as to gain a representative picture of the overall strain pattern of Fox Glacier. The sites were selected according to the presence of evolving surface crevasse patterns that indicate deforming ice undergoing strain.

7.4.1 Lower Fox Glacier and Victoria Flat

The lower Glacier and Victoria Flat strain study area (Figure 7.7) constitutes the valley-confined tongue of Fox Glacier between the bottom of the Upper Icefall where the glacier flows from the accumulation area, and the snout where the glacier terminates in

a valley-confined proglacial sandur. Strain surveys in this area were undertaken during January and February 2011, part of the Austral summer.

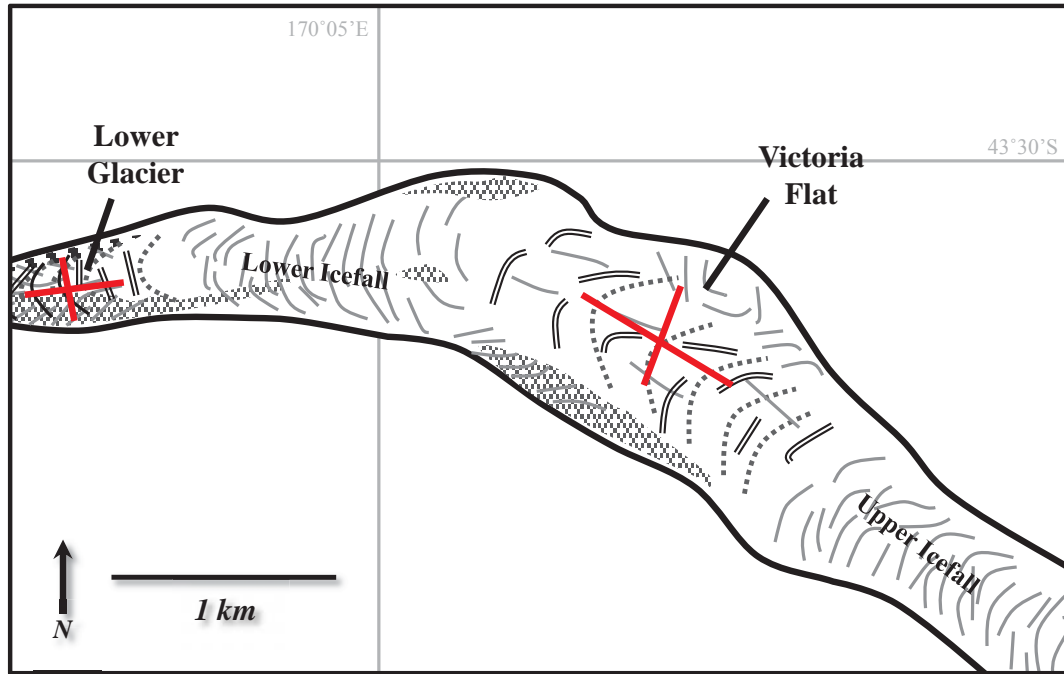


Figure 7.7: Strain stake transect locations on the lower Glacier and Victoria Flat.

The strain stake network on the lower glacier (Figure 7.8) covered an area from above the terminus to just below the Lower Icefall, and from close (~50 m) to the true right valley side across to the medial moraine on the true left of the glacier.

Longitudinally, the Victoria Flat strain stake network (Figure 7.9) covered the low relief area between the Upper and Lower Icefalls that define the boundaries of Victoria Flat. Laterally, the stake network extended from the true left moraine beneath Paschendale Ridge to the true right margin, immediately down-valley of the former Victoria Glacier-Fox Glacier confluence.



Figure 7.8: Location of 'lower glacier' strain stake transects on the lower Fox Glacier. (Photo: J. Appleby, February, 2009)



Figure 7.9: Location of 'Victoria Flat' strain stake transects on Victoria Flat, viewed from Chancellor Shelf near Chancellor Hut. The lower part of the Upper Icefall can be seen at the bottom left of the photograph, below Paschendale Ridge. (Photo: J. Appleby, January, 2010)

7.4.2 Fox Glacier Névé

The Fox névé strain rate study area was on areas centred by Pioneer Ridge in the upper half of the accumulation zone (Figure 7.10). Strain stake networks were located on the Albert Glacier, one of the main tributary glaciers that constitute the Fox Glacier névé, and on Pioneer Ridge. Strain surveys in this area were undertaken during February and March 2010, part of the Austral summer.

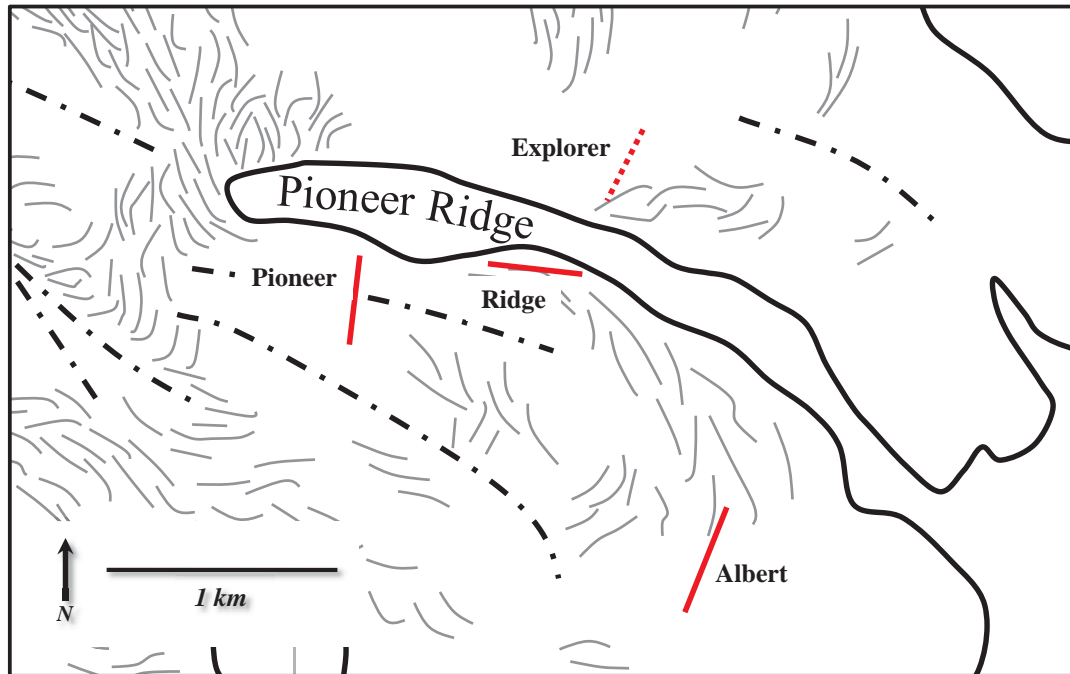


Figure 7.10: Strain stake transect locations in Fox névé. The dashed line indicates the location of the ‘Explorer’ stake transect that was not re-surveyed at the end of the study period due to increased crevassing. Crevasses are represented by grey lines, while flow unit boundaries are represented by dashed lines.

The ‘Pioneer’ strain stake network (Figures 7.11 and 7.12) covered an area of the Albert Glacier south of Pioneer Ridge, characterised by a low surface slope ($<10^\circ$) and extensive transverse crevassing. This area is situated below the steeper sections of the Albert Glacier that abut the Main Divide, and above the highly crevassed Pioneer Icefall. The area is also a convergence zone for ice flowing from the Albert Glacier and Pioneer Ridge, along with ice flowing from the Heemskerck and Abel Janszoon Glaciers at the base of Lendenfeld Peak (3194 m) and Mt Tasman (3497 m), respectively.

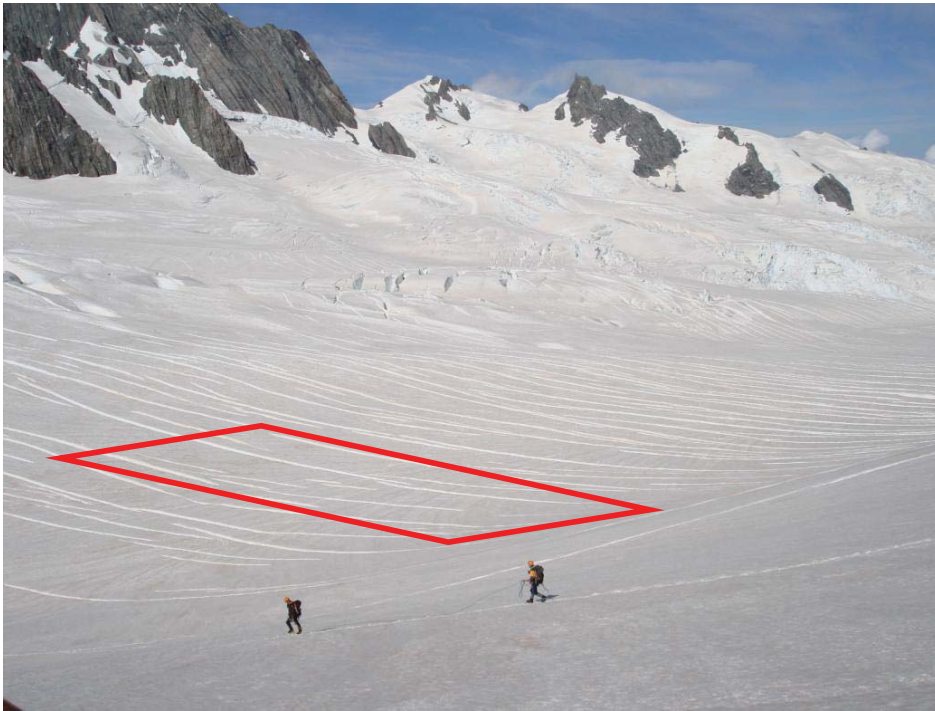


Figure 7.11: Location of 'Pioneer' strain stake transect on the Albert Glacier, viewed from Pioneer Ridge looking southwest. Ice flow is from left to right. Scale of transverse crevasses is shown in Figure 7.12. (Photo: J. Appleby, February, 2010)



Figure 7.12: Location of 'Pioneer' strain stake transect on the Albert Glacier, looking northeast towards Pioneer Ridge from the Albert Glacier. Crevasse scale can be seen relative to the people. (Photo: J. Appleby, February, 2010)

The ‘Ridge’ strain stake network was located on the southern side of Pioneer Ridge (Figures 7.13 and 7.14), and covered an area where ice was beginning to flow downslope towards the Albert Glacier. The area is characterised by crevasses oriented parallel to the axis of Pioneer Ridge, transverse to the direction of flow. The location of the stake transects is bounded by rock outcrops at the upper end of the network, and by steep snow slopes at the downslope end.

The strain stake network in the ‘Albert’ study area (Figures 7.15 and 7.16) is located immediately beneath the steep snow-covered slopes of the Main Divide at the headwall of the Albert Glacier, and immediately above a topographic drop into the main part of the Albert Glacier where the ‘Pioneer’ strain network was located. The strain network was located on a low ($<10^\circ$) gradient ‘terrace’ separating these two zones.

A strain network was also established on the Explorer Glacier (Figure 7.17) immediately north of Pioneer Ridge. Unfortunately, deep crevassing at the end of the study period (late in the summer melt season) prevented access to the stakes for re-surveying, and so this network could not be used.



Figure 7.13: Location of ‘Ridge’ strain stake transect on Pioneer Ridge. Ice flow is from right to left, towards the south face of the ridge. Width of crevasses is shown in figure 5.14. (Photo: J. Appleby, February, 2010)



Figure 7.14: Location of ‘Ridge’ strain stake transect on Pioneer Ridge, looking west towards the distal end of the ridge. (Photo: J. Appleby, February, 2010)



Figure 7.15: Location of ‘Albert’ strain stake transect on the Albert Glacier. Ice flow is from left to right. View is southwest towards the Main Divide, with Pioneer Pass and the prominent north buttress of Mt Haast (3114 m) at the top right of the photograph. (Photo: J. Appleby, February, 2010)



Figure 7.16: Location of 'Albert' strain stake transect situated on a low gradient terrace viewed from Pioneer Ridge. The skyline is the Main Divide of the Southern Alps, with Douglas Peak (3077 m) being prominent at the left side of the photograph. (Photo: J. Appleby, February, 2010)



Figure 7.17: Location of 'Explorer' strain stake transect on the Explorer Glacier, looking northwest from Pioneer Hut. Ice flow is from right to left. The strain network was inaccessible for re-surveying due to increased crevassing. (Photo: J. Appleby, February, 2010)

7.4.3 Flow and Deformation of Fox Glacier

7.4.3.1 Deformation of Polygons

Strain transect polygons have been graphed to give a visual representation of two-dimensional deformation of the ice surface (Figures 7.18 to 7.22), including approximate areal change, and strain directions. Location and scale of polygons is determined according to Eastings and Northings, with primary and final polygons being represented by solid and dashed lines respectively.

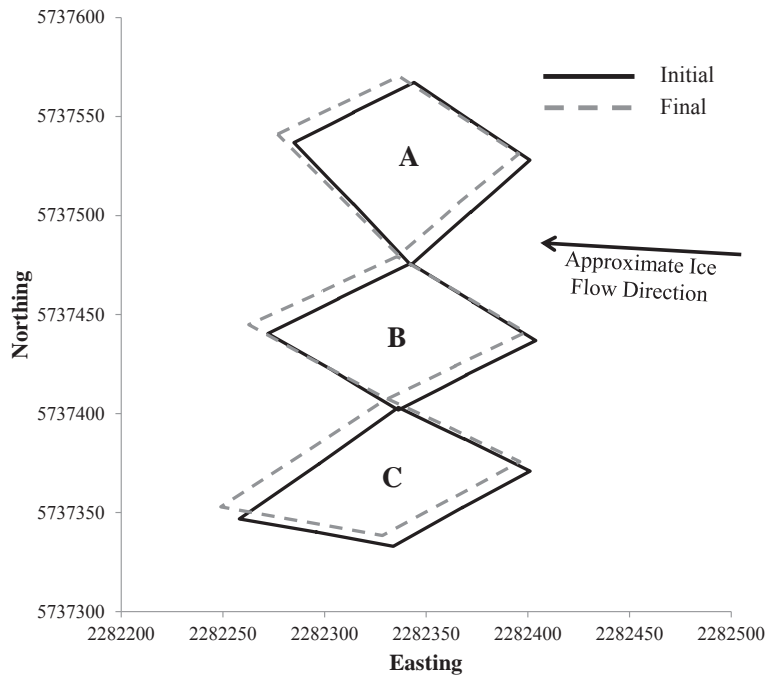


Figure 7.18: Albert Glacier deformation transect showing initial and final (deformed) polygons A to C.

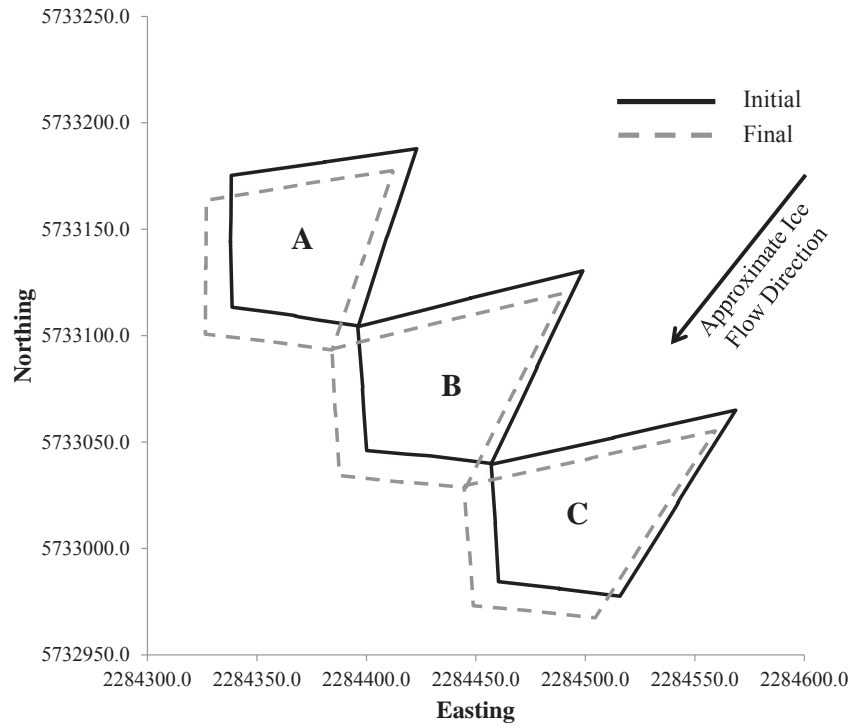


Figure 7.19: Ridge deformation transect showing initial and final (deformed) polygons A to C.

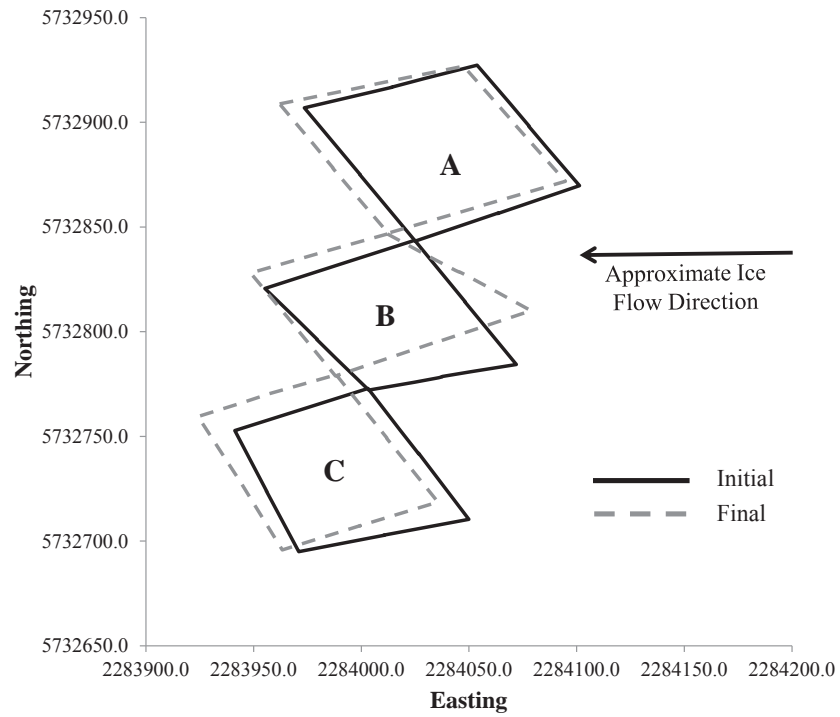


Figure 7.20: Pioneer deformation transect showing initial and final (deformed) polygons A to C.

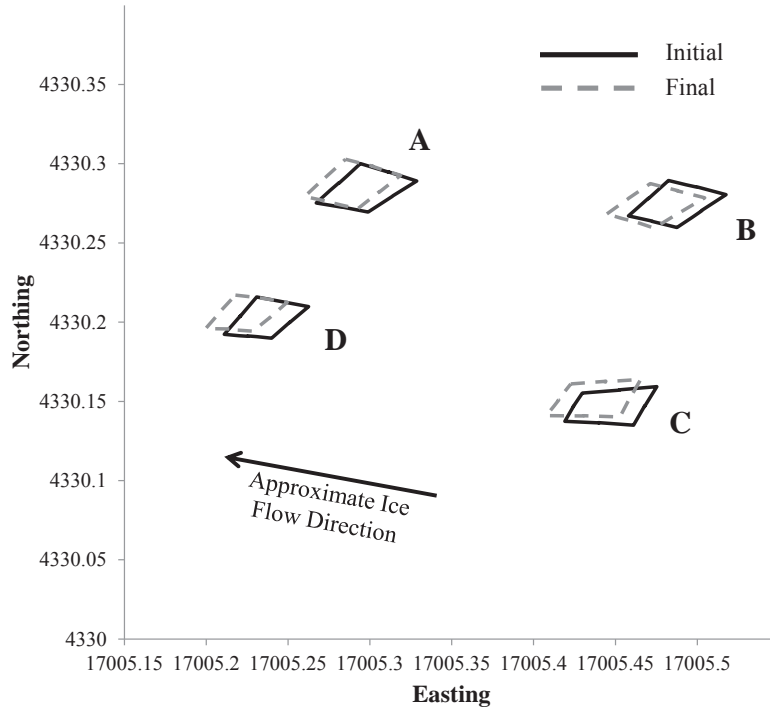


Figure 7.21: Victoria Flat deformation polygons showing initial and final (deformed) polygons A to D.

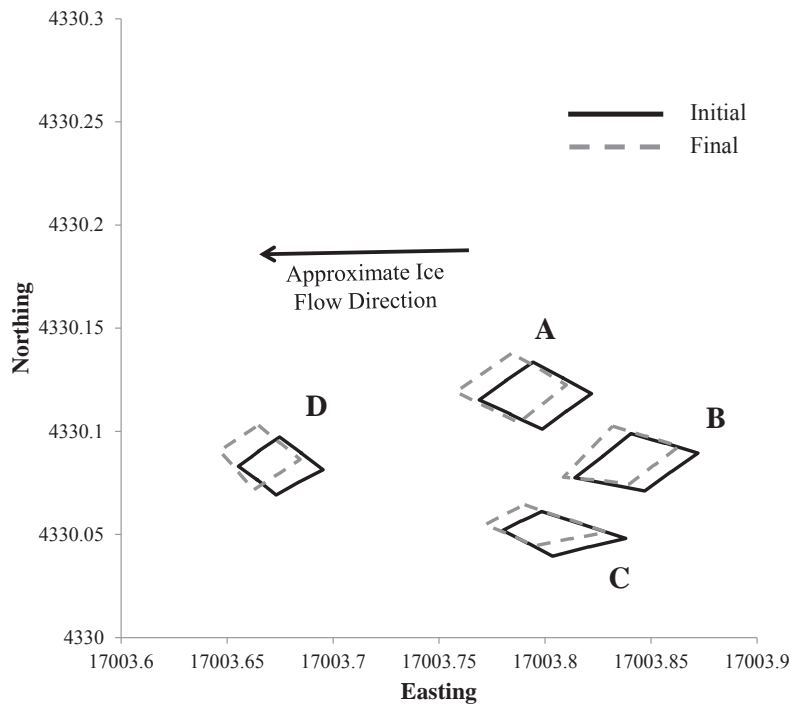


Figure 7.22: Lower Glacier deformation polygons showing initial and final (deformed) polygons A to D.

7.4.3.2 Ice Flow Velocity

Average daily and annual horizontal ice flow velocities have been calculated for each of the strain polygons using the changing position of each individual stake (Table 7.1). Daily velocities have been recorded during the Austral summer. These daily averages have been multiplied by 365 to give an average annual velocity. It must be remembered that these annual velocities will be artificially high due to measurement being taken during the summer ablation season, rather than over the whole year. Ice velocities give a quick indication as to which areas are undergoing compression or extension.

Table 7.1: Average daily (m/d) and annual (m/a) horizontal ice surface velocities of each strain polygon calculated from the changing position of individual stakes.

	Average velocity	
	(m/d)	(m/a)
Albert Glacier		
A	0.88	322
B	0.84	307
C	0.86	314
Pioneer		
A	0.91	333
B	0.85	311
C	0.80	292
Ridge		
A	0.88	321
B	0.92	337
C	0.93	339
Victoria Flat		
A	1.08	397
B	1.07	393
C	1.77	429
D	0.90	328
Lower Glacier		
A	1.42	519
B	1.35	494
C	1.21	442
D	1.18	433

Daily velocities range from 0.8 m/d (Pioneer C) to 1.77 m/d (Victoria C), with the highest average velocities being record on Victoria Flat and the lower glacier, whilst the lowest velocities are observed in the névé. These patterns closely approximate the trends in horizontal ice surface displacement calculated by Herman *et al.* (2011) (Figure 7.23) from feature tracking of ASTER images during the Austral summer of 2006, who

identified increasing velocities above and immediately below the upper and Lower Icefalls with a peak in velocity with the icefalls. A small increase in velocity was also identified as ice passed through the Pioneer Icefall.

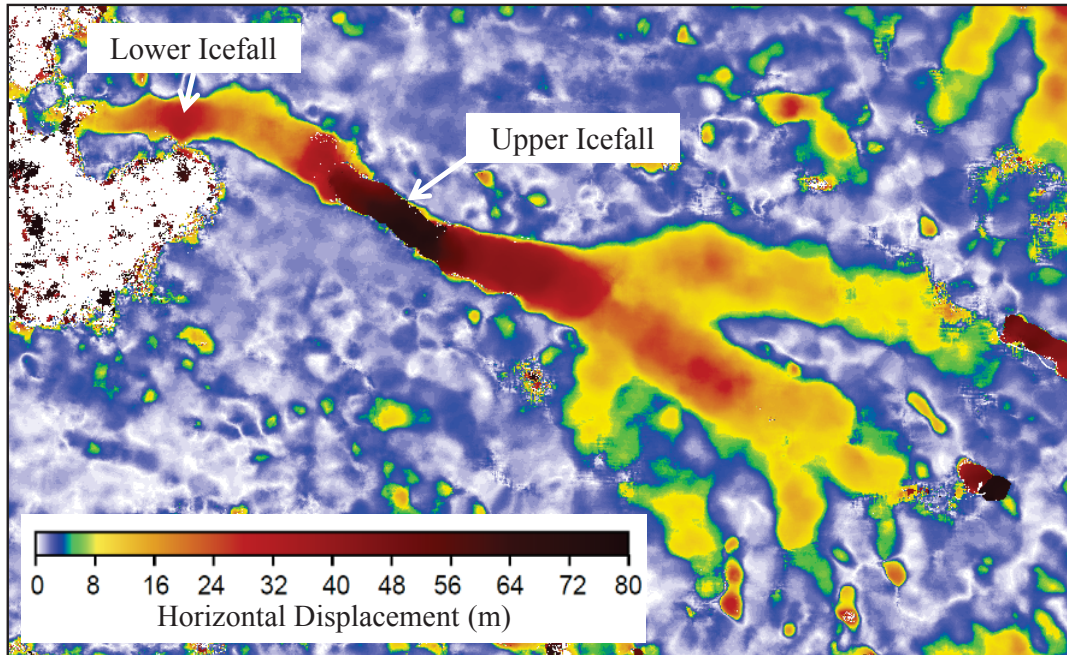


Figure 7.23: Horizontal ice surface displacement of Fox Glacier determined from ASTER images with a 15 m ground resolution over a 15 day period during the Austral summer. Highest velocities (displacement/time) can be seen through the upper and Lower Icefalls with the lowest in the névé (Developed from Herman and others, 2011).

7.4.3.3 Strain Rate

Principal positive strain-rates (Table 7.2) range from 0.048 (Victoria D) to 1.374 (Pioneer B), with only two of the seventeen principal strain-rates showing a negative value, these being Victoria A (-0.157) and Lower Glacier C (-0.142). Positive strain-rates suggest extensional flow for most of the deformation polygons.

The strain-rate method used here assumes homogenous deformation and strain both spatially at all points of the triangles, and temporally at all times of the year. However, Knight (1992) showed that this assumption is incorrect over small areas (e.g. 1–10 m²), but that the method when applied to larger areas (100–1000 m²) does provide a useful approximation of strain.

Table 7.2: Surface-parallel logarithmic strain-rates ($\dot{\epsilon}_1$ and $\dot{\epsilon}_2$), orientation of maximum strain of triangles, shear strain-rates and % surface area change of triangle.

	$\dot{\epsilon}_1$ (a^{-1})	$\dot{\epsilon}_2$ (a^{-1})	Orientation of $\dot{\epsilon}_1$ (°E of N)	Shear strain-rates $0.5(\dot{\epsilon}_1 - \dot{\epsilon}_2)$	Surface area change (%)
Albert Glacier					
A	0.276	-0.425	264	0.350	-0.133
B	0.354	-0.168	272	0.261	0.188
C	0.243	-0.037	260	0.140	0.209
Pioneer					
A	0.436	-0.424	286	0.430	0.012
B	1.374	-0.533	294	0.953	0.886
C	0.480	-0.852	288	0.666	-0.337
Ridge					
A	0.128	-0.168	228	0.148	-0.039
B	0.363	-0.161	230	0.262	0.204
C	0.232	0.063	234	0.085	0.301
Victoria Flat					
A	-0.157	-0.866	260	0.355	-0.957
B	0.280	-0.722	256	0.501	-0.425
C	0.975	-0.239	248	0.607	0.809
D	0.048	-1.186	254	0.617	-1.058
Lower Glacier					
A	0.341	-0.181	266	0.261	0.171
B	0.198	-0.608	254	0.403	-0.398
C	-0.142	-0.623	272	0.241	-0.729
D	1.337	-0.959	275	1.148	0.387

7.4.3.4 Strain Orientation

Orientations (vectors) of principal strains ($\dot{\epsilon}_1$) range from 230° to 294° east of north, and are all approximately parallel to the main flow at each transect location. The strain vectors measured as part of the Victoria Flat and Albert transects display diverging flow of individual polygons suggesting lateral extension of the ice surface. In contrast, the vectors measured as part of the Lower Glacier transect display converging flow of individual polygons suggesting lateral compression.

7.4.3.5 Areal Change

According to Hambrey and Müller (1978), a more representative measure of ice deformation is the percentage change in areal extent of deformation polygons over time. Percentage changes in the area of each polygon measured on Fox Glacier are presented in Table 7.2. An increase in the area of a triangle (two per polygon) is indicated by positive values, with negative values indicating a decrease in area. When

combined with principal strain-rates and orientations, percentage areal change can determine the flow characteristics of surface ice. Increases in area suggest extending flow, whilst decreases in area suggest compressive flow. However, if it is assumed that glacier ice is incompressible, positive values would suggest glacier thinning whilst, conversely, negative values would indicate glacier thickening.

Percentage increases in areal extent range from 0.012 % (Pioneer A) to 0.886 % (Pioneer B), with percentage decreases ranging from -0.039 % (Ridge A) to -1.058 % (Victoria D). Each transect shows at least one polygon which has experienced a decrease in area, with three (A, B and D) of the four polygons constituting the Victoria Flat transect experiencing a decrease in area.

An increase in horizontal surface velocity can be seen both in the measured results from this study and also from the work of Herman *et al.* (2011) as ice travels from the névé down through the Upper Icefall into Victoria Flat and then again through the Lower Icefall to the lower glacier. The lowest surface velocities are recorded in the névé strain transects (Albert Glacier, Pioneer and Ridge) with the lowest recorded in the lower strain transects (Victoria Flat and Lower Glacier). The measured surface velocities are similar to those recorded by Purdie (2005) (0.87 m/d), Ruddell (1995) (0.28-0.7 m/d) and Purdie *et al.* (2008a, 2008b) (0.64 m/d).

Most of the deformation polygons experienced a positive principal strain with vector orientations approximately parallel to the main flow of the glacier at each of the study locations, whilst eight of the seventeen polygons experienced a decrease in overall area. These strain-rates, orientations and percentage areal changes are good indicators of the spatially variable patterns of strain observable on the surface of Fox Glacier.

7.5 Interpretation and Discussion on the Dynamics of Fox Glacier

7.5.1 Ice Velocity

Measured velocities vary spatially across the surface of Fox Glacier, both longitudinally and transversely, although some trends can be identified. A longitudinal trend is observable whereby higher velocities are observable on the surface of Victoria Flat and the lower glacier, compared with the névé. The causes of this longitudinal trend are suggested as being due to three main factors, surface slope, changes to valley geometry, and the ablation gradient.

First, the average surface slope of the main valley glacier is steeper than that of the névé (the only exception being Victoria Flat). This steeper gradient exerts a greater stress on the ice body causing higher velocities (Benn & Evans, 2010). Gradient-related velocity increases are expected to peak within the icefalls as these regions display the steepest surface slope. Velocity within the icefalls has not been recorded during the present research, but these patterns are supported by the work of Herman *et al.* (2011) and Ruddell (1995).

Second, theories of conservation of mass and volume (e.g. Cutnell & Johnson, 2012) can be applied to Fox Glacier, as the glacier transits from the expansive névé to the narrow valley. A rapid increase in ice volume per unit area occurs as the tributary glaciers that form the névé converge into the narrow confines of the main Fox valley. Changes in geometry of the ice body (i.e. loss of mass through ablation, compression of ice or glacier thickening) are unlikely to occur fast enough or to a sufficient extent to counteract this increase in volume and so lateral compression will cause longitudinal expansion, manifested as an increase in velocity of ice flow down the Upper Icefall and into the Fox Valley.

Third, the ablation gradient at Fox Glacier is typical of steep valley glaciers (e.g. Schytt, 1967), with ablation increasing with decreasing elevation toward the snout. Hence, at Victoria Flat and the lower glacier, average temperatures and ablation rates are higher relative to the névé, which causes increases in ice velocity in these zones through the

supply of meltwater to the subglacial zone, facilitating basal sliding (e.g. Müller & Iken, 1973, Jobard & Dzikowski, 2006, Willis, 1995, Palmer and others, 2011).

In addition to the longitudinal trends apparent down-glacier, some transverse and in-transect trends are also identifiable. The lowest velocity (0.9 m d^{-1}) recorded within Victoria Flat occurs toward the true left margin of Victoria Flat and the Lower Icefall (polygon D (Figure 7.22)). Flow is retarded in this area due to friction from the true left valley side and the reorientation of the glacier's aspect. As the glacier turns left at the lower end of Victoria Flat, ice flow on the true left slows relative to that on the true right, which has a longer transit path. Retarded flow is also manifested as a decrease in areal extent of polygon D. The next lowest velocity measured (1.07 m d^{-1}) on Victoria Flat was in the region closest to the base of the Upper Icefall (polygon B (Figure 7.21)). This area experiences longitudinal compressive flow as ice rapidly decelerates due to the sudden change in surface slope between the Upper Icefall and Victoria Flat. In particular, compressive flow experienced in this area is illustrated by the decrease in areal extent of the polygon.

The lowest velocity recorded on the lower glacier (1.18 m d^{-1}) was in the region closest to the terminus (polygon D (Figure 7.22)). In this area compression is occurring as the snout of the glacier flows into the proglacial sandur, causing a rapid decrease in velocity. This decrease in velocity is also responsible for the development of the zone of thrusting and reverse faulting (*refer Section 4.3.2.5*).

The second lowest velocity (1.21 m d^{-1}) recorded in the lower glacier deformation transect was in the region to the true left (polygon C (Figure 7.22)). This lower velocity coincides with the only semi-permanent area of supraglacial debris cover on the lower glacier, the medial moraine (*refer Section 5.5.2*), which prevail from the Lower Icefall to the terminus. As the thickness of supraglacial debris here (generally $>0.1 \text{ m}$) easily exceeds the minimum thickness required for producing an insulation effect at Fox Glacier (e.g. Brook & Paine, 2012), ablation rates are significantly reduced compared to the adjacent debris-free ice (e.g. Braun and others, 1993, Mattson and others, 1993, Brook & Paine, 2012). This may, in turn, decrease the supply of meltwater to the subglacial zone in this sector of the glacier, potentially diminishing meltwater-induced basal sliding, although this is a tentative supposition.

7.5.2 Areal Change

No patterns are discernible in the change in areal extent of the deformation polygons measured in the névé. Each of the three névé transects (Albert Glacier, Pioneer and Ridge) experienced a decrease in areal extent for one of their polygons, and an increase for each of the other two polygons which made up the strain transects. The total increase in area of each of these transect relative to the small amount of areal decrease suggests that either snow and firn in the areas of the névé surveyed is deforming too slowly to experience a substantial change in areal extent over the study period; or, that these areas of ice move through the system relatively unchanged until they reach the Pioneer Icefall.

Three of the four polygons measured on Victoria Flat experienced an overall decrease in areal extent, suggesting compression in this area. Polygon D, located close to the true left margin of Victoria Flat and the top of the Lower Icefall, experienced the greatest reduction in area (-1.058 %). This reduction can be explained by the reorientation of the glacier to a more westerly azimuth. At this point, ice decelerates and compresses on the true left, whilst expansion and an increase in velocity occurs on the true right as the glacier here flows through a longer transit distance.

On the lower glacier, polygon D closest to the snout experienced an overall increase in area (+0.387 %), suggesting horizontal expansion of the ice surface at this point. However, the thrust fault zone present in this area suggests that this area is actually experiencing longitudinal compression. It is therefore suggested that the increase in area of the polygons is due to lateral expansion of the glacier terminus. This is consistent with the splaying crevasses evident in the lower glacier, (*refer Section 4.3.2.4*).

Polygons B and C on the lower glacier both experienced a decrease in areal extent (-0.398 % and -0.729 %, respectively), and this is interpreted as being due to their locations immediately below the Lower Icefall in the case of polygon B, and toward the true left margin of the glacier in the case of polygon C. Longitudinal compressive flow and a narrow valley width below the Lower Icefall explain the areal compression of both polygon B and C.

7.5.3 Strain Rates

Unlike ice velocity and areal change, very few trends can be observed in the strain rate data. Each polygon experienced principal strain rates ($\dot{\epsilon}$) within approximately the same order of magnitude (0.128 a^{-1} to 0.975 a^{-1}) with the only exceptions being Pioneer B (1.374 a^{-1}), Lower Glacier D (1.337 a^{-1}), and Victoria Flat D (0.048 a^{-1}). Victoria Flat A (-0.157 a^{-1}) and Lower Glacier C (-0.142 a^{-1}) are the only two strain polygons to experience a negative principal strain.

The substantially larger strain measured at the Pioneer B polygon may be explained by its location at the centre of the Pioneer transect which is oriented transverse to the flow of the Albert Glacier, and would therefore be expected to experience the highest velocity of the transect. This is not supported by the measured velocities in that location, however, with the highest velocities being recorded within the Albert A (0.88 m d^{-1}) and Albert C (0.86 m d^{-1}) polygons (*refer Section 7.4.3.1*). The high Lower Glacier D polygon strain rate and shear strain rate (1.148 a^{-1}) help to explain the presence of the zone of thrusting close to the terminus in the lower glacier, probably due to the resistant barrier created by the proglacial sandur.

The only distinct pattern observable within the measured strain data is that of the strain vectors. Orientations (vectors) of principal strains ($\dot{\epsilon}_1$) range from 230° to 294° east of north, and are all approximately parallel to the main flow at each transect location.

7.5.3.1 Fox Glacier Strain Rates in a Global Context

The maximum extensional and compressive strain rates ($\dot{\epsilon}$) recorded on Fox Glacier can be compared with results obtained by researchers undertaking studies on a range of glacier systems globally (Table 7.3). Most previous research has been undertaken on glaciers in the polar regions in locations such as Antarctica, northern Canada and Alaska, and Svalbard (Spitsbergen) in the high Arctic, making direct comparisons with mid latitude temperate maritime glaciers difficult.

Table 7.3: Previous strain rate research undertaken on a variety of glacier types and locations.

Location	Type of Glacier	Maximum Extensional		Maximum Compressive	
		Strain Rate a^{-1}	Strain Rate a^{-1}	Strain Rate a^{-1}	Strain Rate a^{-1}
Austerdalsbreen, Norway	Temperate, Alpine Valley	0.32		-0.97	Nye (1959)
Saskatchewan Glacier, Alaska	Polar, Icefield Outlet	0.15		-0.19	Meier (1960)
Taku Glacier, Alaska	Polar, Tidewater	0.11		-0.13	Wu & Christensen (1964)
Mendenhall Glacier, Alaska	Polar, Calving, Icefield Outlet	0.31		-0.18	Higashi (1967)
Hinterisferner, Austria	Temperate, Alpine Valley	0.08		-0.15	Ambach (1968)
Athabasca Glacier, Canada	Polar, Icefield Outlet	0.16		-0.12	Raymond (1969)
Meserve Glacier, Wright Valley, Antarctica	Polar, Icecap Outlet	0.02		*	Holdsworth (1969)
Kaskawulsh Glacier, Alaska	Polar, Icefield Outlet	0.29		-0.29	Anderton (1973)
Blue Glacier, Washington	Temperate, Alpine Valley	0.12		-0.1	Meier <i>et al.</i> (1974)
Griegletscher, Switzerland	Temperate, Alpine Valley	0.1		-0.16	Hambrey & Müller (1978)
White Glacier, Canada	Polar, Outlet	0.16		-0.43	Hambrey & Müller (1978)
Urumqi Glacier Number 1, China	Cold Based, Alpine	0.06		*	Echelmeyer & Wang (1987)
Storglaciären, Sweden	Polythermal, Alpine	0.02		*	Hooke <i>et al.</i> (1989)
Jutulstraumen, Antarctica	Polar, Outlet	0.05		*	Hoydal (1996)
Unterargletscher, Switzerland	Temperate, Alpine Valley	0.05		*	Guddmundsson <i>et al.</i> (1997)
Haut Glacier d'Arolla, Switzerland	Temperate, Alpine Valley	0.015		*	Hubbard <i>et al.</i> (1998)
Glacier Upsala, Patagonia	Mountain, Calving Outlet	0.22		*	Naruse & Skvarca (2000)
Amery Ice Shelf, East Antarctica	Polar, Calving Iceshelf	0.1		*	Young & Hyland (2002)
Hiorthfjellet Glacier, Svalbard	Polar, Valley	8×10^{-5}		*	Ødegård <i>et al.</i> (2003)
Shirase Glacier, East Antarctica	Polar, Calving Icecap Outlet	5×10^{-4}		*	Pattyn & Naruse (2003)
Bas Glacier d'Arolla, Switzerland	Temperate, Alpine Valley	0.126		-0.152	Goodsell (2005)
Koryto Glacier, Russia	Polar, Valley	*		-0.36	Sugiyama <i>et al.</i> (2005)
Fox Glacier, New Zealand	Temperate, Maritime Valley	8.57		-8.034	Appleby <i>et al.</i> (2010)

*No data

Those studies that have been undertaken on temperate, alpine-type glaciers have reported strains at a much lower rate than those that have been recorded as part of this study. For example, Nye (1959) reported strain rates of 0.32 a^{-1} on Austerdalsbreen, Norway, whilst Meier *et al.* (1974) reported strain rates of 0.12 a^{-1} on Blue Glacier, Washington; each of which are a full 1.0 a^{-1} lower than Fox Glacier. The lowest strain rate recorded on a temperate, alpine-type glacier was reported by Hubbard *et al.* (1998) who reported a maximum extensional strain rate of 0.015 a^{-1} on the haut Glacier d'Arolla, Switzerland.

The strain rates measured in the present study are not as high as those recorded by Appleby *et al.* (2010), also on Fox Glacier. However, that study concentrated solely on the lower glacier and Victoria Flat, and was for a shorter study period (<30 days). For these reasons, the extrapolated annual strain rates (a^{-1}) may be exaggerated.

In considering the results for the present study, limitations of the data should be noted. First, the strain data were calculated from a limited temporal (<60 days) and spatial extent, and second, the time of year (January/February) is at the peak of the ablation season, when ablation is highest, as are velocities (Purdie and others, 2008a). Indeed, the relatively high temperatures during the ablation season create large quantities of melt water which help increase ice velocity (0.5 to 1.4m/day) (Purdie and others, 2008a, Purdie and others, 2008b) and strain. Hence, as this study was undertaken over a short period, extrapolating these results to the entire year is problematic, considering the highly seasonal ablation and velocities recorded at Fox Glacier in the past. Indeed, a large intra-annual variation in velocity (Purdie and others, 2008b, Purdie and others, 2008a) does occur, and so the recorded strain rates give only a 'snap-shot' of the summer melt season. If the study period was extended to include the entire year, strain rates are likely to be lower, but more representative and robust. Despite this, it is likely that Fox Glacier experiences higher than average velocity and strain rates even during the winter months, as the temperature remains relatively high and the large volume of winter precipitation in the form of rain experienced on the West Coast will continue the basal lubricating effect seen with summer melt water.

Chapter 8 : General Discussion

8.1 Introduction

Chapter Eight draws on *Chapters Four, Five, Six and Seven* to provide a general discussion on the relationship between the flow dynamics and structural glaciology of Fox Glacier. The chapter concludes by providing a synthesis of the ‘life-cycle’ of a unit of ice as it passes through the glacier system.

8.2 Relationship between Dynamics and Structure

Although the structures identified on Fox Glacier are typical of those reported from other valley glaciers (e.g. Hambrey & Lawson, 2000), the spatial distribution of structures on Fox Glacier is difficult to relate unequivocally to measured strain-rates. The continuous layering evident in the upper-most part of the study area is interpreted as primary stratification (S_0), and the presence of highly tilted layers, visible in crevasse walls as foliation (S_1) within the Lower Icefall, supports these difficulties. It would appear that the original snow stratification in the névé is heavily modified by melting and refreezing. A winter’s accumulation typically consists of a layer of high-density clear blue ice representing re-frozen slush as the base of the snowpack, and a layer of low-density coarse ice representing snow that has undergone wetting and refreezing (e.g. Müller, 1962). The primary stratification (S_0) is then tilted and deformed by transport from the broad névé into the narrow valley trunk, and then via flow through the upper and Lower Icefalls. Foliation (S_1) is a pervasive planar structure found in almost all glaciers (Hambrey & Lawson, 2000) and two alternative theories of foliation formation have been proposed: First, foliation may form due to dynamic recrystallization of ice crystals parallel to the maximum strain-rate tensor, potentially cross-cutting primary stratification (e.g. Allen and others, 1960). Second, foliation may be transposed from existing inhomogenities such as primary stratification or crevasses, under laterally compressive and longitudinally tensile stresses (Hambrey & Milnes, 1977, Hooke & Hudleston, 1978). Both explanations are possible at Fox Glacier, because there is visible contact and cross-cutting relationships between primary

stratification and foliation. In addition, primary stratification appears to become progressively folded and rotated as it passes down the Lower Icefall toward the snout.

Crevasses and crevasse traces (S_2) are a feature of most glaciers (Hambrey and others, 2005). The pattern of crevassing in Fox Glacier is typical of many valley glaciers, with zones of extending flow causing crevassing in the upper and Lower Icefalls. Chevron and splaying crevasses are prevalent toward the margins, with transverse crevasses in areas of longitudinal extension and thinning. Longitudinal crevasses are also prevalent near to the snout, where the glacier is extending laterally, in response to the widening channel geometry. Crevasses generally form perpendicular to the direction of maximum extending strain-rate, although some stand at an angle to the direction of maximum extension as a result of either rotation, or because of inhomogeneous strain within a strain triangle (Hambrey & Müller, 1978). Furthermore, Hambrey and Müller (1978) have outlined that no simple relationship exists between strain-rate and fracture. They reported strain-rates as high as $\dot{\epsilon}_1 = 0.16 \text{ a}^{-1}$ at White Glacier, Canada, while crevasses were completely absent. Vaughan (1993) noted that the variation in tensile strength of ice and so the strain rate at which it fractures and produces crevasses, could be ascribed to differences in crystal structure, impurity content, density profiles or other local variables. Vaughan (1993) also found that the critical strain rates for failure of ice can vary by a factor of 500. In addition, van der Veen (1999) described how the orientation of crevasses may differ by up to 20° from the optimum direction according to strain rates, suggesting that the relationship between strain and structure is not a simple one. Similarly at Fox Glacier, the relationship between crevassing and strain appears highly complex. In particular, the dense pattern of crevasse traces is primarily due to the passage of ice units through three icefalls. Although some of these structures may be relict, being transported passively toward the terminus, some could be 'close to crevassing', where crevassing may be imminent (e.g. Vaughan, 1993). These traces may then be reactivated as longitudinal or splaying crevasses, or as arcuate thrust planes (S_3) near the snout.

Maximum principal strain-rates ($\dot{\epsilon}_1$) calculated at Fox Glacier were of the order of 0.048–1.374 a⁻¹, which falls between typical values for temperate ($\dot{\epsilon}_1 = 0.2$ a⁻¹) and surging glaciers ($\dot{\epsilon}_1 = 36$ –100 a⁻¹), as reported by Hambrey and Lawson (2000). This is probably indicative of the high surface velocities at Fox Glacier (>1 m d⁻¹), and rapid response time (<10 yr) of this 12.7 km-long glacier (Purdie and others, 2008b). The correspondence of measured strain-rates to structure is not obvious, with velocity and percentage area change of strain polygons showing a stronger relationship than measured strain-rates. There are several reasons why relating structures to strain-rates is problematic: (1) the orientation of structures reflects the strain history an ice unit has experienced; (2) structures may develop at depth (e.g. 'blind thrusts'; Hambrey and others, 1999), and not extend to the glacier surface even though the glacier is in an extending flow regime; and (3) a structure may be reactivated at strain-rates lower than, or at a different orientation to, those required for their original formation (Hambrey & Lawson, 2000).

8.3 The Evolution of Structures on Fox Glacier

A synthesis of the development of Fox Glacier's contemporary surface structures, including relationships between dynamics, structure and sedimentology, is presented to describe the 'life-cycle' of a unit of ice as it flows through the glacier. As this unit of ice transits through the glacier system, new structures are formed whilst existing structures are deformed and altered, in some cases forming entirely new features. A schematic model of the structural evolution of Fox Glacier is shown in Figure 8.1 to aid in interpretation of this synthesis.

To begin with, snow accumulates in the névé (Figure 8.1 A), allowing for the formation of primary stratification (S_0) and firn. Each layer of stratification varies in its thickness and structure according to synoptic and topographic conditions at the time of formation (e.g. Purdie and others, 2011a). At the headwall of the névé, clastic debris is introduced to the glacier system via sporadic rockfall onto the glacier surface. This debris becomes incorporated into firn either by falling directly into randclufts and bergshrunds or by being covered with snowfall (e.g. Goodsell and others, 2005b).

Crevasses (S_2) are first seen in the névé, and develop in areas of variable topography and surface slope as ice flow velocity increases, causing fracture of the surface. The orientation of these crevasses is controlled by localised topography and slope (Pioneer Ridge, for example), which dictates the direction in which firn flows, and therefore the orientation of crevasses visible on the névé surface. These localised flow patterns cause convergent flow in some parts of the névé. Indeed, it is possible in some areas to identify the convergent flow of distinct units separated by obvious flow unit boundaries. These flow unit boundaries emanate from ridges and rock buttress that protrude into the Fox Glacier névé from the main divide of the Southern Alps. Approximately halfway down the névé, ice flows over the Pioneer Icefall, the first of the icefalls on the journey through Fox Glacier, where longitudinal extensional flow causes a zone of dense crevassing of the névé surface.

As ice flows down the Upper Icefall (Figure 8.1 B), an increase in velocity causes extensional flow leading to further transverse crevassing that typifies icefalls. The narrowing of the valley at this point relative to the expansive width of the névé causes lateral compression of the ice which, in turn, causes rotation of primary stratification. Within this region, the debris incorporated into the glacier within the névé becomes concentrated.

At the lower end of the Upper Icefall, the decrease in slope gradient created by the over-deepening at Victoria Flat (Figure 8.1 C) causes longitudinal compressive flow allowing the development of pressure wave ogives (e.g. Haeferli, 1951, 1957, Atherton, 1963) and conditions for enhanced shear. This enhanced shear is the cause of the highly foliated ice (S_1), the surface expression of which is identified as band ogives (e.g. Posamentier, 1978, Goodsell and others, 2005c). These weak band ogives can be followed for the full length of Victoria Flat, increasing in curvature until they reach the Lower Icefall. In addition, compressive flow causes the closure of most of the transverse crevasses formed higher up in the Upper Icefall, producing crevasse traces (S_2) which, down-glacier from this point, are omnipresent on the surface of the glacier.

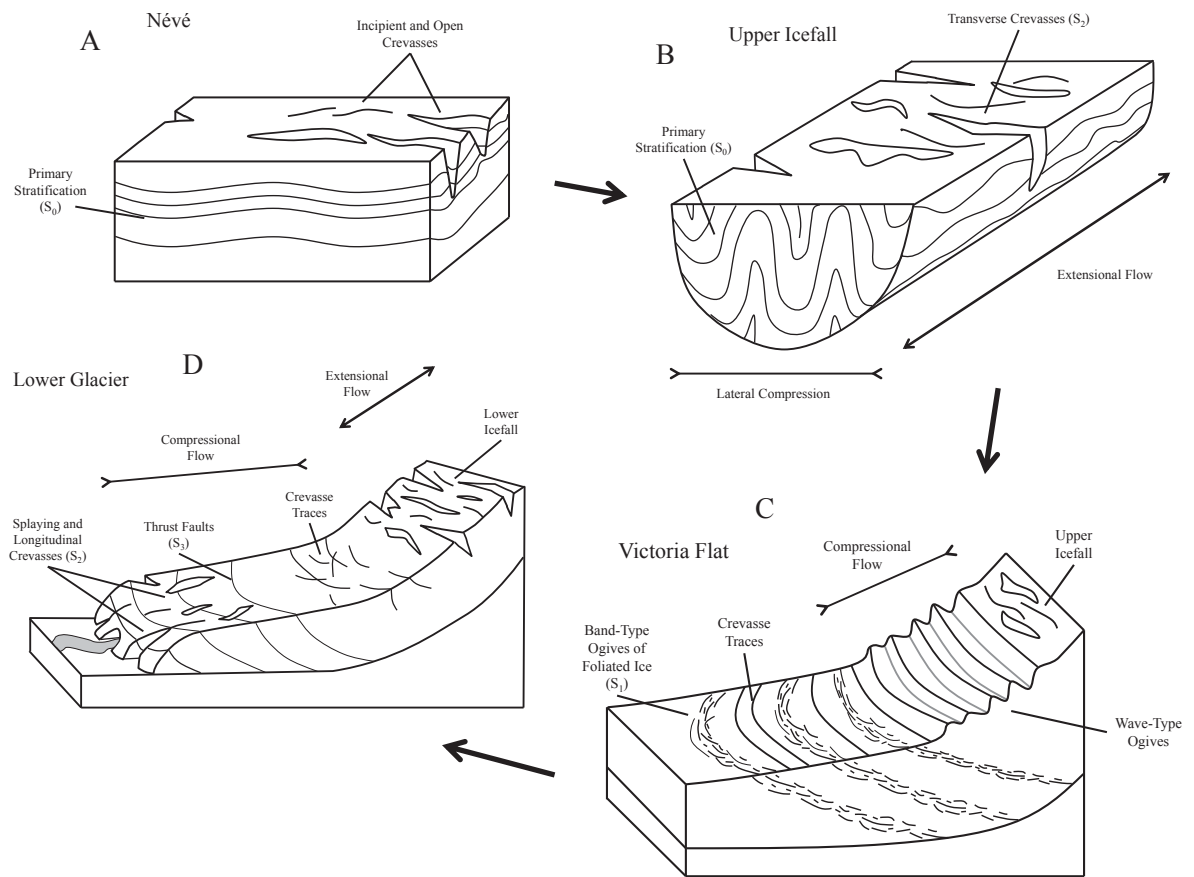


Figure 8.1: Schematic diagram of the evolution of surface structures of Fox Glacier, beginning in the névé (A) then moving down through the Upper Icefall (B), Victoria Flat (C) and finally the lower glacier (D).

Across the surface of Victoria Flat, a well-developed dendritic drainage network forms in response to increasing ablation below the ELA and rainfall. This is possible due to the gentle topography and closure of many of the transverse crevasses as previously mentioned. For most of the length of Victoria Flat, the surface of the glacier receives more debris in the form of rockfall from Paschendale Ridge which forms the true left (southern) Fox valley wall. At the far right margin of Victoria Flat, longitudinal foliation (S_1) is evident immediately beneath the Victoria waterfall. This foliation is formed from primary stratification rotated and laterally compressed in the Upper Icefall (e.g. Lawson and others, 1994, Goodsell and others, 2005c).

Immediately after the glacier changes orientation to a westerly azimuth at the lower end of Victoria Flat, ice velocity again increases as ice transits down the Lower Icefall into the lower glacier (Figure 8.1 D). Extensional flow in the Lower Icefall once again causes the formation of transverse crevasses; some of which are reactivated crevasses from higher up the glacier, whilst some may be entirely new features. Within the icefall towards the true left of the glacier, the debris incorporated in the névé and concentrated in the Upper Icefall is exhumed via ablation to form the medial moraine (e.g. Eyles & Rogerson, 1978, Vere & Benn, 1989) which then pervades to the terminus, gradually increasing in height as more and more ice is ablated.

At the base of the Lower Icefall, ice velocity rapidly decreases as the snout of the glacier ‘pushes’ into the proglacial sandur. This rapid deceleration causes longitudinal compressive flow which, again, closes most of the transverse crevasses allowing for the development of an intricate pattern of crevasse traces. Many of these cross-cut pre-existing crevasse traces formed at the base of the Upper Icefall. Close to the snout, longitudinal compressive flow causes reverse faulting of the ice (e.g. Hambrey and others, 1999, Goodsell and others, 2005b, Murray and others, 2000b, Hambrey & Dowdeswell, 1997), with thrust planes also observable on the surface, along which subglacial material is elevated to supraglacial positions (e.g. Glasser & Hambrey, 2003, Hambrey and others, 1999, Glasser & Hambrey, 2002a).

As well as being visible below the Upper Icefall at Victoria Flat, weak band ogives are also observable on the lower glacier below the Lower Icefall. Similarly, it is proposed that these ogives are formed due to enhanced shear within the Lower Icefall; forming

highly foliated ice (omitted from Figure 8.1 D for clarity) which is then thrust to the ice surface.

Chapter 9 : Conclusions

9.1 Introduction

The structures identified on Fox Glacier during this study display similar patterns to structural features of temperate valley glaciers reported in other studies. The type and pattern of structures has been successfully determined using a combination of field observations, analysis of remotely sensed images and ground-penetrating radar. The structural glaciology of Fox Glacier primarily consists of: the development of primary stratification (S_0) in the névé; the development of foliation (S_1); the folding (F_1) of primary stratification and foliation (S_1); intersecting sets of crevasse traces (S_2); the formation of transverse crevasses (S_2) at the top of, and within, the Pioneer, Upper and Lower Icefalls; wave-type and weak band-type ogives forming mainly below the Upper Icefall on the surface of Victoria Flat; Chevron and splaying crevasses (S_2) intersecting the glacier margins; longitudinal and splaying crevasses (S_2) near to the snout; and the development of arcuate up-glacier dipping fractures as part of a thrust (S_3) complex near the snout.

Three distinct structural domains have been studied on Fox Glacier (Névé, Victoria Flat and Lower Glacier), each separated by an icefall. Each of these domains are unique in their topography, the types of surface structure that are observed and the increasing degree of structural complexity and deformation experienced by ice as it transits through the structural domains from the névé down to the snout.

An apparent similarity exists between structures identified on the surface of Fox Glacier and those identified on polythermal glaciers. This suggests that rather than basal thermal regime being a key control on structure, the structural patterns evident in valley glaciers may be more closely linked with valley geometry. In particular, two factors appear to be important in terms of valley geometry: (1) nuances of the subglacial bedrock long-profile; and (2) the size of the accumulation zone relative to the valley 'trunk'. Regarding the bedrock long-profile, steps in the profile cause a steepening of surface gradient, and associated increases in velocity. With regards to the relative sizes of the

accumulation zone and valley trunk, the high steady state accumulation area ratio (AAR) of Fox Glacier (~ 0.8) means that the rapidly-accumulating precipitation ($\sim 15 \text{ m a}^{-1}$) within adjacent basins in the névé is laterally compressed as it is discharged down the valley trunk. In this sense, a diminished ‘accommodation space’ leads to the formation of a myriad of structures as ice transits down a constrictive, steep-sided channel.

Specific conclusions to the research are determined by revisiting the aims, objectives and research questions identified in *Chapter One*, and can be summarised as follows:

- 1) No single theory of ogive formation is sufficient to explain the processes by which ogives are produced on Fox Glacier. The modified thrusting theory of Posamentier (1978) as described by Goodsell (2005) along with the rhythmic compression hypothesis of Haeferli (1951, 1957) are proposed as the most appropriate theories for Fox Glacier.
- 2) Ice deformation and structure have an important influence on the transport and deposition of sediments at Fox Glacier. For example, thrusting has been shown to be actively elevating subglacial material to a supraglacial position in the lower glacier, whilst a variation on fluted moraines are suggested as forming in the proglacial zone due to the structure and processes occurring beneath the ice.
- 3) The medial moraine emanating from the Lower Icefall and pervading to the true left of the terminus, corresponds with the ablation-dominant model (AD2) proposed by Eyles and Rogerson (1978). This indicates debris is ingested into the glacier above the ELA, is then passively transported through the glacier system before re-emerging supraglacially below the lower-most icefall.
- 4) The origin of thrust planes in the lower-section of Fox Glacier can be explained by the theory of a longitudinally compressive flow regime created by a topographical barrier (e.g. Glasser & Hambrey, 2003, Hambrey and others, 1999); the barrier in the case of Fox Glacier being created by the proglacial sandur.

- 5) Current deformation models that explain the formation of smaller scale structures such as foliation, folds and crevasse traces at other alpine glaciers are accepted as appropriate models to explain the processes occurring at Fox Glacier.
- 6) A limited relationship is observable between surface structures and two-dimensional strain-rates on the surface of Fox Glacier, although the locations and orientations of crevasses do correspond to principal strain orientations and compressive and extensional flow regimes.

9.2 Glacier Dynamics and Structure: Summary

Strain-rates measured on the surface of Fox Glacier are higher than those reported for both cold-based glaciers and warm-based alpine-style glaciers in the European Alps. However, strain rates are lower than values typically reported for surging glaciers during surge phases. Unequivocal relationships between measured strain-rates and structures are not evident from this research. This may be because many structures are undergoing passive transport down-glacier, and do not reflect the prevailing local stress regime. Or, some structures, such as crevasse traces, may be close to crevassing, without crevasses actually forming. In addition, the resolution of measurements and the size of strain polygons may be insufficient to capture strain patterns at smaller or larger scales, supporting the work of Knight (1992). In reality, for a number of strain polygons, measurements of surface area change provide a closer, albeit tentative correspondence between the prevailing stress field and the local stress pattern, as indicated by structure.

9.3 Broader Implications of this study

Results and findings from this study are a useful addition to the accumulating body of work that has emerged over the last decade on the South Westland glaciers. The vast majority of that research has typically focused on glacier fluctuations in response to climate, or has attempted to link late-glacial moraine-forming events to glacier dynamics. In contrast, the present study has attempted for the first time in New Zealand, to characterise and explain the spatial pattern of structures within a valley glacier in its

entirety from the névé to the snout. While such studies have been attempted on several northern hemisphere ice masses, of lower mass flux, this has rarely been attempted in the Southern Hemisphere. Despite the limitations of the study, and issues associated with meltwater and GPR, results gained and the methods applied could be implemented to many different glaciological studies. For the sake of brevity, only three of several possible broader implications are outlined below.

First, a combination of ground-penetrating radar, surface strain analysis and the mapping of evolving features might be employed to inform investigations into future ice shelf stability, which have typically focused on time lapse analysis of satellite images (e.g. Glasser and others, 2009). Research on ice shelves is becoming ever more important due to predictions of future sea level rise and mass loss from polar ice sheets (e.g. Wild and others, 2003, Overpeck and others, 2006). The present study has shown that a combination of different research tools can be used to elucidate information about the structural deformation and evolution of glaciers.

Second, the use of ground-penetrating radar (GPR), despite its limited value on southwestland glaciers, could be employed elsewhere for identifying spatial variations in snow and firn accumulation. Data can be rapidly collected along transect lines and with adequate ground-truthing, and post-processing, the technique could be applied over large accumulation basins to determine volumetric quantities of snow and/or firn. Application of GPR to snow stratigraphy could be useful in the field of water resources, particularly in remote areas such as the Himalaya, Karakorum and Central Asia (e.g. Stokes and others, 2007, Popovnin & Rozova, 2002, Bolch and others, 2012) or alpine zones in New Zealand where such data is difficult to estimate across large areas due to marked spatial differences in accumulation (Purdie & Bardsley, 2010). Furthermore, deployment of GPR from aerial platforms (e.g. helicopter, light aircraft) to obtain snow stratigraphic data in such areas would allow rapid data collection over large surface areas (cf. Lalumiere, 2006).

Third, the findings also indicate that there are important parallels between analyses of the structural development of glaciers, and the field of structural geology (Allen and others, 1960, Hambrey & Lawson, 2000, Herbst & Neubauer, 2000). In particular, the development of brittle structures such as thrust and reverse faults can be observed in

temperate maritime glaciers over weeks, which is several orders of magnitude less than many tectonic structures. Likewise, the development of foliation and folding can potentially be observed over a space-time continuum of ~3 km, equivalent to only a few years in terms of ice transit time's down-valley. Moreover, ice structures are denuded by ablation at different rates as they are produced, analogous to denudation in areas of crustal shortening and tectonic uplift. Hence, field analyses of deformation within alpine glaciers may prove a useful proxy for structural geologists, for testing either empirical observations or numerical models of the development of geological structures (Di Toro and others, 2012).

9.4 Future Work at South Westland Glaciers

Whilst undertaking research on the structure and dynamics of Fox Glacier, the need for future work in certain areas has become apparent:

- 1) Coring along with low frequency ground-penetrating radar or radio echo sounding surveys of Victoria Flat could be used to determine the extent of the overdeepening suggested at this site. This would allow for a more accurate estimation of the total volume of Fox Glacier and better inform terminus reaction terms and future prediction of mass loss under changing climate.
- 2) Strain and velocity measurements of 'The Trough' will help to determine the extent of flow separation occurring next to the Upper Icefall.
- 3) Investigations into the presence or absence of medial debris septa at flow unit confluences within the Fox Glacier névé will better inform knowledge of the fracture, entrainment and transport histories of sediments. For example, supraglacial rock wall erosion rates in accumulation zones are difficult to quantify due to access issues (Ward & Anderson, 2010). Indeed, medial moraines and associated englacial debris serve as conveyor systems, bringing supraglacial rockfall debris from accumulation-zone valley walls to the moraine crest in the ablation zones. Hence, application of cosmogenic ^{10}Be in amalgamated rock samples from active, ice-cored medial moraines such as at Fox Glacier could be used to constrain glacial valley sidewall back-wearing rates.
- 4) A more spatially and temporally expansive study of the dynamics of Fox Glacier would allow for a more accurate estimation of annual strain rates and may prove

more useful when attempting to identify the relationships between dynamics and structure of temperate maritime glaciers. In conjunction with a geodetic survey proposed above, application of a broadband seismometer and geophones (e.g. would allow determination of acoustic sources and locations, delineating conditions conducive to fracture propagation (e.g. subglacial meltwater availability), deformation and development of brittle structures (West and others, 2010).

- 5) Related to the above, a detailed investigation into the englacial and subglacial drainage networks operating within the Fox Glacier system would be pertinent. Ablation and velocity both show strong seasonality at Fox Glacier, and nearby Franz Josef Glacier, and how this seasonality relates to different combinations of hydrological inputs (melt, direct precipitation, runoff) is intriguing. Water input probably controls basal sliding rates, and hence surface strain, but also probably impacts on fracture propagation and crevasse enlargement (Benn and others, 2009). Likewise, such fractures allow water flow to the subglacial zone, enhancing basal sliding. To this end, dye tracing experiments using an array of dye-injection points within the system and a detailed analysis of return curves, in conjunction with geodetic analyse of deformation, would prove a very fruitful study.
- 6) Most recently, both Franz Josef and Fox Glaciers have entered into a phase of retreat and down-wasting, with the increasing emergence of debris on the surface in the ablation zone, as shown by results in the present study. Using a regional scale energy balance model, Anderson and Mackintosh (2012) found that in the central Southern Alps, debris covers reduce glacier mass balance sensitivity. At South Westland glaciers, understanding the effects of debris cover on ablation is very important, because when supraglacial debris covers a significant proportion of the ablation zone, the glacier mass balance may become significantly less negative, influencing the behaviour of the terminus. This may, in turn, generate a terminal moraine that has only a partial climate-related cause (Reznichenko and others, 2011). Hence, analysis of the effect of the enlarging areas of debris over on the dynamics of both glaciers would be opportune.

References

- Adams, J. 1978. Late Cenozoic erosion in New Zealand. PhD Thesis, Victoria University of Wellington.)
- Agassiz, L. 1847. *Système glaciaire ou recherches sur les glaciers, pt I: Nouvelles études et expériences sur les glaciers actuels*
Paris, V. Masson.
- Allen, C., B. Kamb, M. Meier and R. Sharp 1960. Structure of the lower Blue Glacier, Washington. *Journal of Geology*, **68**: 601-625.
- Alley, R. 1992. Flow-law hypotheses for ice-sheet modelling. *Journal of Glaciology*, **38**: 200-207.
- Alley, R., K. Cuffey, E. Evenson, J. Strasser, D. Lawson and G. Larson 1997. How glaciers entrain and transport basal sediment: physical constraints. *Quaternary Science Reviews*, **16**: 1017-1038.
- Almond, P., N. Moar and O. Lian 2001. Reinterpretation of the glacial chronology of South Westland, New Zealand. *New Zealand Journal of Geology and Geophysics*, **44**: 1-15.
- Anderson, B., W. Lawson and I. Owens 2008. Response of Franz Josef Glacier Ka Roimata o Hine Hukatere to climate change. *Global and Planetary Change*, **63**(1): 23-30.
- Anderson, B., W. Lawson, I. Owens and B. Goodsell 2006a. Past and future mass balance of 'Ka Roimata o Hine Hukatere' Franz Josef Glacier, New Zealand. *Journal of Glaciology*, **52**(179): 597-607.
- Anderson, B. and A. Mackintosh 2006. Temperature change is the major driver of late-glacial and Holocene glacier fluctuations in New Zealand. *Geology*, **34**(2): 121-124.
- Anderson, B. and A. Mackintosh 2012. Controls on mass balance sensitivity of maritime glaciers in the Southern Alps, New Zealand: The role of debris cover. *J. Geophys. Res.*, **117**(F1): F01003.
- Anderson, R., P. Molnar and M. Kessler 2006b. Features of glacial valley profiles simply explained. *Journal of Geophysical Research*, **111**(F01004): 1-14.
- Anderson, R.S. 2000. A model of ablation-dominated medial moraines and the generation of debris-mantled glacier snouts. *Journal of Glaciology*, **46**(154): 459-469.
- Andrews, J. and B. Smithson 1966. Till fabrics of the cross-valley moraines of north-central Baffin Island, NWT, Canada. *Bulletin of the Geological Society of America*, **77**: 271-290.
- Annan, A. 2002. GPR- History, trends, and future developments. *Subsurface Sensing Technologies and Applications*, **3**(4): 253-270.

References

- Annan, A. and J. Davis 1976. Impulse radar sounding in permafrost. *Radio Science*, **11**(4): 383-394.
- Anonymous 1895. The Westland Alps, New Zealand. *The Geographical Journal*, **5**(1).
- Anonymous 2003. Pulse EKKO Pro User's Guide. Mississauga, Ontario, Sensors & Software Inc.
- Appleby, J. 2007. Strain and Structure of a Temperate, Maritime Glacier: Te Moeka o Tuawe / Fox Glacier, South Westland, New Zealand. MSc Thesis, Massey University.)
- Appleby, J., M. Brook, S. Vale and A. Macdonald-Creevey 2010. Structural glaciology of a temperate maritime glacier: Lower Fox Glacier, New Zealand. *Geografiska Annaler*, **92**(4): 1-18.
- Applegate, P., T. Lowell and R. Alley 2008. Comment on "absence of cooling in New Zealand and the adjacent ocean during the younger dryas chronozone". *Science*, **320**(5877): 2.
- Arcone, S., V. Spikes and G. Hamilton 2005. Phase structure of radar stratigraphic horizons within Antarctic firn. *Annals of Glaciology*, **41**: 10-16.
- Arnason, B. 1969. Exchange of hydrogen isotopes between ice and water in temperate glaciers. *Earth and Planetary Science Letters*, **6**(6): 423.
- Arslan, A., C. Passchier and D. Koehn 2008. Foliation boudinage. *Journal of Structural Geology*, **30**(3): 291-309.
- Atherton, D. 1963. Comparisons of ogive systems under various regimes. *Journal of Glaciology*, **4**: 547-557.
- Augustinus, P.C. 1995. Glacial valley cross-profile development: the influence of in situ rock stress and rock mass strength, with examples from the Southern Alps, New Zealand. *Geomorphology*, **14**(2): 87-97.
- Azam, M., P. Wagnon, A. Ramanathan, C. Vincent, P. Sharma, Y. Arnaud, A. Linda, J. Pottakkal, P. Chavallier, V. Singh and E. Berthier 2012. From balance to imbalance: a shift in the dynamic behaviour of Chhota Shigri glacier, western Himalaya, India. *Journal of Glaciology*, **58**(208): 315-324.
- Bailey, J., G. Robin and S. Evans 1964. Radio echo sounding of Polar ice sheets. *Nature*, **204**(495): 420.
- Barnes, J. 1997. *Basic Geological Mapping*. 3rd ed. Chichester, John Wiley & Sons.
- Barrell, D., B. Andersen and G. Denton 2011. Glacial geomorphology of the Central South Island. *GNS Science Monographs*, **27**.
- Barringer, A. 1965. Research directed to the determination of subsurface terrain properties and ice thickness by pulsed VHF propagation methods. *Air Force Cambridge Research Laboratories Contribution, AF19*, **628**: 2998.

- Barringer, A. 1966. The use of radio and audio frequency pulses for terrain sensing. *In. Selected papers on remote sensing of the environment*, American Society of Photogrammetry, 215-226.
- Barrows, T., S. Lehman, L. Fifield and P. De Deckker 2007. Absence of cooling in New Zealand and the adjacent ocean during the younger dryas chronozone. *Science*, **318**(5847): 86-89.
- Batt, G., J. Braun, B. Kohn and I. McDougall 2000. Thermochronological analysis of the dynamics of the Southern Alps, New Zealand. *Geological Society of America Bulletin*, **112**(2): 250-266.
- Bell, J. and R. Grenville 1911. *A geographical report on the Franz Josef Glacier, with topographical maps and data by R.P Grenville and botanical notes by Leonard Cockayne*. Wellington, New Zealand Geological Survey.
- Benn, D. 1994. Fluted moraine formation and till genesis below a temperate valley glacier: Slettmarkbreen, Jotunheimen, southern Norway. *Sedimentology*, **41**: 279-292.
- Benn, D. and C. Ballantyne 1993. The description and representation of clast shape. *Earth Surface Processes and Landforms*, **18**: 665-672.
- Benn, D. and C. Ballantyne 1994. Reconstructing the transport history of glacial sediments: a new approach based on the co-variance of clast form indices. *Sedimentary Geology*, **91**: 215-227.
- Benn, D. and D. Evans 1996. The interpretation and classification of subglacially-deformed materials. *Quaternary Science Reviews*, **15**: 23-52.
- Benn, D. and D. Evans 1998. *Glaciers & Glaciation*. London, Arnold.
- Benn, D. and D. Evans 2010. *Glaciers & Glaciation*. 2nd ed. Abingdon, Hodder Education.
- Benn, D. and A. Gemmell 2002. Fractal dimensions of diamictic particle-size distributions: Simulations and evaluation. *Geological Society of America Bulletin*, **114**(5): 528-532.
- Benn, D., J. Gulley, A. Luckman, A. Adamek and P.S. Glowacki 2009. Englacial drainage systems formed by hydrologically driven crevasse propagation. *Journal of Glaciology*, **55**(191): 513-523.
- Bennett, M., M. Hambrey and D. Huddart 1997. Modification of clast shape in high-arctic glacial environments. *Journal of Sedimentary Petrology*, **A67**: 550-559.
- Bennett, M., M. Hambrey, D. Huddart, N. Glasser and K. Crawford 1999. The landform and sediment assemblage produced by a tidewater glacier surge in Kongsfjorden, Svalbard. *Quaternary Science Reviews*, **18**(10-11): 1213-1246.
- Bennett, M., D. Huddart, M. Hambrey and J. Ghienne 1996. Moraine Development at the High-Arctic Valley Glacier Pedersenbreen, Svalbard. *Geografiska Annaler. Series A, Physical Geography*, **78**(4): 209-222.

References

- Bennett, M., D. Huddart and R. Waller 2000. Glaciofluvial crevasse and conduit fills as indicators of supraglacial dewatering during a surge, Skeiðarárjökull, Iceland. *Journal of Glaciology*, **46**: 25-34.
- Binder, D., E. Brückl, K. Roch, M. Behm, W. Schöner and B. Hynek 2009. Determination of total ice volume and ice-thickness distribution of two glaciers in the Hohe Tauern region, Eastern Alps, from GPR data. *Annals of Glaciology*, **50**(51): 71-79.
- Bingham, R. and M. Siegert 2007. Radio-echo sounding over polar ice masses. *Journal of Environmental and Engineering Geophysics*, **12**(1): 47-62.
- Biondi, F., A. Gershunov and D. Cayan 2001. North Pacific decadal climate variability since 1661. *Journal of Climate*, **14**(1): 5-10.
- Bishop, B. 1957. *Shear moraines in the Thule area, northwest Greenland. Research Report 17.*, US Snow, Ice and Permafrost Research Establishment.
- Bjornsson, H., Y. Gjessing, S. Hamran, J. Hagen, O. Liestol, F. Palsson and B. Erlingsson 1996. The thermal regime of sub-polar glaciers mapped by multi-frequency radio-echo sounding. *Journal of Glaciology*, **42**(140): 23-32.
- Blair, R. 1994. Moraine and valley wall collapse due to rapid deglaciation in Mount Cook National park, New Zealand. *Mountain Research and Development*, **14**: 347-358.
- Blunier, T., J. Schwander, B. Stauffer, T. Stocker, A. Dällenbach, A. Indermühle, J. Tschumi, J. Chappellaz, D. Raynaud and J.-M. Barnola 1997. Timing of the Antarctic Cold Reversal and the atmospheric CO₂ increase with respect to the Younger Dryas event. *Geophysical Research Letters*, **24**(21): 2683-2686.
- Blunier, T., T. Stocker, J. Chappellaz and D. Raynaud 1999. Phase lag of Antarctic and Greenland temperature in the last glacial and link between CO₂ variations and Heinrich events. In Abrantes, F. and A. Mix, eds. *Reconstructing Ocean History: A window into the future (Proceedings of the Sixth International Conference on paleoceanography)*, New York, Plenum Publishing Corporation.
- Bolch, T., A. Kulkarni, A. Käab, C. Huggel, F. Paul, J. Cogley, H. Frey, J. Kargel, K. Fujita, M. Scheel, S. Bajracharva and M. Stoffel 2012. The state and fate of Himalayan glaciers. *Science*, **336**: 310-314.
- Boulton, G. 1967. The development of a complex supraglacial moraine at the margin of Sørbreen, Ny Friesland, Vestspitsbergen. *Journal of Glaciology*, **6**(47): 717-735.
- Boulton, G. 1974. Processes and Patterns of Subglacial Erosion. In Coates, D., ed. *Glacial geomorphology*, Binghamton, State University of New York.
- Boulton, G. 1976. The origin of glacially-fluted surfaces - observations and theory. *Journal of Glaciology*, **17**: 287-309.
- Boulton, G. 1978. Boulder shapes and grain-size distributions as indicators of transport paths through a glacier and till genesis. *Sedimentology*, **25**: 773-799.

- Boulton, G. 1996. Theory of glacial erosion, transport and deposition as a consequence of subglacial sediment deformation. *Journal of Glaciology*, **42**: 43-62.
- Boulton, G. and N. Eyles 1979. Sedimentation by valley glaciers: a model and genetic classification In Schlüchter, C., ed. *Moraines and Varves*, Rotterdam, Balkema.
- Boulton, G. and R. Hindmarsh 1987. Sediment deformation beneath glaciers: rheology and geological consequences. *Journal of Geophysical Research-Earth Surface*, **92**: 9059-9082.
- Bowen, F. 1960. Advances and retreats of the Franz Josef Glacier. *Journal of Glaciology*, **3**(28): 742.
- Boyce, E., R. Motyka and M. Truffer 2007. Flotation and retreat of a lake-calving terminus, Mendenhall Glacier, southeast Alaska, USA. *Journal of Glaciology*, **53**: 211-224.
- Bozhinskiy, A., M. Krass and V. Popovnin 1986. Role of debris cover in the thermal physics of glaciers. *Journal of Glaciology*, **32**(111): 255-266.
- Brandt, O., K. Langley, J. Kohler and S. Hararan 2007. Detection of buried ice and sediment layers in permafrost using multi-frequency Ground Penetrating Radar: A case examination on Svalbard. *Remote Sensing of Environment*, **111**(2-3): 212-227.
- Braun, L., W. Grabs and B. Rana 1993. Application of a conceptual precipitation-runoff model in the Langtang Khola basin, Nepal Himalaya. *IAHS Publication*, **218**: 221-237.
- Broecker, W. 2000. Abrupt climate change: Casual constraints provided by the paleoclimate record. *Earth Science Review*, **51**: 137-154.
- Brook, M. and S. Lukas 2012. Lithological and fluvial influences on clast shape measurements in a temperate alpine environment: a case study from Fox Glacier, New Zealand. *Geophysical Research Abstracts*, **14**(EGU2012-1539).
- Brook, M. and S. Paine 2012. Ablation of ice-cored moraine in a humid, maritime climate: Fox Glacier, New Zealand. *Geografiska Annaler*, (10.1111/j.1468-0459.2011.00442): 1-11.
- Burke, M., J. Woodward, A. Russell and P. Fleisher 2009. Structural controls on englacial esker sedimentation: Skeiðarárjökull, Iceland. *Annals of Glaciology*, **50**(51): 85-92.
- Burke, M., J. Woodward, A. Russell, P. Fleisher and P. Bailey 2010. The sedimentary architecture of outburst flood eskers: A comparison of ground-penetrating radar data from Bering Glacier, Alaska and Skeidararjokull, Iceland. *Geological Society of America Bulletin*, **122**(9-10): 1637-1645.
- Caldecott, R. 1967. Electromagnetic pulse sounding for surveying underground water. *Electroscience Laboratory Report 40IX-1*, (Ohio State University): 429.
- Camerlenghi, A., E. Domack, M. Rebesco, R. Gilbert, S. Ishman, A. Leventer, S. Brachfeld and A. Drake 2001. Glacial morphology and post-glacial contourites in

References

northern Prince Gustav Channel (NW Weddell Sea, Antarctica). *Marine Geophysical Researches*, **22**(5-6): 417-443.

Carrivick, J. and E. Rushmer 2007. Inter- and Intra-catchment Variations in Proglacial Geomorphology: An Example from Franz Josef Glacier and Fox Glacier, New Zealand. *2nd Sediment Budgets in Cold Environments Workshop*, Abisko, SWEDEN, Inst Arctic Alpine Res, 18-36.

Carter, S., D. Blankenship, D. Young and J.W. Holt 2009. Using radar-sounding data to identify the distribution and sources of subglacial water: application to Dome C, East Antarctica. *Journal of Glaciology*, **55**(194): 1025-1040.

Catania, G. and T. Neumann 2010. Persistent englacial drainage features in the Greenland Ice Sheet. *Geophysical Research Letters*, **37**: 5.

Chamberlain, R. 1928. Instrumental work on the nature of glacier motion. *Journal of Geology*, **36**: 1-30.

Chamberlain, T. 1895. Recent glacial studies in Greenland. *Geological Society of America Bulletin*, **6**: 199-220.

Chinn, T. 1995. Glacier fluctuations in the Southern Alps of new Zealand determined from snowline elevations. *Arctic and Alpine Research*, **27**(2): 187-198.

Chinn, T. 1996. New Zealand glacier responses to climate change of the past century. *New Zealand Journal of Geology and Geophysics*, **39**: 415-428.

Chinn, T. 1997. New Zealand glacier response to climate change of the past 2 decades. *International Symposium on Glaciers of the Southern Hemisphere*, Melbourne, Australia, Elsevier Science Bv, 155-168.

Chinn, T. 1999. New Zealand glacier response to climate change of the past 2 decades. *Global and Planetary Change*, **22**: 155-168.

Chinn, T. 2000. *United States Geological Survey Professional Paper 1386-H. Satellite Image Atlas of Glaciers of the World: Irian Jaya, Indonesia, and New Zealand*. Boulder, United States Geological Survey.

Chinn, T., C. Heydenrych and J. Salinger 2002. Glacier Snowline Survey 2002. National Institute of Water and Atmospheric Research, Auckland.

Chinn, T., C. Heydenrych and M. Salinger 2005a. Use of the ELA as a practical method of monitoring glacier response to climate in New Zealand's Southern Alps. *Journal of Glaciology*, **51**(172): 85-95.

Chinn, T., M. McSaveney and E. McSaveney 1992. *The Mt Cook rock avalanche of 14 December 1991*. New Zealand, Institute of Geological and Nuclear Sciences.

Chinn, T., J. Salinger, B. Fitzharris and A. Willsman 2008. Glaciers and Climate. *Bulletin of the Federated Mountain Clubs of New Zealand*, **171**: 20-29.

- Chinn, T., A. Willsman and J. Salinger 2005b. Glacier Snowline Survey 2005. National Institute of Water and Atmosphere, Auckland.
- Chinn, T., S. Winkler, J. Salinger and N. Haakensen 2005c. Recent Glacier advances in Norway and New Zealand: A comparison of their glaciological and meteorological causes. *Geografiska Annaler*, **87A**: 141-157.
- Citterio, M., S. Turri, A. Bini and V. Maggi 2004. Observed trends in the chemical composition, $\delta^{18}\text{O}$ and crystal sizes vs. depth in the first ice core from LoLc 1650 "Abisso sul Margine dell'Alto Bregai" ice cave (Lecco, Italy). *Theoretical and Applied Karstology*, **17**: 45-50.
- Clapperton, C. 1993. Glacier readvances in the Andes at 12500-10000 yr BP; implications for mechanism of late-glacial climate change. *Journal of Quaternary Science*, **8**: 197-215.
- Clare, G., B. Fitzharris, T. Chinn and J. Salinger 2002. Interannual variation in end-of-summer snowlines of the Southern Alps of New Zealand, and relationships with southern hemisphere atmospheric circulation and sea surface temperature patterns. *International Journal of Climatology*, **22**(22): 107-120.
- Clarke, G. 1987. Subglacial till: a physical framework for its properties and processes. *Journal of Geophysical Research-Earth Surface*, **92**: 9023-9036.
- Clason, C., D. Mair, D. Burgess and P. Nienow 2012. Modelling the delivery of supraglacial meltwater to the ice/bed interface: application to southwest Devon Ice Cap, Nunavut, Canada. *Journal of Glaciology*, **58**(208): 361-374.
- Coates, G. and T. Chinn 1999. *The Franz Josef and Fox Glaciers*. 3 ed. Wellington, Institute of Geological and Nuclear Sciences Ltd.
- Cook, J. 1960. Proposed monocycle-pulse, VHF radar for airborne ice and snow measurements. *IEE Transactions on Communications and Electronics*, **79**(2): 588-594.
- Cox, S. 1876. Notes on the Valley System on the Western Flanks of Mount Cook. *Transactions and Proceedings of the Royal Society of New Zealand 1868-1961*, **9**: 577-581.
- Cox, S. 1877. Report on Westland District. *Reports of Geological Exploration during 1874-1876*, **9**: 63-93.
- Cox, S. and D. Barrell 2007. Geology of the Aoraki Area. Institute of Geological & Nuclear Sciences 1:250 000 geological map 15. *Q Map*, Lower Hutt, New Zealand, Institute of Geological and Nuclear Sciences.
- Cui, X., B. Sun, G. Tian, X. Tang, X. Zhang, Y. Jiang, J. Guo and X. Li 2010. Ice radar investigation at Dome A, East Antarctica: Ice thickness and subglacial topography. *Chinese Science Bulletin*, **55**(4-5): 425-431.
- Cutler, E. and B. Fitzharris 2005. Observed surface snowmelt at high elevation in the Southern Alps of New Zealand. *Annals of Glaciology*, **40**: 163-168.

References

- Cutnell, J. and W. Johnson 2012. *Physics*. 9th ed. United States, John Wiley & Sons, Inc.
- Davies, T., C. Smart and J. Turnbull 2003. Water and sediment outbursts from advanced Franz Josef Glacier, New Zealand. *Earth Surface Processes and Landforms*, **28**(10): 1081-1096.
- Davis, J., W. Scott, R. Morey and A. Annan 1976. Impulse radar experiments on permafrost near Tuktoyaktuk, Northwest-Territories. *Canadian Journal of Earth Sciences*, **13**(11): 1584-1590.
- De Pascale, G., W. Pollard and K. Williams 2008. Geophysical mapping of ground ice using a combination of capacitive coupled resistivity and ground-penetrating radar, Northwest Territories, Canada. *Journal of Geophysical Research-Earth Surface*, **113**(F2).
- Denton, G. and C. Hendy 1994. Younger Dryas age advance of Franz Josef Glacier in the Southern Alps of New Zealand. *Science*, **264**: 1434-1437.
- Di Toro, G., S. Mittempergher, F. Ferri, T. Mitchell and G. Pennacchioni 2012. The contribution of structural geology, experimental rock deformation and numerical modelling to an improved understanding of the seismic cycle. *Journal of Structural Geology*, **38**: 3-10.
- DigitalGlobe 2010. Basic Satellite Imagery. (21st July).
- Douglas, C. and W. Wilson 1896. Topographical plan of Fox Country, Westland. From a reconnaissance survey of 1894-95. *Appendix to the Journal of the House of Representatives of New Zealand*, **1**(C-1).
- Echelmeyer, K. and B. Kamb 1986. Stress-gradient coupling in glacier flow, 2. Longitudinal averaging in the flow response to small perturbations in ice thickness and surface slope. *Journal of Glaciology*, **32**(111): 285-298.
- Eisen, O., A. Bauder, M. Lüthi, P. Riesen and M. Funk 2009. Deducing the thermal structure in the tongue of Gornergletscher, Switzerland, from radar surveys and borehole measurements. *Annals of Glaciology*, **50**(51): 63-70.
- Eisen, O., U. Nixdorf, L. Keck and D. Wagenbach 2003. Alpine ice cores and ground penetrating radar: combined investigations for glaciological and climatic interpretations of a cold Alpine ice body. *Tellus Series B-Chemical and Physical Meteorology*, **55**(5): 1007-1017.
- Eisen, O., U. Nixdorf, F. Wilhelms and H. Miller 2002. Electromagnetic wave speed in polar ice: validation of the common-midpoint technique with high-resolution dielectric-profiling and gamma-density measurements. *Annals of Glaciology*, **34**: 150-156.
- Eklund, A. and J. Hart 1996. Glaciotectonic deformation within a flute from the Isfallsgläciären, Sweden. *Journal of Quaternary Science*, **11**: 299-310.

- Ensminger, S., R. Alley, E. Evenson, D. Lawson and G. Larson 2001. Basal-crevasse-fill origin of laminated debris bands at Matanuska Glacier, Alaska, USA. *Journal of Glaciology*, **47**: 412-422.
- Evans, D. 2008. Avalanches and moraines. *Nature Geoscience*, **1**: 493.
- Evans, D. and D. Benn, eds. 2003. *A practical guide to the study of glacial sediments* London, Arnold.
- Evans, D. and D. Twigg 2002. The active temperate glacial landsystem: a model based on Breiðamerkurjökull and Fjallsjökull, Iceland. *Quaternary Science Reviews*, **21**(20-22): 2143-2177.
- Evans, E. 2003. Ablation at the Terminus of the Franz Josef Glacier. BSc Honours Thesis, Otago University.)
- Eyles, N. and R. Rogerson 1978. A framework for the investigation of medial moraine formation: Austerdalsbreen, Norway, and Berendon Glacier, British Columbia, Canada. *Journal of Glaciology*, **20**: 99-113.
- Farinotti, D., M. Huss, A. Bauder, M. Funk and M. Truffer 2009. A method to estimate the ice volume and ice-thickness distribution of alpine glaciers. *Journal of Glaciology*, **55**: 422-430.
- Farzaneh, M., I. Fofana and H. Hemmatjou 2007. Effects of temperature and impurities on the DC conductivity of snow. *Ieee Transactions on Dielectrics and Electrical Insulation*, **14**(1): 185-193.
- Fisher, J. 1947. Forbes and Alaskan dirt bands on glaciers and their origins. *American Journal of Science*, **245**(3): 137.
- Fisher, J. 1962. Ogives of the Forbes type on alpine glaciers and a study of their origins. *Journal of Glaciology*, **4**: 53-61.
- Fitzharris, B., T. Chinn and G. Lamont 1997. Glacier balance fluctuations and atmospheric circulation patterns over the Southern Alps, New Zealand. *International Journal of Climatology*, **17**(7): 745-763.
- Fitzharris, B., G. Clare and J. Renwick 2007. Teleconnections between Andean and New Zealand glaciers. *Global and Planetary Change*, **59**(1-4): 159-174.
- Fitzharris, B., J. Hay and P. Jones 1992. Behaviour of New Zealand glaciers and atmospheric circulation changes over the past 130 years. *The Holocene*, **2**: 97-106.
- Fitzharris, B., W. Lawson and I. Owens 1999. Research on glaciers and snow in New Zealand. *Progress in Physical Geography*, **23**(4): 469-500.
- Fitzsimons, S. 1997. Late-glacial and early Holocene glacier activity in the Southern Alps, New Zealand. *Quaternary International*, **38/39**: 69-76.

References

- Forbes, J. 1845. *Travels through the Alps of Savoy and other parts of the Pennin chain with observations on the phenomena of glaciers*. 2nd ed. Edinburgh, Adam & Charles Black.
- Forbes, J. 1859. *Occasional papers on the theory of glaciers*. Edinburgh, Adam & Charles Black.
- Fossen, H. 2010. *Structural Geology*. Cambridge, Cambridge University Press.
- Fountain, A. and J. Walder 1998. Water flow through temperate glaciers. *Reviews of Geophysics*, **36**(3): 299-328.
- Fox, W. 1872. Travels on the West Coast of the South Island. *Transactions of the Royal Society of New Zealand*, **5**: 433-434.
- Frezzotti, M., S. Gandolfi, F. La Marca and S. Urbini 2002a. Snow dunes and glazed surfaces in Antarctica: new field and remote-sensing data. *Annals of Glaciology*, **34**: 81-88.
- Frezzotti, M., S. Gandolfi and S. Urbini 2002b. Snow megadunes in Antarctica: Sedimentary structure and genesis. *Journal of Geophysical Research-Atmospheres*, **107**(D18).
- Furkert, F. 1947. Westport Harbour. *Transactions of the Royal Society of New Zealand*, **76**: 373-402.
- Gao, J. and Y. Liu 2001. Applications of remote sensing, GIS and GPS in glaciology: a review. *Progress in Physical Geography*, **25**(4): 520-540.
- Gardiner, K. 1934. Tasman from the West. *The New Zealand Alpine Journal*, **5**(21): 289-294.
- Gardner, J. and K. Hewitt 1990. A surge of Bualtar Glacier, Karakorum Range, Pakistan: a possible landslide trigger. *Journal of Glaciology*, **36**: 159-162.
- Gellatly, A. 1985. Historic records of glacier fluctuations in Mt Cook National Park, New Zealand: A century of change. *The Geographic Journal*, **151**(1): 86-89.
- Gellatly, A. and D. Norton 1984. Possible warming and glacier recession in the South Island, New Zealand. *New Zealand Journal of Science*, **27**: 381-388.
- Glasser, N. and M. Hambrey 2001. Styles of sedimentation beneath Svalbard valley glaciers under changing dynamic and thermal regimes. *Journal of the Geology Society of London*, **158**: 697-707.
- Glasser, N. and M. Hambrey 2002a. Sedimentary facies and landform genesis at a temperate outlet glacier: Soler Glacier, North Patagonian Icefield. *Sedimentology*, **49**(1): 43-64.
- Glasser, N. and M. Hambrey 2002b. δD - $\delta^{18}O$ relationships on polythermal valley glacier: Midtre Lovénbreen, Svalbard. *Polar Research*, **21**(1): 123-131.

- Glasser, N. and M. Hambrey 2003. Ice-marginal terrestrial landsystems: Svalbard polythermal glaciers. In Evans, D., ed. *Glacial Landsystems*, London, Arnold, 65-88.
- Glasser, N., M. Hambrey, K. Crawford, M. Bennett and D. Huddart 1998. The structural glaciology of Kongsvegen, Svalbard, and its role in landform genesis. *Journal of Glaciology*, **44**(146): 136-148.
- Glasser, N., M. Hambrey, J. Etienne, P. Jansson and R. Pettersson 2003. The origin and significance of debris-charged ridges at the surface of Storglaciären, Northern Sweden. *Geografiska Annaler*, **85 A**: 127-147.
- Glasser, N., K. Jansson, W. Mitchell and S. Harrison 2006. The geomorphology and sedimentology of the 'Témpanos' moraine at Laguna San Rafael, Chile. *Journal of Quaternary Science*, **21**(6): 629-643.
- Glasser, N., B. Kulesa, A. Luckman, D. Jansen, E. King, P. Sammonds, T. Scambos and K. Jezek 2009. Surface structure and stability of the Larsen C ice shelf, Antarctic Peninsula. *Journal of Glaciology*, **55**(191): 400-410.
- Glasser, N. and T. Scambos 2008. A structural glaciological analysis of the 2002 Larsen B ice-shelf collapse. *Journal of Glaciology*, **54**(184): 3-16.
- Glen, J. 1955. The creep of polycrystalline ice. *Proceedings of the Royal Society, Series A*, **228**(1175): 519-538.
- Godwin, H. 1949. Pollen analysis of glaciers in special relation to the formation of various types of glacier bands. *Journal of Glaciology*, **1**: 325-329.
- Gogineni, S., D. Braaten, C. Allen, J. Paden, T. Akins, P. Kanagaratnam, K. Jezek, G. Prescott, G. Jayaraman, V. Ramasami, C. Lewis and D. Dunson 2007. Polar radar for ice sheet measurements (PRISM). *Remote Sensing of Environment*, **111**(2-3): 204-211.
- Goldthwait, R. 1951. Development of end moraines in east-central Baffin Island. *Journal of Geology*, **59**: 567-577.
- Gomez, B. and R. Small 1985. Medial moraines of the Haut Glacier D'Arolla. Valais, Switzerland: Debris supply and implications for moraine formation. *Journal of Glaciology*, **31**(109): 303-307.
- Gonzales, J. and A. Aydin 2008. The origin of oriented lakes in the Andean foreland, Parque Nacional Torres del Paine (Chilean Patagonia). *Geomorphology*, **97**(3-4): 502-515.
- Goodsell, B. 2005. The structure, dynamics and debris transport of two alpine glaciers: Haut Glacier d'Arolla and Bas Glacier d'Arolla, Valais, Switzerland. PhD Thesis, University of Wales.)
- Goodsell, B., B. Anderson and W. Lawson 2003. Supraglacial routing of subglacial water at Franz Josef Glacier, South Westland, New Zealand. *Journal of Glaciology*, **49**(166): 469-470.

References

- Goodsell, B., B. Anderson, W.J. Lawson and I.F. Owens 2005a. Outburst flooding at Franz Josef Glacier, South Westland, New Zealand. *New Zealand Journal of Geology and Geophysics*, **48**(1): 95-104.
- Goodsell, B., M. Hambrey and N. Glasser 2002. Formation of band ogives and associated structures at Bas Glacier d'Arolla, Valais, Switzerland. *Journal of Glaciology*, **48**(161): 287-300.
- Goodsell, B., M. Hambrey and N. Glasser 2005b. Debris transport in a temperate valley glacier: Haut Glacier d'Arolla, Valais, Switzerland. *Journal of Glaciology*, **51**(172): 139-146.
- Goodsell, B., M. Hambrey, N. Glasser, P. Nienow and D. Mair 2005c. The structural glaciology of a temperate valley glacier: Haut Glacier d'Arolla, Valais, Switzerland. *Arctic Antarctic and Alpine Research*, **37**(2): 218-232.
- Gordon, J. and R. Birnie 1986. Production and transfer of subaerially generated rock debris and resulting landforms on South Georgia: an introductory perspective. *British Antarctic Survey Bulletin*, **72**: 25-46.
- Gordon, J., W. Darling, W. Whalley and A. Gellatly 1988. δD - $\delta^{18}O$ Relationships and the thermal history of basal ice near the margins of two glaciers in Lyngen, North Norway. *Journal of Glaciology*, **34**(118): 265-268.
- Gordon, J., W. Whalley, A. Gellatly and D. Vere 1992. The formation of glacial flutes: assessment of models with evidence from Lyngsdalen, north Norway. *Quaternary Science Reviews*, **11**: 709-731.
- Gorman, M. and M. Siegert 1999. Penetration of Antarctic subglacial lakes by VHF electromagnetic pulses: Information on the depth and electrical conductivity of basal water bodies. *Journal of Geophysical Research-Solid Earth*, **104**(B12): 29311-29320.
- Graham, D. and N. Midgley 2001. Graphical representation of particle shape using triangular diagrams: an excel spreadsheet method. *Earth Surface Processes and Landforms*, **25**: 1473-1476.
- Gravenor, C. and W. Kupsch 1959. Ice disintegration features in western Canada. *Journal of Geology*, **67**: 48-64.
- Greaves, R., D. Lesmes, J. Lee and M. Nafi Toksoz 1996. Velocity variations and water content estimated from multi-offset, ground-penetrating radar. *Geophysics*, **61**(3): 683-695.
- Grey, D. and D. Male, eds. 2004. *Handbook of Snow: Principles, Processes, Management and Use*, New Jersey, Blackburn Press.
- Grove, J. 1988. *The Little Ice Age*. London, Methuen.
- Grove, J. 2001. The initiation of the "Little Ice Age" in regions round the North Atlantic. *Climatic Change*, **48**: 53-82.

- Gudmundsson, H., A. Iken and M. Funk 1997. Measurements of ice deformation at the confluence area of Unteraargletscher, Bernese Alps, Switzerland. *Journal of Glaciology*, **43**(145): 548-556.
- Gulley, J. 2009. Structural control of englacial conduits in the temperate Matanuska Glacier, Alaska, USA. *Journal of Glaciology*, **55**(192): 681-690.
- Gulley, J., D. Benn, D. Müller and A. Luckman 2009. A cut-and-closure origin for englacial conduits in uncrevassed regions of polythermal glaciers. *Journal of Glaciology*, **55**(189): 66-80.
- Gunn, B. 1964. Flow rates and secondary structures of Fox and Franz Josef Glaciers, New Zealand. *Journal of Glaciology*, **5**(38): 173-190.
- Guy, B., M. Daigneault and G. Thomas 2002. Reflections on the formation of Forbes ogives: the instability of fusion of dirty ice. *Comptes Rendus Geoscience*, **334**(15): 1061-1070.
- Haeferli, R. 1951. Some observations on glacier flow. *Journal of Glaciology*, **1**: 497-500.
- Haeferli, R. 1957. Notes on the formation of ogives as pressure waves. *Journal of Glaciology*, **3**: 27-29.
- Hales, T. and J. Roering 2002. Estimates of erosion rates from the Central Southern Alps, New Zealand. *American Geophysical Union, Fall meeting 2002, Abstract #T12E-11*, American Geophysical Union.
- Hall, D., K. Bayr, W. Schöner, R. Bindschadler and J. Chien 2003. Consideration of the errors inherent in mapping historical glacier positions in Austria from the ground and space (1893-2001). *Remote Sensing of Environment*, **86**: 566-577.
- Hallet, B. 1979. A theoretical model of glacial abrasion. *Journal of Glaciology*, **17**: 39-50.
- Hallet, B. 1981. Glacial abrasion and sliding: their dependence on the debris concentration in basal ice. *Annals of Glaciology*, **2**: 23-28.
- Hambrey, M. 1975. The origin of foliation in glaciers: Evidence from some Norwegian examples. *Journal of Glaciology*, **14**(70): 181-185.
- Hambrey, M. 1994. *Glacial Environments*. London, UCL Press.
- Hambrey, M. and J. Alean 2004. *Glaciers*. 2nd ed. Cambridge, Cambridge University Press.
- Hambrey, M., M. Bennett, J. Dowdeswell, N. Glasser and D. Huddart 1999. Debris entrainment and transfer in polythermal valley glaciers. *Journal of Glaciology*, **45**(149): 69-86.

References

- Hambrey, M. and J. Dowdeswell 1994. Flow regime of the Lambert Glacier-Amery Ice Shelf system, Antarctica: Structural evidence from Landsat imagery. *Annals of Glaciology*, **20**: 401-406.
- Hambrey, M. and J. Dowdeswell 1997. Structural evolution of a surge-type polythermal glacier: Hessbreen, Svalbard. *Annals of Glaciology*, **24**: 375-381.
- Hambrey, M., J. Dowdeswell, T. Murray and P. Porter 1996. Thrusting and debris entrainment in a surging glacier: Bakaninbreen, Svalbard. *Annals of Glaciology*, **22**: 241-249.
- Hambrey, M. and W. Ehrmann 2004. Modification of sediment characteristics during glacial transport in high-alpine catchments: Mount Cook area, New Zealand. *Boreas*, **33**(4): 300 - 318.
- Hambrey, M. and N. Glasser 2003. The Role of Folding and Foliation Development in the Genesis of Medial Moraines: Examples from Svalbard Glaciers. *The Journal of Geology*, **111**(4): 471-485.
- Hambrey, M. and D. Huddart 1995. Englacial and proglacial glaciotectionic processes at the snout of a thermally complex glacier in Svalbard. *Journal of Quaternary Science*, **10**(4): 313-326.
- Hambrey, M., D. Huddart, M. Bennett and N. Glasser 1997. Genesis of 'hummocky moraines' by thrusting in glacier ice: evidence from Svalbard and Britain. *Journal of the Geology Society of London*, **154**: 623-632.
- Hambrey, M. and W. Lawson 2000. Structural styles and deformation fields in glaciers: a review. *Geological Society, London, Special Publications*, **176**(1): 59-83.
- Hambrey, M. and A. Milnes 1975. Boudinage in glacier ice: some examples. *Journal of Glaciology*, **14**(72): 383-393.
- Hambrey, M. and A. Milnes 1977. Structural geology of an Alpine glacier (Griesgletscher, Valais, Switzerland). *Eclogae Geologicae Helvetiae*, **70**(3): 667-684.
- Hambrey, M. and F. Müller 1978. Structures and ice deformation in the White Glacier, Axel Heiberg Island, Northwest Territories, Canada. *Journal of Glaciology*, **20**(82): 41-66.
- Hambrey, M., T. Murray, N. Glasser, A. Hubbard, B. Hubbard, G. Stuart, S. Hansen and J. Kohler 2005. Structure and changing dynamics of a polythermal valley glacier on a centennial timescale: Midre Lovenbreen, Svalbard. *Journal of Geophysical Research-Earth Surface*, **110**(F1).
- Hambrey, M.J. 1977. Foliation, minor folds and strain in glacier ice. *Tectonophysics*, **39**(1-3): 397-416.
- Harbor, J., B. Hallet and C. Raymond 1988. A numerical model of landform development by glacial erosion. *Nature*, **333**: 347-349.
- Harper, A. 1934. Glacial Retreat. *The New Zealand Alpine Journal*, **5**(21): 323-326.

- Hatcher, R. 2007. *Structural geology: Principles, concepts, and problems*. 2nd ed. New York, Macmillan Publishing Company.
- Hausmann, H., K. Krainer, E. Bruckl and W. Mostler 2007. Internal structure and ice content of reickenkar rock glacier (Stubai alps, Austria) assessed by geophysical investigations. *Permafrost and Periglacial Processes*, **18**(4): 351-367.
- Hay, J. and B. Fitzharris 1988. The synoptic climatology of ablation on a New Zealand glacier. *Journal of Climatology*, **8**: 201-215.
- He, Y., H. Pang, W. Theakstone, D. Zhang, A. Lu, B. Song, L. Yuan and B. Ning 2005. Spatial and temporal variations of oxygen isotopes in snowpacks and glacial runoff in different types of glacial area in western China. In MosleyThompson, E. and L.G. Thompson, eds. *International Symposium on High-Elevation Glaciers and Climate Records*, Lanzhou, Peoples Republic of China, Int Glaciological Soc, 269-274.
- Heim, A. 1885. *Handbuch der Gletscherkunde*. Stuttgart, Engelhorn.
- Herbst, P., T. Flandera and F. Neubauer 2002. A three-dimensional model of the Pasterze Glacier, Austria. *Zeitschrift für Gletscherkunde und Glazialgeologie*, **38**(2): 179-184.
- Herbst, P. and F. Neubauer 2000. The Pasterze Glacier, Austria: an analogue of an extensional allochthon. In Maltman, A., B. Hubbard and M. Hambrey, eds. *Deformation of Glacial Materials*, London, Geological Society.
- Herbst, P., F. Neubauer and M. Schopfer 2006. The development of brittle structures in an alpine valley glacier: Pasterzenkees, Austria, 1887-1997. *Journal of Glaciology*, **52**(176): 128-136.
- Herman, F., B. Anderson and S. Leprince 2011. Mountain glacier velocity variation during a retreat/advance cycle quantified using sub-pixel analysis of ASTER images. *Journal of Glaciology*, **57**(202): 197-207.
- Hess, H. 1904. *Die Gletscher, Braunschweig*. Berlin, F. Vieweg & Sohn.
- Hessel, J. 1983. Climatic effects on the recession of the Franz Josef Glacier. *New Zealand Journal of Science*, **26**(3): 315-320.
- Hewitt, K. 2009. Rock avalanches that travel onto glaciers and related developments, Karakouram Himalaya, Inner Asia. *Geomorphology*, **103**: 66-79.
- Hochstein, M., D. Claridge, S. Henrys, A. Pyne, D. Nobes and S. Leary 1995. Downwasting of the Tasman Glacier, South Island, New Zealand: Changes in the terminus region between 1971 and 1993. *New Zealand Journal of Geology and Geophysics*, **38**(1): 1-16.
- Hochstein, M., M. Watson, B. Malengreau, D. Nobes and I. Owens 1998. Rapid melting of the terminal section of the Hooker Glacier (Mt Cook National Park, New Zealand). *New Zealand Journal of Geology and Geophysics*, **41**(3): 203-218.

References

- Hoelzle, M., T. Chinn, D. Stumm, F. Paul, M. Zemp and W. Haeberli 2007. The application of glacier inventory data for estimating past climate change effects on mountain glaciers: A comparison between the European Alps and the Southern Alps of New Zealand. *Global and Planetary Change*, **56**(1-2): 69-82.
- Holdsworth, G. 1965. An examination and analysis of the formation of transverse crevasses, Kaskawulsh glacier, Yukon. *Ohio State University Institute of Polar Studies, Report 3*: 110pp.
- Holmlund, P. 1988. Internal geometry and evolution of moulins, Storglaciären, Sweden. *Journal of Glaciology*, **34**(117): 242-248.
- Holtedahl, H. 1967. Notes on the formation of fjord and fjord-valleys. *Geografiska Annaler*, **49 A**: 188-203.
- Hooke, R. 1973. Structure and flow at the margin of the Barnes Ice Cap, Baffin Island, NWT, Canada *Journal of Glaciology*, **12**: 423-438.
- Hooke, R. 2005. *Principles of Glacier Mechanics*. 2nd ed. Cambridge, Cambridge University Press.
- Hooke, R. and P. Hudleston 1978. Origin of foliation in glaciers. *Journal of Glaciology*, **20**: 285-299.
- Hooke, R. and N. Iverson 1995. Grain-size distribution in deforming subglacial tills: role of grain fracture. *Geology*, **23**(1): 57-60.
- Hooker, B. and B. Fitzharris 1999. The correlation between climatic parameters and the retreat and advance of Franz Josef Glacier, New Zealand. *Global and Planetary Change*, **22**: 39-48.
- Horwath, M., R. Dietrich, M. Baessler, U. Nixdorf, D. Steinhage, D. Fritzsche, V. Damm and G. Reitmayr 2006. Nivlisen, an Antarctic ice shelf in Dronning Maud Land: geodetic-glaciological results from a combined analysis of ice thickness, ice surface height and ice-flow observations. *Journal of Glaciology*, **52**(176): 17-30.
- Hubbard, A., H. Blatter, P. Nienow, D. Mair and B. Hubbard 1998. Comparison of a three-dimensional model for glacier flow with field data from Haut Glacier d'Arolla, Switzerland. *Journal of Glaciology*, **44**(147): 368-378.
- Hubbard, B. and N. Glasser 2005. *Field Techniques in Glaciology and Glacial Geomorphology*. Chichester, Wiley.
- Hubbard, B., N. Glasser, M. Hambrey and J. Etienne 2004. A sedimentological and isotopic study of the origin of supraglacial debris bands: Kongsfjorden, Svalbard. *Journal of Glaciology*, **50**(169): 157-170.
- Hubbard, B. and P. Nienow 1997. Alpine subglacial hydrology. *Quaternary Science Reviews*, **16**: 939-955.
- Hubbard, B. and M. Sharp 1989. Basal ice formation and deformation: a review. *Progress in Physical Geography*, **13**(4): 529-558.

- Hubbard, B. and M. Sharp 1993. Weertman regelation, multiple refreezing events and the isotopic evolution of the basal ice layer. *Journal of Glaciology*, **39**(132): 275-291.
- Hubbard, B. and M. Sharp 1995. Basal ice facies and their formation in the Western Alps. *Arctic and Alpine Research*, **27**(4): 301-310.
- Huddart, D., M. Bennett and N. Glasser 1999. Morphology and sedimentology of a high-arctic esker system: Vegbreen, Svalbard. *Boreas*, **28**: 257-273.
- Hudleston, P. 1976. Recumbent folding in the base of the Barnes Ice Cap, Baffin Island, Northwest Territories, Canada. *Geological Society of America Bulletin*, **87**(112): 1678-1683.
- Hudleston, P. and R. Hooke 1980. Cumulative deformation in the Barnes Ice Cap and implications for the development of foliation. *Tectonophysics*, **66**(1-3): 127-146.
- Huybrechts, P., O. Rybak, D. Steinhage and F. Pattyn 2009. Past and present accumulation rate reconstruction along the Dome Fuli-Kohnen radio-echo sounding profile, Dronning Maud land, East Antarctica. *Annals of Glaciology*, **50**(51): 112-120.
- IAEA 2006. Isotope Hydrology Information System. The ISOHIS Database. (16th January 2012).
- Iken, A. and R. Bindshadler 1986. Combined measurements of subglacial water pressures and surface velocity of the Findelengletscher, Switzerland. Conclusions about drainage systems and sliding mechanisms. *Journal of Glaciology*, **32**(110): 101-119.
- IPCC 2007. *Climate Change 2007: The Physical Science Basis, summary for policy makers. Contribution of Working Group I to the Fourth Assessment report of the Intergovernmental Panel on Climate Change*. United Nations Environment Programme.
- Iriondo, M. 1999. Last Glacial Maximum and Hypsithermal in the Southern Hemisphere. *Quaternary International*, **62**(1): 11-19.
- Irvine-Fynn, T., B. Moorman, J. Williams and F. Walter 2006. Seasonal changes in ground-penetrating radar signature observed at a polythermal glacier, Bylot Island, Canada. *Earth Surface Processes and Landforms*, **31**(7): 892-909.
- Ishikawa, N., I. Owens and A. Sturman 1992. Heat balance characteristics during fine periods on the lower parts of the Franz Josef Glacier, South Westland, New Zealand. *International Journal of Climatology*, **12**: 397-410.
- Iverson, N., T. Hooyer and R. Hooke 1996. A laboratory study of sediment deformation: stress heterogeneity and grain-size evolution. *Annals of Glaciology*, **22**: 167-175.
- Ives, J. and C. King 1954. Glaciological observations on Morsárjökull, S.W. Vatnajökull (Part I: The ogive banding). *Journal of Glaciology*, **2**: 423-428.
- Ivy-Ochs, S., C. Schlüchter, P. Kubik and G. Denton 1999. Moraine exposure dates imply synchronous Younger Dryas glacier advances in the European Alps and in the Southern Alps of New Zealand. *Geografiska Annaler*, **81A**(2): 313-323.

References

- Jacobel, R., B. Welch, D. Osterhouse, R. Pettersson and J. MacGregor 2009. Spatial variation of radar-derived basal conditions on Kamb Ice Stream, West Antarctica. *Annals of Glaciology*, **50**(51): 10-16.
- Jaeger, J. and N. Cook 1979. *Fundamentals of Rock Mechanics*. 3rd ed. London, Chapman & Hall.
- JISAO 2010. PDO Monthly Values: January 1900-present. Joint Institute for the Study of the Atmosphere and Ocean. (25th June).
- Jobard, S. and M. Dzikowski 2006. Evolution of glacial flow and drainage during the ablation season. *Journal of Hydrology*, **330**: 663-671.
- Johannesson, T., C. Raymond and E. Waddington 1989. Time-scale for adjustment of glaciers to changes in mass balance. *Journal of Glaciology*, **35**: 355-369.
- Jol, H. 1995. Ground penetrating radar antennae frequencies and transmitter powers compared for penetration depth, resolution and reflection continuity. *Geophysical Prospecting*, **43**: 693-709.
- Jol, H., B. Goodsell, D. Nobes, M. Finnemore, T. Cussins, B. de Passille and J. Tealby 2004. Preliminary results from high frequency GPR surveys and a 3D grid: Davis Snowfield, Franz Josef Glacier, New Zealand. In Slob, E.V.Y.A.R.J., ed. *10th International Conference on Ground Penetrating Radar (GPR 2004)*, Delft, Netherlands, 773-776.
- Jorgensen, A. and F. Andreasen 2007. Mapping of permafrost surface using ground-penetrating radar at Kangerlussuaq Airport, western Greenland. *Cold Regions Science and Technology*, **48**(1): 64-72.
- Jouzel, J. and R. Souchez 1982. Melting-refreezing at the glacier sole and the isotopic composition of the ice. *Journal of Glaciology*, **28**(98): 35-42.
- Kamb, B. 1970. Sliding motion of glaciers. *Reviews of Geophysics*, **8**: 673-728.
- Kamb, B. 1987. Glacier surge mechanism based on linked cavity configuration of the basal water conduit system. *Journal of Geophysical Research-Earth Surface*, **92**: 9083-9100.
- Kaplan, M., H. Schaefer, G. Denton, D. Barrell, T. Chinn, A. Putnam, B. Anderson, R. Finkel, R. Schwartz and A. Doughty 2010a. Glacier retreat in New Zealand during the Younger Dryas Stadial. *Nature*, **467**: 194-197.
- Kaplan, M., J. Schaefer, G. Denton, D. Barrell, T. Chinn, A. Putnam, B. Andersen, R. Finkel, R. Schwartz and A. Doughty 2010b. Glacier retreat in New Zealand during the Younger Dryas stadial. *Nature*, **467**(7312): 194-197.
- Karato, S., S. Zang, M. Zimmerman, M. Daines and D. Kohlstedt 1998. Experimental studies of shear deformation of mantle materials: Towards structural geology of the mantle. *Pure and Applied Geophysics*, **151**(2-4): 589-603.

- Karlsson, N., D. Rippin, D. Vaughan and H. Corr 2009. The internal layering of Pine Island Glacier, West Antarctica, from airborne radar-sounding data. *Annals of Glaciology*, **50**: 141-146.
- Kavanaugh, J. and G. Clarke 2001. Abrupt glacier motion and reorganization of basal shear stress following the establishment of a connected drainage system. *Journal of Glaciology*, **47**(158): 472-480.
- Kehle, R. 1964. Deformation of the Ross Ice Shelf, Antarctica. *Geological Society of America Bulletin*, **75**: 259-286.
- Kelliher, F., I. Owens, A. Sturman, J. Byers, J. Hunt and T. McSeveny 1996. Radiation and ablation on the Neve of Franz Josef Glacier. *Journal of Hydrology*, **35**: 131-150.
- Kelly, M., T. Lowell, B. Hall, J. Schaefer, R. Finkel, B. Goehring, R. Alley and G. Denton 2008. A ^{10}Be chronology of lateglacial and Holocene mountain glaciation in the Scoresby Sund region, east Greenland: implications for seasonality during lateglacial time. *Quaternary Science Reviews*, **27**(25-26): 2273-2282.
- Kennet, M. 1989. A possible radio-echo method of locating englacial and subglacial waterways. *Annals of Glaciology*, **13**: 135-139.
- Kennet, M., T. Laumann and C. Lund 1993. Helicopter-borne radio-echo sounding of Svartisen, Norway. *Annals of Glaciology*, **17**: 23-26.
- Kim, K., J. Lee, M. Hong, J. Hong and H. Shon 2010. Helicopter-borne and ground-towed radar surveys of the Fourcade Glacier on King George Island, Antarctica. *Exploration Geophysics*, **41**(1): 51-60.
- King, C. and J. Ives 1954. Glaciological investigations on some of the outlet glaciers of South-West Vatnajökull, Iceland, Part 1: The ogive banding. *Journal of Glaciology*, **2**: 646-650.
- King, C. and W. Lewis 1961. A tentative theory of ogive formation. *Journal of Glaciology*, **3**: 913-939.
- Kirkbride, M. 1993. The temporal significance of transitions from melting to calving termini at glaciers in the Central Southern Alps of New Zealand. *The Holocene*, **3**: 232-240.
- Kirkbride, M. 2002. Processes of Glacial Transportation. In Menzies, J., ed. *Modern and past Glacial Environments*, Burlington, Butterworth-Heinemann.
- Kirkbride, M. 2010. Climate change: A glacial test of timing. *Nature*, **467**(7312): 160-161.
- Kirkbride, M. and N. Spedding 1996. The influence of englacial drainage on sediment transport pathways and till texture of temperate valley glaciers. *Annals of Glaciology*, **22**: 160-166.
- Kirkbride, M. and D. Sugden 1992. New Zealand loses its top. *Geographical magazine*, 30-34.

References

- Kjær, K. 1999. Mode of subglacial transport deduced from till properties, Myrdalsjökull, Iceland. *Sedimentary Geology*, **128**(3-4): 271-292.
- Knight, P. 1992. Ice deformation very close to the ice sheet margin in west Greenland. *Journal of Glaciology*, **38**(128): 3-8.
- Knighton, D. 1972. Meandering habit of supraglacial streams. *Geological Society of America Bulletin*, **83**: 201-204.
- Koch, J., B. Menounos and J. Clague 2009. Glacier change in Garibaldi Provincial Park, southern Coast Mountains, British Columbia, since the Little Ice Age. *Global and Planetary Change*, **66**(3-4): 161-178.
- Kohler, J., J. Moore, M. Kennet, R. Engeset and H. Elvehoy 1997. Using ground-penetrating radar to image previous years' summer surfaces for mass balance measurements. *Annals of Glaciology*, **24**: 355-360.
- König, M., J.-G. Winther and E. Isaksson 2001. Measuring snow and glacier ice properties from satellite. *Reviews of Geophysics*, **39**(1): 1-27.
- Krüger, J. 1994. Glacial processes, sediments, landforms, and stratigraphy in the terminus region of Myrdalsjökull, Iceland. *Folia Geographica, Danica*, **XXI**.
- Krumbein, W. 1941. Measurement and geological significance of shape and roundness of sedimentary particles. *Journal of Sedimentary Petrology*, **11**: 64-72.
- Kulesa, B. 2007. A critical review of the low-frequency electrical properties of ice sheets and glaciers. *Journal of Environmental and Engineering Geophysics*, **12**(1): 23-36.
- Laird, C., W. Blake, K. Matsuoka, H. Conway, C. Allen, C. Leuschen and S. Gogineni 2010. Deep Ice Stratigraphy and Basal Conditions in Central West Antarctica Revealed by Coherent Radar. *Ieee Geoscience and Remote Sensing Letters*, **7**(2): 246-250.
- Lalumiere, L. 2006. Ground penetrating radar for helicopter snow and ice surveys. Canadian Technical Report in Hydrographic & Ocean Sciences.
- Lamont, G., T. Chinn and B. Fitzharris 1997. Slopes of glacier ELAs in the Southern Alps of New Zealand in relation to atmospheric circulation patterns. *International Symposium on Glaciers of the Southern Hemisphere*, Melbourne, Australia, Elsevier Science Bv, 209-219.
- Lamont, G., T. Chinn and B. Fitzharris 1999. Slopes of glacier ELAs in the Southern Alps of new Zealand in relation to atmospheric circulation patterns. *Global and Planetary Change*, **22**: 209-219.
- Langley, K., S. Hamran, K.A. Hogda, R. Storvold, O. Brandt, J. Hagen and J. Kohler 2007. Use of C-band ground penetrating radar to determine backscatter sources within glaciers. *Ieee Transactions on Geoscience and Remote Sensing*, **45**(5): 1236-1246.

- Larsen, S., T. Davies and M. McSaveney 2005. A possible coseismic landslide origin of late Holocene moraines of the Southern Alps, New Zealand. *New Zealand Journal of Geology and Geophysics*, **48**(2): 311-314.
- Lawson, W. 1996. Structural evolution of Variegated Glacier, Alaska, U.S.A., since 1948. *Journal of Glaciology*, **42**(141): 261-270.
- Lawson, W., M. Sharp and M. Hambrey 1994. The structural geology of a surge-type glacier. *Journal of Structural Geology*, **10**(5): 499-515.
- Lee, J., K. Kim, J. Hong and Y. Jin 2010. An englacial image and water pathways of the fourcade glacier on King George Island, Antarctic Peninsula, inferred from ground-penetrating radar. *Science China-Earth Sciences*, **53**(6): 892-900.
- Leighton, F. 1951. Ogives of the East Twin Glacier, Alaska- Their nature and origin. *Geological Society of America Bulletin*, **62**(12): 1505-1505.
- Lemke, P., J. Ren, R. Alley, I. Allison, J. Carrasco, G. Flato, G. Fujii, Y. Kaser, P. Mote, R. Thomas and T. Zhang 2007. Observations: Changes in Snow, Ice and Frozen Ground. *Climate Change 2007: The Physical Science Basis. Contribution of Working Group I to the Fourth Assessment Report of the Intergovernmental Panel on Climate Change*, Cambridge, Cambridge University Press.
- Liboutry, L. 1958. Studies of the shrinkage after sudden advance, blue bands and wave ogives on glacier Universidad (Central Chilean Andes). *Journal of Glaciology*, **3**: 261-268.
- Liboutry, L. and L. Reynaud 1981. Global dynamics of a temperate valley glacier, Mer de Glace, and past velocities deduced from Forbes bands. *Journal of Glaciology*, **27**: 207-226.
- Liebinger, A., G. Haberhauer, W. Papesch and G. Heiss 2006. Correlation of the isotopic composition in precipitation with local conditions in alpine regions. *Journal of Geophysical Research-Atmospheres*, **111**(D5): 10.
- Lillie, A., B. Gunn and P. Robinson 1957. Structural observations in Central Alpine Region of New Zealand. *Transactions of the Royal Society of New Zealand*, **85**(1): 113-129.
- Lillie, A. and B. Mason 1955. Geological reconnaissance of Districts between Franz Josef Glacier and Copland Valley. *Transactions of the Royal Society of New Zealand*, **82**(5): 1123-1128.
- Lloyd, C., C.D. Clark and D. Swift 2012. Controls on the location and geometry of glacial overdeepening. *Geophysical Research Abstracts*, **14**(EGU2012-173).
- Lockwood, G. 1949. On the Fox Glacier. *The New Zealand Alpine Journal*, **13**(36): 38-41.
- Lonne, I. and T. Lauritsen 1996. The architecture of a modern push-moraine at Svalbard as inferred from ground-penetrating radar measurements. *Arctic and Alpine Research*, **28**(4): 488-495.

References

- Lowell, T. and M. Kelly 2008. Was the Younger Dryas global? *Science*, **321**(5887): 348-349.
- Lutz, P., S. Garambois and H. Perroud 2003. Influence of antenna configurations for GPR survey: information from polarization and amplitude versus offset measurements. *Geological Society, London, Special Publications*, **211**(1): 299-313.
- MacGregor, K., C. Riihimaki and R. Anderson 2005. Spatial and temporal evolution of rapid basal sliding on Bench Glacier, Alaska, USA. *Journal of Glaciology*, **51**(172): 49-63.
- Macheret, Y., M. Moskalevsky and E. Vasilenko 1993. Velocity of radio waves in glaciers as an indicator of their hydrothermal state, structure and regime. *Journal of Glaciology*, **39**(132): 373-385.
- Macheret, Y., J. Otero, F. Navarro, E. Vasilenko, M. Corcuera, M. Cuadrado and G. A. 2009. Ice thickness, internal structure and subglacial topography of Bowles Plateau ice cap and the main ice divides of Livingston Island, Antarctica, by ground-based radio-echo sounding. *Annals of Glaciology*, **50**(51): 49-56.
- Machguth, H., O. Eisen, F. Paul and M. Hoelzle 2006. Strong spatial variability of snow accumulation observed with helicopter-borne GPR on two adjacent Alpine glaciers. *Geophysical Research Letters*, **33**: 1-5.
- Magnusson, E., H. Bjornsson, H. Rott and F. Palsson 2010. Reduced glacier sliding caused by persistent drainage from a subglacial lake. *Cryosphere*, **4**(1): 13-20.
- Mair, D., P. Nienow, I. Willis and M. Sharp 2001. Spatial patterns of glacier motion during a high-velocity event: Haut Glacier d'Arolla, Switzerland. *Journal of Glaciology*, **47**(156): 9-20.
- Male, D. and D. Gray 1981. Snowcover ablation and runoff. In Gray, D. and D. Male, eds. *Handbook of Snow. Principles, Processes, Management & Use*, New Jersey, The Blackburn Press.
- Mann, M. 2002. Little Ice Age. In MacCracken, M. and J. Perry, eds. *Encyclopedia of Global Environmental Change*, Chichester, John Wiley & Sons, Ltd.
- Marcus, M., R. Moore and I. Owens 1985. Short-term estimates of surface energy transfers and ablation on the lower Franz Josef Glacier, South Westland, New Zealand. *New Zealand Journal of Geology and Geophysics*, **28**: 559-567.
- Matsuoka, K., H. Maeno, S. Uratsuka, S. Fujita, T. Furukawa and O. Watanabe 2002. A ground-based, multi-frequency ice-penetrating radar system. *Annals of Glaciology*, Vol 34, 2002, 171-176. (*Annals of Glaciology*).
- Mattson, L., J. Gardner and G. Young 1993. Ablation on debris covered glaciers: an example from Rakhiot Glacier, Panjab, Himalaya. *IAHS Publication*, **218**: 289-296.
- Maurer, H. and C. Hauck 2007. Instruments and methods - Geophysical imaging of alpine rock glaciers. *Journal of Glaciology*, **53**(180): 110-120.

- McClay, K. 1997. *The mapping of Geological Structures*. Chichester, John Wiley & Sons.
- McClymont, W. 1935. Historical summary of the Mid-Southern Alps, 1642-1883. *The New Zealand Alpine Journal*, **6**(22): 112-128.
- McKinzey, K., W. Lawson, D. Kelly and A. Hubbard 2004. A revised little ice age chronology of the Franz Josef Glacier, Westland, New Zealand. *Journal of the Royal Society of New Zealand*, **34**(4): 381-394.
- McSaveney, M. and M. Gage 1968. Ice flow measurements on Franz Josef Glacier, New Zealand, in 1966. *New Zealand Journal of Geology and Geophysics*, **11**(3): 564-592.
- Meier, M. 1960. Mode of flow of Saskatchewan Glacier, Alberta, Canada. *United States Geological Survey Professional Paper*, **351**.
- Meier, M. 1961. Mass budget of South Cascade Glacier, 1957-1960. *US Geological Survey Professional Paper*, **424**(B): 206-211.
- Meier, M., B. Kamb, C. Allen and R. Sharp 1974. Flow of Blue Glacier, Olympic Mountains, Washington. *Journal of Glaciology*, **13**(68): 187-212.
- Meier, M., S. Lundstrom, D. Stone, B. Kamb, H. Engelhardt, N. Humphrey, W. Dunlap, M. Fahnestock, R. Krimmel and R. Walters 1994. Mechanical and hydrologic basis for the rapid motion of a large tidewater glacier 1. Observations. *Journal of Geophysical Research-Solid Earth*, **99**(B8): 15219-15229.
- Meier, M. and W. Tangbourn 1965. Net budget and flow of South Cascade Glacier, Washington. *Journal of Glaciology*, **5**(41): 547-566.
- Miller, M. 1949. *Progress Report of the Juneau Ice Field Research Project*. New York, American Geographical Society.
- Miller, M. 1952. Preliminary notes concerning certain glacier structures and glacial lakes on the Juneau Ice Field *Juneau ice Field Research Project Report No. 6*: 49-86.
- Milnes, A. and M. Hambrey 1976. A method of estimating approximate cumulative strains in glacier ice. *Tectonophysics*, **34**: T23-T27.
- Moar, N., P. Suggate and C. Burrows 2008. Environments during the Kaihinu Interglacial and Otiran Glaciation, coastal north Westland, New Zealand. *New Zealand Journal of Botany*, **46**: 49-63.
- Monnier, S., C. Camerlynck and F. Rejiba 2008. Ground penetrating radar survey and stratigraphic interpretation of the Plan du Lac rock glaciers, Vanoise Massif, northern French Alps. *Permafrost and Periglacial Processes*, **19**(1): 19-30.
- Moore, P., N. Iverson and D. Cohen 2010. Conditions for thrust faulting in a glacier. *Journal of Geophysical Research-Earth Surface*, **115**: 2005.

References

- Moorman, B. and F. Michel 2000. Glacial hydrological system characterization using ground-penetrating radar. *Hydrological Processes*, **14**(15): 2645-2667.
- Moorman, B., S. Robinson and M. Burgess 2003. Imaging periglacial conditions with ground-penetrating radar. *Permafrost and Periglacial Processes*, **14**(4): 319-329.
- Moran, T., S. Marshall, E. Evans and K. Sinclair 2007. Altitudinal gradients of stable isotopes in lee-slope precipitation in the Canadian Rocky Mountains. *Arctic, Antarctic and Alpine Research*, **39**(3): 455-467.
- Moreno, P., M. Kaplan, J. François, R. Villa-Martínez, C. Moy, C. Stern and P. Kubik 2009. Renewed glacial activity during the Antarctic cold reversal and persistence of cold conditions until 11.5 ka in southwestern Patagonia. *Geology*, **37**(4): 375-378.
- Morey, R. 1974. Continuous subsurface profiling by impulse radar. In. *Engineering Foundation Conference on Subsurface Exploration for Underground Excavation and Heavy Construction* Nenniker, New Hampshire, American Society of Civil Engineers.
- Morgenstern, U., L. Fifield and A. Zondervan 2000. New frontiers in glacier ice dating: measurement of natural ^{32}Si by AMS. *Nuclear Instruments and Methods in Physics Research*, **B**(172): 605-609.
- Morgenstern, U., P. Mayewski, N. Bertler and R. Ditchburn 2006. Ice core research in the New Zealand Southern Alps. *Geochimica et Cosmochimica Acta*, **70**(18, Supplement 1): A430-A430.
- Mottram, R., C. Nielsen, A. Ahlstrøm, N. Reeh, S. Kristensen, E. Christensen, R. Forsberg and L. Stenseng 2009. A new regional high-resolution map of basal and surface topography for the Greenland ice-sheet margin at Paakitsoq, West Greenland. *Annals of Glaciology*, **50**(51): 105-111.
- Müller, F. 1962. Zonation in the accumulation area of the glaciers of Axel Heiberg Island, N.W.T., Canada. *Journal of Glaciology*, **4**: 302-313.
- Müller, F. and A. Iken 1973. Velocity fluctuations and water regime of Arctic valley glaciers. *International Association of Hydrological Sciences Publication*, **95**: 165-82.
- Mullan, B. 1996. Effects of ENSO on New Zealand and the South Pacific. In Braddock, D., ed. *Prospects and needs for climate forecasting. Miscellaneous Series 34*, Wellington, Royal Society of New Zealand.
- Munroe, J., J. Doolittle, M. Kanevskiy, K. Hinkel, F. Nelson, B. Jones, Y. Shur and J. Kimble 2007. Application of ground-penetrating radar imagery for three-dimensional visualisation of near-surface structures in ice-rich permafrost, Barrow, Alaska. *Permafrost and Periglacial Processes*, **18**(4): 309-321.
- Murray, T., A. Booth and D. Rippin 2007a. Water-content of glacier-ice: Limitations on estimates from velocity analysis of surface ground-penetrating radar surveys. *Journal of Environmental and Engineering Geophysics*, **12**(1): 87-99.

- Murray, T., A. Booth and D.M. Rippin 2007b. Water-content of Glacier-ice: Limitations on Estimates from Velocity Analysis of Surface Ground-penetrating Radar Surveys. *Journal of Environmental & Engineering Geophysics*, **12**(1): 87-99.
- Murray, T., D. Gooch and G. Stuart 1997. Structures within the surge front at Bakaninbreen, Svalbard, using ground-penetrating radar. *Annals of Glaciology*, **24**: 122-129.
- Murray, T., G. Stuart, M. Fry, N. Gamble and M. Crabtree 2000a. Englacial water distribution in a temperate glacier from surface and borehole radar velocity analysis. *Journal of Glaciology*, **46**(154): 389-398.
- Murray, T., G. Stuart, P. Miller, J. Woodward, A. Smith, P. Porter and H. Jiskoot 2000b. Glacier surge propagation by thermal evolution at the bed. *Journal of Geophysical Research*, **105**(B6): 13491-13507.
- NASA 2007. The South Island, New Zealand. NASA Earth Observatory. (15th May).
- Navarro, F., Y. Macheret and B. Benjumea 2005. Application of radar and seismic methods for the investigation of temperate glaciers. *Journal of Applied Geophysics*, **57**(3): 193-211.
- Nesje, A. and S. Dahl 2000. *Glaciers and Environmental Change*. Oxford, Hodder Arnold.
- Neumann, T. and E. Waddington 2004. Effects of firn ventilation on isotopic exchange. *Journal of Glaciology*, **50**(169): 183-194.
- Newnham, R. , J. Shulmeister, C. Singer, McLea and B. 1999. Temperature Changes During the Younger Dryas in New Zealand. *Science*, **283**(5403): 759a-.
- Newnham, R., D. Eden, D. Lowe and C. Hendy 2003. Rerewhakaaitu Tephra, a land-sea marker for the Last Termination in New Zealand, with implications for global climate change. *Quaternary Science Reviews*, **22**(2-4): 289-308.
- Newton, H. 1939. Fox Glacier First Ascents. The Teichelmann-Newton Expedition, 1907. *The New Zealand Alpine Journal*, **8**(26): 1-14.
- Nicollin, F., Y. Barbin, W. Kofman, D. Mathieu, S. Hamran, P. Bauer, J. Achache and J. Blamont 1992. An HF bi-phase shift keying radar-application to ice sounding in Western Alps and Spitzbergen glaciers. *Ieee Transactions on Geoscience and Remote Sensing*, **30**(5): 1025-1033.
- Nobes, D. 1999. The directional dependence of the ground penetrating radar response on the accumulation zones of temperate alpine glaciers. *First Break*, **17**(7): 249-259.
- Nobes, D. and A. Annan 2000. Broadside versus end-fire radar response: some simple illustrative examples. In David, A.N., F.S. Glen and L. Dennis, eds., SPIE, 696-701.
- Nobes, D., S. Leary, M. Hochstein and S. Henry 1994. Ground-penetrating radar profiles of rubble-covered temperate glaciers: Results from the Tasman and Mueller

References

Glaciers of the Southern Alps of New Zealand. *Society of Exploration Geophysicists Annual Meeting, Expanded Abstracts*, **64**: 826-829.

Nobes, D. and I. Owens 1995. Preliminary results from the 1995 ground penetrating radar profiling programme of the Tasman Glacier and the neve of the Franz Josef Glacier. *Programme, and Abstracts, Geological Society of New Zealand 1995 Annual Conference*.

Nolan, M., R. Motyka, K. Echelmeyer and D. Trabant 1996. Ice-thickness measurements of Taku Glacier, Alaska, USA, and their relevance to its recent behavior *Journal of Glaciology*, **42**(141): 400-400.

Nye, J. 1951. The flow of glaciers and ice sheets as a problem of plasticity. *Proceedings of the Royal Society, Series A*, **207**(1091): 554-572.

Nye, J. 1952. The mechanics of glacier flow. *Journal of Glaciology*, **2**: 82-93.

Nye, J. 1957. *Physical Properties of Crystals*. Oxford, Clarendon Press.

Nye, J. 1958. Surges in Glaciers. *Nature*, **181**: 1450-1451.

Nye, J. 1959. A method of determining the strain-rate tensor at the surface of a glacier. *Journal of Glaciology*, **3**(25): 409-419.

Nye, J. 1969. A calculation of the sliding of ice over a wavy surface using a Newtonian viscous approximation. *Proceedings of the Royal Society, Series A*, **311**: 445-467.

Nye, J. 1970. Glacier sliding without cavitation in a linear viscous approximation. *Proceedings of the Royal Society, Series A*, **315**: 381-403.

NZGS 1973. Quaternary Geology, South Island, Map 6. *New Zealand Geological Survey Miscellaneous Map Series*, New Zealand Geological Survey.

Odell, N. 1960. The mountains and glaciers of New Zealand. *Journal of Glaciology*, **3**: 739-741.

Oerlamans, J. 1997. Climate sensitivity of Franz Josef Glacier, New Zealand, as revealed by numerical modelling. *Arctic and Alpine Research*, **29**: 233-239.

Oerlamans, J. 2001. *Glaciers and Climate Change*. Lisse, Swets & Zeitlinger BV.

Olhoeft, G. 1996. Application of Ground Penetrating Radar. *6th International Conference on Ground Penetrating Radar (GPR '96)*, Sendai, Japan, 1-4.

Olhoeft, G. 2000. Maximizing the information return from ground penetrating radar. *Journal of Applied Geophysics*, **43**(2-4): 175-187.

Olhoeft, G. 2002. Applications and frustrations in using ground penetrating radar. *Aerospace and Electronic Systems Magazine, IEEE*, **17**(2): 12-20.

- Overpeck, J.T., B.L. Otto-Bliesner, G.H. Miller, D.R. Muhs, R.B. Alley and J.T. Kiehl 2006. Paleoclimatic Evidence for Future Ice-Sheet Instability and Rapid Sea-Level Rise. *Science*, **311**(5768): 1747-1750.
- Owens, I. 2005. GPS observations of recent terminus behaviour of the Franz Josef Glacier, New Zealand. *Snow and Ice Research Group 3rd Annual Workshop*, Harihari, Westland.
- Owens, I., A. Sturman and N. Ishikawa 1992. High rates of ablation on the lower part of the Franz Josef Glacier, South Westland. *New Zealand Geographical Society Conference Series*, **16**: 576-582.
- Palmer, S., A. Shepherd, P. Nienow and I. Joughin 2011. Seasonal speedup of the Greenland Ice Sheet linked to routing of surface water. *Earth and Planetary Science Letters*, **302**(3-4): 423-428.
- Paterson, W. 1994. *The Physics of Glaciers*. 3rd ed. Amsterdam, Elsevier Science.
- Paterson, W. 2000. *The Physics of Glaciers*. 3rd ed. Burlington, Butterworth-Heinemann.
- Pelto, M. 1988. The annual balance of North Cascade glaciers, Washington, USA, measured and predicted using an activity-index method. *Journal of Glaciology*, **34**(117): 194-199.
- Plewes, L. and B. Hubbard 2001. A review of the use of radio-echo sounding in glaciology. *Progress in Physical Geography*, **25**(2): 203-236.
- Popovnin, V. and A. Rozova 2002. Influence of sub debris thawing on ablation and runoff of the Djankuat Glacier in the Caucasus. *Nordic Hydrology*, **33**: 79-94.
- Porter, H. 1934. Douglas Peak, New Zealand. *The New Zealand Alpine Journal*, **5**(21): 402-408.
- Porter, S. 2000. Onset of Neoglaciation in the Southern Hemisphere. *Journal of Quaternary Science*, **15**(4): 395-408.
- Posamentier, H. 1978. Thoughts on ogive formation *Journal of Glaciology*, **20**: 218-220.
- Price, R. 1970. Moraines at Fjallsjökull, Iceland. *Arctic and Alpine Research*, **2**: 27-42.
- Priscu, J., R. Powell and S. Tulaczyk 2010. Probing subglacial environments under the Whillans Ice Stream. *EOS, Transactions, American Geophysical Union*, **91**(29): 253-254.
- Purdie, H. 2005. Intra-annual Variations in Ablation and Surface Velocity on the Lower Fox Glacier, South Westland, New Zealand. MSc Thesis, Massey University.)
- Purdie, H., B. Anderson, W. Lawson and A. Mackintosh 2011a. Controls on spatial variability in snow accumulation on glaciers in the Southern Alps, New Zealand; as revealed by crevasse stratigraphy. *Hydrological Processes*, **25**(1): 54-63.

References

- Purdie, H., M. Brook and I. Fuller 2008a. Seasonal variation in ablation and surface velocity on a temperate maritime Glacier: Fox Glacier, New Zealand. *Arctic Antarctic and Alpine Research*, **40**(1): 140-147.
- Purdie, H., M. Brook, I. Fuller and J. Appleby 2008b. Seasonal variability in velocity and ablation of Te Moeka o Tuawe/Fox glacier, South Westland, New Zealand. *New Zealand Geographer*, **64**(1): 5-19.
- Purdie, H., A. Mackintosh, W. Lawson, B. Anderson, U. Morgenstern, T. Chinn and P. Mayewski 2011b. Interannual variability in net accumulation on Tasman Glacier and its relationship with climate. *Global and Planetary Change*, **77**(3-4): 142-152.
- Purdie, J. and W. Bardsley 2010. Seasonal prediction of lake inflows and rainfall in a hydro-electricity catchment, Waitaki River, New Zealand. *International Journal of Climatology*, **20**: 218-220.
- Putnam, A., G. Denton, H. Schaefer, D. Barrell, B. Andersen, R. Finkel, R. Schwartz, A. Doughty, M. Kaplan and C. Schluchter 2010. Glacier advance in south middle-latitudes during the Antarctic Cold Reversal. *Nature Geoscience*, **3**: 700-704.
- Radzevicius, S., E. Guy and J. Daniels 2000. Pitfalls in GPR data interpretation: Differentiating stratigraphy and buried objects from periodic antenna and target effects. *Geophysical Research Letters*, **27**(20): 3393-3396.
- Ragan, D. 1969. Structures at the base of an icefall. *Journal of Geology*, **77**: 647-667.
- Ramsay, J. and M. Huber 1987. *The techniques of modern structural geology, volume 2: Folds and fractures*. London, Academic Press.
- Reheis, M. 1975. Source, transportation and deposition of debris on Arapaho Glacier, Front Range, Colorado, U.S.A. *Journal of Glaciology*, **14**(72): 407-419.
- Renssen, H., H. Goosse and T. Fichefet 2007. Simulation of Holocene cooling events in a coupled climate model. *Quaternary Science Reviews*, **26**(15-16): 2019-2029.
- Reynolds, J. 1997. *An Introduction to Applied and Environmental Geophysics*. Chichester, Wiley.
- Reznichenko, N.V., T.R.H. Davies and D.J. Alexander 2011. Effects of rock avalanches on glacier behaviour and moraine formation. *Geomorphology*, **132**(3-4): 327-338.
- Richardson, J. and M. Brook 2010. Ablation of debris-covered ice: some effects of the 25 September 2007 Mt Ruapehu eruption. *Journal of the Royal Society of New Zealand*, **40**(2): 45-55.
- Roberson, S. 2008. Structural composition and sediment transfer in a composite cirque glacier: Glacier de St. Sorlin, France. *Earth Surface Processes and Landforms*, **33**(13): 1931-1947.
- Robin, G. 1974. Correspondence. Depth of water-filled crevasses that are closely spaced. *Journal of Glaciology*, **13**(69): 543.

- Robin, G. 1976. Is the basal ice of a temperate glacier at the pressure melting point? *Journal of Glaciology*, **16**: 183-196.
- Rose, J. 1989. Glacier stress patterns and sediment transfer associated with the formation of superimposed flutes. *Sedimentary Geology*, **62**: 151-176.
- Rose, J. 1992. Boulder clusters in glacial flutes. *Geomorphology*, **6**: 51-58.
- Rossiter, J., A. Annan, J. Redman and D. Strangway 1975. Radio interferometry over ice and permafrost. *Geophysics*, **40**(1): 154-154.
- Rother, H. and J. Shulmeister 2006. Synoptic climate change as a driver of late Quaternary glaciations in the mid-latitudes of the Southern Hemisphere. *Climate of the Past*, **2**(1): 11-19.
- Röthlisberger, H. and A. Iken 1981. Plucking as an effect of water-pressure variations at the glacier bed. *Annals of Glaciology*, **2**: 57-62.
- Röthlisberger, H. and H. Lang 1987. Glacial Hydrology. In Gurnell, A. and M. Clark, eds. *Glacio-fluvial sediment transfer: an alpine perspective*, Chichester, Wiley, 207-284.
- Ruddell, A. 1995. Recent Glacier and Climate Change in the New Zealand Alps. PhD Thesis, University of Melbourne.)
- Saarenketo, T. 1998. Electrical properties of water in clay and silty soils. *Journal of Applied Geophysics*, **40**(1-3): 73-88.
- Sadura, S., I. Martini, A. Endres and K. Wolf 2006. Morphology and GPR stratigraphy of a frontal part of an end moraine of the Laurentide Ice Sheet: Paris Moraine near guelph, ON, Canada. *Geomorphology*, **75**(1-2): 212-225.
- Salinger, M., J. Renwick and A. Mullan 2001. Interdecadal Pacific Oscillation and South Pacific climate. *International Journal of Climatology*, **21**(14): 1705-1721.
- Sara, W. 1968. Franz Josef and Fox Glaciers, 1951-67. *New Zealand Journal of Geology and Geophysics*, **11**(3): 768-780.
- Sara, W. 1970. Glaciers of Westland National Park. *New Zealand Department of Scientific and Industrial Research, Information Series No.75*.
- Sass, O. 2006. Determination of the internal structure of alpine talus deposits using different geophysical methods (Lechtaler Alps, Austria). *Geomorphology*, **80**(1-2): 45-58.
- Sass, O. and K. Wollny 2001. Investigations regarding alpine talus slopes using ground-penetrating radar (GPR) in the Bavarian Alps, Germany. *Earth Surface Processes and Landforms*, **26**(10): 1071-1086.
- Schaefer, J., G. Denton, M. Kaplan, A. Putnam, R. Finkel, D. Barrell, B. Andersen, R. Schwartz, A. Mackintosh, T. Chinn and C. Schluchter 2009. High-Frequency Holocene

References

glacier fluctuations in New Zealand differ from the Northern signature. *Science*, **324**(5927): 622-625.

Schwamborn, G., D. Wagner and H.-W. Hubberten 2008. The use of GPR to detect active layer in young periglacial terrain of Livingston Island, Maritime Antarctica. *Near Surface Geophysics*, **6**: 327-332.

Schytt, V. 1967. A study of "ablation gradient". *Geografiska Annaler*, **49A**(2-4): 327-332.

Sharp, M. 1985a. 'Crevasse-fill' ridges- A landform type characteristic of surging glaciers? *Geografiska Annaler*, **67A**: 213-220.

Sharp, M. 1985b. Sedimentation and stratigraphy at Eyjabakkajökull--An Icelandic surging glacier. *Quaternary Research*, **24**(3): 268-284.

Sharp, M. and B. Gomez 1986. Processes of debris comminution in the glacial environment and implications for quartz-sand-grain micromorphology. *Sedimentary Geology*, **46**: 33-47.

Sharp, M., D. Lawson and R. Anderson 1988a. Tectonic processes in a surge-type glacier. *Journal of Structural Geology*, **10**: 499-515.

Sharp, M., W. Lawson and W. Anderson 1988b. Tectonic processes in a surge type glacier. *Journal of Glaciology*, **40**: 327-340.

Sharp, M., K. Richards, I. Willis, N. Arnold, P. Nienow, W. Lawson and J. Tison 1993. Geometry, bed topography and drainage system structure of the haut glacier d'Arolla, Switzerland. *Earth Surface Processes and Landforms*, **18**(6): 557-571.

Shi, Y., R. Allis and F. Davey 1996. Thermal modelling of the Southern Alps, New Zealand. *Pure and Applied Geophysics*, **146**(3-4): 469-501.

Shulmeister, J., T. Davies, D. Evans, O. Hyatt and D. Tovar 2009. Catastrophic landslides, glacier behaviour and moraine formation: A view from an active plate margin. *Quaternary Science Reviews*, **28**: 1085-1096.

Siegert, M. 1999. On the origin, nature and uses of Antarctic ice-sheet radio-echo layering. *Progress in Physical Geography*, **23**(2): 159-179.

Siegert, M. 2000. Antarctic subglacial lakes. *Earth-Science Reviews*, **50**(1-2): 29-50.

Siegert, M. 2005. Lakes beneath the ice sheet: The occurrence, analysis, and future exploration of Lake Vostok and other Antarctic subglacial lakes. *Annual Review of Earth and Planetary Sciences*, **33**: 215-245.

Siegert, M., J. Dowdeswell, M. Gorman and N. McIntyre 1996. An inventory of Antarctic sub-glacial lakes. *Antarctic Science*, **8**(3): 281-286.

Sinclair, K. and S. Marshall 2008. Post-depositional modification of stable water isotopes in winter snowpacks in the Canadian Rocky Mountains. *Annals of Glaciology*, **49**: 96-106.

- Sinclair, K. and S. Marshall 2009. Temperature and vapour-trajectory controls on the stable-isotope signal in Canadian Rocky Mountain snowpacks. *Journal of Glaciology*, **55**(91): 485-498.
- Singer, C., J. Shulmeister and B. McLea 1998. Evidence Against a Significant Younger Dryas Cooling Event in New Zealand. *Science*, **281**(5378): 812-814.
- Sneed, E. and R. Folk 1958. Pebbles in the lower Colorado River, Texas: A study in particle morphogenesis. *Journal of Geology*, **66**(2): 114-150.
- Soons, J. 1971. Recent changes in the Franz Josef Glacier. In Johnston, R. and J. Soons, eds. *Proceedings of the Sixth New Zealand Geography Conference, Christchurch, August 1970*, New Zealand Geographical Society, 195-200.
- Souchez, R. and J. De Groot 1985. δD - $\delta^{18}O$ Relationship in ice formed by subglacial freezing: Paleoclimatic implications *Journal of Glaciology*, **31**(109): 229-233.
- Souchez, R. and J. Jouzel 1984. On the isotopic composition in δD and $\delta^{18}O$ of water and ice during freezing. *Journal of Glaciology*, **30**(106): 369-372.
- Souchez, R. and R. Lorrain 1987. The Subglacial Sediment System. In Gurnell, A. and M. Clark, eds. *Glaciofluvial Sediment Transfer: An Alpine Perspective*, Chichester, Wiley, 147-163.
- Souchez, R., D. Samyn, R. Lorrain, F. Pattyn and S. Fitzsimons 2004. An isotopic model for basal freeze-on associated with subglacial upward flow of pore water. *Geophysical Research Letters*, **31**(2): 4.
- Speight, R. 1921. Recent changes in the terminal face of the Franz Josef Glacier. *Transactions of the New Zealand Institute* **53**: 53-57.
- Speight, R. 1934. Notes on the Franz Josef Glacier, February, 1934. *Transactions of the Royal Society of New Zealand*, **64**: 315-328.
- Speight, R. 1941. Notes on the Franz Josef Glacier, December, 1940. *Transactions of the Royal Society of New Zealand*, **71**: 128-133.
- Stenson, B. 1951. Radar methods for the exploration of glaciers. PhD Thesis, California Institute of Technology.)
- Steinhage, D., O. Eisen and H. Clausen 2005. Regional and temporal variation of accumulation around NorthGRIP derived from ground-penetrating radar. *Annals of Glaciology*, **42**: 326-330.
- Stenborg, T. 1969. Studies of the internal drainage of glaciers. *Geografiska Annaler*, **51A**: 13-41.
- Stern, W. 1929. Versuch einer elektrodynamischen Dickenmessung von Gletschereis. *Ger. Beitr. zur Geophysik*, **23**: 292-333.

References

- Stern, W. 1930. Über Grundlagen, Methodik und bisherige Ergebnisse elektrodynamischer Dickenmessung von Gletschereis. *Z. Gletscherkunde*, **15**: 24-42.
- Stichler, W., U. Schotterer, K. Frohlich, P. Ginot, C. Kull, H. Gaggeler and B. Pouyaud 2001. Influence of sublimation on stable isotope records recovered from high-altitude glaciers in the tropical Andes. *Journal of Geophysical Research-Atmospheres*, **106**(D19): 22613-22620.
- Stokes, C.R., V. Popovnin, A. Aleynikov, S.D. Gurney and M. Shahgedanova 2007. Recent glacier retreat in the Caucasus Mountains, Russia, and associated increase in supraglacial debris cover and supra-/proglacial lake development. *Annals of Glaciology*, **46**(1): 195-203.
- Streiff-Becker, R. 1943. Beitrag zur Gletscherfunde Forschungen am Claridfirn im Kt. Glauris, Schwiezer. *Naturf. Gessel. Denkschr.*, **75**: 111-132.
- Sugden, D., C. Clapperton, J. Gemmell and P. Knight 1987. Stable isotopes and debris in basal glacier ice, South Georgia, Southern Ocean. *Journal of Glaciology*, **33**(115): 324-329.
- Sugden, D. and B. John 1976. *Glaciers and Landscape*. London, Edward Arnold.
- Suggate, P. and P. Almond 2005. The Last Glacial Maximum (LGM) in western South Island, New Zealand: implications for the global LGM and MIS 2. *Quaternary Science Reviews*, **24**(16-17): 1923-1940.
- Suggate, R. 1950. Franz Josef and other glaciers of the Southern Alps, New Zealand. *Journal of Glaciology*, **1**(8): 422-429.
- Sun, J. and R. Young 1995. Recognizing surface scattering in ground-penetrating radar data. *Geophysics*, **60**(5): 1378-1385.
- Sutherland, R., K. Kim, A. Zondervan and M. McSaveney 2007. Orbital forcing of mid-latitude Southern Hemisphere glaciation since 100 ka inferred from cosmogenic nuclide ages of moraine boulders from the Cascade Plateau, southwest New Zealand. *Geological Society of America Bulletin*, **119**(3-4): 443-451.
- Swift, D., D. Evans and A. Fallick 2006. Transverse englacial debris-rich ice bands at Kvíárjökull, southeast Iceland. *Quaternary Science Reviews*, **25**: 1708-1718.
- Swinson, G. 1962. Investigation of shear zones in the ice sheet margin, Thule area, Greenland. *Journal of Glaciology*, **4**: 215-229.
- Taurisano, A., S. Tronstad, O. Brandt and J. Kohler 2006. On the use of ground penetrating radar for detecting and reducing crevasse-hazard in Dronning Maud Land, Antarctica. *Cold Regions Science and Technology*, **45**(3): 166-177.
- Thompson, D., D. Van Hollen, G. Osborn, C. Ryane, B. Menounos, J. Clague, J. Koch, J. Riedel, K. Scott and M. Reasoner 2006. Did Neoglaciation begin as early as 6400 cal years ago? *Geological Society of America Abstracts with Programs*, **38**(7): 236.

- Thomson, G. 1909. Botanical evidence against the recent glaciation of New Zealand. *Transactions of the Royal Society of New Zealand*, **42**: 348-353.
- Thomson, J. 2005. A radio echo sounding survey of the tasman Glacier neve area, mount Cook National Park, New Zealand. *Institute of Geological & Nuclear Science Report 2005/08*.
- Tippett, J. and P. Kamp 1995. Geomorphic evolution of the Southern Alps, New Zealand. *Earth Surface Processes and Landforms*, **20**(2): 177-192.
- Tovar, D., J. Shulmeister and T. Davies 2008. Evidence for a landslide origin of New Zealand's Waiho Loop moraine. *Nature Geoscience*, **1**(8): 524-526.
- Travassos, J. and J. Simões 2004. High-resolution radar mapping of internal layers of a subpolar ice cap, King George Island, Antarctica. *Pesquisa Antártica Brasileira*, **4**: 57-65.
- Truffer, M., W. Harrison and K. Echelmeyer 2000. Glacier motion dominated by processes deep in underlying till. *Journal of Glaciology*, **46**(153): 213-221.
- Turney, C., M. McGlone and J. Wilmshurst 2003. Asynchronous climate change between New Zealand and the North Atlantic during the last deglaciation. *Geology*, **31**(3): 223-226.
- Tutton, A. 1927. *The High Alps; A natural History of Ice and Snow*. London, Paul, Trench, Trubner & Co.
- Twiss, R. and E. Moores 1992. *Structural Geology*. New York, Freeman & Co.
- Twiss, R. and E. Moores 2007. *Structural Geology*. 2nd ed. New York, Freeman.
- Urbini, S., L. Vittuari and S. Gandolfi 2001. GPR and GPS data integration: examples of application in Antarctica. *Annali Di Geofisica*, **44**(4): 687-702.
- Vacco, D., R. Alley and W. Pollard 2010. Glacier advance and stagnation caused by rock avalanches. *Earth and Planetary Science Letters*, **294**: 123-130.
- van de Meer, J. 1997. Short-lived streamlined bedforms (annual small flutes) formed under clean ice, Turtmann Glacier, Switzerland. *Sedimentary Geology*, **111**: 107-118.
- van der Veen, C.J. 1999. Crevasses on glaciers. *Polar Geography*, **23**: 213-245.
- van Overmeeren, R. 1994. High speed georadar data acquisition for groundwater exploration in the Netherlands. *5th International Conference on ground Penetrating Radar*, Ontario, Canada.
- Vandergoes, M., A. Dieffenbacher-Krall, R. Newnham, G. Denton and M. Blaauw 2008. Cooling and changing seasonality in the Southern Alps, New Zealand during the Antarctic Cold Reversal. *Quaternary Science Reviews*, **27**(5-6): 589-601.

References

- Vandergoes, M. and S. Fitzsimons 2003. The Last Glacial-Interglacial Transition (LGIT) in south Westland, New Zealand: paleoecological insight into mid-latitude Southern Hemisphere climate change. *Quaternary Science Reviews*, **22**(14): 1461-1476.
- Vareschi, V. 1942. Die pollenanalytische untersuchung der Gletscherbewegung. *Veröffentlichungen des Geobotanischen Instituts Rübel in Zürich*, **19**: 142.
- Vaughan, D. 1993. Relating the occurrence of crevasses to surface strain rates. *Journal of Glaciology*, **39**(132): 255-265.
- Vere, D. and D. Benn 1989. Structure and debris characteristics of medial moraines in Jotunheimen, Norway: Implications for moraine classification. *Journal of Glaciology*, **35**(120): 276-280.
- Vimeux, F., V. Masson, J. Jouzel, J. Petit, E. Steig, M. Stievenard, R. Vaikmae and J. White 2001. Holocene hydrological cycle changes in the Southern Hemisphere documented in East Antarctica deuterium excess records. *Climate Dynamics*, **17**: 503-513.
- Vincent, C., G. Kappenberger, F. Valla, A. Bauder, M. Funk and E. Le Meur 2004. Ice ablation as evidence of climate change in the Alps over the 20th century. *J. Geophys. Res.*, **109**(D10): D10104.
- von Haast, J. 1871. Notes on the geology of the Central Portion of the Southern Alps, including Mount Cook. *Reports of Geological Exploration during 1870-1871*, **6**: 19-25.
- Vonder Muhll, D., C. Hauck and H. Gubler 2002. Mapping of mountain permafrost using geophysical methods. *Progress in Physical Geography*, **26**(4): 643-660.
- Waddington, E. 1986. Wave ogives. *Journal of Glaciology*, **32**(112): 325-334.
- Waite, A. and S. Schmidt 1962. Gross errors in height indication from pulsed radar altimeters operating over thick ice or snow. *Proceedings of the Institute of Radio Engineers*, **50**(6): 1515.
- Walford, M. 1964. Radio echo sounding through ice shelf. *Nature*, **204**(495): 317.
- Ward, D.J. and R.S. Anderson 2010. The use of ablation-dominated medial moraines as samplers for ¹⁰Be-derived erosion rates of glacier valley walls, Kichatna Mountains, AK. *Earth Surface Processes and Landforms*, **36**(4): 495-512.
- Ward, W. 1952. the physics of deglaciation in central Baffin Island. *Journal of Glaciology*, **2**(11): 9-22.
- Wardle, P. 1973. Variations of the glaciers of Westland National Park and the Hooker Range, New Zealand. *New Zealand Journal of Botany*, **11**: 349-388.
- Washburn, B. 1935. Morainic bandings of Malaspina and other Alaskan glaciers. *Bulletin of the Geological Society of America*, **46**(9/12): 1879-1889.
- Watson, M. 2008. Ground and airborne GPR measurements of ice thickness, Minarets, Mt Cook Range. *GNS Science Report 2008/36*.

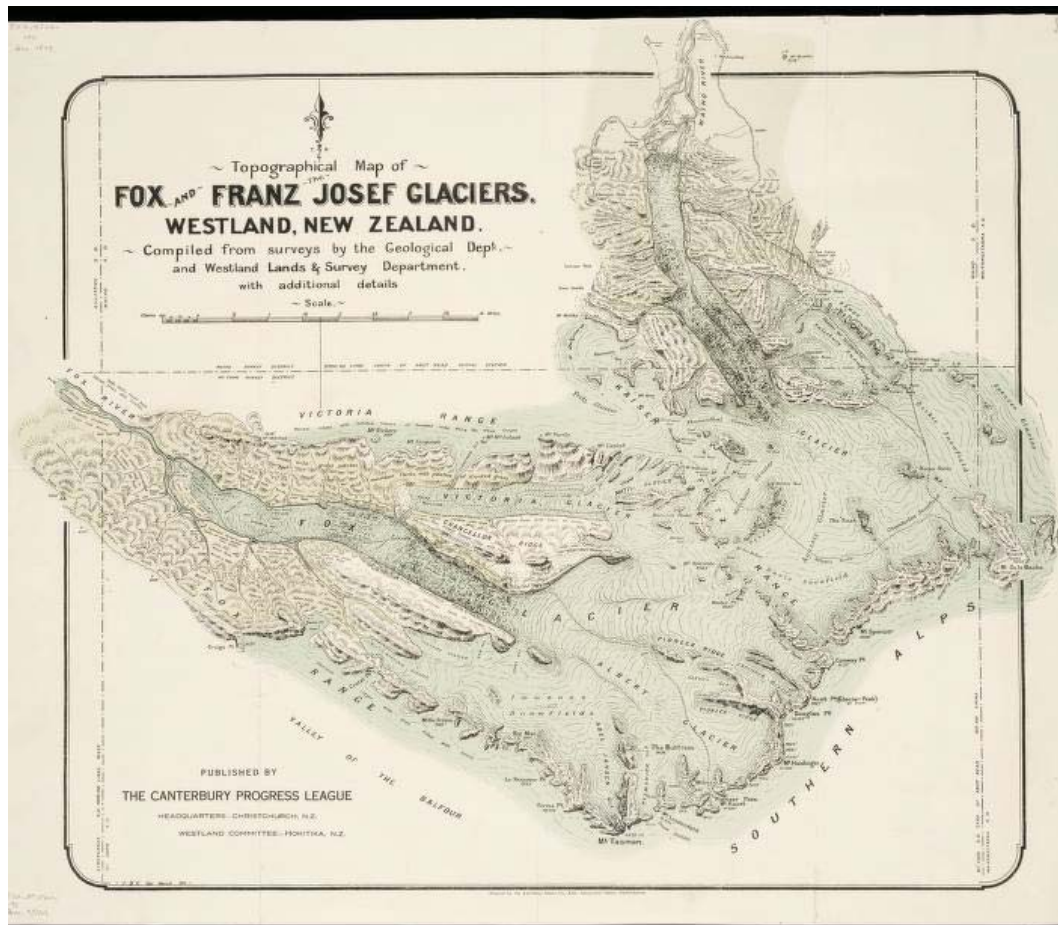
- Watts, R. and D. Wright 1981. Systems for measuring thickness of temperate and polar ice from the ground or from the air. *Journal of Glaciology*, **27**(97): 459-469.
- Weertman, J. 1957. On the sliding of glaciers. *Journal of Glaciology*, **3**: 33-38.
- Weertman, J. 1961. Mechanisms for the formation of inner moraine found near the edge of cold ice caps and ice sheets. *Journal of Glaciology*, **3**: 965-978.
- Weertman, J. 1964. The theory of glacier sliding. *Journal of Glaciology*, **5**: 287-333.
- Weertman, J. and G. Birchfield 1983. Stability of sheet water flow under a glacier. *Journal of Glaciology*, **29**: 374-382.
- Welch, B., T. Pfeffer, J. Harper and N. Humphrey 1998. Mapping subglacial surfaces of temperate valley glaciers by two-pass migration of a radio echo sounding survey. *Journal of Glaciology*, **44**: 1-11.
- Wellman, H. 1955. New Zealand Quaternary tectonics. *Geologische Rundschau*, **43**: 248-257.
- Wellman, H. 1979. An uplift map for the South Island of New Zealand, and a model for uplift of the Southern Alps. In Walcott, R. and M. Cresswell, eds. *The origin of the Southern Alps. Bulletin 18*, Wellington, The Royal Society of New Zealand.
- Wellman, H. and R. Willett 1942. The geology of the West Coast from Abut Head to Milford Sound. Part 2: Glaciation. *Transactions of the Royal Society of New Zealand*: 199-219.
- West, M.E., C.F. Larsen, M. Truffer, S. O'Neel and L. LeBlanc 2010. Glacier microseismicity. *Geology*, **38**(4): 319-322.
- WGMS 2008. Global glacier changes: facts and figures. UNEP, World Glacier Monitoring Service.
- Wild, M., P. Calanca, S.C. Scherrer and A. Ohmura 2003. Effects of polar ice sheets on global sea level in high-resolution greenhouse scenarios. *J. Geophys. Res.*, **108**(D5): 4165.
- Williams, L. and P. Knight 1987. A computer program for plane strain analysis. Aberdeen, University of Aberdeen, Department of Geography. *Discussion paper No.10*.
- Willis, I. 1995. Intra-annual variations in glacier motion: a review. *Progress in Physical Geography*, **19**(1): 61-106.
- Willis, I., W. Lawson, I. Owens, B. Jacobel and J. Autridge 2009. Subglacial drainage system structure and morphology of Brewster Glacier, New Zealand. *Hydrological Processes*, **23**(3): 384-396.
- Willsman, A., J. Salinger and T. Chinn 2008. *Glacier snowline survey 2008*. Auckland, NIWA.

References

- Wilson, W. 1896. The Fox Glacier. *Appendix to the Journal of the House of Representatives of New Zealand*, **C 1**: 108-109.
- Woo, M.-k. and B. Fitzharris 1992. Reconstruction of Mass Balance Variations for Franz Josef Glacier, New Zealand, 1913 to 1989. *Arctic and Alpine Research*, **24**(4): 281-290.
- Woodward, J. 1999. Structural glaciology of Kongsvegen, Svalbard, using ground-penetrating radar. PhD Thesis, University of Leeds.)
- Woodward, J. and M. Burke 2007. Applications of ground-penetrating radar to glacial and frozen materials. *Journal of Environmental and Engineering Geophysics*, **12**(1): 69-85.
- Woodward, J. and E. King 2009. Radar surveys of the Rutford Ice Stream onset zone, West Antarctica: indications of flow (in)stability? *Annals of Glaciology*, **50**(51): 57-62.
- Woodward, J., T. Murray, R. Clark and G. Stuart 2003. Glacier surge mechanisms inferred from ground-penetrating radar: Kongsvegen, Svalbard. *Journal of Glaciology*, **49**(167): 473-480.
- Woodward, J., T. Murray and A. McCaig 2002. Formation and reorientation of structure in the surge-type glacier Kongsvegen, Svalbard. *Journal of Quaternary Science*, **17**(3): 201-209.
- Wu, T. and R. Christensen 1964. Measurement of surface strain-rate on Taku Glacier, Alaska. *Journal of Glaciology*, **5**(39): 305-313.
- Ximenis, L., J. Calvet, D. Garcia, J. Casas and F. Sàbat 2000. Folding in the Johnsons Glacier, Livingston Island, South Shetland Islands, Antarctica. In Maltman, A., B. Hubbard and M. Hambrey, eds. *Deformation of Glacial Materials*, London, Geological Society, 147-157.
- Yamaguchi, S., T. Sawagaki, T. Matsumoto, Y. Muravyev and R. Naruse 2007. Influence of debris cover on ogive-like surface morphology of Bilchenok Glacier in Kamchatka. *Arctic Antarctic and Alpine Research*, **39**(2): 332-339.
- Yamamoto, T., K. Matsuoka and R. Naruse 2004. Observation of internal structures of snow covers with a ground-penetrating radar. *Annals of Glaciology*, **38**: 21-24.
- Zamora, R., D. Ulloa, G. Garcia, R. Mella, J. Uribe, J. Wendt, A. Rivera, Gacit, G. a and G. Casassa 2009. Airborne radar sounder for temperate ice: initial results from Patagonia. *Journal of Glaciology*, **55**: 507-512.

Appendices

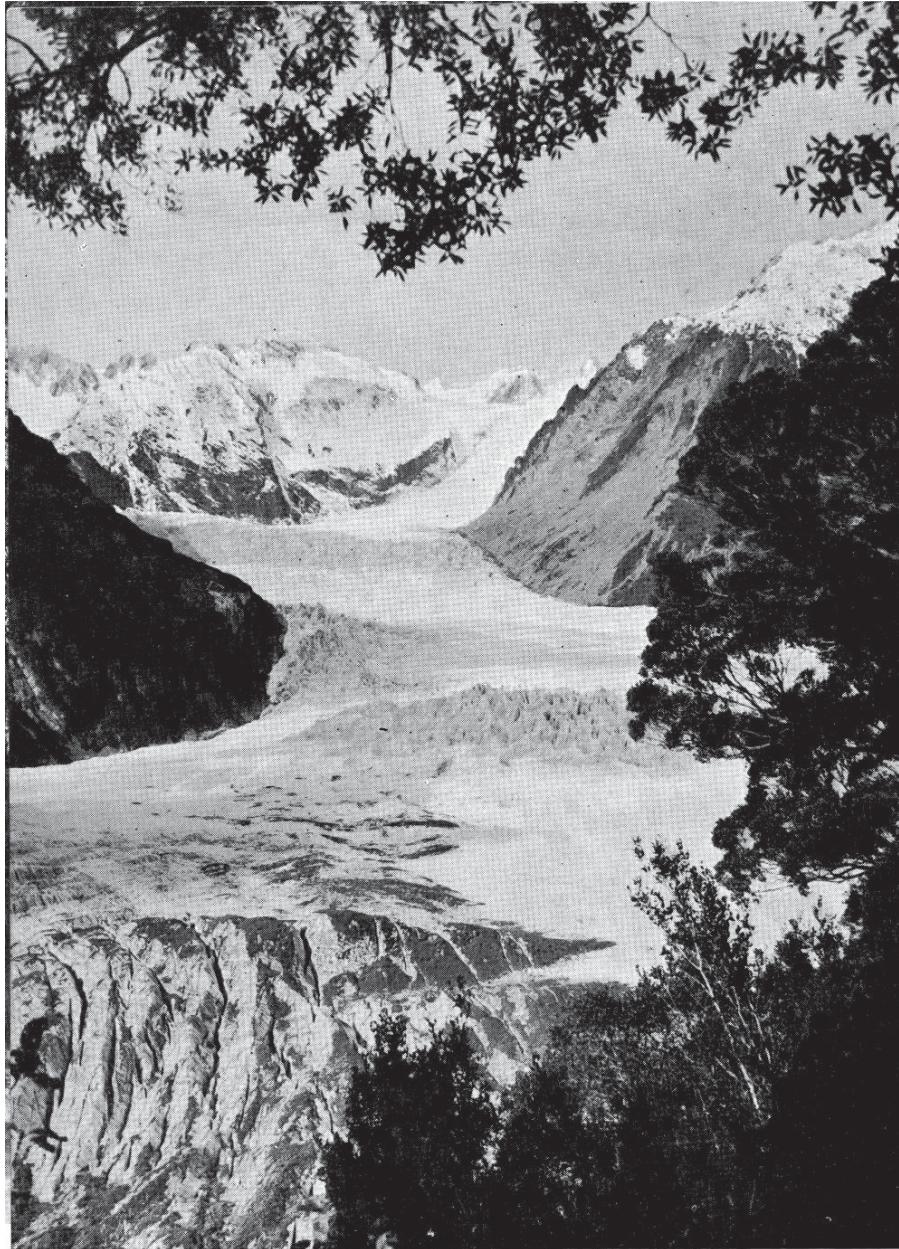
Appendix 1: Structural Evolution Images



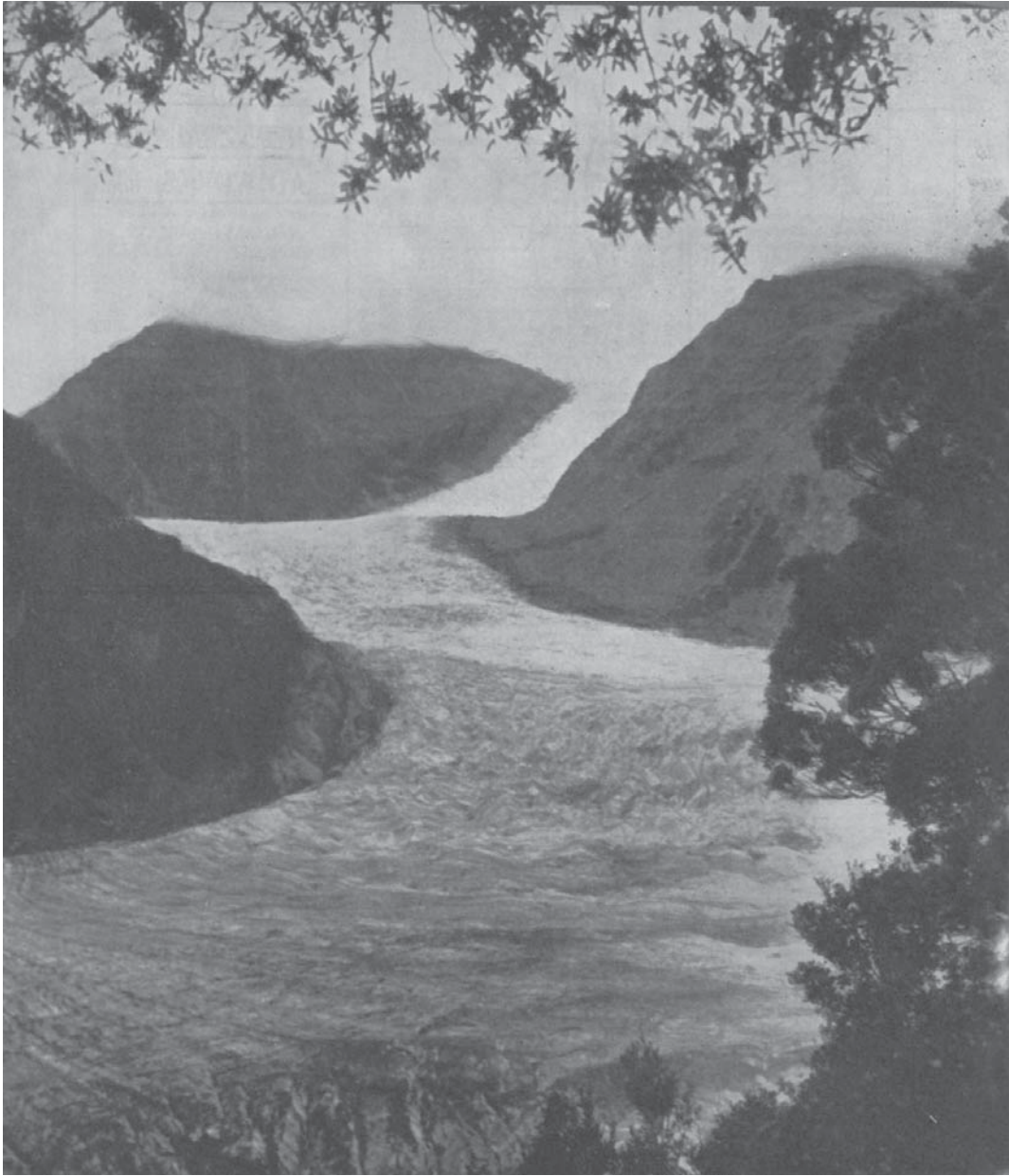
Appendix 1.1: Topographical Map of Fox and Franz Josef Glaciers, Westland, New Zealand (Bell & Grenville, 1911).



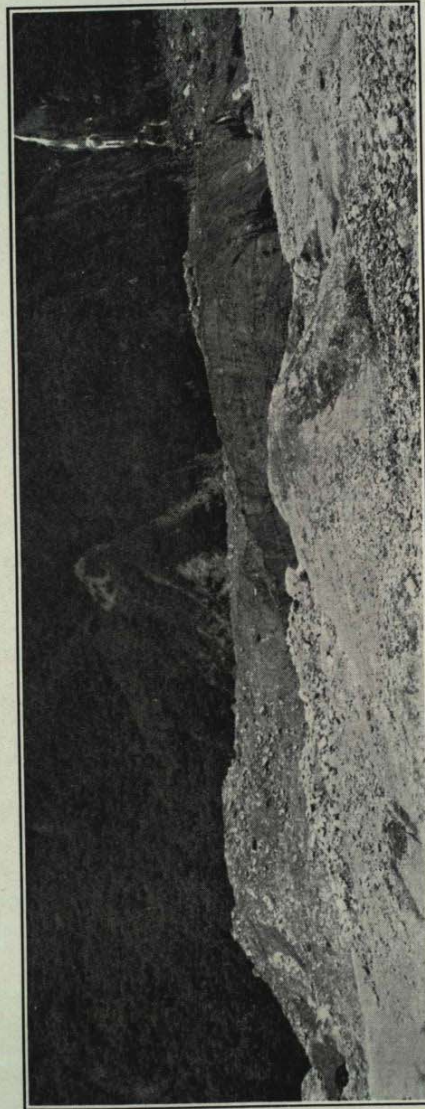
Appendix 1.2: Topographical Plan of Fox Country, Westland (Douglas and Wilson, 1896).



Appendix 1.3: The lower Fox Glacier from Cone Rock in the 1930's (Photo courtesy of Trevor Chinn).



Appendix 1.4: Fox Glacier from Cone Rock in 1936 (Photo courtesy of Trevor Chinn).



View of the frontal part of the Fox Glacier taken from Cairn B on Cone Rock, the spot identical with that from which the picture shown in Plate 61 (*front*, N. 100° E., 641) was taken. The foreground consists of the abandoned bed of the issuing river; in the middle distance is the down-wasted moraine-covered ice. In the earlier picture the ice was higher than the cairn, whereas now the river-bed and the moraine-covered ice is far below it.

To follow plate 141

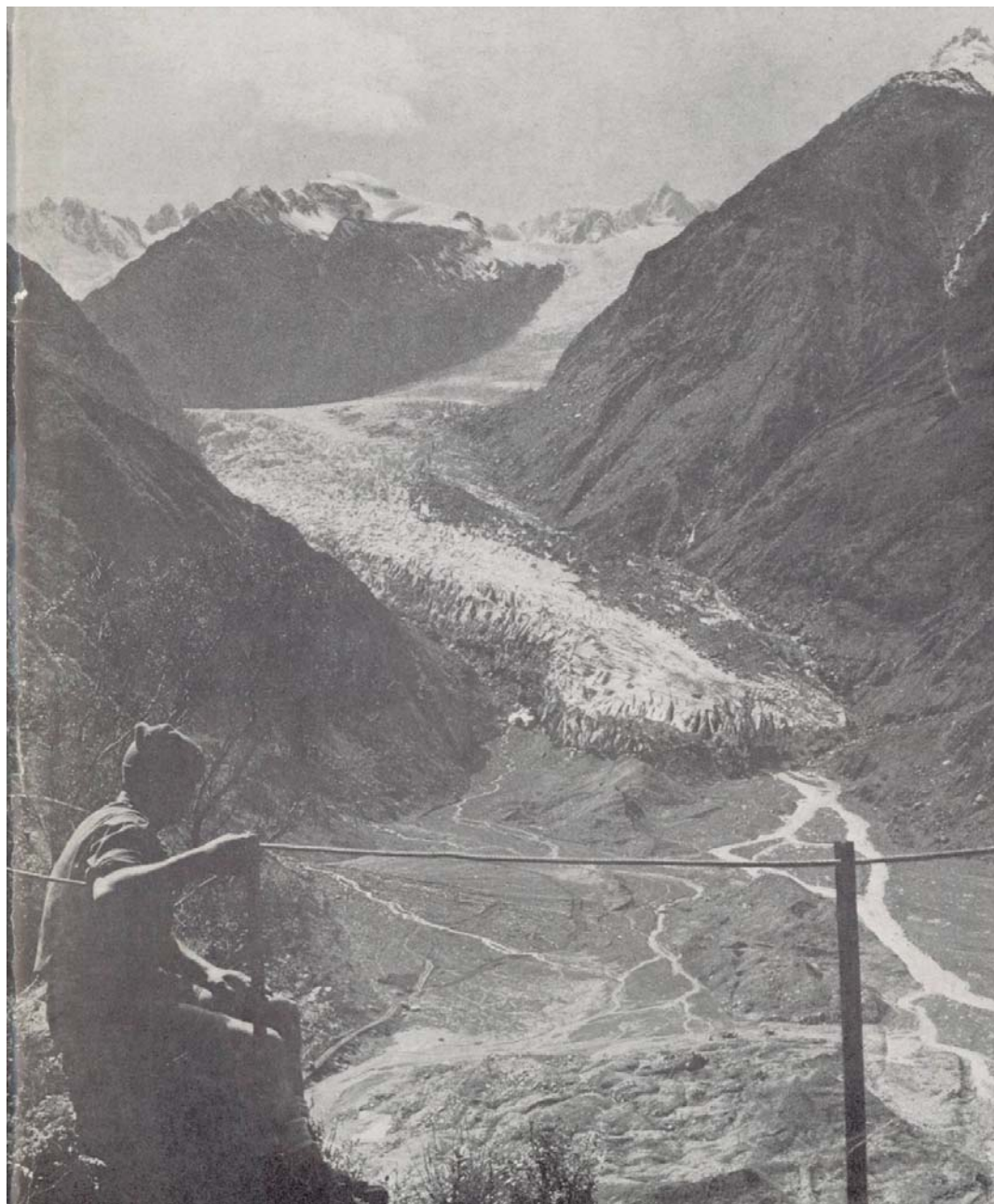
Appendix 1.5: View of the frontal part of Fox Glacier taken from Cone Rock (Speight, 1942).



Appendix 1.6: Fox Glacier terminus in 1948 (Whites Aviation).



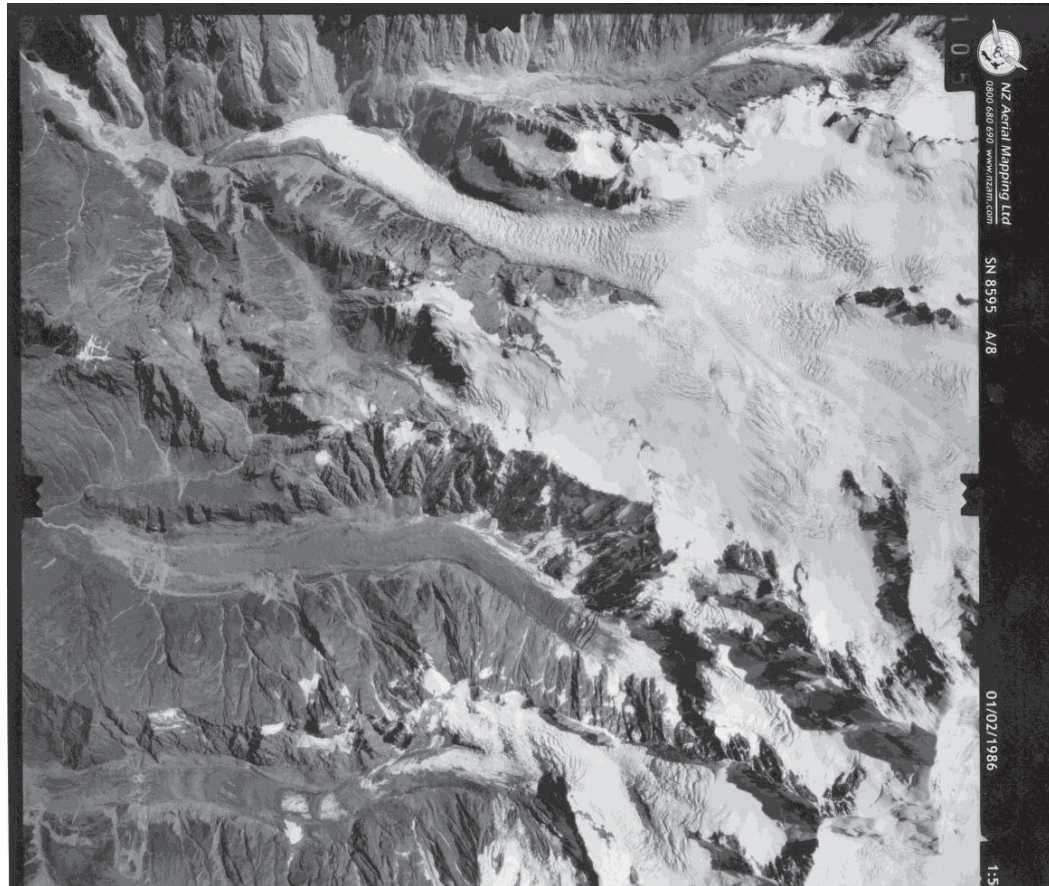
Appendix 1.7: Fox Glacier névé and the Upper IcefallUpper Icefall in 1948 (Whites Aviation).



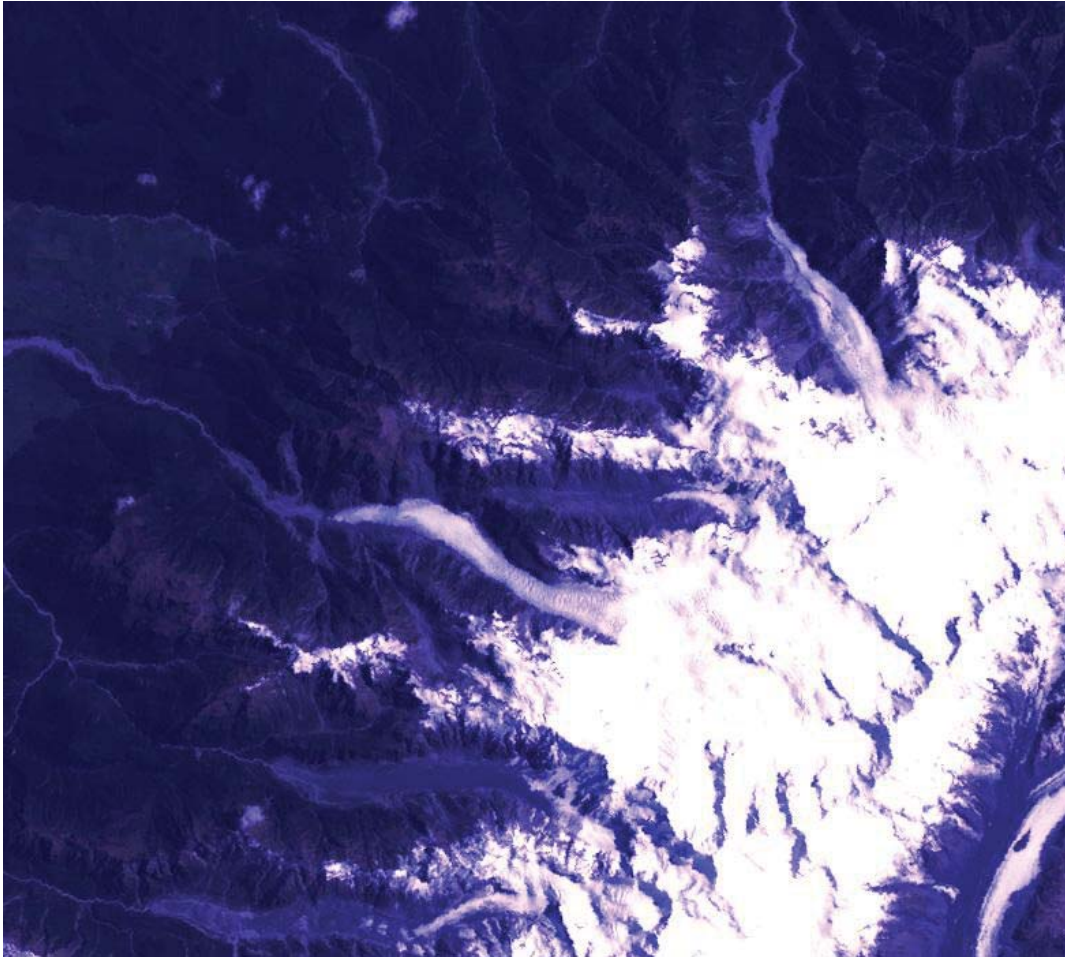
Appendix 1.8: Fox Glacier from Cone Rock in 1966 (Sara, 1970).



Appendix 1.9: Fox Glacier terminus in 1968 (Photo courtesy of Trevor Chinn).



Appendix 1.10: Aerial photograph of Fox Glacier acquired in 1986 (New Zealand Aerial Mapping Ltd).



Appendix 1.11: Landsat image of the Mount Cook Region, March 1990 (courtesy of Mike Tuohy).

Appendix 2: Isotope Analysis Data

Sample	δD (‰ V-SMOW)	St. Dev. ($\pm 1\sigma$)	$\delta^{18}O$ (‰ V-SMOW)	St. Dev. ($\pm 1\sigma$)	<i>d</i> -excess
A3.1	-65.40	0.17	-9.49	0.19	10.52
A3.2	-66.99	0.64	-9.43	0.15	8.49
A3.3	-65.88	0.38	-9.53	0.13	10.34
A3.4	-64.31	0.35	-9.29	0.06	10.03
BASE1.1	-60.46	0.31	-8.90	0.11	10.77
BASE1.2	-60.40	0.25	-8.92	0.12	10.98
BASE1.3	-60.39	0.51	-8.81	0.04	10.07
BASE1.4	-60.22	0.18	-8.64	0.08	8.91
BASE2.1	-65.51	0.30	-9.51	0.10	10.57
BASE2.2	-65.76	0.44	-9.52	0.18	10.42
BASE2.3	-65.20	0.64	-9.53	0.07	11.06
BASE2.4	-64.95	0.47	-9.33	0.17	9.72
B3.1	-63.59	0.30	-9.05	0.13	8.81
B3.2	-62.80	0.31	-9.13	0.16	10.26
B3.3	-63.22	0.38	-9.29	0.15	11.07
B3.4	-62.55	0.23	-9.18	0.05	10.85
L1.1	-65.10	0.45	-9.41	0.17	10.14
L1.2	-65.45	0.31	-9.41	0.13	9.86
L1.3	-62.32	0.35	-9.13	0.11	10.71
L1.4	-62.36	0.62	-9.17	0.18	10.97
L2.1	-69.58	0.48	-10.12	0.05	11.40
L2.2	-70.21	0.30	-10.10	0.15	10.62
L2.3	-71.10	0.09	-10.20	0.05	10.47
L2.4	-71.81	0.23	-10.33	0.08	10.87
L8.1	-59.60	0.51	-8.79	0.14	10.71
L8.2	-59.43	0.57	-8.45	0.37	8.13
L8.3	-59.63	0.29	-8.69	0.15	9.89
L8.4	-59.44	0.18	-8.55	0.18	8.93
T1.1	-64.90	0.50	-9.24	0.14	9.01
T1.2	-65.61	0.54	-9.36	0.05	9.24
T1.3	-69.54	0.34	-9.85	0.06	9.23
T1.4	-67.93	0.25	-9.83	0.14	10.69
T2.1	-64.48	0.02	-9.29	0.09	9.87
T2.2	-66.06	0.06	-9.54	0.11	10.28
T2.3	-65.70	0.08	-9.79	0.04	12.61
T2.4	-64.89	0.53	-9.73	0.04	12.92
T3.1	-63.05	0.07	-9.17	0.04	10.34
T3.2	-63.36	0.54	-9.40	0.15	11.87
T3.3	-64.77	0.22	-9.44	0.00	10.74
T3.4	-64.07	0.08	-9.35	0.03	10.75
T4.1	-60.93	0.73	-9.16	0.11	12.32
T4.2	-61.39	0.39	-9.15	0.12	11.85
T4.3	-61.51	0.25	-9.19	0.06	12.03
T4.4	-60.95	0.33	-9.02	0.04	11.21

Apendices

Sample	δD (‰ V-SMOW)	St. Dev. ($\pm 1\sigma$)	$\delta^{18}O$ (‰ V-SMOW)	St. Dev. ($\pm 1\sigma$)	<i>d</i> -excess
A1.1	-64.05	0.30	-9.37	0.12	10.94
A1.2	-66.37	0.13	-9.52	0.12	9.79
A1.3	-63.33	0.26	-9.36	0.03	11.56
A1.4	-64.88	0.22	-9.39	0.13	10.21
L3.1	-67.30	0.45	-9.80	0.05	11.10
L3.2	-66.98	0.33	-9.65	0.09	10.21
L3.3	-67.03	0.24	-9.76	0.10	11.03
L3.4	-68.37	0.40	-9.76	0.05	9.72
B1.1	-58.07	0.30	-8.37	0.15	8.91
B1.2	-57.87	0.28	-8.52	0.16	10.27
B1.3	-57.81	0.62	-8.25	0.16	8.16
B1.4	-58.05	0.05	-8.27	0.08	8.13
C4.1	-63.24	0.14	-9.12	0.12	9.73
C4.2	-63.29	0.08	-9.16	0.04	9.95
C4.3	-62.89	0.27	-9.06	0.04	9.57
C4.4	-63.17	0.46	-9.08	0.18	9.45
L9.1	-54.92	0.08	-8.07	0.15	9.65
L9.2	-55.43	0.63	-8.24	0.07	10.50
L9.3	-55.19	0.27	-8.29	0.11	11.14
L9.4	-55.29	0.18	-7.97	0.16	8.45
C3.1	-55.48	0.13	-8.25	0.17	10.53
C3.2	-55.10	0.22	-8.32	0.08	11.44
C3.3	-54.98	0.71	-7.83	0.03	7.66
C3.4	-55.19	0.75	-7.42	0.11	4.14
L6.1	-57.64	0.23	-8.34	0.08	9.06
L6.2	-58.08	0.14	-8.48	0.16	9.72
L6.3	-58.38	0.46	-8.24	0.05	7.55
L6.4	-58.72	0.29	-8.15	0.07	6.45
L10.1	-63.45	0.25	-9.13	0.11	9.57
L10.2	-62.20	0.27	-8.75	0.06	7.83
L10.3	-61.99	0.15	-8.41	0.03	5.29
L10.4	-63.57	0.10	-9.04	0.15	8.72
I4.1	-63.18	0.15	-8.93	0.17	8.24
I4.2	-61.73	0.31	-8.93	0.07	9.73
I4.3	-62.75	0.19	-8.71	0.14	6.91
I4.4	-62.29	0.23	-8.95	0.12	9.31
C1.1	-71.88	0.17	-10.05	0.15	8.52
C1.2	-71.50	0.53	-9.72	0.19	6.25
C1.3	-68.87	0.10	-9.68	0.16	8.53
C1.4	-69.24	0.18	-9.81	0.16	9.25
L5.1	-61.44	0.08	-8.94	0.06	10.09
L5.2	-61.20	0.21	-8.95	0.08	10.42
L5.3	-61.21	0.39	-8.83	0.13	9.44
L5.4	-60.83	0.09	-8.97	0.09	10.96
L7.1	-57.85	0.50	-8.27	0.12	8.33
L7.2	-57.27	0.80	-8.41	0.10	9.98
L7.3	-57.79	0.26	-8.31	0.06	8.68
L7.4	-57.50	0.22	-8.40	0.02	9.72

Appendix 3: Clast Analysis Data

Lower Glacier

True Left 1				True Left 2			
a	b	c	Shape	a	b	c	Shape
70	45	22	a	125	62	28	a
83	50	28	a	100	76	16	a
74	41	31	sa	111	67	57	a
104	38	34	sa	113	74	16	va
143	46	22	va	109	40	20	va
67	32	14	sa	125	65	29	a
88	58	21	sa	109	61	45	sa
97	52	25	a	64	55	20	a
60	44	32	sa	147	131	25	a
55	55	27	sa	90	83	42	sa
81	30	22	a	148	59	54	sa
90	50	30	a	106	43	35	sa
116	75	15	va	106	54	12	va
90	40	27	a	111	35	23	a
85	38	33	va	66	46	23	va
123	40	36	sa	131	81	29	a
81	57	21	a	80	46	15	a
180	100	31	va	146	97	32	sa
100	69	29	a	114	49	31	a
81	53	27	sa	87	63	40	va
170	118	33	a	76	74	17	va
132	51	35	a	109	66	15	a
92	83	22	sa	100	60	35	sa
85	61	31	sa	115	65	44	sa
138	67	15	a	103	49	31	sa
110	66	21	sa	94	65	23	a
57	50	33	a	112	84	14	va
134	34	15	a	92	54	26	a
115	42	27	a	103	69	22	a
95	57	25	sa	166	102	21	va
120	76	31	a	97	71	33	a
121	74	41	a	66	36	21	va
140	130	24	va	91	86	44	sa
119	51	30	sa	126	41	37	a
78	61	25	a	152	97	63	a
60	35	20	a	144	55	16	va
78	70	25	sa	103	62	42	a
81	67	25	sa	97	76	52	sa
130	35	30	a	116	69	43	a
81	46	20	a	58	48	12	va
75	60	25	sa	131	102	40	a
100	75	35	a	91	49	35	a
115	44	27	sa	114	53	50	a
85	50	12	a	128	116	14	va
60	40	5	va	77	58	31	sa
77	41	17	a	84	71	21	a
90	54	49	sa	106	63	23	va
94	41	23	a	106	55	44	a
80	35	26	a	92	84	62	sa
58	48	9	a	61	58	8	va

Apendices

True Left 3				True Left 4			
a	b	c	Shape	a	b	c	Shape
110	69	27	sa	132	72	55	va
109	78	65	sa	132	53	16	va
110	75	23	va	105	94	51	a
148	87	50	a	114	94	31	a
100	61	47	a	56	48	23	sa
68	50	28	a	128	72	51	a
102	72	69	a	72	52	30	va
57	46	21	sa	80	54	26	sa
116	44	23	a	171	75	57	a
74	49	17	a	129	95	48	sa
101	57	32	a	93	62	16	va
61	45	23	a	111	61	14	a
82	37	29	a	67	58	18	a
131	79	50	sa	84	71	42	sa
80	67	19	a	51	36	26	sa
165	106	72	sa	95	47	41	sa
132	91	66	sa	92	79	11	va
71	58	24	a	96	56	45	a
45	71	31	a	92	36	22	va
115	73	37	sa	83	54	12	a
69	54	19	a	82	56	28	va
86	62	57	sa	82	63	46	sa
161	111	24	va	79	46	31	a
82	29	23	a	119	36	31	a
132	74	56	a	115	76	18	a
71	34	8	va	100	52	36	a
139	106	17	a	74	42	17	a
167	52	34	a	94	77	17	a
90	66	16	a	91	45	13	va
134	88	24	va	68	56	12	va
82	56	40	a	81	42	20	a
96	86	30	va	86	71	22	a
90	53	10	va	122	85	73	sa
74	62	46	a	71	59	22	a
79	44	17	va	96	88	32	a
134	78	36	a	122	50	49	a
130	45	25	a	79	56	25	va
71	59	46	a	112	88	44	a
114	61	16	va	72	49	9	va
106	85	26	a	132	98	26	a
104	82	40	sa	124	62	56	a
114	81	46	a	95	72	19	va
89	57	42	a	98	45	19	a
131	82	20	va	144	67	12	va
36	59	27	a	79	52	31	a
119	67	30	a	152	64	17	va
101	73	28	a	88	59	15	va
108	52	13	va	92	64	34	a
96	68	41	a	144	79	17	a
76	55	20	a	93	54	42	a

Victoria Flat

True Left 1				True Left 2			
a	b	c	Shape	a	b	c	Shape
56	46	9	a	128	57	36	a
66	42	42	a	73	46	13	va
90	49	15	va	109	72	46	a
74	53	31	a	171	95	28	a
103	86	45	a	92	71	51	a
94	80	46	a	92	54	26	a
66	57	23	va	108	78	24	va
51	30	11	va	67	61	52	sa
51	44	20	a	115	76	46	sa
62	46	29	a	86	45	34	a
74	55	11	va	75	44	33	a
68	39	26	a	164	96	52	va
46	14	9	a	107	52	34	a
145	79	38	a	92	66	56	sa
74	49	9	va	143	58	37	sa
85	42	27	va	60	41	19	a
81	34	16	a	80	40	32	sa
60	42	21	va	112	80	29	a
66	49	34	sa	111	66	55	a
91	84	25	a	61	43	36	sa
64	50	23	a	114	100	31	sa
35	30	10	a	94	50	32	sa
46	34	12	va	91	38	36	a
48	18	14	a	106	84	58	a
76	52	28	a	144	105	30	a
23	21	10	va	75	58	36	va
58	35	7	va	116	56	29	a
54	34	11	a	111	68	29	va
31	21	16	a	74	59	36	sa
94	38	10	va	101	75	31	sa
37	17	8	a	122	76	53	a
65	45	12	va	84	47	34	a
56	44	19	a	76	66	39	a
94	51	17	a	101	62	14	va
49	40	12	a	74	66	28	va
41	29	12	va	89	57	24	sa
54	40	16	a	119	67	34	va
92	54	22	va	146	105	47	a
111	65	23	va	61	34	31	a
60	49	18	a	102	82	33	a
80	51	23	a	106	41	37	a
120	64	19	va	98	25	14	va
155	43	40	va	76	49	49	sa
72	34	17	a	116	56	28	sa
102	51	15	va	56	49	20	a
69	63	22	a	110	72	58	a
130	58	33	a	149	35	21	va
74	57	19	va	86	77	20	va
61	42	32	va	106	86	33	sa
111	64	15	va	164	80	48	a

Apendices

True Left 3

a	b	c	Shape
74	43	23	va
122	78	30	a
109	49	25	a
99	67	18	a
58	52	23	a
136	68	51	sa
101	85	42	a
63	54	36	a
77	56	12	va
181	88	39	sa
97	63	22	va
76	74	31	va
119	62	31	va
162	66	46	a
82	49	30	a
122	94	42	a
153	61	40	a
80	72	23	a
57	61	17	a
71	63	49	sa
59	47	21	sa
115	61	51	a
82	66	25	va
75	46	31	a
147	39	33	sa
126	55	17	a
154	69	27	sa
96	71	38	a
86	57	19	a
73	61	24	a
130	62	23	a
81	38	29	sa
98	61	43	a
94	50	25	a
106	42	31	sa
87	54	40	a
116	50	27	sa
120	70	50	a
93	58	20	va
138	72	16	a
55	41	26	a
92	53	21	sa
85	41	18	a
47	39	12	va
111	74	57	a
100	62	41	sa
94	62	36	a
76	61	42	sa
76	46	12	va
84	72	61	a

True Right 1				True Right 2			
a	b	c	Shape	a	b	c	Shape
90	57	22	a	84	47	41	a
150	80	26	a	41	30	20	a
120	57	44	va	85	47	31	sr
118	95	41	va	41	40	23	a
150	66	32	a	89	78	67	sr
120	61	54	va	61	45	33	a
150	52	25	a	45	39	22	sa
100	61	57	va	51	32	13	sr
106	71	40	a	49	34	13	a
126	72	53	a	57	49	37	a
118	80	44	a	38	26	15	sa
190	78	31	va	73	57	30	va
190	60	40	a	84	66	48	sr
113	59	21	a	120	44	44	sa
118	61	25	a	33	19	16	a
79	49	19	a	50	50	34	sr
52	28	12	sa	98	75	52	a
100	78	24	a	108	54	27	a
130	38	35	a	104	73	65	a
93	66	42	a	70	60	36	sr
98	75	45	va	125	73	67	va
177	55	37	a	87	77	46	sa
115	78	44	sa	110	94	49	a
100	54	54	a	66	55	33	va
77	55	29	a	50	40	26	sa
90	67	36	a	99	63	30	sa
100	82	47	sa	79	57	27	a
192	73	58	sa	95	82	38	sa
116	68	14	a	28	27	18	sr
153	82	32	va	50	43	14	sr
80	62	32	a	30	24	13	va
92	55	21	a	55	28	12	a
125	56	26	a	75	38	38	va
196	97	80	a	44	38	25	sr
95	50	25	a	63	60	42	va
180	24	12	va	41	20	15	sr
76	46	18	va	65	40	19	a
125	77	18	a	58	33	32	a
75	54	30	va	54	29	16	a
192	73	58	sa	52	48	22	a
130	72	40	sa	57	44	30	a
95	50	29	va	34	17	15	sa
105	69	46	a	47	14	14	sa
77	70	19	a	63	48	27	sr
160	90	32	va	33	22	13	a
77	55	35	sa	110	103	58	sr
89	60	20	va	80	69	48	a
115	84	50	a	56	37	26	sr
113	100	76	va	35	35	16	a
89	60	64	va	63	42	27	a

Apendices

Proglacial

a	b	c	Shape	a	b	c	Shape
97	63	57	sa	115	64	40	a
93	49	21	a	66	34	22	sa
117	78	25	a	117	65	38	sr
103	53	35	a	86	50	32	r
75	43	30	sa	120	70	53	sa
41	39	18	sa	119	70	28	sa
121	88	46	a	82	46	38	a
78	65	25	sa	115	70	20	sa
121	88	53	sa	85	76	35	sr
93	65	21	a	105	70	40	sr
75	49	18	va	48	33	12	r
58	43	31	sa	85	54	18	sa
90	53	31	a	115	65	45	sa
50	32	18	a	114	76	28	sr
55	55	31	sa	98	58	30	r
148	61	49	a	72	35	35	sr
128	63	49	sa	86	47	28	va
87	58	35	sr	79	45	30	sr
78	65	18	va	100	78	46	sr
100	68	49	sr	66	48	22	sa
70	24	24	sa	100	73	52	sr
78	45	22	a	60	41	20	sr
22	12	9	sa	96	68	24	sr
27	11	7	a	74	31	29	sr
41	41	24	sa	78	62	21	sr
81	40	30	a	70	61	24	sr
72	44	24	a	82	55	39	sr
38	38	9	a	135	54	30	sa
72	41	18	va	121	83	56	va
70	40	32	a	134	85	36	sa
89	74	36	a	61	40	25	sa
122	115	54	a	48	35	31	sr
101	62	46	a	43	28	20	sa
84	62	24	a	55	35	11	sa
128	83	40	sa	82	61	56	sr
75	74	36	sa	45	31	21	sr
99	73	58	va	33	24	12	r
50	35	22	sa	45	33	31	a
94	53	30	a	83	50	20	a
70	40	32	a	80	53	36	sa
54	27	5	a	152	82	21	sa
86	52	30	sa	41	33	21	sa
150	115	30	sa	102	55	38	sa
129	85	60	va	83	33	31	sa
63	30	12	a	102	75	70	sa
75	61	18	a	94	82	53	a
43	33	22	sa	160	60	37	a
55	50	28	a	75	55	50	a
40	20	15	sa	85	43	20	a
38	30	10	sa	70	50	45	sr

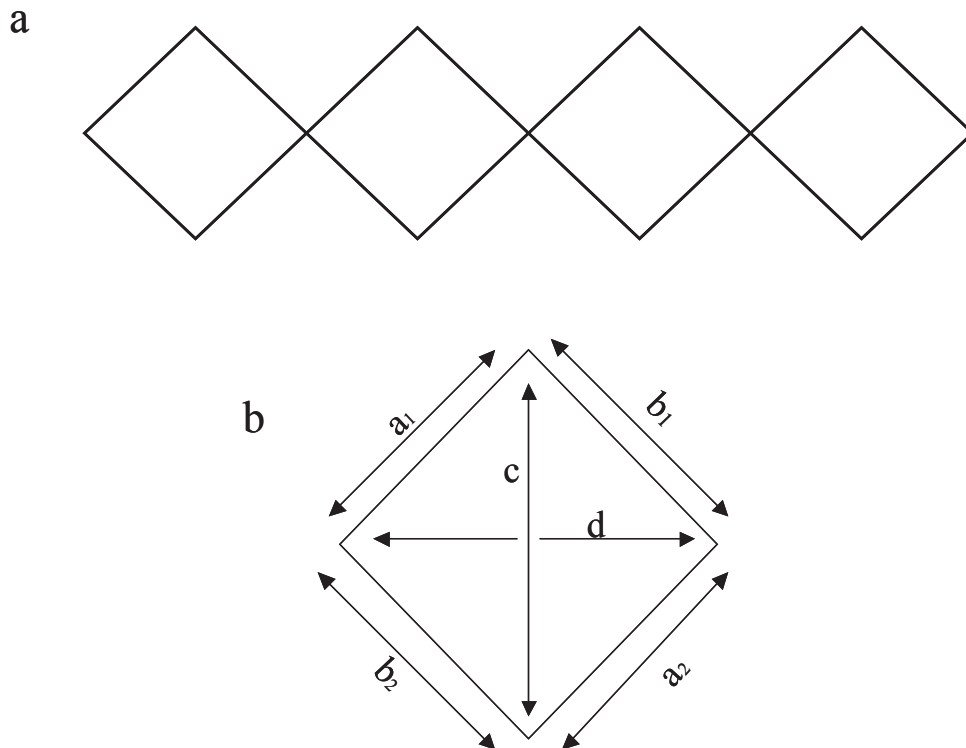
Appendix 4: Mathematical Calculation of Strain

The mathematic method of calculating surface parallel strain rates is given, if software is unavailable:

Determining the Distance between Two Points

The distance d between two points in a plane of known co-ordinates (i.e. point A = (x_1, y_1) and point B = (x_2, y_2)) is given by

$$d = \sqrt{(x_2 - x_1)^2 + (y_2 - y_1)^2} \quad (\text{A 2.1})$$



Appendix 2.1: Idealised pattern of transect polygons to measure deformation of ice surface with each point of the diamonds being an ablation stake (a), and averaged components of deformation vectors (b) with c representing the down-valley y -axis.

Apendices

Equation A 2.1 is used to determine the initial distance between two ablation stakes at the start of the study period and then again at the end of the study period, allowing the deformation in shape of the triangles to be calculated.

Over greater distances, for example ice caps or ice sheets, the haversine formula can be used to determine distance between two points whilst taking into account the curvature of the Earth's surface as described by Sinnott (1984). For two points with latitudes ϕ_1 and ϕ_2 respectively and longitudinal separation $\Delta\lambda$, where angles are in radians on the surface of a sphere (e.g. the Earth) of radius R , the distance d between them is related to their locations by the formula

$$\text{haversine}\left(\frac{d}{R}\right) = \text{haversine}(\phi_1 - \phi_2) + \cos \phi_1 \cos \phi_2 \text{haversine}(\Delta\lambda), \quad (\text{A } 2.2)$$

Where $\Delta\phi = \phi_1 - \phi_2$. Let h denote $\text{haversine}\left(\frac{d}{R}\right)$. Distance d is given by

$$d = R \text{haversine}^{-1}(h) = 2R \arcsin \sqrt{h}. \quad (\text{A } 2.3)$$

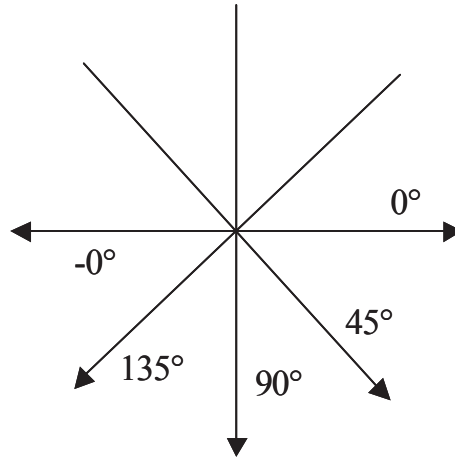
Although intended for greater distances, the haversine formula is still accurate for the distances involved in mountain and valley glaciology, but the curvature of the Earth will be insignificant on this scale. The localised topography of the ice will negate any influence the curvature the plane has.

Measurements made of distance between the stakes of the diamonds will yield six values for change in distance ϵ . Averaging the intervals a_1 & a_2 , and b_1 & b_2 then reduces these six measurements into four, which give us values of ϵ corresponding to the directions $\theta = 0, 45, 90,$ and 135° relative to the centre point of the diamond (Appendix 2.2).

According to Nye (1959) an immediate check on consistency comes from the fact that theoretically

$$\dot{\epsilon}_0 + \dot{\epsilon}_{90} = \dot{\epsilon}_{45} + \dot{\epsilon}_{135}.$$

(A 2.4)



Appendix 2.2: Angle θ of averaged change in distance $\dot{\epsilon}$ relative to the centre of a diamond. The average of a_1 & a_2 produces a change in the 135° direction, b_1 & b_2 in the 45° direction and c in the 90° direction, whilst any change in d is shown in the 0° direction.

Determining Strain Rate of Surface Ice

The values of three strain rate components $\dot{\epsilon}_x$, $\dot{\epsilon}_y$, and $\dot{\epsilon}_{xy}$ can be determined from the four distance $\dot{\epsilon}$ measurement using the simplified equation system

$$\begin{aligned} \dot{\epsilon}_x &= -\frac{1}{4} \dot{\epsilon}_0 + \frac{1}{4} \dot{\epsilon}_{45} + \frac{1}{4} \dot{\epsilon}_{90} + \frac{1}{4} \dot{\epsilon}_{135} \\ \dot{\epsilon}_{xy} &= \frac{1}{2} \dot{\epsilon}_{45} - \frac{1}{2} \dot{\epsilon}_{135} \\ \dot{\epsilon}_y &= \frac{3}{4} \dot{\epsilon}_0 + \frac{1}{4} \dot{\epsilon}_{45} - \frac{1}{4} \dot{\epsilon}_{90} + \frac{1}{4} \dot{\epsilon}_{135} . \end{aligned}$$

(A 2.5)

Apendices

The full method of reaching this system using four simultaneous linear equations is described by Nye (1957).

The measured strain rates are simply determined by comparing these $\dot{\epsilon}$ values with a certain unit of time, in this case the study period.. Once these strain components are known, the magnitude and direction of the principal strain rate can be graphed using Mohr's Circles. The major principal strains can be denoted by $\dot{\epsilon}_1$ and $\dot{\epsilon}_3$, with the angle between the y-axis and the $\dot{\epsilon}_1$ vector being denoted by θ . Assuming there has been no area change of the diamond, an intermediate strain $\dot{\epsilon}_2$ can be determined by means of the relationship

$$\dot{\epsilon}_1 + \dot{\epsilon}_2 + \dot{\epsilon}_3 = 0 .$$

(A 2.6)

Appendix 5: Strain Data

Transect	Polygon	Triangle	Change	Primary d	Secondary d	Transect	Polygon	Triangle	Change	Primary d	Secondary d
Albert	A	1	A-B	46.00	47.00	Victoria	A	1	A-B	19.00	18.00
Albert	A	1	B-C	50.00	52.00	Victoria	A	1	B-C	18.00	16.00
Albert	A	1	C-A	60.00	59.00	Victoria	A	1	C-A	16.00	15.00
Albert	A	2	A-B	56.00	56.00	Victoria	A	2	A-B	17.00	16.00
Albert	A	2	B-C	49.00	45.00	Victoria	A	2	B-C	18.00	18.00
Albert	A	2	C-A	60.00	59.00	Victoria	A	2	C-A	16.00	15.00
Albert	B	1	A-B	48.00	49.00	Victoria	B	1	A-B	19.00	19.00
Albert	B	1	B-C	50.00	51.00	Victoria	B	1	B-C	18.00	18.00
Albert	B	1	C-A	49.00	48.00	Victoria	B	1	C-A	15.00	14.00
Albert	B	2	A-B	50.00	52.00	Victoria	B	2	A-B	15.00	15.00
Albert	B	2	B-C	53.00	55.00	Victoria	B	2	B-C	16.00	17.00
Albert	B	2	C-A	49.00	48.00	Victoria	B	2	C-A	15.00	14.00
Albert	C	1	A-B	48.00	48.00	Victoria	C	1	A-B	23.00	22.00
Albert	C	1	B-C	51.00	52.00	Victoria	C	1	B-C	14.00	14.00
Albert	C	1	C-A	45.00	45.00	Victoria	C	1	C-A	18.00	18.00
Albert	C	2	A-B	52.00	54.00	Victoria	C	2	A-B	20.00	22.00
Albert	C	2	B-C	64.00	66.00	Victoria	C	2	B-C	10.00	12.00
Albert	C	2	C-A	45.00	45.00	Victoria	C	2	C-A	18.00	18.00
Pioneer	A	1	A-B	49.00	47.00	Victoria	D	1	A-B	16.00	16.00
Pioneer	A	1	B-C	54.00	57.00	Victoria	D	1	B-C	15.00	13.00
Pioneer	A	1	C-A	58.00	57.00	Victoria	D	1	C-A	13.00	12.00
Pioneer	A	2	A-B	54.00	53.00	Victoria	D	2	A-B	15.00	14.00
Pioneer	A	2	B-C	55.00	58.00	Victoria	D	2	B-C	15.00	14.00
Pioneer	A	2	C-A	58.00	57.00	Victoria	D	2	C-A	13.00	12.00
Pioneer	B	1	A-B	50.00	54.00	Lower	A	1	A-B	21.00	21.00
Pioneer	B	1	B-C	47.00	54.00	Lower	A	1	B-C	19.00	20.00
Pioneer	B	1	C-A	49.00	47.00	Lower	A	1	C-A	21.00	22.00
Pioneer	B	2	A-B	46.00	55.00	Lower	A	2	A-B	22.00	22.00
Pioneer	B	2	B-C	49.00	50.00	Lower	A	2	B-C	21.00	21.00
Pioneer	B	2	C-A	49.00	47.00	Lower	A	2	C-A	21.00	22.00
Pioneer	C	1	A-B	51.00	51.00	Lower	B	1	A-B	22.00	22.00
Pioneer	C	1	B-C	54.00	48.00	Lower	B	1	B-C	21.00	19.00
Pioneer	C	1	C-A	54.00	50.00	Lower	B	1	C-A	19.00	19.00
Pioneer	C	2	A-B	42.00	44.00	Lower	B	2	A-B	22.00	21.00
Pioneer	C	2	B-C	43.00	45.00	Lower	B	2	B-C	22.00	22.00
Pioneer	C	2	C-A	54.00	50.00	Lower	B	2	C-A	19.00	19.00
Ridge	A	1	A-B	57.00	58.00	Lower	C	1	A-B	28.00	27.00
Ridge	A	1	B-C	58.00	59.00	Lower	C	1	B-C	24.00	23.00
Ridge	A	1	C-A	61.00	60.00	Lower	C	1	C-A	15.00	14.00
Ridge	A	2	A-B	39.00	39.00	Lower	C	2	A-B	18.00	17.00
Ridge	A	2	B-C	41.00	41.00	Lower	C	2	B-C	14.00	14.00
Ridge	A	2	C-A	61.00	60.00	Lower	C	2	C-A	15.00	14.00
Ridge	B	1	A-B	71.00	73.00	Lower	D	1	A-B	18.00	17.00
Ridge	B	1	B-C	66.00	67.00	Lower	D	1	B-C	17.00	17.00
Ridge	B	1	C-A	59.00	58.00	Lower	D	1	C-A	18.00	21.00
Ridge	B	2	A-B	38.00	39.00	Lower	D	2	A-B	15.00	16.00
Ridge	B	2	B-C	38.00	38.00	Lower	D	2	B-C	16.00	15.00
Ridge	B	2	C-A	59.00	58.00	Lower	D	2	C-A	18.00	21.00
Ridge	C	1	A-B	77.00	79.00						
Ridge	C	1	B-C	67.00	69.00						
Ridge	C	1	C-A	56.00	57.00						
Ridge	C	2	A-B	36.00	37.00						
Ridge	C	2	B-C	36.00	36.00						
Ridge	C	2	C-A	56.00	57.00						